Applications of Cosmogenic Nuclides in Understanding Quaternary Events

A thesis submitted in partial fulfilment of

the requirements for the degree of

Doctor of Philosophy

by

Partha Sarathi Jena

(Roll No. 17330021)

Under the guidance of

Prof. Ravi Bhushan

Geosciences Division

Physical Research Laboratory, Ahmedabad, India

Discipline of Earth Sciences

Indian Institute of Technology Gandhinagar, India

2022

Dedicated to

My Parents

DECLARATION

I declare here that this thesis report represents my own ideas in my own words, and I have included others' ideas with appropriate citations from original sources. I also declare that I have followed all principles of academic honesty and integrity and have not misrepresented or fabricated or falsified any idea/fact/source/data in my submission. I understand that any violation of the above can cause disciplinary action by the Institute and can also evoke penal action from the sources which have thus not been properly cited or from whom proper permission has not been taken when needed.

Partha Sarathi Jena

Date: (Roll No.: 17330021)

Discipline of Earth Sciences

Indian Institute of Technology, Gandhinagar

Gujarat-382355

CERTIFICATE

It is certified that the work contained in the thesis titled **"Applications of Cosmogenic Nuclides in Understanding Quaternary Events"** by **Mr. Partha Sarathi Jena** (Roll no: 17330021) has been carried out under my supervision and that this work has not been submitted elsewhere for a degree. I have read this dissertation, and in my opinion, it is fully adequate, in scope and quality, for the degree of Doctor of Philosophy.

Prof. Ravi Bhushan
(Thesis Supervisor)
Geosciences Division,
Physical Research Laboratory,
Ahmedabad, India **Date:**

Acknowledgements

Finally, the incredible journey with hurdles and joyous experiences comes to an end. I thank everyone for being associated with this journey by showing your support, being part of the fun occasions, and sharing encouraging words during difficult times.

I wish to express profound gratitude to my mentor Prof. Ravi Bhushan for the extensive support he provided during this period. I believe this thesis is a result of the freedom to work that he offered in the lab. As I continue this journey as a researcher, I will always be grateful to him for not only being a guide but also a friend during these days.

I would also like to express my sincere regard to my DSC members, Dr. Anil Shukla, Prof. M. G. Yadava, and Prof. Dibyendu Chakraborty, for their helpful discussions, evaluation, and crucial comments. I'm grateful to Navin Sir (Dr. Navin Juyal; my Quaternary Guruji) for helping me look at the Himalaya through a geologist's vision. I also had the great pleasure of working with Shubhra Di (Dr. Shubhra Sharma), who has been an outstanding mentor and collaborator throughout this period. I would also like to extend my deepest gratitude to geoscience faculty members at PRL, Prof. R. D. Deshpande, Prof. J. S. Ray, Dr. Arvind Singh, Dr. N. Rastogi, Dr. Sanjeev Kumar, Dr. A. K. Sudheer, Dr. V. Goswami, and Dr. A. H. Laskar for their valuable inputs and comments during area seminars. This PhD thesis would not have been possible without the support of the director, dean, academic committee members of PRL, as well as IITGN academics. I would also like to acknowledge the support of the staff members of the PRL library, computer centre, administration, account section, workshop, CMG, purchase, and stores during this period. I'm deeply indebted to Dr. Raj K Singh (IIT Bhubaneswar), Dr. Rajeev Saraswat (NIO, Goa), and all the members in their respective labs for helping me see the beauty of scientific research during my master's.

I would like to acknowledge the continuous support of my labmates, without which the thesis would have never been completed. I could never thank Harsh Bhai (Dr. Harsh Raj) enough for his guidance and care towards me during the initial research phases and for the radiocarbon lessons. I want to thank Romi (Ms. Romi Nambiar) for her limitless effort in making me learn chemistry. I miss our whole day-long chatter in the lab while performing experiments. I would like to thank Nisha di (Dr. Nisha Bharti) for being the most caring senior and for her delicious food. I would like to show my appreciation to Ankur Bhai, for being a wonderful friend, for being my field partner, and for training me with the graphitisation system. I would like to thank Shivam for taking special care of my beryllium samples and for his endless chit-chat. I am very grateful to Sanjit for the discussions in the lab. Though I could spend less time with Chandana Di, Upasana Di,

Chinmay Bhaiya, and Muruga, they have been amazing seniors, and I would like to thank them all for never leaving a chance to guide me in my work.

I am very grateful to all the chemistry lab members (Mahesh, Anil bhaiya, Satish bhaiya, Damu anna, Subha anna, Venky bhaiya, Naman bhaiya, Rohit, Rahul, Jaldhi, Devaprasad, Chandrima, and Pravin bhai) for their kind support, cooperation, and encouragement during my Ph.D. tenure. I will always cherish the time spent with Pandey Ji (Amit), Atif, Milan Bhai, and Rajesh during the coursework. I should also appreciate my geoscience colleagues Swagatika, Abdur Bhai, Deepak, Sidharth, Deepika di, and Ajayetha for every little support they have extended to me. I gratefully acknowledge the assistance of the members of luminescence, XRF, and planetary remote sensing labs during my sample analysis.

I'm deeply indebted to Tumpa, Tanu, Satya, Himanshu, Sana, and Shanwlee, with whom I shared the most joyous moments. Many thanks to all my batchmates (Pravin, Neeraj, Hrushi, Ritu, Aravind, Ankit, Abhay, Alka, Shivani, Madhu, Sushant, Biswa, Anshika, Subith, Sarika, Ramanuj, Sovan, Sudipta, Tanmay, Vishal, Deepak, Kamlesh, Suraj, Hridesh, Vipin, Abhijeet) for every cheerful occasion we shared either during classes or during IITGN journey. I'd also like to extend my gratitude to people (Vikas, Meghna, Monica, Sunil, Kimi, Yash, Naval, Deepak, Daya, Akanksha, Birendra, Priyank, Harish, Surendra, Binal, Shreya, Mallika, Vineet, Sandip Bhai) who were part of numerous blissful moments while playing badminton, TT, and cricket or during short duration gossips. I am very grateful to my friends from VAB, Rtapalli Vidyapitha, SJC, Ravenshaw University, and IIT Bhubaneswar for the encouragement everyone provided.

I want to thank my parents for their immense love, care, and sacrifice, without which this work would not have been possible. I would like to mention Biju, Silu, Aju, Raju, and Milu (my dear brothers and sisters) for the affection, love, and admiration they have shown for me. I wish to thank my family members and each member of my maternal uncle's house for the care each one has always delivered.

Along with the reviewers, I would like to show my gratitude to a few of my colleagues at PRL for their feedback which helped in improving the thesis.

Although I tried, it is almost impossible to mention everyone who has contributed to this journey of research. I am thankful to every one of them who has supported me both professionally and personally during the completion of this thesis work.

Abstract

The cosmogenic nuclides are produced from the interaction of highly energetic cosmic ray particles with terrestrial and extra-terrestrial material. In this study, both meteoric (formed in the earth's atmosphere) and in-situ (formed on the earth's surface) cosmogenic nuclides were employed to understand paleoclimatic and paleomagnetic processes during the Quaternary period.

In the northwestern (NW) Himalaya the spatial and temporal changes in the late Quaternary glaciation were modulated by a combination of two contrasting moisture sources viz., the Indian Summer Monsoon (ISM) and the mid-latitude westerlies. This study attempts to understand late Quaternary glacier fluctuations in the NW Himalaya and to infer the climatic factors responsible for driving glaciation cycles based on detailed geomorphological mapping and chronology obtained from the Terrestrial Cosmogenic Nuclide (TCN) exposure age dating method. The bedrock-derived ages show less spread (compared to boulders), suggesting a minimal effect of post and pre-depositional changes, and thus, are the most appropriate samples for TCN dating. The oldest Tirith II glaciation event in the Nubra Valley was dated to be Marine Isotopic Stage (MIS)-5/4, while the younger Tirith I (contemporaneous with the Puche Glacier Advance 1 in Ganglas valley) event was dated to be MIS-2. Reduction in temperature was found to be the primary factor driving the late quaternary glaciation in the northwestern Himalaya, while the glaciers were sustained by the moisture derived from the westerly precipitation.

A near-continuous proglacial relict lake sediment succession exposed at Spituk, Leh, was investigated to reconstruct the hydrological changes during the late Quaternary period. The sedimentology supported by geochemical proxies indicates that the lake sedimentation was modulated by the hydrological fluctuations controlled by the valley glaciers. The varve sedimentation between 27.5 ka and 22 ka indicates an overall cold phase. This hypothesises that the valley glaciers began to expand, although there was moderate humidity. The increase in precipitation during mid MIS-2 can be attributed to the enhanced contribution from the westerlies.

Based on beryllium isotopic measurements on surface sediments from the central and northern Indian Ocean, an attempt has been made to understand the processes controlling beryllium isotopic distribution. Owing to higher terrestrial flux, the sediment samples from the Bay of Bengal show a high ^{9}Be concentration and a low $^{10}Be/^{9}Be$ ratio. The study suggests that scavenging by sediment particles plays a vital role in the distribution of Be isotopes in well-mixed open ocean. The higher residence time of beryllium observed in the central Indian Ocean indicates low scavenging in the water column due to reduced particulate concentration.

$^{10}Be/^{9}Be$ records estimated from the marine sediment cores have the potential to serve as an important proxy to reconstruct past geomagnetic field strength. High-resolution beryllium isotopic measurement in a sediment core (SK-312/10) from the central Indian Ocean shows a higher $^{10}Be/^{9}Be$ ratio during 26 to 21 ka, which can be associated with lower geomagnetic field strength. A peak of $^{10}Be/^{9}Be$ ratio observed at ~ 41 ka in two sediment cores (SK-312/09 and 08), can be ascribed to the Laschamp event. During this event, a ~ 40-60% increase in the $^{10}Be/^{9}Be$ ratio was observed, which can be attributed to an increase in ^{10}Be production due to low geomagnetic field intensity.

One of the essential components of Quaternary studies is the use of appropriate dating techniques to build chronology of the marine sediment cores. With a relatively long half-life of 1.39 Ma, cosmogenic ^{10}Be has the potential to provide chronology of marine sediment cores as old as 10-12 Ma. We present the results of measurements made in a sediment core from the central Indian Ocean for both beryllium isotopes (^{10}Be and ^{9}Be). While ignoring the points showing a high anomalous $^{10}Be/^{9}Be$ ratio (associated with magnetic field intensity variation), a continuous decrease in the $^{10}Be/^{9}Be$ ratio with depth was observed. Based on the decay of ^{10}Be, the 5.7 m long sediment core was dated to be ~ 350 ka with an average sedimentation rate of 1.6 cm/ka.

To summarise, the present study has exploited the use of cosmogenic nuclides (^{10}Be, and ^{14}C) to investigate paleoclimatic and paleomagnetic studies. The study could delineate the major factors driving the Quaternary glaciation in the NW Himalaya using both glacial and paleolake deposits. Significantly diverse Be isotopic distribution and residence time of Be observed in the central and northern Indian Ocean Basins indicates strong control by terrestrial flux. Temporal records of Be isotope show a drastic increase in ^{10}Be production during the Laschamp event (~41 ka). Based on the ^{10}Be decay method, the applicability of meteoric ^{10}Be to date marine sediment cores older than the radiocarbon dating limit has been established.

Contents

List of Figures

List of Tables

Abbreviations

AGE	:	Automated Graphitisation Equipment
AMS	:	Accelerator Mass Spectrometer
AURiS	:	Accelerator Unit for Radioisotope Studies
BoB	:	Bay of Bengal
BP	:	Before Present
CAM	:	Central Age Model
CHS	:	Carbonate Handling System
CID	:	Charge Injection Device
CIW	:	Chemical Index of Weathering
CRM	:	Chemical Remanent Magnetisation
DBD	:	Dry Bulk Density
DC	:	Dead Carbon
DR	:	Dose Rate
DRM	:	Depositional Remanent Magnetization
EA	:	Elemental Analyser
Ed	:	Equivalent Dose
ESA	:	Electrostatic analyser
ESR	:	Electron Spin Resonance
FIRI	:	Fourth International Radiocarbon Intercomparison
GB	:	Gas Bench
GCC	:	Gas Chromatographic Column
GIC	:	Gas Ionisation Chamber
HE	:	High Energy
HOSS	:	High Organic content Sediment Standard
HVEE	:	High Voltage Engineering Europa
IAEA	:	International Atomic Energy Agency
IC	:	Inorganic Carbon

ICP-OES	:	Inductively Coupled Plasma Optical Emission Spectrometer
IRMS	:	Isotopic Ratio Mass Spectrometer
IRSL	:	Infrared Stimulated Luminescence
ISM	:	Indian Summer Monsoon
ITCZ	:	Inter Tropical Convergence Zone
LE	:	Low Energy
LGM	:	Last Glacial Maxima
LOSS	:	Low Organic content Soil Standard
MIS	:	Marine Isotopic Stage
NADW	:	North Atlantic Deep Water
OC	:	Organic Carbon
OD	:	Oldest Dryas
OSL	:	Optically Stimulated Luminescence
PDRM	:	Post Depositional Remanent Magnetization
RF	:	Radio Frequency
SWJ	:	Subtropical Westerly Jet stream
TCN	:	Terrestrial Cosmogenic Nuclide
TRM	:	Thermoremanent Magnetisation
VADM	:	Virtual Axial Dipole Moment
VFC	:	Voltage-to-Frequency Converter
VPDB	:	Vienna Pee Dee Belemnite
VIRI	:	Fifth International Radiocarbon Intercomparison
WD	:	Western Disturbance
XRF	:	X-Ray Fluorescence
YD	:	Younger Dryas

Chapter 1 Introduction

1.1 Current Understanding

The Quaternary period (spanning between 2.6 Ma to the present) has undergone several glacial and deglacial cycles due to changes in the Earth's orbit around the sun, along with plate tectonics and atmospheric CO_2 variations (Broecker et al., 1968; Sarnthein et al., 2003). These glacial-interglacial intervals within the Quaternary period are further divided into cold and warm periods, defined as Marine Isotopic Stages (Emiliani, 2015). During these cold and warm periods, significant changes in the polar ice sheet volume have been discerned due to temperature change, and signatures of these fluctuations are observed in global records (Grootes and Stuiver, 1997; Gupta et al., 2006; Johnsen et al., 1997; Thompson et al., 1997; Wang et al., 2001).

However, the low-latitude mountain glaciers show complex variabilities. For example, in the Himalayan regions, glaciers show drastic spatial as well as temporal variability based on the complex interactions of climate (temperature and precipitation) as well as topography (Ali et al., 2013; Benn and Owen, 2002, 1998). Further, it has also been observed that the Himalayan glaciers get strongly modulated by a combination of two contrasting moisture sources (viz., the Indian Summer Monsoon and the mid-latitude westerlies) (Benn and Owen, 2002). Detailed investigation of glacial landforms based on geomorphological mapping and appropriate chronology would help infer the climate factors responsible for driving glaciation cycles in the Himalayan region (Ali et al., 2013). Yet, in the northwestern Himalaya, the strong divergence observed in the chronology obtained from previous studies restricts from drawing any proper climatic inferences (Dortch et al., 2010; Ganju et al., 2018; Nagar et al., 2013; Owen et al., 2006; Shukla et al., 2020). On the other hand, it has been suggested that the sediments from proglacial lakes provide a near-continuous record of glacier dynamics and climate variability, which can be used to reconstruct the glacier fluctuations at centennial and millennial time scales (Benn

and Owen, 1998; Dahl and Nesje, 1996; Karlen and Matthews, 1992; Ohlendorf et al., 1997). The proglacial lakes are intrinsically linked to climate through the surface energy balance and wide geological systems through glacier dynamics, glacial meltwater, and sediment fluxes (Larsen et al., 2011). In view of this, it is evident that there is a dire need for an extensive exploration based on glacial and lacustrine deposits to reconstruct the chronology of glaciation in the northwestern Himalaya, which will help understand the glacial response to Quaternary climate change.

During the Quaternary period, the Earth has undergone significant changes in geomagnetic field intensity, starting from small-scale secular variations to major reversals and excursions (Valet, 2003). Paleomagnetic information retrieved from both sediments and lava flows has provided crucial learning about geomagnetic field characteristics (Valet, 2003). Yet these records are discontinuous in time scale, and continuous records can be retrieved by analysing magnetic minerals in sediment cores. However, various syn-depositional and post-depositional processes tend to modify the magnetic mineral deposition, introducing further complexities in these records (Simon et al., 2020). Hence, additional records unaffected by such processes can provide a crucial understanding to our current knowledge of the geomagnetic field.

Chronological methodologies play an increasingly important role in Quaternary studies. The widely used techniques used in dating marine sediment cores are radioisotope dating, stratigraphic chronology (utilising $\delta^{18}O$ of foraminifera as well as magnetostratigraphy), luminescence, and Electron Spin Resonance (ESR) dating (Li et al., 2021). In the Indian Ocean, most of the Quaternary studies are limited to the last 50 ka, and ^{14}C (longer sediment cores) and ^{210}Pb (short and coastal sediment cores) methods are the most widely used for chronology (i.e., Bhushan et al., 2019a, 2001; Chandana et al., 2017; Nambiar et al., 2020; Shah et al., 2020). Limited studies have utilised the stratigraphic and natural radionuclides to date older sediment cores (Beaufort, 1996; Bolton et al., 2013; Gupta et al., 2006; Pattan et al., 2005). This suggests a need for the development of chronological methods based on which chronologies can be extended beyond the radiocarbon dating limit.

The cosmogenic nuclides have played a crucial role in Quaternary studies in providing chronology, deciphering rates of Earth processes, carbon cycle, and paleo

reconstruction studies. Cosmogenic Nuclides are produced through the interaction of highly energetic cosmic ray particles with terrestrial and extra-terrestrial material. The cosmogenic nuclides are produced in the earth's atmosphere (defined as meteoric cosmogenic nuclides) as well as exposed rocks on the earth's surface (defined as in-situ cosmogenic nuclides). The cosmogenic nuclides (particularly ^{10}Be) have been extensively utilised in Quaternary research for paleoclimatic and paleomagnetic studies. Hence, based on the above-mentioned research gaps, the present study was designed to utilise cosmogenic ^{10}Be (along with ^{14}C) to understand Quaternary processes. ^{10}Be exposure age dating of glacial landforms as well as sedimentological and geochemical analysis of a paleolake sequence has been utilised in the present study to understand Quaternary glaciation in the northwestern Himalaya. Cosmogenic records from marine sediment cores have been utilised to understand past geomagnetic field intensity variations as the production gets modulated by geomagnetic field strength. With a half-life of 1.39 Ma, ^{10}Be can be used to date marine sediment cores up to ~10 Ma. Its efficiency in dating marine sediment cores beyond the radiocarbon limit has been tested and ascertained in the study. To summarise, both meteoric and in-situ cosmogenic nuclides have been potentially utilised to understand paleoclimatic and paleomagnetic processes during the late Quaternary period.

1.2 Cosmic Ray and Cosmogenic Nuclides

1.2.1 Cosmic Ray

Cosmic rays are high-energy, charged particles that intrude on the Earth from all directions. The typical energy levels of cosmic rays range from a few MeV up to ~10^{20} eV. At the top of the earth's atmosphere, the cosmic rays are primarily composed of protons (87 %), α-particles (12 %), and a minor contribution from heavier nuclei (~1%). The cosmic rays ray can be divided into two types based on their origin, i.e., galactic cosmic rays and solar cosmic rays. The galactic cosmic rays originate from the outside solar system and have higher energy (mostly between 100 MeV to 10 GeV). On the other hand, low energy (mostly between 1-100 MeV) cosmic rays approach the earth's atmosphere, which has an origin related to solar flares. The solar cosmic rays do not contribute significantly

to cosmogenic nuclide production at the earth's surface (Masarik and Reedy, 1995). Hence, in earth science applications, cosmic rays usually refer to galactic cosmic rays.

1.2.2 Production of Cosmogenic Nuclides

Cosmogenic nuclides are produced due to the interaction of primary and secondary cosmic ray particles with atomic nuclei. At the earth's surface, more than 98% of the cosmogenic nuclide production happens due to secondary cosmic ray particles such as neutrons and muons (Masarik and Beer, 1999).

In spallation reactions, high-energy neutrons (or protons) interact with atomic nuclei and the excited nucleus spalls off fragments (sputter off protons and neutrons), leaving behind a lighter nucleus. The majority of secondary neutrons, which have slowed down due to continuous interaction (Phillips et al., 2001) and have lower energy (~0.025 eV), can also still produce an appreciable amount of cosmogenic nuclides. This process is termed thermal neutron capture. These reactions are supported by the lower total nucleon binding energy of the reaction products, and (n, α) reactions are common (Dunai, 2010). Decelerated negative muons having thermal energy can be captured by the nucleus and produce cosmogenic nuclides in the procedure termed negative muon capture.

Various nuclides are produced due to the interaction of cosmic rays with earth material. Both stable and radioactive cosmogenic nuclides are produced, and a few of them are listed in **Table 1.1**.

Table 1.1: *List of major cosmogenic nuclides* (Dunai, 2010).

Sl. No.	Isotope	Half-life
1	^{3}He	Stable
2	^{10}Be	1.39 ± 0.012 Ma
3	^{14}C	5730 ± 40 yr
4	^{26}Al	708 ± 17 ka
5	^{36}Cl	301 ± 2 ka
6	^{41}Ca	104 ± 4 ka
7	^{53}Mn	3.7 ± 0.4 Ma

1.2.3 Beryllium Isotope Systematics

Beryllium-10 (^{10}Be) is produced in the atmosphere by the interaction of cosmic-ray particles with oxygen and nitrogen (defined as meteoric ^{10}Be) (Dunai, 2010; Lal and Peters, 1967; Masarik and Beer, 1999). After its production, ^{10}Be gets converted mainly to $Be(OH)_2$ and rains on the earth's surface through dry and/or wet deposition after getting attached to atmospheric aerosols (Deng et al., 2020a; McHargue and Damon, 1991). ^{10}Be is also produced due to the interaction of cosmic ray particles with silicon and oxygen in the earth's surface rocks (defined as in-situ ^{10}Be) (Lal and Peters, 1967).

The meteoric ^{10}Be (^{10}Be produced in the atmosphere) has been used to date marine sediments (Bourles et al., 1989; Tanaka and Inoue, 1979) to reconstruct past changes in biogenic particle fluxes and productivity (Frank et al., 2000; Kumar et al., 1995), to reconstruct past changes in the earth's magnetic field strength (Carcaillet et al., 2004a; Christl et al., 2010; Frank et al., 1997; Simon et al., 2016b), to determine denudation rate of river basins (Dannhaus et al., 2018; Deng et al., 2020b; Portenga et al., 2019; Rahaman et al., 2017; Wittmann et al., 2015), as well as to understand variation in past denudation rates (von Blanckenburg et al., 2012). On the other hand, the in-situ ^{10}Be has been extensively utilised for paleo glaciation studies (Dortch et al., 2010; Owen et al., 2006), though it found applications in multiple studies, such as denudation rate estimation (Vance et al., 2003).

The present study has utilised both meteoric and in-situ ^{10}Be to understand Quaternary paleoclimatic and paleomagnetic processes. In-situ ^{10}Be has been used for exposure age dating of glaciation events in the northwestern Himalaya. At the same time, meteoric ^{10}Be has been utilised to understand paleomagnetic changes and to build chronology of marine sediment core. An effort has also been made to access the processes that control the spatial distribution of Be isotopes in the Indian Ocean.

1.3 Response of Himalayan Glaciers to Quaternary Climate Change

The Himalaya-Karakoram region is one of the highly glaciated regions outside the polar region containing ~40,800 km^2 of glacier cover (Bolch et al., 2012). The Himalayan glaciers play an important role in socio-economic development as the meltwater generated from these glaciers supplements the rivers and streams of the region, including several of Asia's great river systems, such as the Indus, the Ganga, and the Brahmaputra. In recent times it has been observed that the glaciers from the higher central Himalaya are retreating at a rapid rate, while glaciers from the western Himalaya are nearly stagnant (Kääb et al., 2015; Zhou et al., 2017). This provides a hint about strong spatial changes in processes controlling the glacier-ice volume. Apart from temperature, the growth of Himalayan glaciers is also controlled by variations in moisture supply and local topography (Benn and Owen, 1998). A complex combination of these factors results in varying growth of valley glaciers in the Himalayan region.

1.3.1 Moisture Sources to the Himalaya: The Indian Monsoon System and Mid-latitude Westerlies

Western Disturbances (WDs) or westerlies are a weather phenomenon that causes precipitation over the Indian region significantly during the winter (December-January-February). WDs are in part extra-tropical cyclones originating as mid-latitude frontal systems and migrating eastward embedded in the Subtropical Westerly Jet stream (SWJ) (Dimri and Chevuturi, 2016). The moisture in the westerly storms is generated over the Mediterranean Sea and the Atlantic Ocean (Dimri et al., 2015). These extra-tropical storms are generally a global phenomenon with moisture usually carried in the upper atmosphere. The frontal systems (discontinuity surfaces) are generated due to the interaction of air masses with varying characteristics, i.e., colder polar and warmer equatorial air masses. The temperature gradient between polar and equatorial regions is most pronounced during the winter, and thus these storms are more intense during the winter (Dimri and Chevuturi, 2016). The vertical structure of westerly disturbances (WDs) is characterised by two

synoptic components, an upper-level trough and a lower-level cyclonic circulation (Singh, 1963). The extra-tropical cyclones move eastward with the upper-level trough in the Subtropical Westerly Jet (SWJ) and subsequently become linked to existing stationary low-level cyclonic circulations forming a WD (Dimri and Chevuturi, 2014).

The Indian Summer Monsoon (ISM) is a part of the Asian Summer Monsoon system. The land-ocean thermal contrast leads to the seasonal reversal of winds. During summer (June-September), the monsoonal winds flow in a south-westerly direction, while, during winter (November-February), the monsoonal winds flow in the opposite (north-easterly) direction (**Figure 1.1**) (Tomczak and Godfrey, 2003).

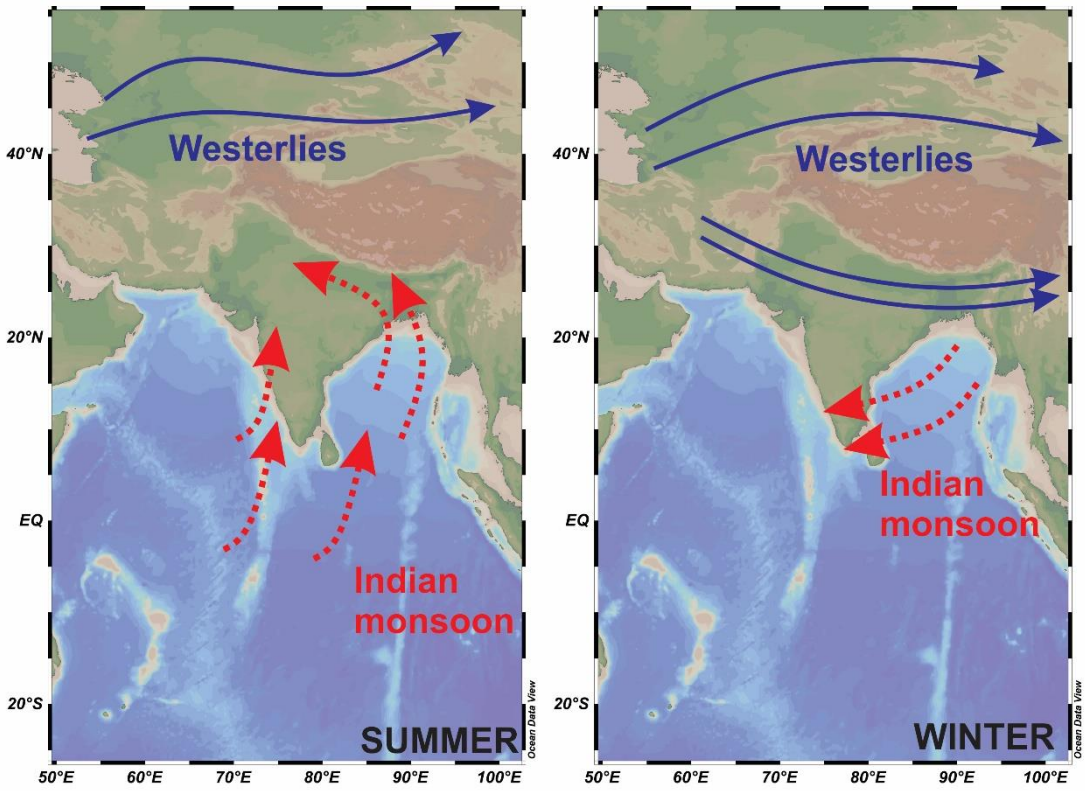

Figure 1.1: *Dynamics of the Indian monsoon system and the westerlies in the Indian subcontinent.*

1.3.2 Chronology of Quaternary Glaciation using Glacial Deposits

There are several techniques developed for dating quaternary glaciation events, such as., radiocarbon dating, luminescence dating, terrestrial cosmogenic nuclides (TCN)

exposure age dating, and electron spin resonance dating. However, considering constraints about suitable dating materials, in the Indian Himalayan region, luminescence dating and the TCN exposure age dating are widely used.

The TCN exposure age dating is based on the production of specific cosmogenic nuclides on a rock surface due to the interaction with cosmic rays. With the available information on the production rate of cosmogenic nuclide known for a particular location and subsequently measuring the cosmogenic nuclide concentration, the time since the surface has been exposed can be estimated (Gosse and Phillips, 2001). For estimating the chronology of glaciation events, commonly, boulders sitting on the top of moraines, erratic boulders, and scoured bedrocks have been used (**Figure 1.2**) (Benn and Owen, 2002; Dortch et al., 2010). For estimation of the exposure age, prior knowledge of the production rate is also essential (Stone, 2000). The production rate of a cosmogenic nuclide varies both spatially and temporally due to changes in atmospheric pressure, geomagnetic field, and solar activity (Lifton et al., 2008). Therefore, in the recent past, a significant effort has been made in the development of models (scaling factors) to estimate the production rate on the earth's surface, including variations over time. The scaling factors are also calibrated with on-site production rate measurements (Balco et al., 2009; Kelly et al., 2015).

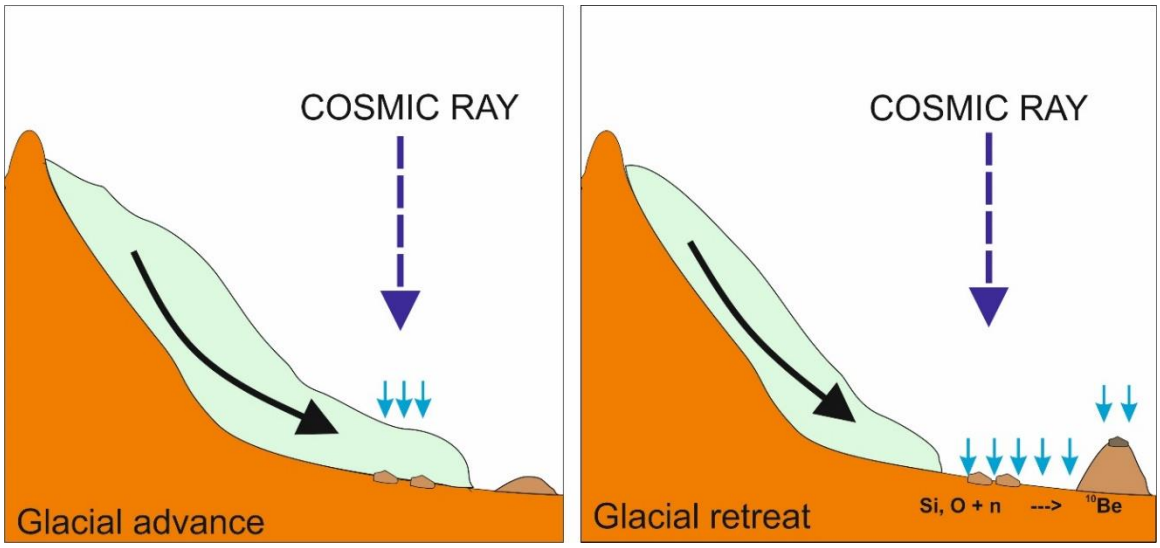

Figure 1.2: *Schematic showing the principle of cosmogenic nuclide exposure age dating. The advancing glacier shields the bedrock from cosmic rays. However, once the glacier retreats, cosmogenic nuclide production starts as the bedrock gets exposed to cosmic radiation. (Redrawn after www.antarcticglaciers.org)*

The Optically Stimulated Luminescence (OSL) dating measures the duration of time since the sediment grains have been buried by measurement of the luminescence signal intensity emitted by mineral grains under laboratory stimulation. During the burial, the mineral grains accumulate energy (luminescence signal) from surrounding radiation (from radioactive elements such as ^{238}U, ^{232}Th, ^{40}K etc.). The stored energy gets released when the grains are exposed to sunlight during transportation. Hence, the OSL age corresponds to the time period when the grains get deposited in a landform after exposure to sunlight.

In the Himalayan region, extensive work has been carried out to understand the late Quaternary glaciation using detailed field mapping supported by TCN and OSL dating. In the central Himalaya, detailed studies have been done using OSL dating. For example, in the Dhauliganga basin, several studies have observed glaciation events during MIS-4, MIS-2, Oldest Dryas (OD), Younger Dryas (YD), mid-Holocene, and mid to early Holocene in Kunti-Banar valley (Ali et al., 2022), Dunagiri valley (V. Kumar et al., 2020; Sati et al., 2014), Kosa valley (Bisht et al., 2017) and Purvi Kamet valley (Bisht et al., 2015). In the Saraswati valley, evidence of glaciation during MIS-2, YD, and mid-Holocene has been found (Rana et al., 2019). Evidence of MIS-2 glaciation has been observed in Pindar valley (Bali et al., 2013) and Goriganga valley (Ali et al., 2013). Similarly, evidence of MIS-2 and MIS-4 glaciation has been observed in the Zanskar mountains and Sarchu Plain (Saha et al., 2016; Sharma et al., 2018, 2016).

In the northwestern Himalaya, evidence of extensive glaciation has been observed during the MIS-2 in both Nubra and Ganglas valley using OSL dating (Ganju et al., 2018; Nagar et al., 2013; Shukla et al., 2020). However, significantly diverse ages obtained from the TCN method by other studies (Dortch et al., 2010; Owen et al., 2006) do not allow us to draw a definitive conclusion based on the chronology obtained using OSL or TCN methods. Thus, there is an utmost need for a thorough investigation utilising detailed geomorphological mapping and dating appropriate landforms/samples that would help narrow down the observed offset in ages derived from varying dating tools and establish the chronology of Quaternary glaciation in the northwestern Himalaya.

1.3.3 Studying Quaternary Glacier Fluctuations using Lacustrine Records

Though glacial deposits such as moraines provide direct evidence of glaciation events, they provide a discontinuous record of past climatic variations. At times unavailability of appropriate datable material in the glacial deposits makes them difficult for paleoclimatic utilisation. Hence, lacustrine sediments can prove as a potential archive for a continuous record of hydrological changes and fluctuations in glacial meltwater (Larsen et al., 2011). Proglacial lakes are waterbodies present at the edge of glaciers or ice sheets and are formed due to impounding by ice, moraine, landslide debris, or bedrock (Costa and Schuster, 1988). The term proglacial has been sometime referred to as ice-contact lakes or lakes which are influenced by glacial meltwater (Carrivick and Tweed, 2013). Sedimentation within proglacial lakes is an important archive for understanding short-term (inter-seasonal and inter-annual) and long-term fluctuations in the glacial meltwater.

In the northwestern Himalaya, multiple attempts have been made to utilise lacustrine records for paleoclimatic and paleotectonic inferences (Bhattacharyya, 1989; Demske et al., 2009; Kramer et al., 2014; Lal et al., 2019; Mishra et al., 2015; Mujtaba et al., 2018; Phartiyal et al., 2020, 2013, 2005; Wünnemann et al., 2010). However, there are limited efforts to understand glacial meltwater fluctuations using lacustrine sediment deposits. Particularly in the northwestern Himalaya, lacustrine sedimentation is largely affected by glacial meltwater as it is the primary source of water. Apart from multiple contemporary lakes, the northwestern Himalaya comprises multiple records of relict lake deposits (Juyal, 2014; Nag et al., 2016), which have the potential to extend the current understanding back in time. Hence, both contemporary and relict lake deposits in the northwestern Himalaya can be utilised extensively to understand past meltwater fluctuations.

1.4 Paleomagnetism

1.4.1 The Geomagnetic Field

Earth is the only terrestrial planet with a strong dipolar magnetic field. The present-day magnetic equator ($I=0^0$) lies very close to the geographic equator. The inclinations are usually positive in the northern hemisphere and negative in the southern hemisphere. Though the present-day geomagnetic field roughly represents a geocentric axial dipole field, it is not exactly similar to the simplest configuration (**Figure 1.3**). The present-day magnetic equator ($I=0^0$) wavers around the geographic equator, and the magnetic poles ($I=\pm 90^0$) also differ from the geographic poles. Hence, the present geomagnetic field is more complex than the geocentric axial dipole field and is better explained by an inclined geocentric dipole field. The inclined dipole field that best describes the present-day geomagnetic field has an angle of ~11.5^0 with the rotation axis. However, the present-day poles do not precisely coincide with the best fitting inclined dipole field poles, suggesting the field is still complicated. At locations, the geomagnetic field deviates from the best fitting inclined geocentric dipole, which is called the nondipole field.

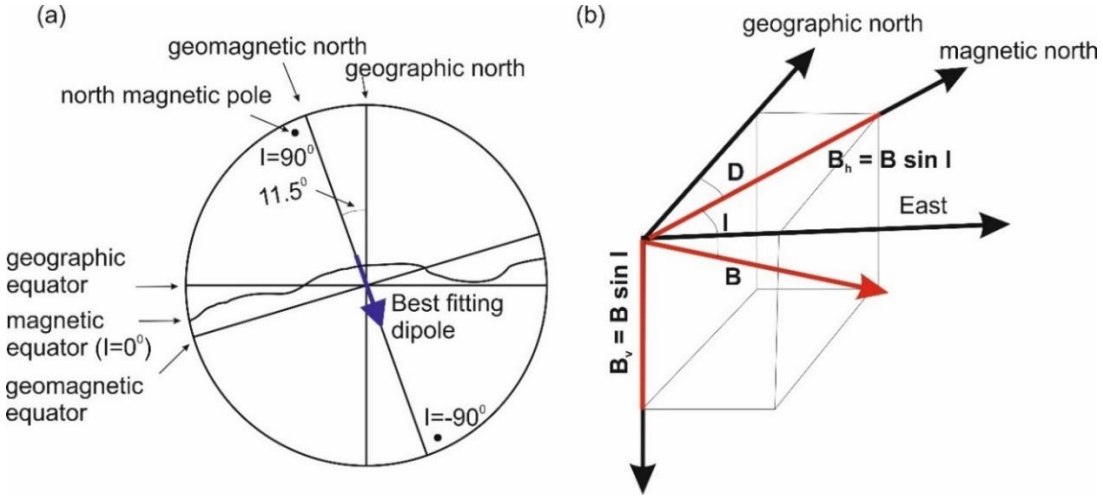

Figure 1.3: *An illustration showing the present-day geomagnetic field. The inclined dipole field that best describes the present-day geomagnetic field has an angle of ~11.5^0 with the rotation axis.*

1.4.2 Past Geomagnetic Field Intensity Changes

The historical record of the secular geomagnetic variation is only available for the last 400 years (Jackson et al., 2000), and thus in order to understand the geomagnetic changes prior to this time, various paleomagnetic techniques have to be relied upon. Paleomagnetic techniques require suitable archives which record the past geomagnetic field variations

Thermoremanent magnetization (TRM) is acquired as any material cools from higher temperatures (**Figure 1.4**). Hence, TRM is mainly observed in igneous rocks and or heated archeological artifacts. Above Curie temperature (T_c), the magnetic moments of atoms in ferro and ferri-magnetic minerals behave randomly due to increased thermal energy. As the material cools through T_c, the atomic magnetic moments align in a direction parallel to the ambient geomagnetic field direction. During erosion and transportation, the magnetic minerals are deposited as sediments, and during deposition, the magnetic particles experience a torque exerted by the geomagnetic field, and thus their magnetic moments rotate along the ambient field. This is defined as depositional remanent magnetization (DRM). However, with minor hydrological disturbances, the perturbation will exceed geomagnetic torque, thus hampering the ideal magnetic alignment (Heslop, 2007). The grains, after deposition into the sedimentary bed, may also experience post-depositional remanent magnetization (PDRM). PDRM is acquired within the unconsolidated uppermost sediments having higher water content (Roberts and Turner, 2013). The lock-in depth where the magnetic minerals lock the PDRM signal can vary from place to place and is usually assumed to be less than 20 cm (Roberts and Winklhofer, 2004). In some environmental conditions, chemical changes may also give rise to magnetic minerals that record the ambient geomagnetic field termed chemical remanent magnetization (CRM).

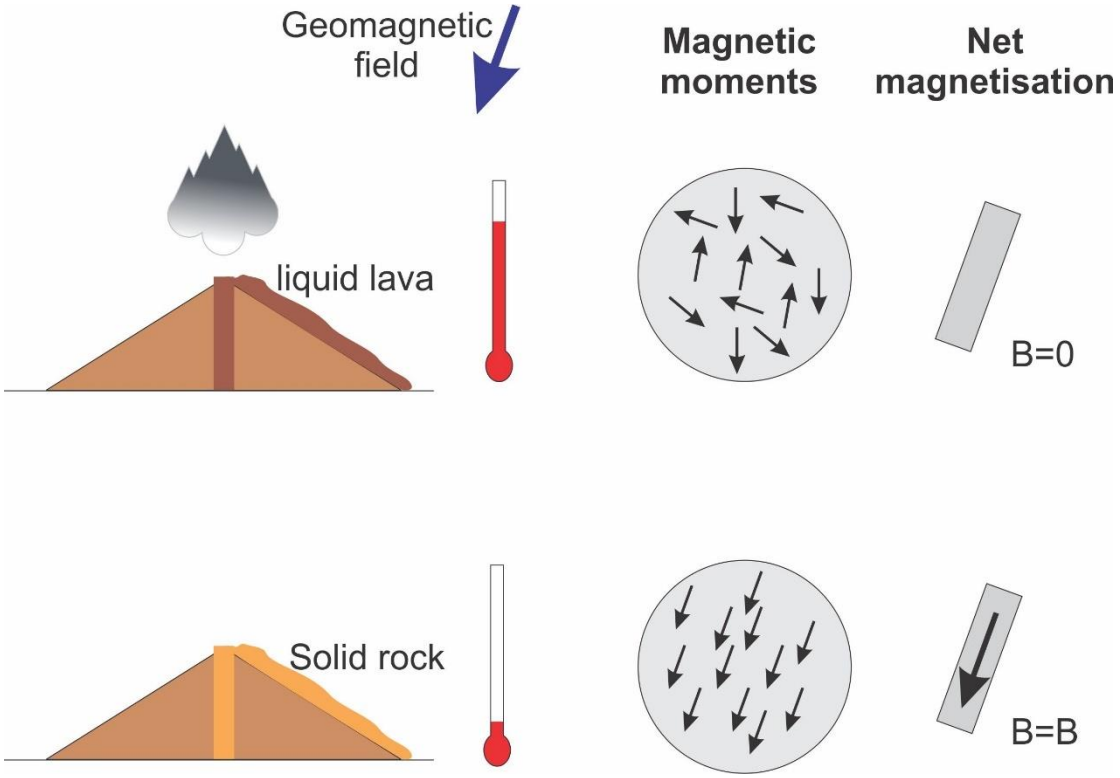

Figure 1.4: *TRM acquisition in igneous rocks. Redrawn from Roberts and Turner (2013). Above Curie temperature (T_c), the magnetic moments of atoms in ferro and ferri-magnetic minerals behave randomly due to increased thermal energy. As the material cools through T_c, the atomic magnetic moments align in a direction parallel to the ambient geomagnetic field direction.*

Absolute paleointensity estimations require measurements of TRM from igneous rocks and archeological artefacts (Thellier, 1959). However, suitable samples with TRM (with proper chronology) are not available globally, and wherever they are present would provide a discontinuous record of paleomagnetic intensity variations (Roberts et al., 2013). Thus, sedimentary records are most suitable for the reconstruction of continuous paleomagnetic intensity records. Yet, the magnetic record from sedimentary cores suffers from changes due to PDRM, which leads to smoothening of the record. Lithological parameters such as mineralogy, the concentration of magnetic grains, and grain size also affect the magnetic record, thus creating further complexity (Savranskaia, 2020). On the other hand, cosmogenic nuclide records from sediment cores have been found to be more dependable in obtaining past geomagnetic field intensity records as the production of cosmogenic nuclides gets modulated by the earth's magnetic field (Lal and Peters, 1967). An inverse relationship between geomagnetic intensity and cosmogenic nuclide (^{10}Be)

concentration has been theoretically established (Lal and Peters, 1967) and observed in geological records (Frank et al., 1997; Muscheler et al., 2005).

Cosmogenic nuclides measurements from both sediment cores (Carcaillet et al., 2004b, 2004a, 2003; Christl et al., 2010; Frank et al., 1997; Simon et al., 2020, 2018a, 2016b) and ice cores (Muscheler et al., 2005) has been employed to understand past geomagnetic field intensity changes. Prior to this work, the cosmogenic nuclide records were sparse from the Indian Ocean, and were mainly limited to the last geomagnetic reversal (Savranskaia et al., 2021; Simon et al., 2016b). Hence, temporal cosmogenic nuclide records from the Indian Ocean sediment cores would fill a major research gap. Such a study will help understand the dipolar geomagnetic intensity changes in the past and ^{10}Be dynamics during the excursion and reversal events.

1.5 Chronology of Marine Sediment Cores

Dating methods play an important role in the reconstruction of Quaternary paleoenvironments. For building chronology of marine sediment cores, the methods applied can be divided into relative and absolute dating. Relative dating does not determine a specific date and instead estimates the relative order of past events. On the other hand, using absolute dating methods, the exact age of an event can be estimated. Overall, the dating techniques can be broadly listed as follows-

(1) Radio-isotope dating of
   a. Natural nuclides: ^{234}Th, ^{210}Pb, and ^{230}Th
   b. Cosmogenic nuclides: ^{14}C, ^{26}Al, and ^{10}Be
   c. Artificial radionuclides: ^{137}Cs, $^{239, 240}$Pu, ^{241}Am and ^{129}I

(2) Radiation exposure dating of luminescence and Electron Spin Resonance (ESR) dating

(3) Stratigraphic dating using oxygen isotope of foraminifera and magnetic records

Table 1.2: *Radio-isotopes with differing half-lives, which can be utilized for building chronology of marine sediment cores.*

		Half-life
Natural Isotopes	^{234}Th	24 d
	^{210}Pb	22.3 yr
	^{230}Th	7.54×10^4 yr
Artificial Isotopes	^{137}Cs	30 yr
	^{239}Pu	2.4×10^4 yr
	^{240}Pu	6.5×10^3 yr
	^{241}Am	4.32×10^2 yr
	^{129}I	1.57×10^7 yr
Cosmogenic Isotopes	^{14}C	5.70×10^3 yr
	^{10}Be	1.39×10^6 yr

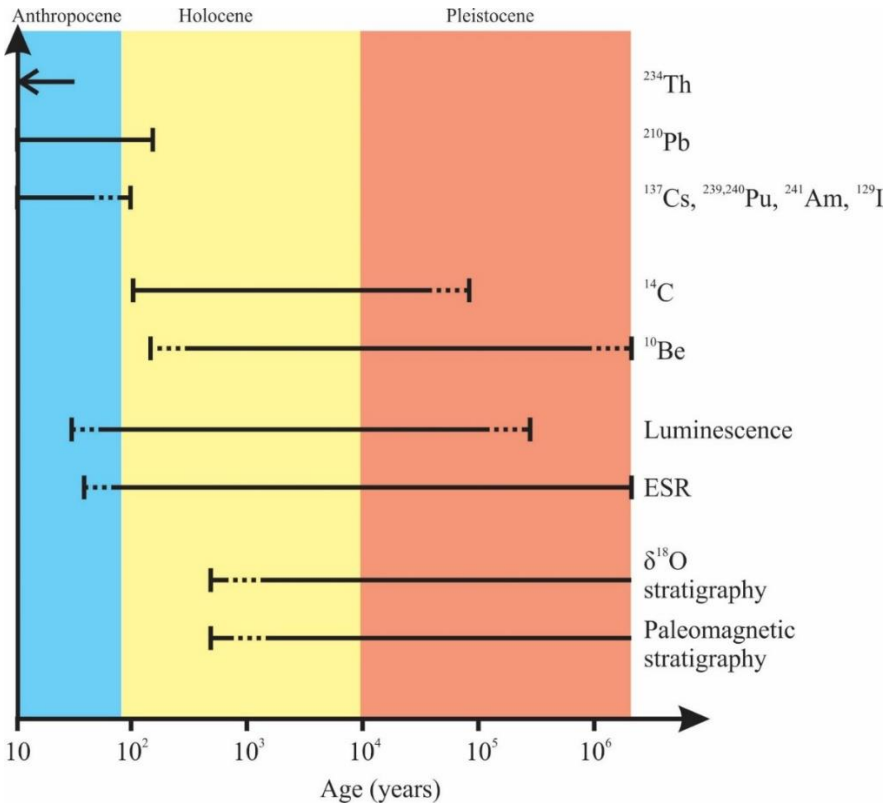

Figure 1.5: *Dating methods and ranges for building chronology of Quaternary events. Redrawn after Blackwell et al. (2016), Li et al. (2021), and Walker (2005)*

The applicability of radio-isotopes in dating marine cores primarily depends upon the half-life of the cosmogenic nuclides and measurement efficiency. For example, ^{234}Th with a half-life of 24 days can be utilised only to date modern sediments (<100 days) (Li et al., 2021) (**Table 1.2; Figure 1.5**). Similarly, ^{14}C with a half-life of 5730 years coupled with advanced AMS measurements can be used to date marine sediment cores up to 50 ka. ^{10}Be, with a half-life of 1.39 Ma, has the capability of dating marine sediment cores up to ~10 Ma (Bourles et al., 1989). Considering the radiocarbon limit of 50 ka, the ^{10}Be method can be employed to extend the chronology of marine sediment cores beyond 50 ka.

1.6 Objectives

The present study employs cosmogenic nuclides (^{10}Be and ^{14}C), along with other elemental and isotopic records from lacustrine, marine, and glacial records, to understand various paleoclimatic and paleomagnetic processes during the Quaternary period. The objective of the study can be listed as follows-

- Identify factors responsible for driving the Quaternary glaciation in northwestern Himalaya
    - Develop Chronology of Quaternary glaciation using exposure age dating.
    - Understand the coupling between regional glaciation and lake sedimentation in the Ladakh region.
    - Reconstruct past fluctuation in meltwater discharge and regional hydrology during the late quaternary using relict lake deposits.
- Understand processes controlling the spatial and temporal variation of beryllium isotopes in the Indian Ocean
    - Identify factors controlling the spatial distribution of Be isotopes in the Indian Ocean
    - Reconstruct past magnetic field changes using the ^{10}Be/^{9}Be ratio record
    - Ascertain the applicability of the meteoric ^{10}Be method in extending the chronology of marine sediment cores beyond the radiocarbon limit.

Chapter 2 Methodology

To understand late Quaternary paleoclimatic and paleomagnetic processes, several geological archives have been utilised, which involve glacial, lacustrine (relict), as well as marine deposits (**Figure 2.1, 2.2**). Cosmogenic nuclides (^{10}Be and ^{14}C), along with other isotopic and elemental proxies, were used to achieve the objectives of this study. The terrestrial cosmogenic nuclide (^{10}Be) exposure age dating method was used to date glacial landforms and to build the chronology of Quaternary glaciation in the northwestern Himalaya. The present study also involves meteoric ^{10}Be measurements to understand spatial and temporal Be isotopic variations in the Indian Ocean. As a part of the study, the protocol was established for beryllium separation and isotopic measurement at the Physical Research Laboratory (PRL), Ahmedabad. Be isotopic measurements were performed using the Accelerator Mass Spectrometer at PRL (AURiS). The stable isotopic concentration of beryllium (^{9}Be) was measured using a Thermo Scientific iCAP 7000 Plus series Inductively Coupled Plasma Optical Emission Spectrometer (ICP-OES). The radiocarbon dating technique was employed for building the chronology of multiple marine sediment cores, and the Optically Stimulated Luminescence (OSL) dating method was employed for dating the paleolake deposit. For radiocarbon measurement, samples were processed using Automated Graphitisation Equipment (AGE) for converting carbon to graphite and were measured in the PRL-AURiS. Similarly, the Optically Stimulated Luminescence (OSL) measurements were performed in the luminescence laboratory at PRL.

Past changes in hydrological conditions have been reconstructed using major and trace element geochemistry from lacustrine sediments (Bhushan et al., 2018; Nesbitt and Young, 1982; Shah et al., 2020). The X-Ray Fluorescence spectrometer was used to measure the major oxide and trace element composition of the paleolake sediments. Organic carbon and bulk nitrogen compositions were measured using a Thermofisher Flash 2000 Elemental Analyser. Carbon and oxygen isotopic composition were measured using a Thermo delta-V plus Isotope Ratio Mass Spectrometer (IRMS). Inorganic carbon

concentration was carried out using a UIC coulometer. All the measurements were performed at Physical Research Laboratory, Ahmedabad, and the procedures for the analyses are explained further in detail. **Table 2.1** shows the chapter wise distribution of various analytical methods used in the study.

Table 2.1: *Chapter wise distribution of various analytical methods used in the study.*

Method	**Ch. 3**	**Ch. 4**	**Ch. 5**	**Ch. 6**	**Ch. 7**
Beryllium isotope measurements	✓		✓	✓	✓
Radiocarbon analysis		✓		✓	✓
OSL Dating		✓			
Stable isotope analysis		✓			
Elemental analysis (XRF)		✓			
Elemental analysis (ICP-OES)	✓		✓	✓	✓
Organic C and bulk N analysis		✓			
Inorganic C analysis		✓	✓	✓	

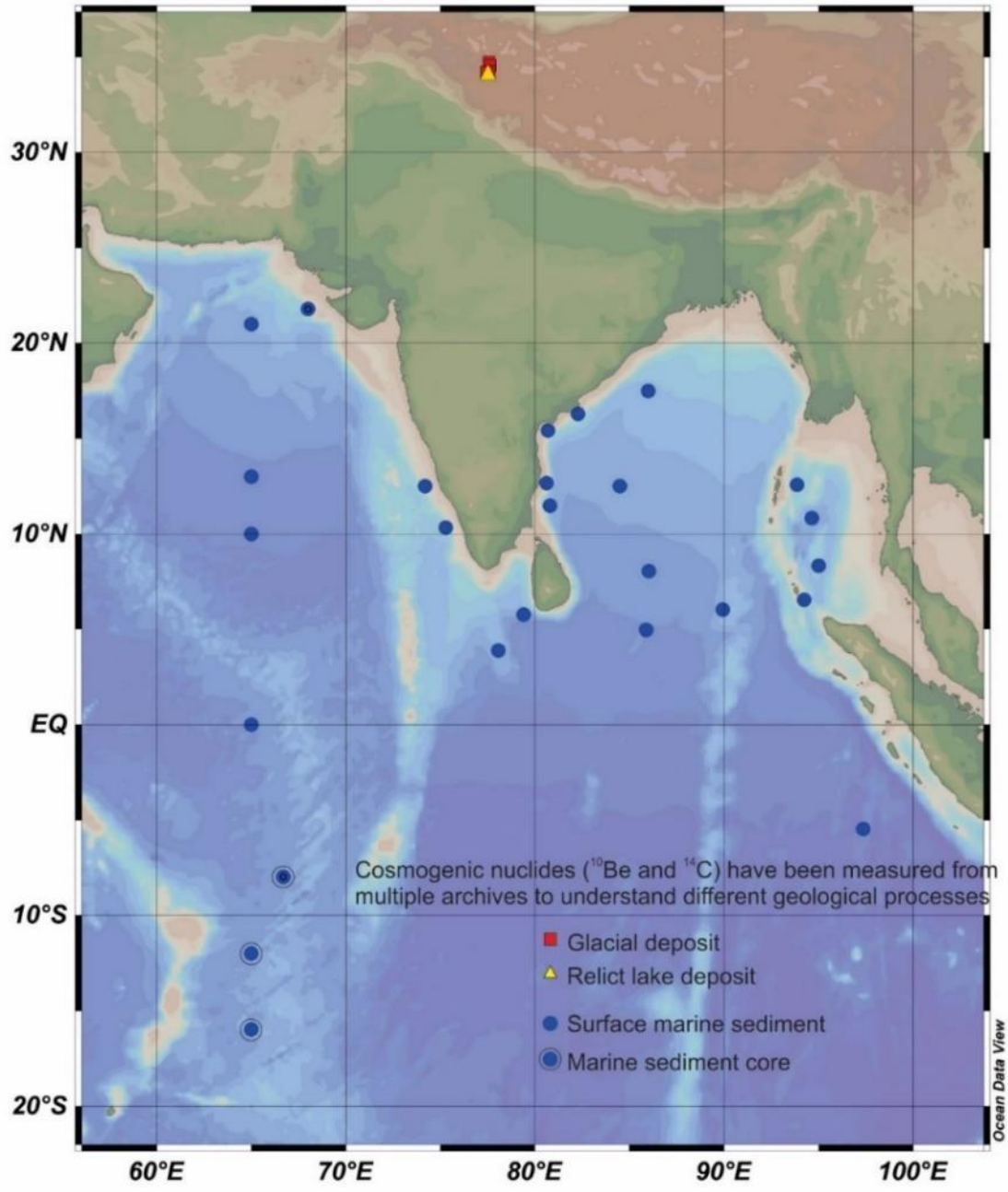

Figure 2.1: *Sampling locations for glacial, lacustrine, and marine sediment deposits used in the present study.*

Figure 2.2: *Field photographs showing sampling of glacial (a-b) and relict lake (c-e) deposits.*

2.1 Beryllium Isotopic Measurement

2.1.1 Separation and Dissolution of Quartz Grains for in-situ Samples

The rock samples were brought to the laboratory, and uneven surfaces were cut using a rock cutter. The rock slabs were crushed using a jaw crusher (grain size less than 1 cm) and further with a roll crusher (grain size less than 1 mm). The samples were sieved to collect the 250–500 micron fraction for further processing. The samples were treated for quartz isolation in a Chemical-Physical-Chemical (CPC) procedure (modified from Kohl and Nishiizumi 1992). Nearly ~500 grams of the sample were treated with 1N HCl for 24 hours and then with 1N HF/HNO_3 solution for 15 days. This procedure helps in the

dissolution of minerals other than quartz and etching of quartz grains to remove the surface layer that might have adsorbed meteoric beryllium. The sample bottles were placed on an automated orbital shaker and were shaken manually in between. The acid solution was changed every 24 hours. While changing the acid solution, we rinsed the grains multiple times with ultrapure deionised water, which also helped in the removal of flaky mica grains. Finally, the grains were washed with deionised water, dried at 60^0C, and again sieved with a 250-micron sieve. After sieving, the magnetic grains were physically picked and discarded by a hand-magnet. The diamagnetic quartz was then separated by passing the grains through a Frantz magnetic separator and by selective picking under a microscope. (**Figure 2.3, 2.4**)

Nearly 0.5 grams of each sample was dissolved, and the aluminium concentration was measured in ICP-OES to check the purity of quartz. Samples with less than 200 ppm aluminium concentration were taken for final cleaning and quartz dissolution. Samples with more than 200 ppm Al concentration were again treated with 1N HF/HNO_3 solution for seven days and rechecked for aluminium concentration.

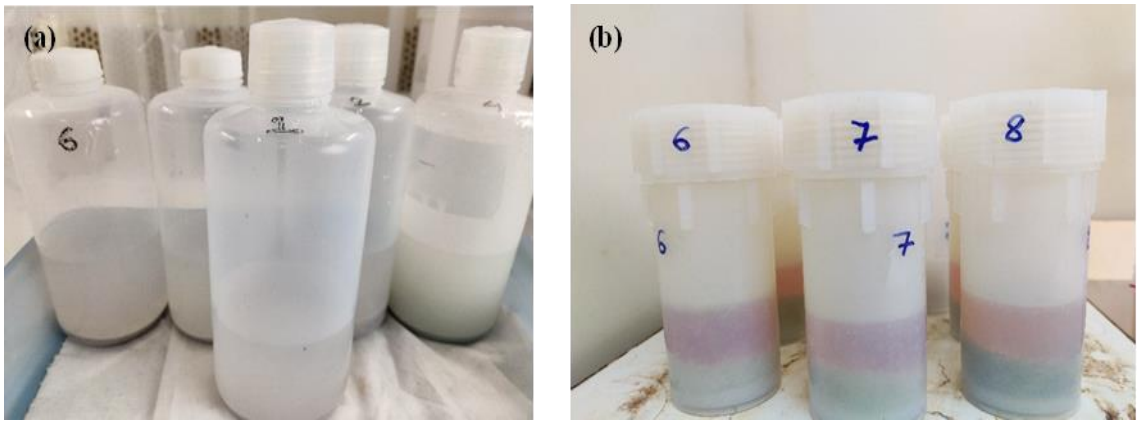

Figure 2.3: *Quartz cleaning procedure. (a) Grains being treated with 1 N HF/HNO_3 solution in the initial chemical cleaning procedure. (b) Magnetically separated quartz grains being heated with aqua regia solution in the final chemical cleaning step.*

Finally, ~20-40 grams of pure quartz grains were taken in 120 ml Teflon vials. The weight of the empty vial and quartz grains was noted. The samples were heated at 80^0C with 10N HF for 1 hour and subsequently with aqua regia for 30 minutes after cleaning with deionized water. The sample was dried at 50^0C for 24 hours. The weight of the vial containing the sample was measured, and the quartz weight was calculated by subtracting

the weight of the empty vial, which was noted earlier. 500 µl of ^{9}Be carrier (Be concentration of 982 µg/g) was added to each sample, and the sample was taken for dissolution. The samples were dissolved using concentrated HF/HNO_3 solution and were finally heated with aqua-regia for chloride conversion.

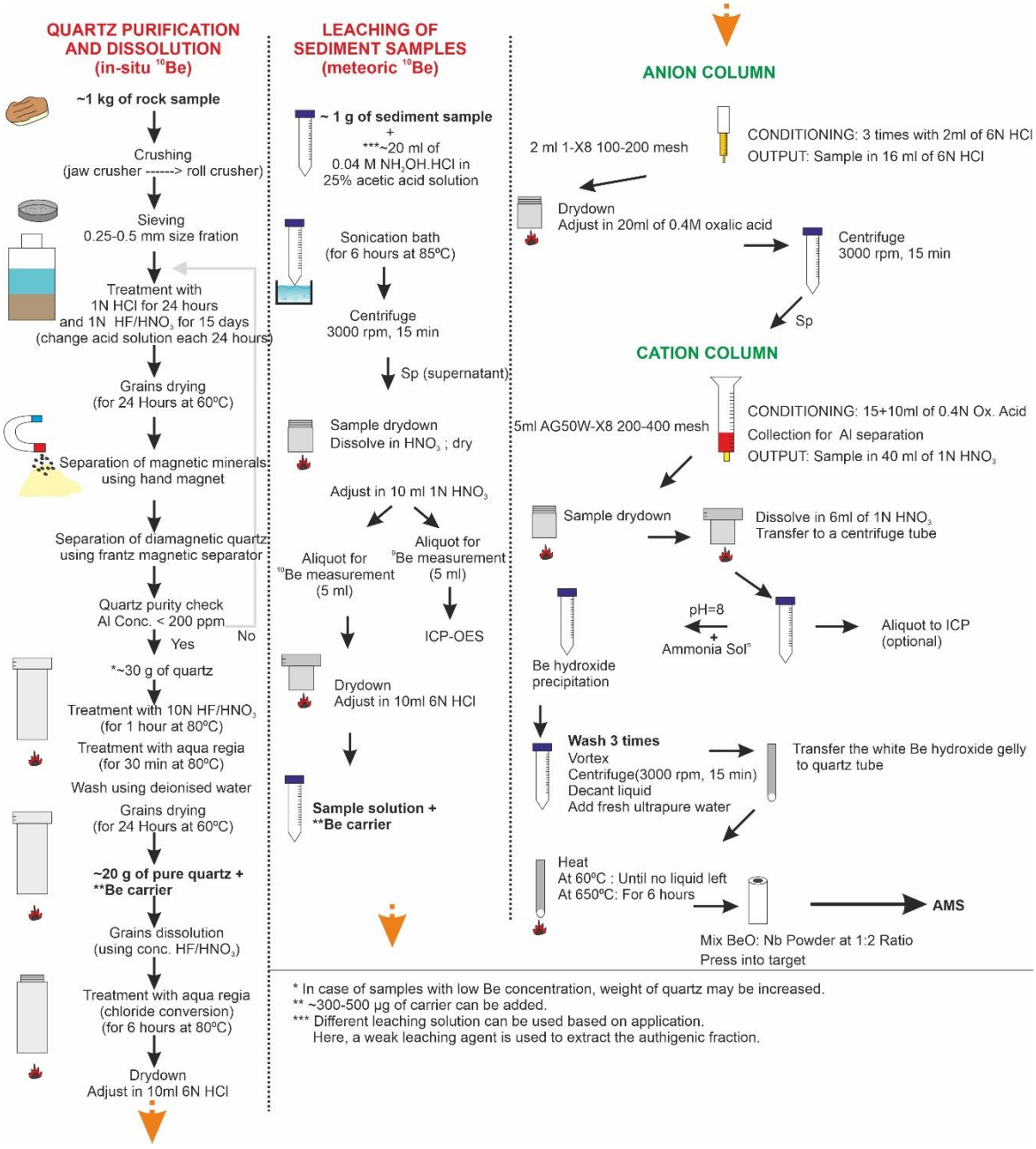

Figure 2.4: *Flowchart showing the procedure followed for in situ and meteoric ^{10}Be extraction.*

2.1.2 Sediment Sample Leaching

Sediment sample of nearly 1 to 2 grams was crushed homogenously and taken in centrifuge tubes. 0.04 M Hydroxylamine hydrochloride ($NH_2OH.HCl$) in 25% acetic acid solution was added to the sample and was kept for sonication in a water bath at 85ºC for 6 hours (Bourles et al., 1989). The sample was centrifuged, and the supernatant was separated for further treatment. The leachate solution was dried and dissolved in HNO_3.

Tessier et al. (1979) showed metals can be sequentially extracted from different phases associated with the sediment fraction, which has also been applied for Be extraction (**Figure 2.5**). Bourles et al. (1989) demonstrated that the beryllium isotopic ratio from carbonate and exchangeable fraction is almost equal to that extracted from the iron and manganese oxyhydroxides. Hence, he proposed a single-step extraction of authigenic beryllium by using hydroxylamine hydrochloride ($NH_2OH.HCl$) in acetic acid solution. The leachate solution comprises authigenic mineral fraction, which has a composition very similar to the chemical constituents of seawater with fractions from exchangeable ions, carbonates, and Fe-Mn oxyhydroxides (Bourles et al., 1989; McHargue et al., 2011, 2000). Other procedures, such as the use of hydrochloric acid (Brown et al., 1985; Henken-Mellies et al., 1990), can attack the mineral bound non-authigenic fraction of beryllium (Bourles et al., 1989). Hence, leaching of sediments with 0.04 M hydroxylamine hydrochloride ($NH_2OH.HCl$) in 25% acetic acid solution has been adapted and followed by many researchers to extract the authigenic fraction (Simon et al., 2016a, 2016b).

Samples were further processed following Jena et al. (2021) for separation of beryllium and its isotopic measurement with an Accelerator Mass Spectrometer (AMS). The sample was finally dissolved in 10 ml of 1 N nitric acid solution (**Figure 2.3; 2.6**). A 5ml aliquot of the solution was taken for ^{9}Be measurement with ICP-OES, and the rest was further processed for ^{10}Be measurement using AMS. The sample was measured for beryllium concentration in a Thermo 7000 series ICP-OES. The ^{10}Be aliquot was further dried and adjusted in 6 N hydrochloric acid. About 300 µl of Be carrier (982 µg/g) was added to the sample.

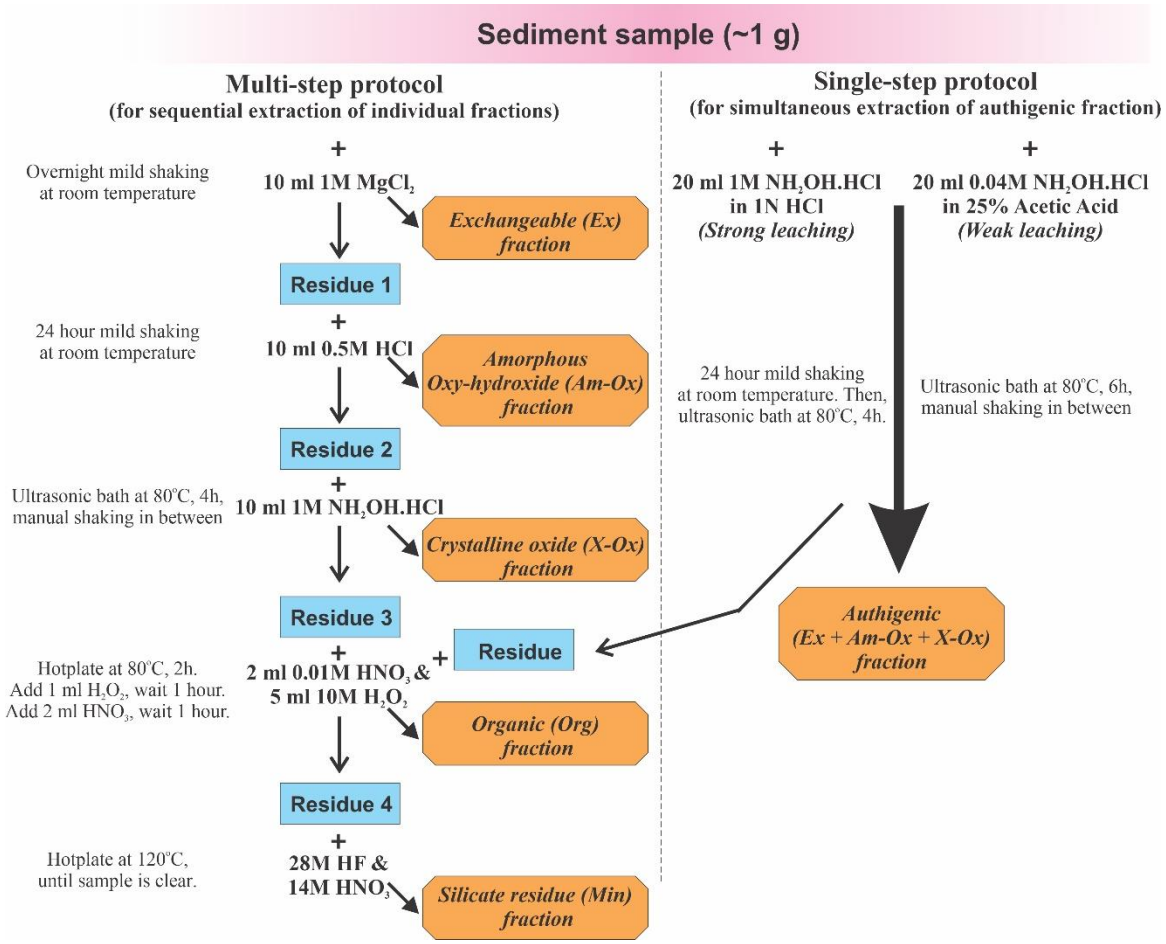

Figure 2.5: *The extraction procedure for separation of beryllium bound in different fractions of sediment sample. The procedure shown above is modified from multiple previous studies* (Bourles et al., 1989; Simon et al., 2016b, 2016a; Wittmann et al., 2012).

2.1.3 Be Separation using Column Chemistry

The samples were further processed with a two-step column chromatography method to separate Be from other ions. The sample solution was passed through an anion column (Biorad Poly-Prep® columns filled with 2ml 1-X8 100-200 mesh resin and conditioned with 6 N HCl) to remove iron from the solution. The sample was then dried and dissolved in 0.4 N oxalic acid and centrifuged to separate calcium oxalate precipitate. The sample in oxalic acid was then passed through a cation column (Biorad Econo-Pac® columns filled with 5ml AG50-X8 200-400 mesh resin and conditioned with 0.4 N Oxalic Acid) to separate beryllium from other ions. Finally, beryllium was precipitated by adding ammonia solution at a pH of 8. Sample was further cleaned with ultrapure water, and the Be precipitate was combusted at 650ºC for 6 hours for its conversion to BeO. The BeO was

mixed with Nb powder in a 1:2 ratio and pressed into an aluminium cathode. The samples were measured for beryllium isotopic ratio, and thus its ^{10}Be concentration at the Accelerator Mass Spectrometer established at Physical Research Laboratory (PRL), Ahmedabad (AURiS) (Bhushan et al., 2019b).

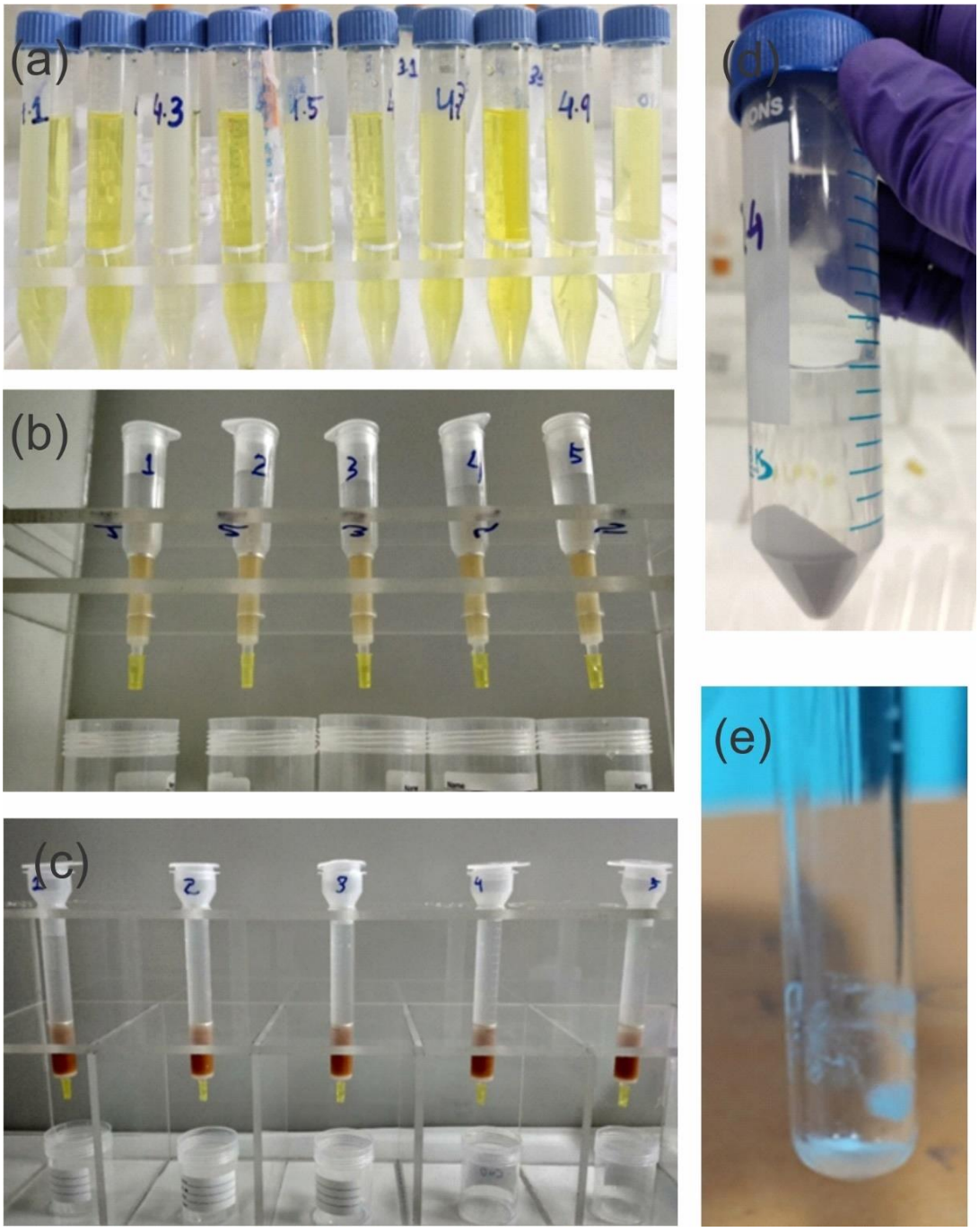

Figure 2.6: *Sequence of procedure followed for the separation of beryllium. (a) Samples in 6N HCl, (b) Fe column, (c) Be column, (d) Calcium oxalate precipitate, (d) Beryllium oxide powder.*

2.1.3.1 Column Calibration and Procedure Setup

For calibration of the columns in the laboratory, an artificial sample was prepared using single-element standards. To each sample, elemental standards were added in such a proportion that it resembles a natural geological sample with Aluminium (1500 µg), Titanium (1000 µg), Iron (1000 µg), Sodium (100 µg), and Boron (100 µg). 300 µg of beryllium was added, such that it represents the Be concentration in a sample after carrier addition. The sample was passed through the column, and multiple aliquots were collected. The elemental concentrations were measured in ICP-OES, and accordingly, the column procedure was set up for the separation of beryllium. The detailed procedure for column chemistry is provided in **Table 2.2, 2.3 and Figure 2.7, 2.8.**

Table 2.2: *Fe column (2 ml Biorad 1-X8 100-200 Mesh in 5 ml polyprep Biorad Columns) chemistry protocol.*

	Step	**Purpose**
Step 1	5ml+5ml 0.3M HCl	Clean Resin
Step 2	2 ml+2ml+2ml 6M HCl	Condition Resin
Step 3	Sample in10 ml 6M HCl	**Collect Be and Al**
Step 4	2 ml+2ml+2ml 6M HCl	**Collect Be and Al**
Step 5	5ml+5ml 0.3M HCl	Clean Resin / Discard Fe

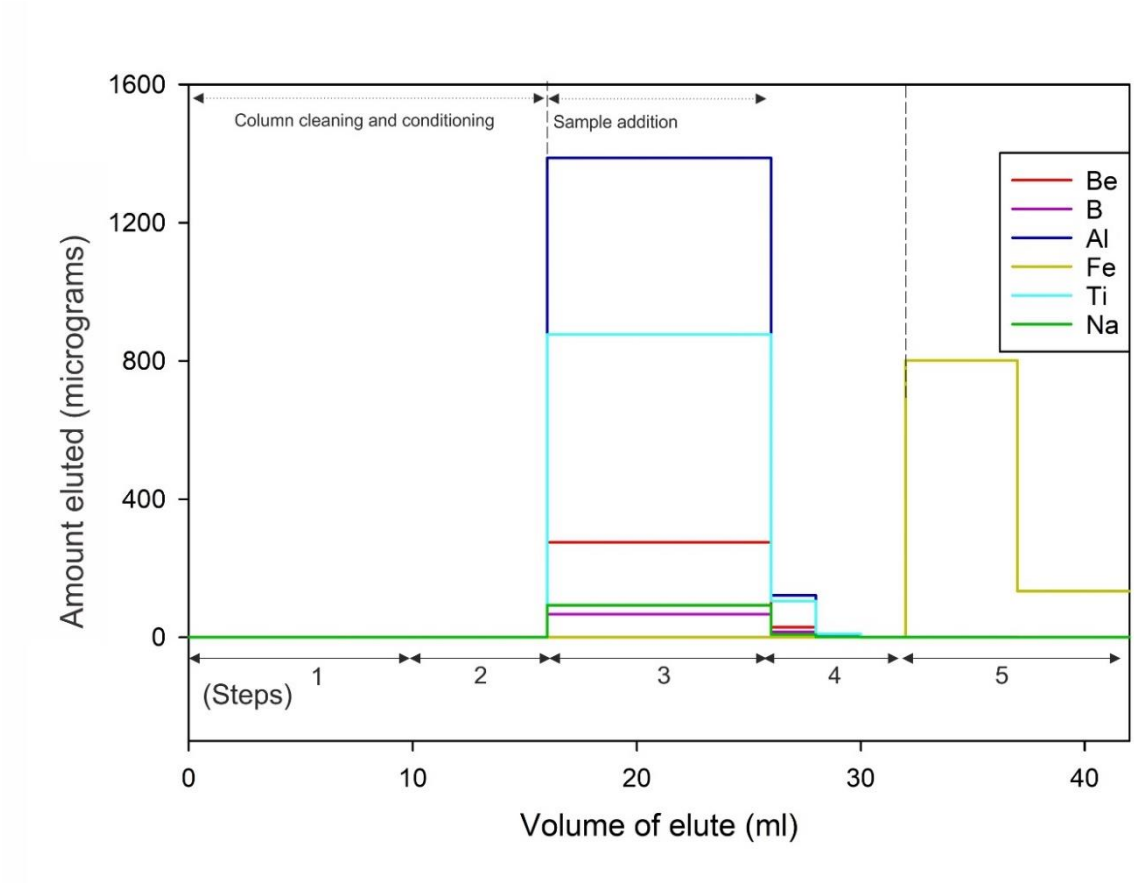

Figure 2.7: *Elements eluted at each step of the Fe column.*

Table 2.3: *Be column (5 ml Biorad AG 50-X8 200-400 mesh in large 20 ml Biorad ecnopac columns) chemistry protocol.*

	Step	Purpose
Step 1	10ml + 10ml + 5ml 5M HNO_3	Clean Resin
Step 2	10ml + 10ml + 5ml deionized water	Remove HNO_3 from resin
Step 3	10 ml + 10ml + 5ml 0.4 M Oxalic Acid	Condition Resin
Step 4	Sample in 20 ml 0.4 M Oxalic Acid	Collect Al
Step 5	5 ml + 5 ml 0.4 M Oxalic Acid	Collect Al
Step 6	10 ml 0.4 M Oxalic Acid (5 times)	Collect Al (Elute Fe, Al, Ti)
Step 7	5 ml + 10 ml deionised water	Remove oxalic acid from column
Step 8	10 ml 0.5 M HNO_3 (4 times)	Elute Na
Step 9	10 ml 1 M HNO_3	Wash

Step 10	10 ml 1M HNO_3 (4 times)	**Collect Be**
Step 11	10 ml 5 M HNO_3 (4 times)	Clean resin
Step 12	5 ml + 5 ml deionized water	Remove HNO_3

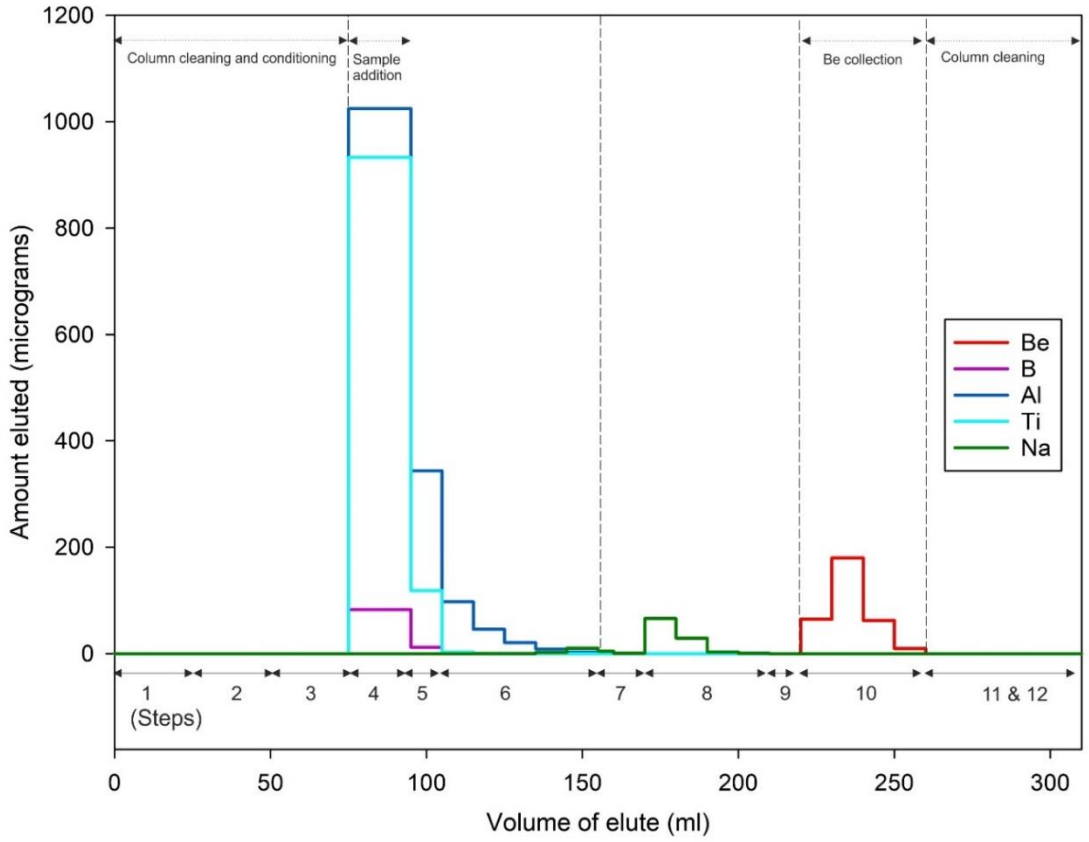

Figure 2.8: *Elution pattern of the Be column for different elements.*

2.1.4 Be Isotopic Measurement with AMS

The samples in the present study were measured with the accelerator mass spectrometer established at Physical Research Laboratory (**Figure 2.9**). The 1 MV AMS was procured from HVEE (High Voltage Engineering Europa, BV, Netherlands) (Klein et al., 2006) and has been named as Accelerator Unit for Radio-isotope Studies (PRL-AURIS). Prior to the present work, the performance of the instrument has been tested for ^{14}C, ^{10}Be, and ^{26}Al, and routine measurements of ^{14}C in geological and archaeological samples have been performed. In the present study, for the first time, the preparation of

geological samples for ^{10}Be isotopic measurement was performed, and the instrument was tuned for routine measurement of ^{10}Be.

PRL-AURiS comprises several parts: negative ion source, low-energy (LE) bouncer-injector magnet, 1 MV tandetron accelerator, high-energy (HE) magnet, 150 nm silicon nitride (SiN) foil, electrostatic analyser (ESA), rare isotope (RI) magnet, and gas ionisation chamber (GIC) detector. The sample carousel can accommodate 50 sample targets. In the ion source (SO-110), cesium is used to produce negative ions in a process called sputtering. In the process, Cs stored in the reservoir is heated at 110^0C to produce Cs vapour which is ionized through an ionizer. The target voltage, applied between the target and ionizer, attracts the positive cesium ions to the target. Cesium ions reaching the sample material release the ions by sputtering. The negative sample ions are accelerated by the target voltage in the direction of the ionizer. The ions that pass the ionizer via its central aperture are further accelerated towards the extraction cone by the extraction voltage between the cone and the ionizer. The ion beam is then passed through the Bouncer-Injector (BI) magnet. The magnet allows isotopes of interest to pass further based on a process called bouncing. During the fast-switching process, the electrically isolated vacuum chamber of the magnet is set on a potential. To allow selected masses, the energy of the ions is adjusted while the magnetic field remains constant. Usually, the abundant isotope is allowed for a shorter time compared to the rare one.

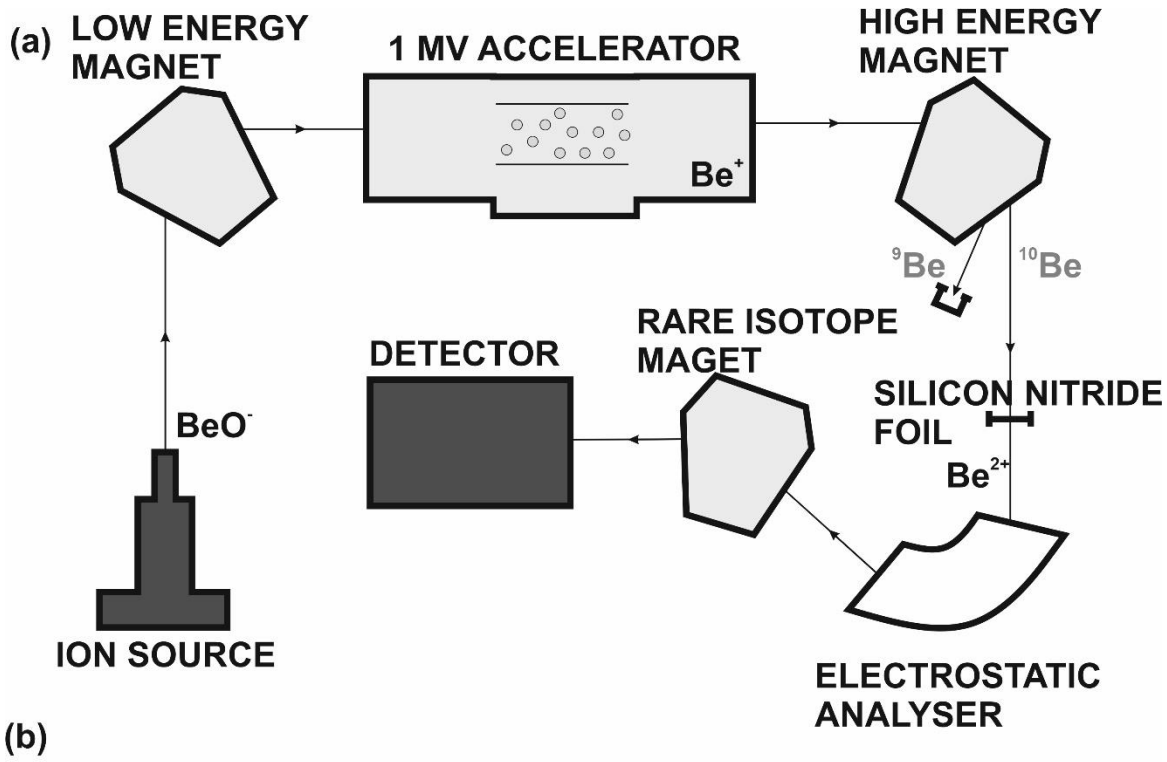

Figure 2.9: *(a) Schematic of Accelerator Mass Spectrometer (PRL-AURiS) established at PRL for ^{10}Be measurements (b) Photograph of the Accelerator Mass Spectrometer facility at PRL.*

The negative ions are further passed towards the terminal of the Tandetron accelerator that contains Argon as stripper gas. The stripping process breaks the molecules

and produces positive elemental ions. The ions leaving the accelerator contain very high energy, which also improves the identification of the ions in the final detector. The beam emerging from the accelerator is a positive ion beam, and it is analysed by a 90º High Energy (HE) magnet (radius 850 mm), which directs abundant stable isotope(s) into offset Faraday cup(s) for ratio measurements. The rare isotope beam is further passed through a 120º Electrostatic Analyser (ESA, radius 650 mm) and passes through a Rare Isotope (RI, radius 850 mm) magnet. This suppresses the unwanted ions and helps reduce the measurement background. The detector consists of a dual anode ionization chamber which helps in identifying the wanted rare isotope based on characteristic residual energy (E_{final}) vs. energy loss (ΔE) (**Figure 2.10**).

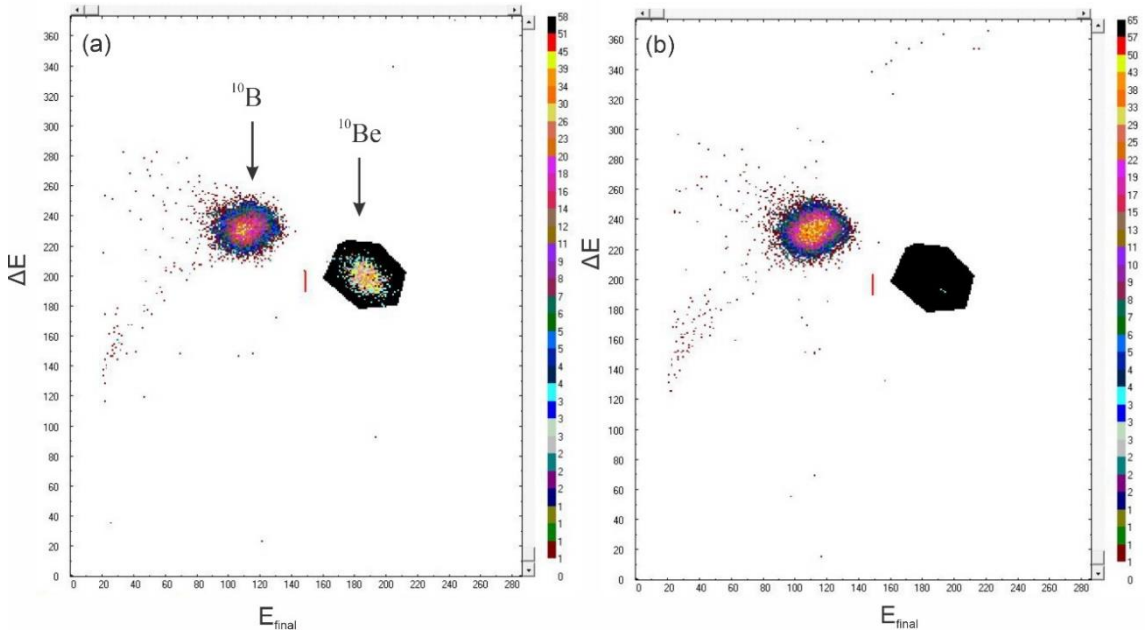

Figure 2.10: *Typical ΔE vs. E_{final} plot for (a) sample and (b) blank measured for Be isotopes with AMS. The black polygon represents the selected Region of Interest (ROI) for ^{10}Be counting.*

The probability of negative ion formation depends on the electron affinity. Beryllium is injected as molecular ion BeO^-, because the sputtering efficiency for the atomic ion Be^- is very low. The ion beam energy is typically 35 keV. Both $^9BeO^-$ and $^{10}BeO^-$ are sequentially injected into the accelerator through the LE magnet. In the accelerator, through the stripping process, BeO molecules are broken into Be ions. The Be^+ beam is then passed through the HE magnet, after which the stable isotope ($^9Be^+$) is measured in an offset faraday cup. The rare isotope beam is further passed through a SiN foil that helps in

removing the boron contamination. The foil causes a difference in the residual energy of the transmitted ^{10}B and ^{10}Be ion (B ions slow down faster than the Be ones), and ESA can differentiate between both ions based on this energy difference. The Be^{2+} is further passed through ESA and RI magnet. Finally, in the detector based on E_{res} and ΔE plot, beryllium is separated from boron.

In the AMS measurement, the $^{10}Be/^{9}Be$ ratio of the samples has to be normalized with standards with a known $^{10}Be/^{9}Be$ ratio. This is because both ^{9}Be and ^{10}Be are measured in different detectors, ^{10}Be travels a longer path, and additional loss of ^{10}Be happens in the SiN foil. For the same, 07 KNSTD standards have been procured from Dr. Kunihiko Nishiizumi, University of California, Berkeley, U.S.A. (Nishiizumi, 2022; Nishiizumi et al., 2007). For routine measurements, the standard ^{10}Be-14-5-6 with a reported $^{10}Be/^{9}Be$ ratio of 1.504 x 10^{-11} was used for normalization (**Figure 2.11**). The continuous measurement of ^{10}Be-14-5-6 standards shows an overall transmission of 13.23 % throughout the AMS (**Table 2.4**). Apart from that, standards with varying $^{10}Be/^{9}Be$ ratios, i.e., ^{10}Be-14-5-7, ^{10}Be-14-5-8A, and ^{10}Be-14-6-3, were measured to check the accuracy of the measurements.

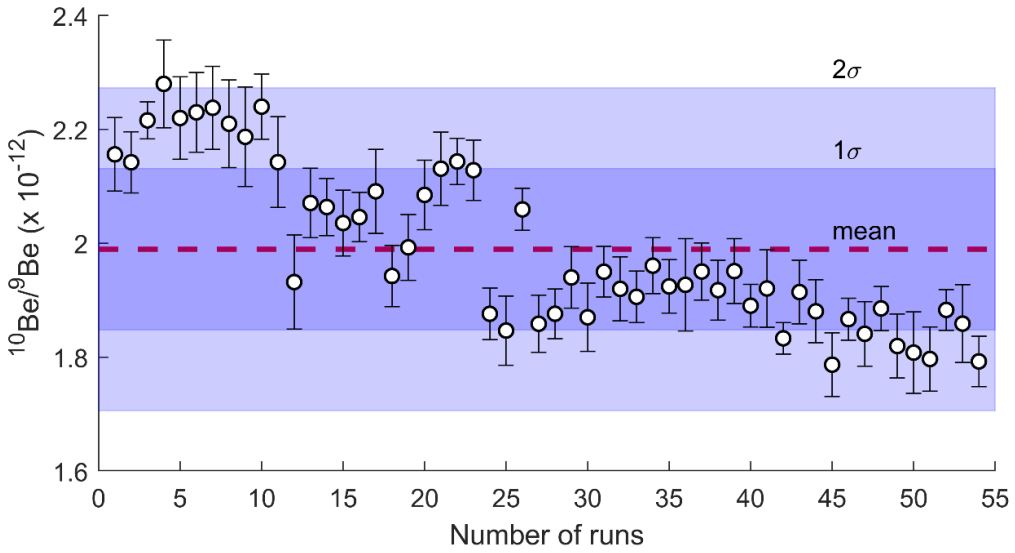

Figure 2.11: *$^{10}Be/^{9}Be$ ratio measured in PRL-AURiS for standard 07KNSTD ^{10}Be 14-5-6 (with consensus value of 1.504 x 10^{-11}) over the last 3 years (2019-2022).*

Table 2.4: *Results of the standard ^{10}Be-14-5-6 routinely measured along with samples for normalization of transmission loss.*

Standard Name	^{10}Be 14-5-6
Consensus Value (S_c)	1.504 x 10^{-11}
Mean value of runs (S_m; n=54)	1.99 x 10^{-12}
Overall efficiency (S_m/S_c x 100)	13.23 %
Transmission through the accelerator	56 % (Bhushan et al., 2019b)

The capability of the AMS to measure up to a blank level of 5.8 x 10^{-16} has been tested. However, during the routine processing of blank materials, the quality of the blank used and the cleanliness of the laboratory can affect the blank value. Based on the routine measurement of processed blanks, a value of ~ 1-2 x 10^{-14} was obtained (**Figure 2.12**). Though this value is one order higher compared to the instrument blank, considering the ^{10}Be/^{9}Be ratio of the measured samples (10^{-12} to 10^{-13} for in situ samples and 10^{-12} to 10^{-11} for meteoric samples), the processing blank is one to three orders lower. However, this further indicates that, for the measurement of samples containing very low ^{10}Be concentration (i.e., in-situ samples with low exposure), effort for further improvement in the blank values is required.

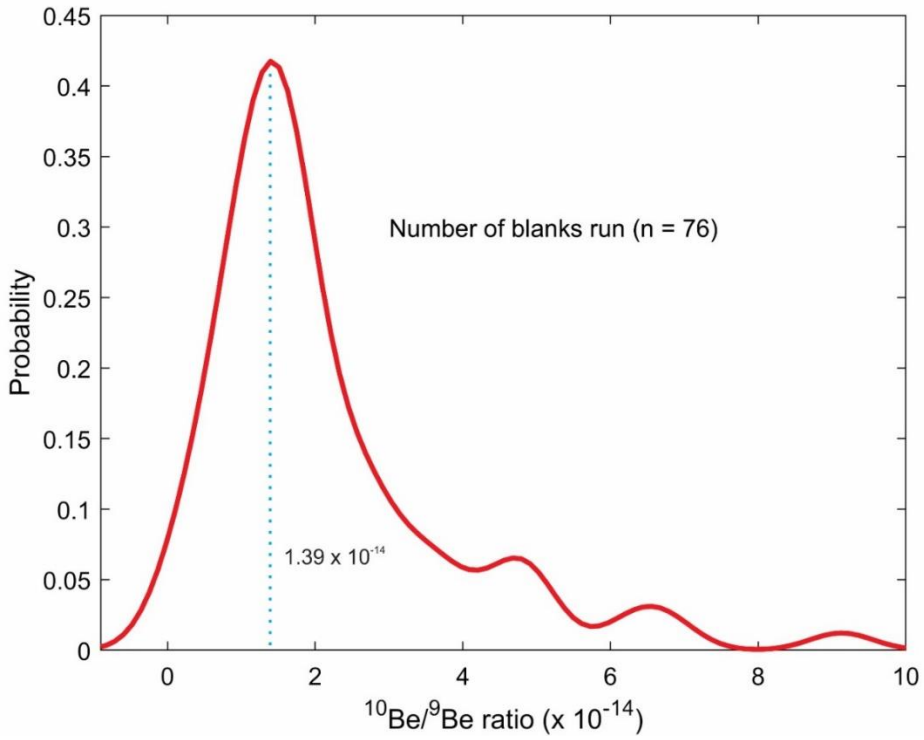

Figure 2.12: Probability distribution of processing blank values obtained during regular measurement of ^{10}Be.

Multiple standards apart from ^{10}Be-14-5-6 (run as a calibration standard) were run to check the accuracy of the measurement. The standards ^{10}Be-14-5-7, ^{10}Be-14-5-8A, and ^{10}Be-14-6-3 with known ^{10}Be/^{9}Be ratios were run as check standards throughout the measurements (**Figure 2.13**). The results show the samples are accurate up to 1 % in measurements with a ^{10}Be/^{9}Be ratio close to 10^{-12}, and up to 3 % in measurements with a ^{10}Be/^{9}Be ratio close to 10^{-13} (**Table 2.5**).

Table 2.5: *Accuracy and precision of ^{10}Be check standards measured in AURiS.*

Beryllium isotopic standards	**Precision (RSD: %)**	**Accuracy (%)**
^{10}Be-14-5-7	2.3	0.7
^{10}Be-14-5-8A	2.0	2.2
^{10}Be-14-6-3	3.0	2.9

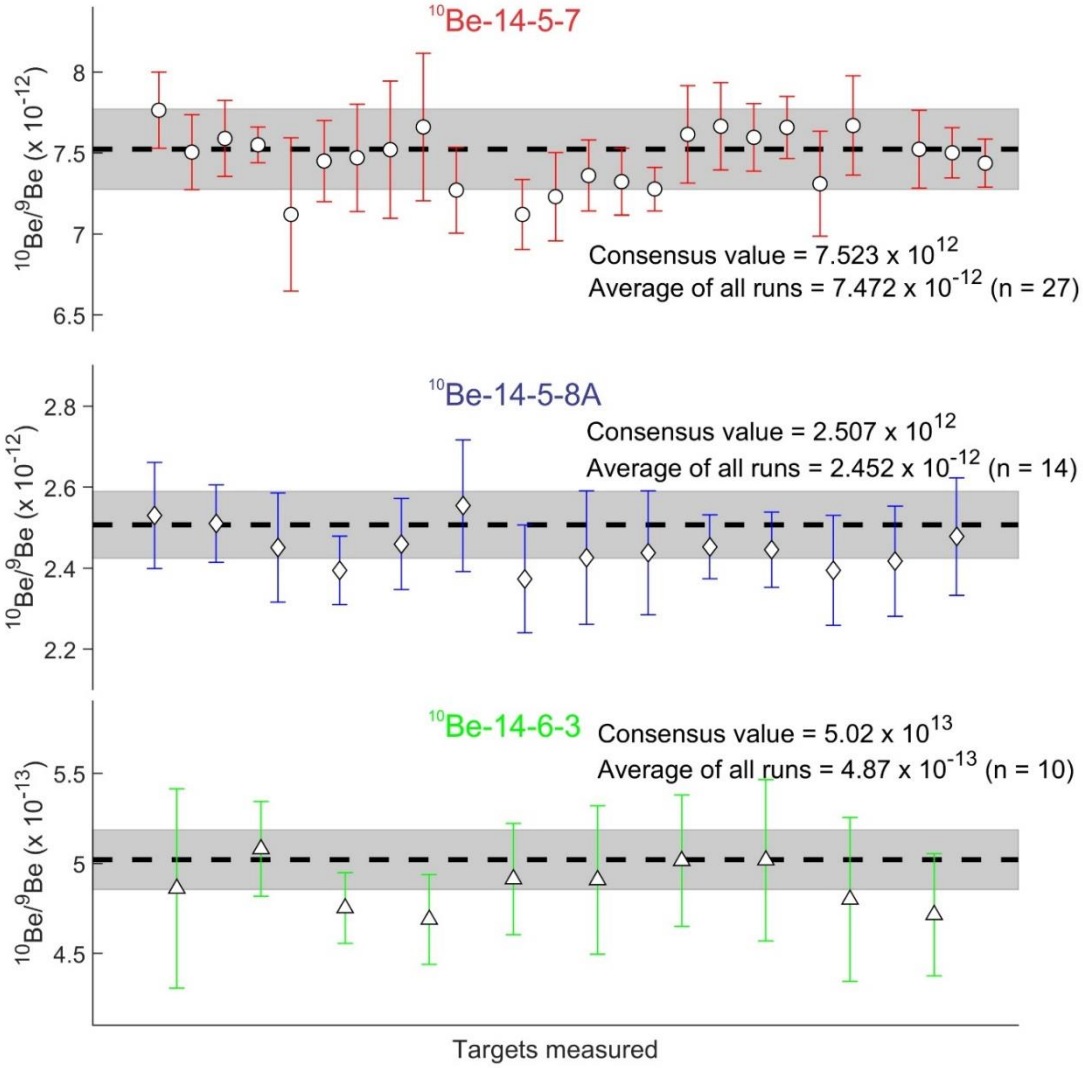

Figure 2.13: *Results of standards ^{10}Be-14-5-7, ^{10}Be-14-5-8A, and ^{10}Be-14-6-3 run along with samples for accuracy check of the measurements.*

2.2 Radiocarbon Measurement

2.2.1 Sample Processing and Graphitisation

Radiocarbon dating was carried out in both organic carbon (OC) and inorganic carbon (IC). For radiocarbon dating of bulk organic matter, about 2-5 grams of crushed and homogenized sample was treated with 0.6 N hydrochloric acid and heated to 85^{O}C for 1

hour to remove the carbonates. Following this, the sample was washed with deionized water and dried. 1-2 grams of the carbonate-free sample was packed in tin foils and put into an autosampler of Elementar Vario MICRO cube Elemental Analyser (EA). The sediment sample was combusted at $950^{O}C$ in the presence of oxygen to liberate CO_2, and CO_2 was further transferred along with helium acting as carrier gas. The excess of oxygen was removed in the reduction column (filled with copper), which also converts NO_x to N_2. In the path, any water is retained on a water trap containing phosphorus pentoxide. The resulting individual gases (mostly N_2, CO_2, and minimal H_2O) in the carrier gas are separated and further detected with the thermal conductivity detector before they leave the EA. Ultimately, purified CO_2 is trapped in the zeolite trap of the Automated Graphitisation Equipment (AGE.) CO_2 is absorbed, and N_2, as well as H_2O, are removed.

For radiocarbon measurement from the inorganic matter, homogenized and powdered samples were taken in 12 ml glass tubes in a Carbonate Handling System (CHS) (Wacker et al., 2013). The vials were closed with a screw cap containing a butyl septum. The atmospheric gas in the overhead space in vials was removed after a continuous flow of helium gas (for 10 minutes). Phosphoric acid (~ 0.5 ml for pure carbonates) was added using a gas-tight syringe. The samples were heated at $85^{0}C$ for nearly one hour for complete decomposition of carbonates and release of CO_2. The CO_2 was then flushed with helium flow to the AGE, and in the path, any water was retained on a phosphorus pentoxide trap.

The CO_2 thus obtained from the organic and inorganic fraction (~ 1 mg of carbon) was transferred to the AGE for graphitization. In the graphitization process, CO_2 is converted into graphite in the presence of hydrogen and iron (Němec et al., 2010; Wacker et al., 2010). The CO_2 gas initially passes through a zeolite trap that absorbs the gas and then releases the trapped CO_2 to the reactors until the desired pressure is reached. The trap is wrapped with a thermocouple-controlled heating wire to thermally release the trapped CO_2. The trap is then cleaned by heating to $500^{0}C$ while flushing it with helium before the next sample is loaded. The CO_2 is transferred to quartz reactor tubes (4.4 ml) that are mounted vertically to allow fast mixing of gases. The iron powder is pre-placed in the tubes, which acts as a catalyst in the graphitization reaction. Prior to sample loading, the iron catalyst undergoes a conditioning process that involves heating with air and subsequent reduction with pure hydrogen. This step removes the carbon species present

and activates the iron catalyst. Finally, the hydrogen is added in a controlled manner to the final preset H_2/CO_2 ratio. The reactors are placed above an electric oven which can move vertically. A graphitisation temperature of 580^0C and an H_2/CO_2 ratio of 2.3 were determined to be optimal (Wacker et al., 2010).

The graphitization process can be shown in a simplified way by a single Bosch reaction, though the reaction is rather complex.

$$CO_2 + 2H_2 = C + H_2O$$

However, there could be multiple ongoing reactions between CO_2, iron, and hydrogen, as shown by Němec et al. (2010). To summarize, iron reduces the CO_2, and hydrogen reduces the resulting Fe_3O_4 back to Fe. This reduction with hydrogen regenerates Fe in the system and causes the iron to act as a catalyst. The continuous conversion of CO_2 to graphite results in a decrease in pressure in the reactor tubes **(Figure 2.14**). Ultimately, the iron powder is coated with the graphite produced in the process. The Peltier thermoelectric cooler ensures the freezing of water that is produced during graphitization reaction. The sample in the form of graphite is pressed into aluminium sample holder targets with copper pins and taken for measurement in the Accelerator Mass Spectrometer in Physical Research Laboratory, Ahmedabad (AURiS) (Bhushan et al., 2019b, 2019a).

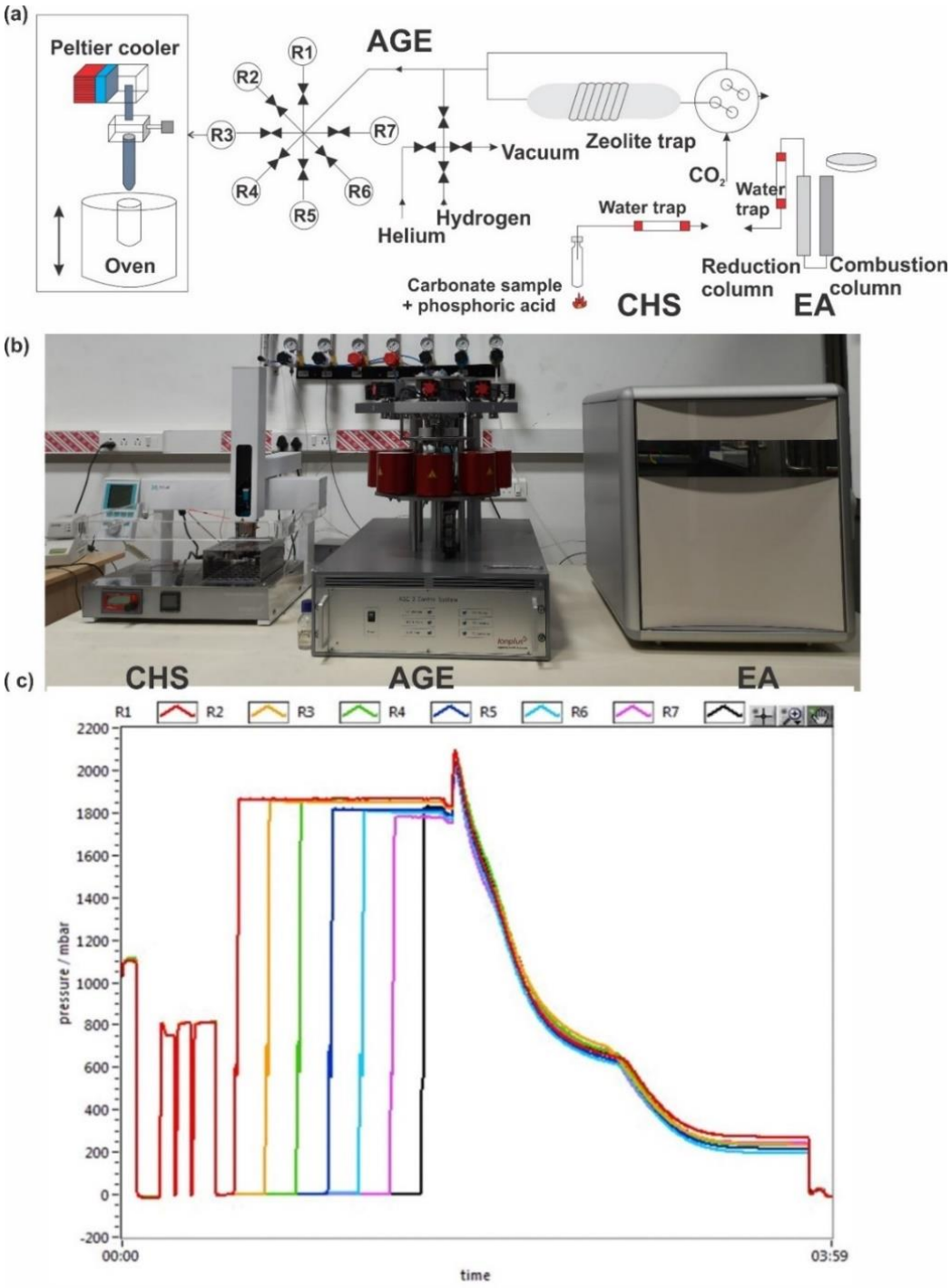

Figure 2.14: *(a) Schematic of the graphitization system. Drawn after Wacker et al. (2010). (b) The Automated Graphitization Equipment (AGE) along with Carbonate Handling System (CHS), and Elemental Analyser. (c) Change in pressure of reactors (R1 – R7) during the graphitization process.*

2.2.2 Radiocarbon Measurement with AMS

The measurement of radiocarbon was performed with the 1 MV AMS (PRL-AURiS). C^- ion is introduced into the LE magnet from the ion source. All the isotopes of carbon (^{12}C, ^{13}C, ^{14}C) are sequentially injected into the 1 MV accelerator. As the ions are accelerated after the stripping process, various charge states of carbon ions are produced. A 2+ charge state is chosen for carbon, as it provides a 44% transmission with higher stripping efficiency (Bhushan et al., 2019b; Raj, 2020). After passing through the HE magnet, both ^{12}C and ^{13}C are measured in the faraday cups while the ^{14}C beam is carried forward. After moving through ESA and RI magnet, the ^{14}C ions reach the detector. Ions like $^{7}Li^{+,}$ having a mass/charge ratio similar to that of $^{14}C^{2+}$, reach the detector and interfere with $^{14}C^{2+}$ signals. However, interferences are removed based on a typical E_{res} and ΔE plot of ^{14}C, and a fine-tuning of the instrument helps suppress the interferences significantly. The instrument is capable of measuring a $^{14}C/^{12}C$ ratio up to a level of 3.9×10^{-16}.

For routine measurements, multiple standards and blanks were prepared and measured with the samples. Oxalic Acid standard (Ox-II) was usually used as a primary standard, and Anthracite was used as blank. Multiple radiocarbon reference materials (FIRI-E, VIRI-U, and VIRI-R) were routinely measured to check the efficiency of graphitisation procedure and isotopic measurement (Boaretto et al., 2002; Rozanski et al., 1992; Scott et al., 2010) (**Table 2.6**).

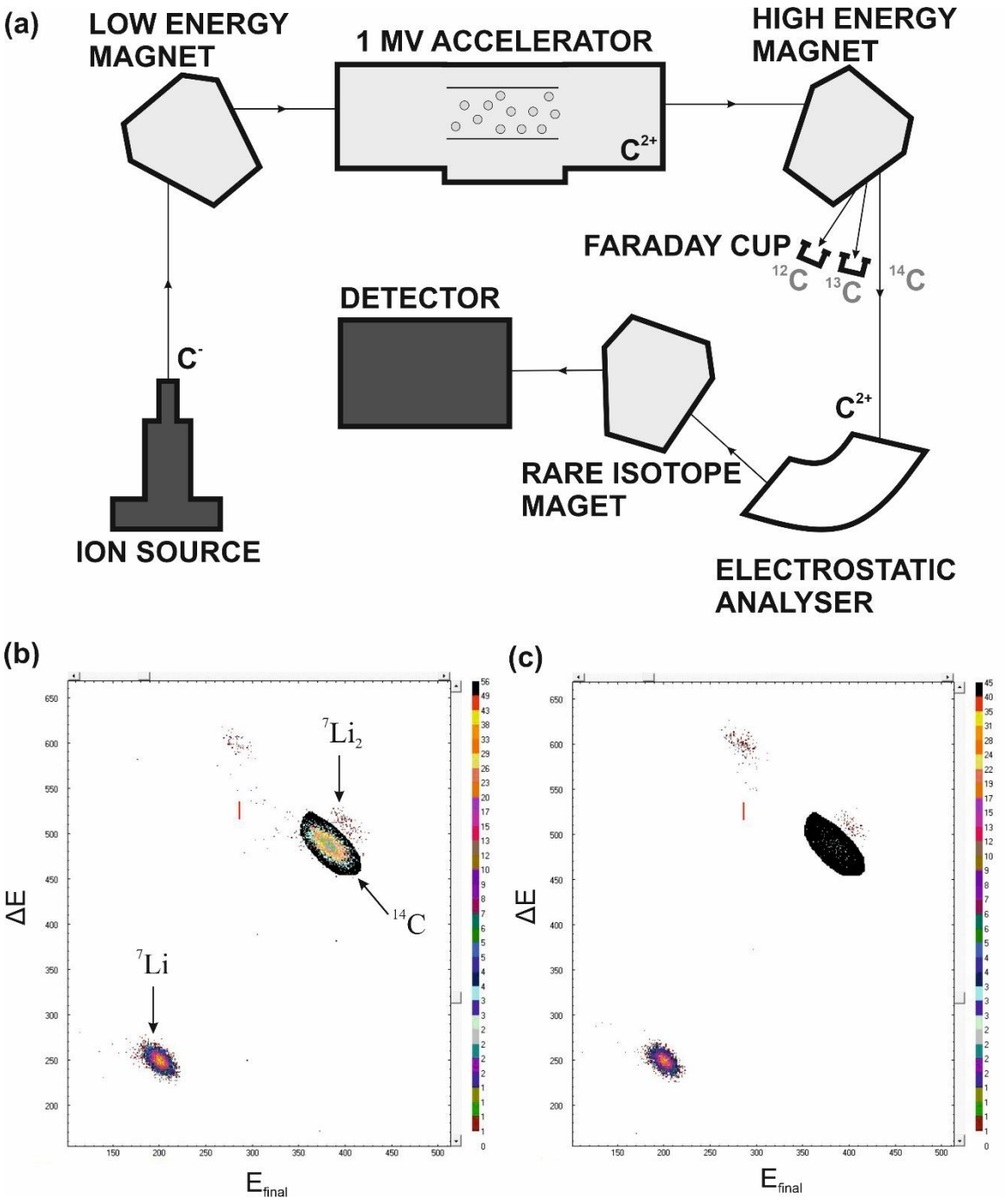

Figure 2.15: *(a) Schematic of Accelerator Mass Spectrometer (PRL-AURiS) established at PRL for ^{14}C measurements. Typical ΔE vs. E_{final} plot for a (b) sample and (c) blank measured for C isotopes with AMS. The black polygon represents the selected Region of Interest (ROI) for ^{14}C counting.*

Table 2.6: *Results of Radiocarbon reference standard measured along with samples.*

Reference Material	Unit	Consensus Value	Measured Value*
FIRI-E	years (BP)	11780 ± 7	11724 ± 74
VIRI-U	pMC	23.079 ± 0.0155	23.39 ± 0.21
VIRI-R	pMC	73.338 ± 0.0368	74.59 ± 0.86
IAEA-C2	pMC	41.14 ± 0.03	42.35 ± 0.34

**Average of multiple measurements*

The obtained radiocarbon ages were further calibrated in Calib 8.2. The Intcal20 calibration curve (Reimer et al., 2020) was used for terrestrial samples, while the Marine20 calibration curve (Heaton et al., 2020) was used for marine samples.

2.3 Optical Stimulated Luminescence Dating

Optical Stimulated Luminescence (OSL) dating relies on the measurement of natural radiation-induced trapped charges in naturally occurring minerals. The most commonly used minerals that occur in all geological environments are quartz and feldspar, which behave as natural radiation dosimeters and thus, can be exploited for the dating of the sediments (Aitken, 1998; Huntley et al., 1985). For OSL dating, samples were collected from the sand-rich horizons in opaque metal pipes. The light-tight samples were opened in the laboratory under subdued red light. The extraction of pure quartz grains was done following the standard protocol. The sample was treated with 10% HCl and 30% H_2O_2 to remove carbonate and organic matter and oven-dried at 40^0C, followed by sieving to retrieve 90-150 μm size fraction. This was followed by HF treatment (~40 minutes) to remove the alpha irradiated outer skin (~20 μm) and dissolve feldspar grains. The pure quartz was finally extracted after being subjected to the sample to Frantz Isodynamic magnetic separator to remove the leftover feldspar and heavy minerals. In order to ascertain the purity of quartz grains (contamination by feldspar grains), a few aliquots were subjected to Infrared Stimulated Luminescence (IRSL). Finally, the pure quartz grains were mounted on a stainless-steel disc and analyzed in an automated Risø TL-OSL recorder (TL/OSL-DA-20; (Bøtter-Jensen et al., 2010)), where samples were stimulated using a blue diode (470±20 nm). The detection optics consists of an EMI 9835QA photomultiplier tube

coupled with a 7.5 mm Hoya U-340 filter (330±35 nm). A $^{90}Sr/^{90}Y$ beta source was used for beta irradiation. The equivalent dose was calculated based on a modified single aliquot regeneration protocol (Murray and Wintle, 2000). A preheat of 240ºC for 10s, and cut off the heat of 240ºC was used. Typically, 48 discs were analyzed for each sample.

In order to eliminate the unstable signal (over the geological timescale), it is important to ascertain the pre-heat temperature imparted to the aliquots. Towards this, various pre-heat temperatures have been suggested, such as 160^0C for 16 hours (Stokes, 1992), 240^0C for 1 minute (Franklin et al., 1995), and 220^0C for 5 minutes (Rhodes, 1988). A pre-heat plateau test has been carried out in two representative samples (SPOSL 01 and 02) at increasing temperatures starting from 200^0C with every 20^0C going up to 280^0C, keeping the time constant (10 sec). We observed a plateau in equivalent doses between 200 and 260^0C in SPOSL 02 and between 200 and 240^0C in SPOSL 01 (**Figure 2.16**). Hence, a pre-heat temperature of 240^0C for 10 seconds was employed. The applicability of the above-mentioned protocol was tested by means of a dose recovery test. A known beta dose was given to optically bleached discs, and the given dose was measured using the SAR protocol. The average of the ratios of the recovered dose to the given dose was indistinguishable from unity, which demonstrated the applicability of the protocol (**Figure 2.16**).

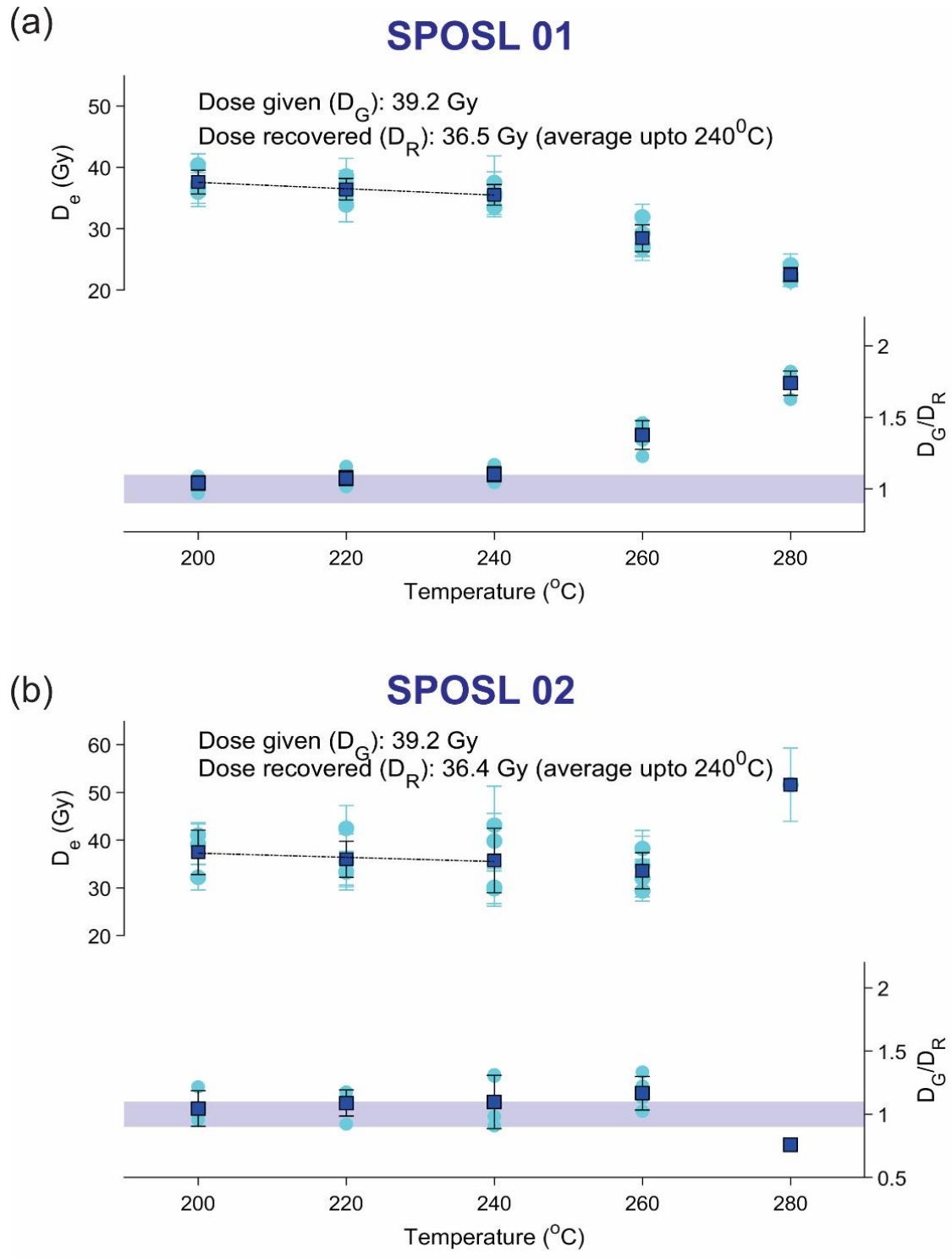

Figure 2.16: *Results of pre-heat plateau and dose recovery test for the two representative samples (SPOSL 01 and 02). The average dose values of multiple runs (cyan circles) are shown as blue squares. The results confirm the applicability of SAR protocol in the samples.*

For the radioactivity assays, ~50 gm of sample, were packed in air-tight vials and left for three weeks to attain the secular equilibrium. The U, Th, and K concentration was measured using an ultra-low background (background at 40K channel is 0.023cpm) high purity germanium detector (HPGe), housed within a 10 cm thick lead shield. Further details of the gamma-ray spectrometry can be followed from Shukla et al. (2002). Since the overdispersion in the equivalent doses was <30%, the Central Age Model (CAM) was employed for the computation of ages as suggested by Bailey and Arnold (2006). CAM equivalent doses were calculated in R programme (Kreutzer et al., 2021). The water content was assumed to be 10 ± 5 % , and ages were calculated using the DRAC online programme (Durcan et al., 2015).

2.4 Elemental Analysis using ICP-OES

A Thermo Scientific iCAP 7000 Plus series Inductively Coupled Plasma Optical Emission Spectrometer (ICP-OES) was used to measure multiple elemental concentrations from leached and digested sediment samples, as well as aliquots for beryllium column calibration (**Figure 2.17**). Though the instrument was primarily used for beryllium concentration measurement, multiple additional elements (aluminium, iron, titanium, iron, sodium, and boron) have also been measured.

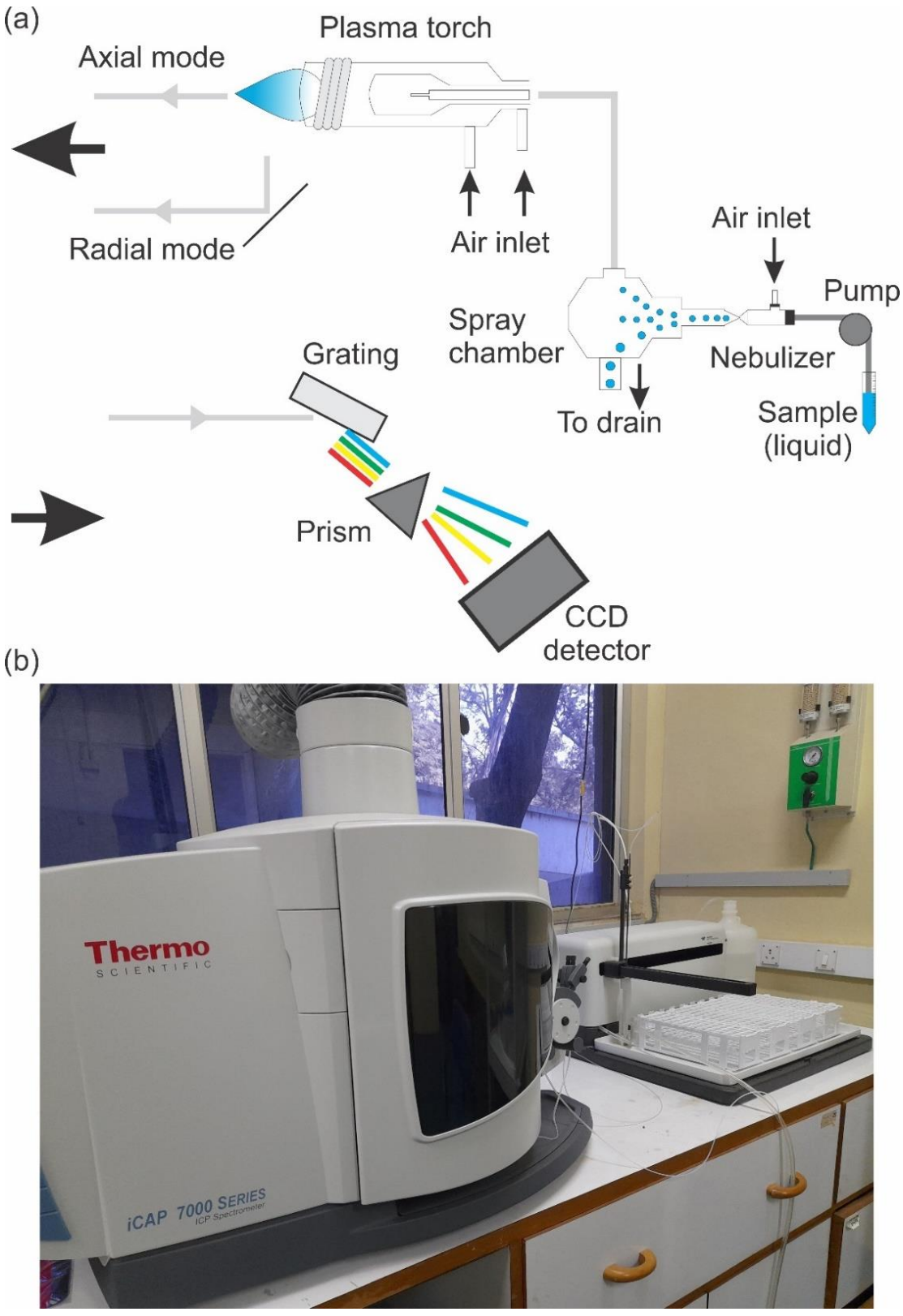

Figure 2.17: *(a) Schematic and (b) photograph of the ICP-OES facility at PRL, Ahmedabad.*

The typical ICP-OES consists of a sample injection system, plasma torch, radiofrequency power generator, an echelle optical design, and a charge injection device (CID) solid-state detector. The ICP-OES intakes samples in liquid form that are injected through an auto-sampler. The samples are pumped through a nebulizer to produce a fine spray of the sample. The larger droplets are passed to the drain, and the fine aerosols are passed to the plasma through the torch assembly. At higher temperatures, the sample is evaporated, and the residual samples decompose into atoms and ions. In the plasma chamber, the sample is excited by the electrical Radio Frequency (RF) generated plasma. The temperature reaches up to 9000 K. When the excited atoms/ions decay to ground energy state, a set of wavelengths of light are emitted. A set of wavelengths are typical for each element. Hence, the measured intensity of that typical wavelength corresponds to the concentration of the sample. The optic system of the ICP-OES consists of an echelle grating and a prism. The typical orientation of prism and the echelle grating generates a two-dimensional spectrum ("echellegram") consisting of a wavelength and order separation. The wavelength in the range of 166 to 847 nm can be measured in the instrument.

The precision of the beryllium concentration measurements was performed by repeated measurement of manually prepared Be elemental ICP standard. The precision was found to be better than 1 %. Digested U.S.G.S. sedimentary rock standards (SCO and MAG) were used for the accuracy check, which was better than 2 %.

2.5 Organic Carbon and Nitrogen Analysis

The sediment sample was physically examined for any extraneous organic/inorganic material, and such materials were removed physically. The sample was dried in an oven at 60ºC for 48 hours and crushed to a fine powder, and homogenized properly before taking a representative fraction of the sample. The standard procedure was followed for the proper removal of carbonates from the samples. Nearly one gram of finely crushed sample was taken centrifuge tube and treated with 0.6 N HCl solution. It was placed in an ultrasonicator at a temperature of 85ºC for 1 hour with manual shaking at a 15-minute interval. Finally, after the complete removal of carbonates, the sample was

thoroughly washed (3-4 times) with ultrapure water for the removal of acid. Following this, the sample was dried at 50ºC for 48 hours, powdered, and mixed homogenously.

Nearly 30-40 mg of the sample was packed in tin foils and inserted in a combustion tube through autosampler of the Thermofisher Flash 2000 Elemental Analyser (**Figure 2.18**). The sediment samples were combusted at 950^{O}C in the presence of oxygen to liberate CO_2, and CO_2 was further transferred with helium acting as carrier gas. The excess oxygen is removed in the reduction column (filled with copper), which also converts NO_x to N_2. In the path, any water was retained on a magnesium perchlorate trap. The combustion gases are separated using a gas chromatographic column (GCC). The detection of gases is performed in a Thermocouple Detector (TCD). The TCD. usually consists of two chambers where the analysis gas and the pure carrier gas flow at the same time. The thermal conductivity of the carrier gas sensitively reacts when a foreign gas (CO_2, N_2, H_2O) is added, and it is measured in the form of an electric signal.

Low Organic content Soil Standard (containing 1.86% carbon and 0.12% nitrogen) with varying C and N weights was used for calibration. High Organic content Sediment Standard (having 6.72 % carbon and 0.50 % nitrogen) and NC soil standard (having 2.31% carbon and 0.23 % nitrogen) was measured throughout the analysis time to check the efficiency of analysis. The precision was found to be 3 % for carbon and 6 % for nitrogen, while the measurements were accurate within 4 % for carbon and 7 % for nitrogen (**Figure 2.19**).

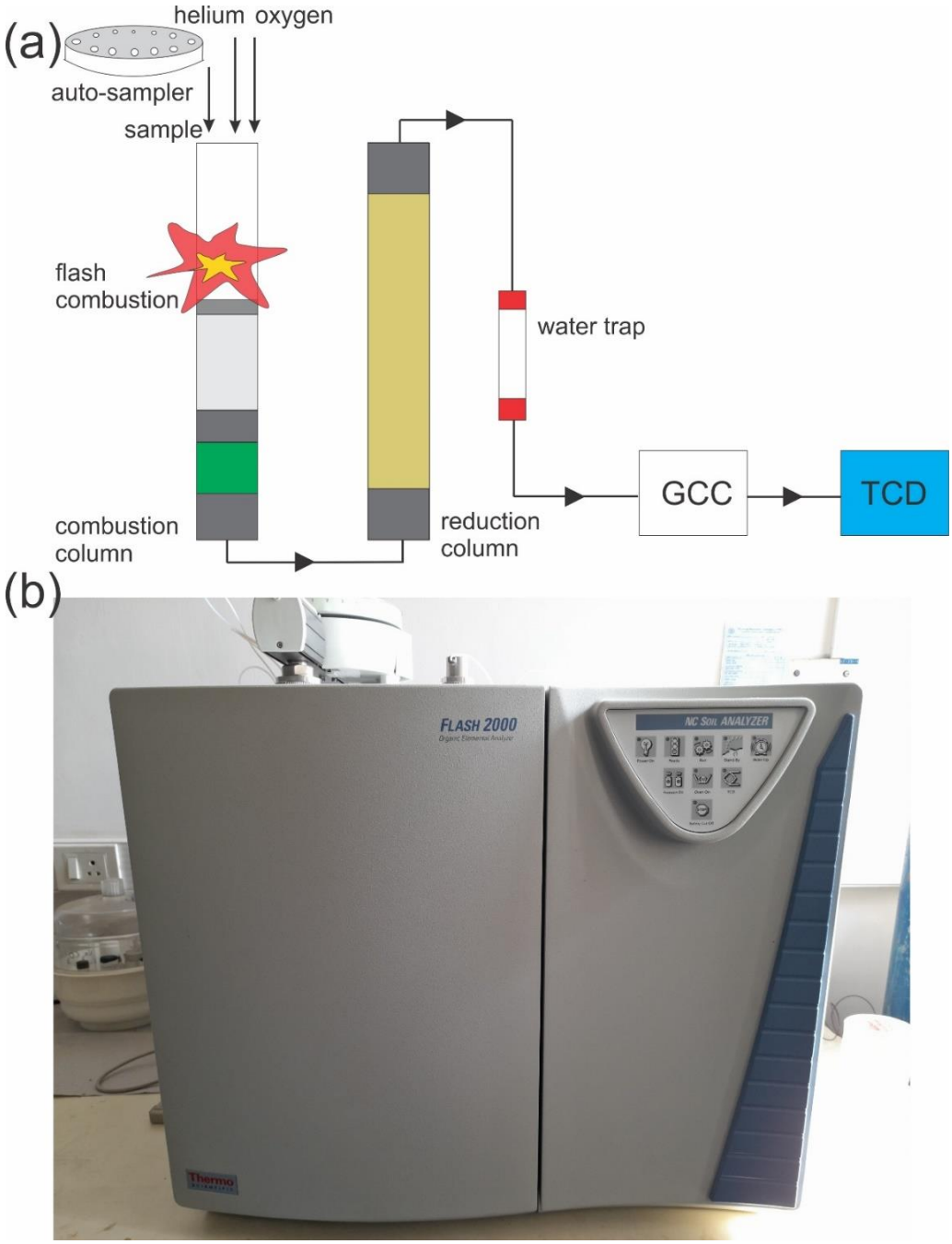

***Figure 2.18**: (a) Schematic and (b) Photograph of the CN elemental analyser at PRL, Ahmedabad.*

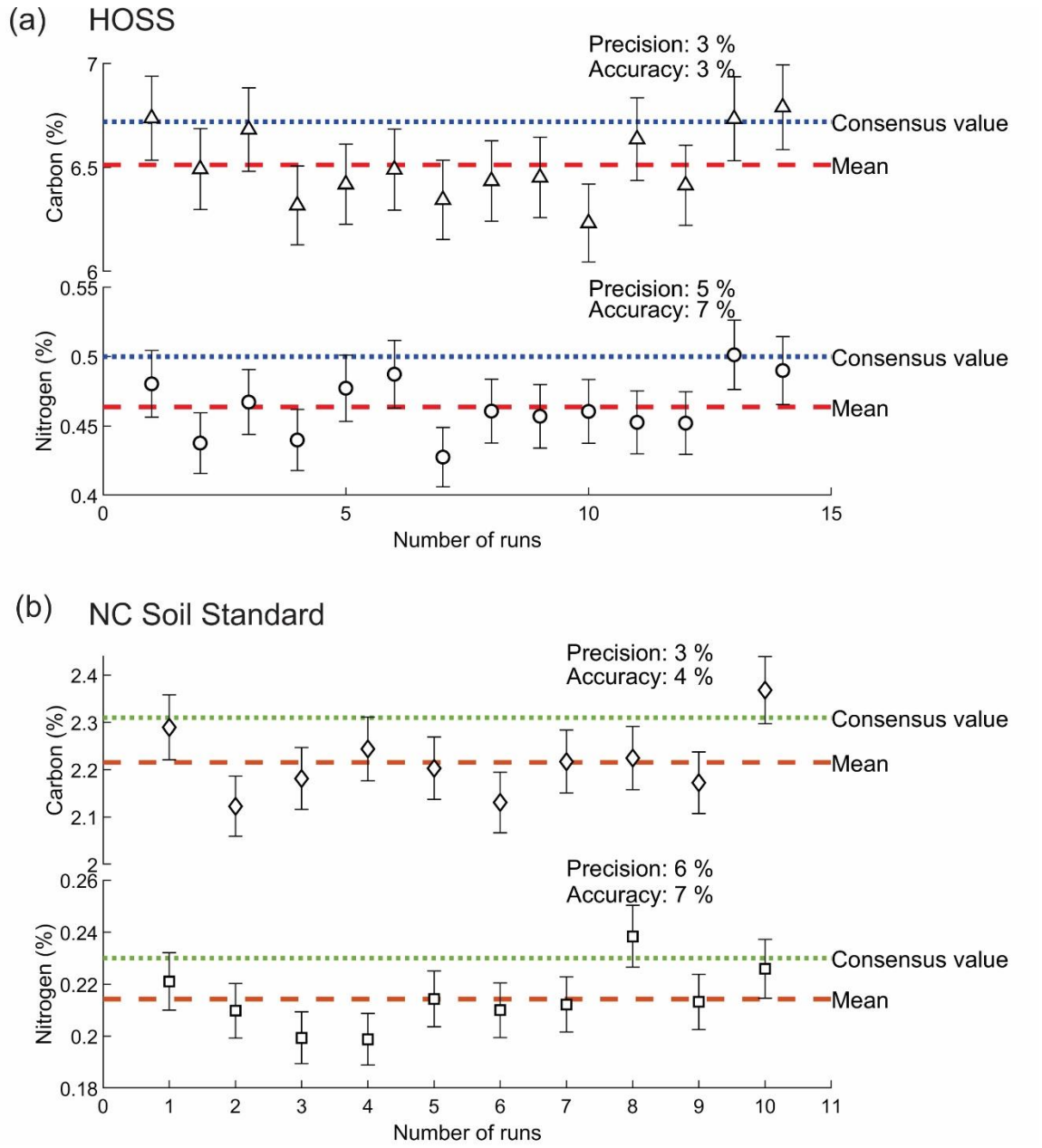

Figure 2.19: *Results of check standards run during the carbon and nitrogen analysis. The errors are reported based on the precision of the batch.*

2.6 Inorganic Carbon Analysis using Coulometer

The inorganic carbon concentration was measured with a UIC coulometer at PRL, Ahmedabad (**Figure 2.20**). Nearly 5-100 mg (depending on the carbonate content) of the sample was taken in a glass tube. 5ml of 40% phosphoric acid was added to the tube containing the sample and heated at 80ºC for the liberation of CO_2 gas by the reaction

between phosphoric acid and carbonates. The CO_2 gas was then transferred to the coulometric cathode cell solution using CO_2-free atmospheric air as a carrier. The moisture in sample CO_2 was removed by passing the gas through silica gel trap.

The CO_2 gas was subsequently passed through the coulometric titration cell. The coulometer cell is filled with a proprietary solution containing monoethanolamine and a coulometric pH indicator. It contains a platinum cathode and a silver anode. The cell assembly is placed between a light source and a photodetector in the coulometer cell compartment. The UIC Coulometer works on the principle of Faraday's law of electrolysis. Faraday's law states that 1 faraday of electricity will result in alteration of 1-gram equivalent weight of substance during electrolysis. CO_2 gas passes into the cell and reacts with monoethanolamine to form a titratable acid (hydroxyethylcarbamic acid) following the below reaction.

$$CO_2 + HOCH_2CH_2NH_2 = HOCH_2CH_2NHCOOH$$

As the acid changes colour of the indicator, the photodetection monitors the change in the colour of the solution as a percent transmittance (%T). As the %T increases, the titration current is automatically activated to electrochemically generate base at a rate proportional to the %T.

The produced acid is subsequently neutralized by a few reactions.

$Ag^0 = Ag^+ + e^-$ (Anode reaction)

$$2H_2O + 2e^- = H_2\,(g) + 2OH^-$$

$$HOCH_2CH_2NHCOOH + OH^- = HOCH_2CH_2NHCOO^- + H_2O$$

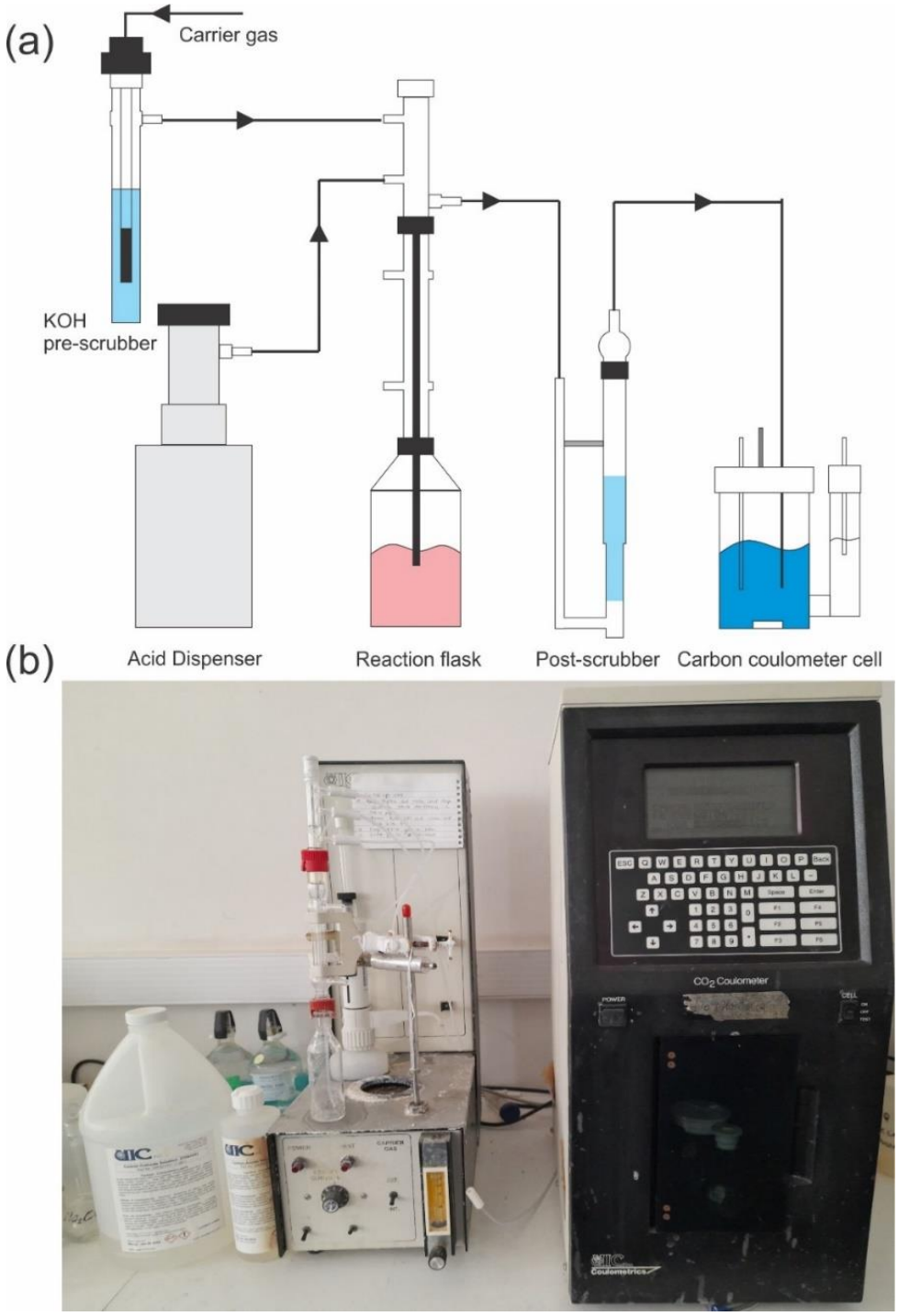

Figure 2.20: *(a) Schematic and (b) photograph of the coulometer used for inorganic carbon measurements.*

Manually prepared Na_2CO_3 standard solution was analysed frequently to check the precision of measurement. The precision of measurement for CO_2 was calculated to be better than 1.5 % and accuracy better than 2.3 % (**Figure 2.21**).

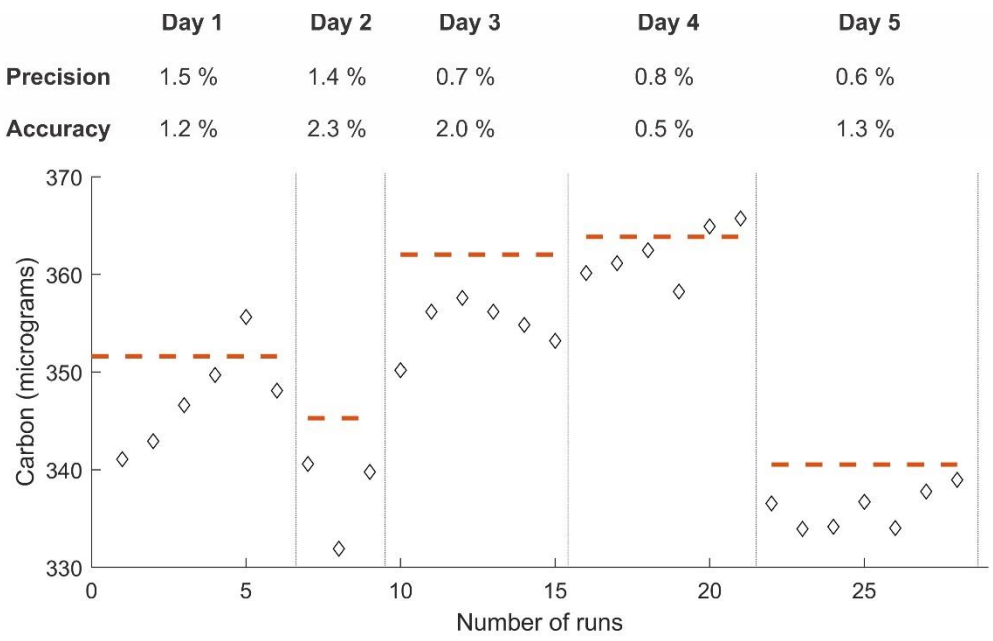

Figure 2.21: *Precision and accuracy of inorganic carbon check standards routinely measured along with the samples.*

2.7 Major and Trace Element Analysis using Xray Fluorescence (XRF)

For elemental concentration measurements, 2 g of finely powdered samples were taken with 0.5 g of wax binder and mixed homogenously in an agate mortar. The sample and binder mixtures were taken in 37 mm aluminium cups. The sample was then subjected to 150 kN pressure using a hydraulic press for nearly one minute. The sample in a pellet form was then taken for major and trace element analysis in an X-Ray Fluorescence (XRF) Spectrometer (Axios, from Panalytical Limited) established at Physical Research Laboratory, Ahmedabad. The instrument is fitted with an Rh X-Ray tube operated at 50 kV and 55 mA.

The calibration curve was prepared using sediment standard samples of varying elemental concentrations (Shukla, 2011). Standards were run at regular intervals to check the precision of the measurement. The precision is better than 5% for major elements and 15% for trace elements.

2.8 Stable Isotopic Analysis using IRMS

Oxygen and Carbon isotope from inorganic fraction and Carbon isotope from organic fraction was measured from sediments from relict lacustrine deposits in a Thermo delta-V plus Isotope Ratio Mass Spectrometer (IRMS) established at PRL, Ahmedabad (**Figure 2.22**).

For inorganic carbon analysis, bulk finely crushed homogenized sample was taken in standard 12 ml borosilicate vials in a GasBench (GB) II device. The GasBench II device is supported by a Combi PAL autosampler that performs fully automated transfer of gas samples. The vials containing carbonate samples were flushed using ultrapure helium gas for 10 minutes to remove atmospheric CO_2 present in the headspace of the vials. 100% phosphoric acid was added to the sample vial and then kept for a minimum of 1 hour at 80ºC for carbonates to react with the acid and CO_2 to get released. The CO_2 was then carried further into the GB II device using a specially designed headspace needle. The gas is transported through the capillaries by helium overpressure, and a drying stage removes the water in the sample gas mixture. In all types of measurements, the isotopic composition of the sample gas is compared to the isotopic composition of a reference gas, and the reference inlet system of the GB II device allows input of reference gas.

The gaseous sample is injected into the ion source through the inlet system. In the ion source, ions are generated by the impact of electrons at a high vacuum level. The ions are accelerated with energies up to ~3 KeV. Electrostatic lenses are used to focus the ions into a beam. The magnetic sector field is generated by an electromagnet with a maximum field strength of 0.75 T. By changing the magnetic field strength and/or the accelerating voltage, ions with a specific m/z ratio are passed to the ion collector. Each collector cup and its amplifier are connected to a Voltage-to-Frequency Converter (VFC), which is used to transform the analog ion current signals into pulses. The pulses are sent to counters for a pre-defined integration time, and at the end of each integration interval, the number of counts is read, and the ion current ratios are calculated.

The CO_2 gas was measured for $\delta^{13}C$ ($^{13}C/^{12}C$ ratio) with respect to the laboratory CO_2 reference gas. Decreasing peak height indicates proper transport of the sample/helium

mixture. All carbonate δ values are required to be referenced to the international standard Vienna Pee Dee Belemnite (VPDB), which is the successor of PDB. However, in regular laboratory measurements, other standards (primary standards provided by NBS or IAEA) whose δ values are known with reference to VPDB are used to estimate δ values of samples. The sample gases are measured with reference to the CO_2 reference gas. The δ value of reference gas is determined using a primary standard, and finally, the sample δ values are converted with reference to VPDB. A laboratory standard can also be used when the δ value of the lab standard is known by calibration with primary standards. Both primary standard (NBS 18; Coplen et al. 2006) and lab standard (MMB; Yadava and Ramesh 1999) were measured along with the samples. The measurement precision was calculated to be better than 0.1‰ through repeated measurement of MMB standards.

In a similar way, for organic samples, about 20-30 mg of carbonate-free sample was packed in tin foils and inserted via autosampler in the Elemental Analyzer (EA). The sample was combusted at 1020ºC for release of CO_2, and the released CO_2 gas was carried using high purity He gas as a carrier to a Thermo delta-V plus IRMS connected with EA. The CO_2 gas was measured for $\delta^{13}C$ ($^{13}C/^{12}C$ ratio) in a similar procedure as described above. IAEA CH_3 ($\delta^{13}C = 24.72 \pm 0.04$) was measured along with the samples (Coplen et al., 2006). The precision of measurement for $\delta^{13}C$ was calculated to be better than 0.1‰ by repeated measurement of IAEA CH_3 standards.

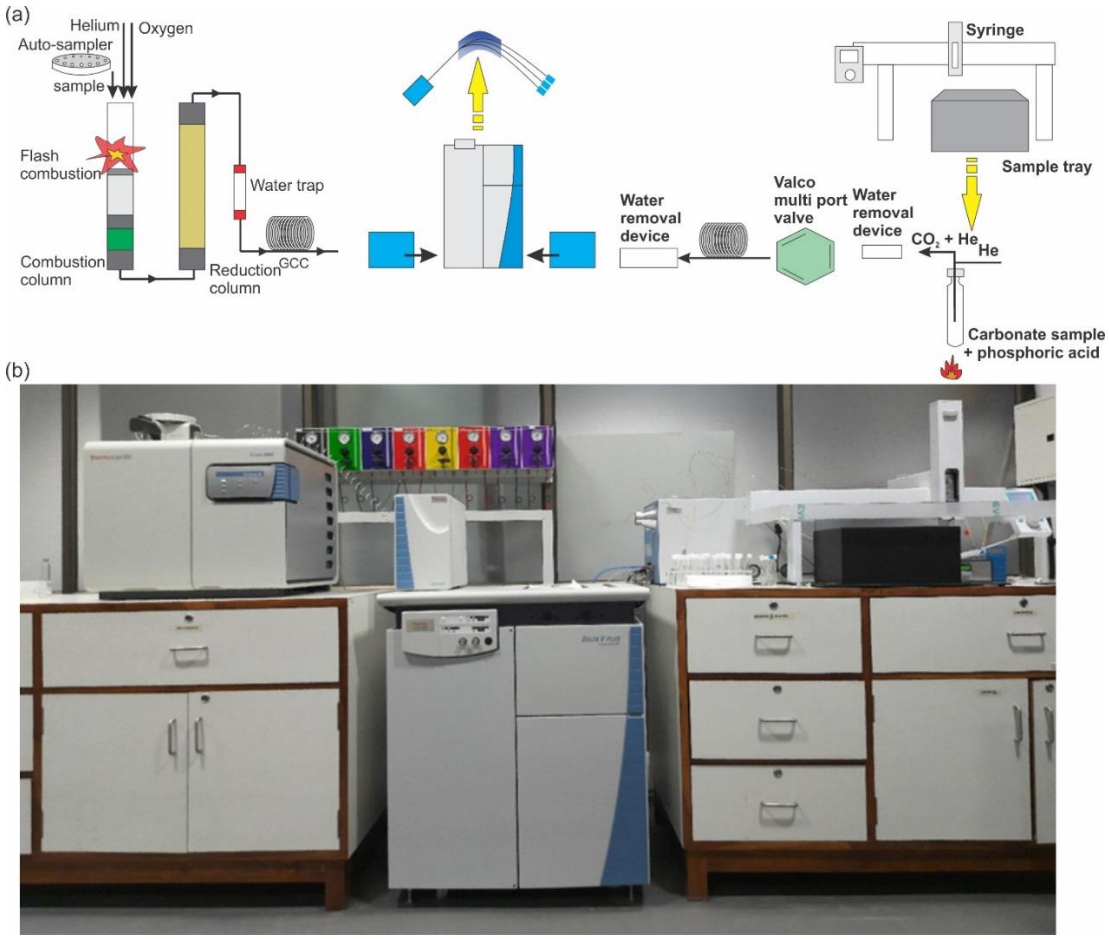

Figure 2.22: *The Isotope Ratio Mass Spectrometer (IRMS) along with the Elemental Analyser and Gas Bench II device at Physical Research Laboratory (PRL). (a) Schematic and (b) photograph of IRMS.*

Chapter 3 Quaternary Glaciation in the Northwestern Himalaya using ^{10}Be Exposure Age Dating

3.1 Introduction

The late Quaternary period experienced multiple phases of glacier advances and retreats in response to climate variability, implying the sensitivity of Himalayan glaciers to climate change. Therefore, the study of past glacier dynamics (millennial/multi-millennial time scale) becomes important as it provides crucial background for our understanding of natural trends and human impacts on climate change to assess the causes and possible future of the contemporary shrinking glaciers (Solomina et al., 2008). Considering that ~45% of the total river flow in the Indus, Ganga and Brahmaputra watersheds is contributed by the glacial melt that supports ~500 million people for agricultural and economic practices (Cruz et al., 2007), it is feared that under the anticipated global warming scenario, the hydrological characteristics of the rivers, which largely depend on snow melt and/or ice, are likely to suffer hydrologic disruptions (Barnett et al., 2005).

Our understanding of the dynamics and controls of late Quaternary glacier advances is largely based on the terrestrial cosmogenic nuclide (TCN) surface exposure dating (Owen and Dortch, 2014). Some of the major inferences based on TCN ages suggested (i) the absence of or less than 10 km lateral extent of glaciers during the global Last Glacial Maximum (gLGM) (Owen et al., 2002), (ii) ISM as the major driver of advances (Owen and Dortch, 2014), (iii) limited role of the mid-latitude westerlies, (iv) and the asynchronous response of the Himalayan region with the northern latitude ice sheets (Dortch et al., 2013). Although it seems clear that the maximum extent of glaciers was

reached before gLGM; it is still debatable whether it occurred during Marine Isotopic Stage (MIS)-3/4/5. The fact that most terrestrial records display spatial variations in response to global climate fluctuations and that the changes recorded on land are often asynchronous leads to difficulties in global correlation (Hughes and Gibbard, 2015). Therefore, making a generalisation about the forcing factors in driving the Himalayan glaciers over a large area in a given geographical setting may be hazardous. For this reason, Hughes and Gibbard (2015) recommended that the term LGM be considered an event-based rather than a time-based unit.

In the NW Himalaya, Dortch et al. (2013) suggested that older advancements (>20 ka) were dictated by the ISM, while the younger advances were driven by the mid-latitude westerlies. The recent studies, however, suggest that the maximum glacier expansion in the NW Himalaya perhaps occurred synchronously during the westerlies dominated MIS-4 and, therefore, suggest a coupling between the glacial expansion and the North Atlantic climatic oscillations for the older advances as well (Ganju et al., 2018; Nagar et al., 2013; Sharma et al., 2016; Sharma and Shukla, 2018; Taylor and Mitchell, 2000). Albeit variable in extent (Dortch et al., 2013; Owen et al., 2002), there seems to be a regional advance during the LGM in the Himalaya and Tibet (Ali et al., 2013; Bisht et al., 2015; Eugster et al., 2016; Ganju et al., 2018; Nagar et al., 2013; Schaefer et al., 2008; Sharma et al., 2016; Sharma and Shukla, 2018). Also, the reasons for the progressive decrease in the extent of valley glaciers observed during the Quaternary period are variedly attributed to the deepening of the glacier valleys and/or decrease in the precipitation caused by the upliftment of the higher Himalaya in the south and Karakoram in the west (Owen et al., 2006; Taylor and Mitchell, 2000). Thus, quantifying the timing and extent of multi-millennial scale glacial advances become significant as it would help in improving our current understanding regarding the causes of (a)synchronous response of the Himalayan glaciers.

In this study, the Nubra, Ganglas, and Tharoo valleys were visited for a detailed investigation of glacial deposits to establish the chronology of Quaternary glaciation. Considering the discrepancies in the previous attempts, additional effort was given 1) To decipher the factors responsible for the discrepancy between OSL and TCN based ages in

the NW Himalaya. 2) To find out possible ways to solve the issue in terms of suitable sampling and/or proper statistical filtering of obtained ages.

3.2 Study Location

The glaciated valleys in the northern Zanskar Ranges (Nubra Valley) and the Ladakh Ranges (Gangalas and Tharoo valleys) (**Figure 3.1**) were investigated. The Siachen Glacier (76 km long; 963 km^2 area) originates from the Gasherbhum ranges in eastern Karakoram (Kumar et al., 2020; Raina and Sangewar, 2007). The Siachen Glacier has carved a broad U-shaped Nubra Valley in at least four generations of glacier advancements with decreasing magnitude (Ganju et al., 2018). In contrast, in the Ladakh Range, most of the glaciers are restricted to cirques. In the Ganglas valley (southern Ladakh Range), the Puche glacier has an area of ~0.62 km^2 and a length of ~ 1.3 km (Brown et al., 2002; Shukla et al., 2020; Thayyen and Dimri, 2014). The evidence of Puche glacier advance is present up to the Ganglas village at a distance of ~8 km downstream from the snout. The region receives an average annual rainfall of ~100-150 mm, and most of the rainfall happens through mid-latitude westerly precipitation (Bhutiyani et al., 2010). In Leh, the mean annual temperature is around 7 ºC, with winter temperatures going below -28 ºC, whereas the summer temperatures rise up to 35 ºC (Chevuturi et al., 2018).

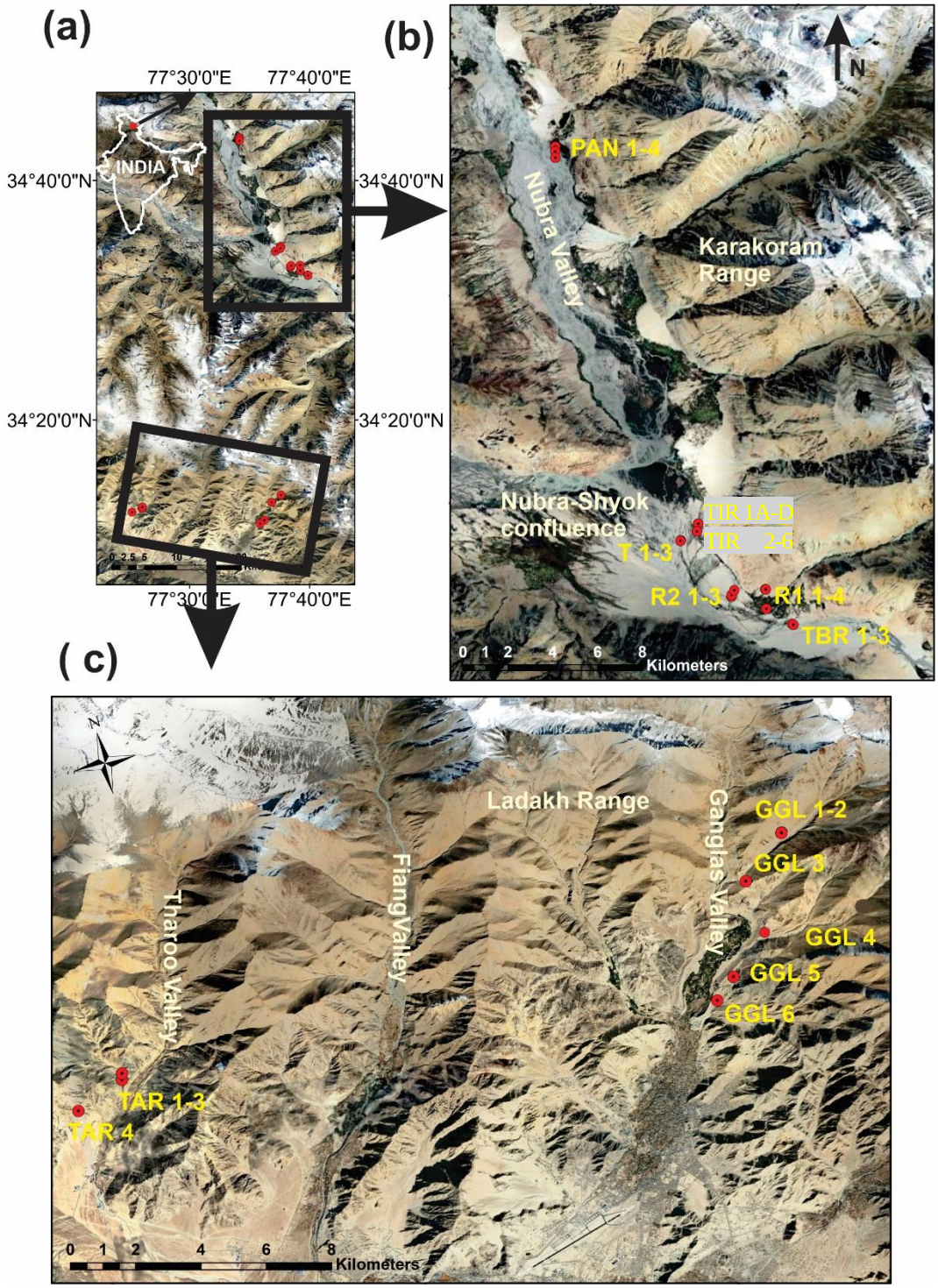

Figure 3.1: *(a) A map showing the studied the northwestern Himalayan region. The sampling locations in the (b) Nubra, (c) Ganglas, and Tharoo valley are shown.*

3.3 Landform Mapping and Sample Collection

A map of the glacial landforms in the region was prepared based on satellite and field-based analysis of the glacial deposits with support from previous studies in the region (Brown et al., 2002; Dortch et al., 2013, 2010; Ganju et al., 2018; Nagar et al., 2013; Owen et al., 2006; Shukla et al., 2020). Moraine stratigraphy was reconstructed using conventional field observations involving a detailed investigation of the moraine elevation, morphology, texture, and degree of weathering and lithification.

Samples for TCN dating were collected during three field trips (2018, 2019, and 2021). Both the striated bedrocks (glacially polished) and moraine boulders were sampled. To ensure that there is insignificant post depositional erosion of the polished bedrock or boulders, effort was made to sample the surfaces with well-developed desert varnish. Where inconsistency in the intensity of desert varnish was observed, only the dark-looking part was selectively sampled. The fresh-looking (poor varnish) part was either not sampled or removed in the laboratory using a rock cutter. However, particularly in the Tharoo valley, no boulders with well-developed varnish were found. Hence, in the valley, the presence of well-developed lichens was considered to be the criteria for minimum surface erosion over time. Large boulders present at the top of moraines were preferred to ensure stability.

Prior to sample collection, the location of the sampling surface, including latitude, longitude, and elevation, was noted using a handheld GPS (Garmin etrex10). The strike and dip of the sampling surface, along with shielding by surrounding mountains, were recorded using a Brunton compass and a clinometer, respectively. Additional features, such as boulder size, position, and sampling surface characteristics, were noted. Nearly 500 g to 1 kg of samples with sample depth varying between 1 cm to 6 cm were removed using a hammer and chisel. We tried to collect more samples for surfaces having a relatively lower quartz concentration. The samples were brought back to the laboratory for further processing.

3.4 Exposure Age Calculation

The shielding correction factor was calculated using the online exposure age calculator version 3 (previously known as CRONUS-Earth online calculator) (Balco et al., 2008) using horizon obstructions and dip, the strike of the sampled surface. The scaling models used for exposure age calculation have been improved significantly through the years through improved models and the addition of calibration datasets. The exposure ages were calculated using the online exposure age calculator version 3 (Balco et al., 2008). Three scaling schemes have been utilized for exposure age estimation, i.e., Lal-Stone time-independent (St) (Lal, 1991; Stone, 2000), Lal-Stone time dependant (Lm) (Lal, 1991; Nishiizumi et al., 1989; Stone, 2000), Lifton-Sato-Dunai (LSDn) (Lifton et al., 2014). The CREP online calculator (Martin et al., 2017) was also used to recalculate the ages to ensure minimum variation in estimated ages using different calculators. The obtained ages from different scaling models do not show a drastic offset in the values. Finally, the exposure ages have been reported with the recently updated scaling model (LSDn).

3.5 Description of Glacial Landforms in NW Himalaya

In the Nubra valley, multiple stages of glacier advances have been identified (Dortch et al., 2010; Ganju et al., 2018). The evidence of two major glacier advances is observed near the Tirith village, suggesting the Siachen glacier had advanced up to the confluence of the Nubra-Shyok rivers (~60 km from the present glacier snout). The younger glaciation was named Deshkit-1 by Dortch et al. (2010), which is equivalent to Tirith-I of Ganju et al. (2018). The older glacier advances were differentiated into two events (Deshkit 2 and 3) by Dortch et al. (2010), which according to Ganju et al. (2018) was a single advance with a recessional phase (reduction in ice volume) and they have named it Tirith II. In this study, we followed the nomenclature of Ganju et al. (2018) viz. Tirith-I and II.

Two distinct moraine ridges representing the two glaciation events are observed near the Tirith village (Karakoram ranges). The highest (stratigraphically older) moraine (Tirith II) is located at an elevation of ~3900 m and at ~700 m above the Nubra River valley

floor. The lower and stratigraphically younger moraine (Tirith I) is present at an elevation of ~3500 m. The Tirith II moraine continues up to the Khalsar village, which is located at a distance of ~7 km southeast of the Tirith village. The Tirith I moraine terminates near the Tirith village with a terminal moraine, where multiple recessional moraines are observed. The moraines are dominated by cobbly granite and granodiorite matrix with subordinate suture zone rocks. Both the Tirith, I, and II moraines contain numerous granitic boulders, which are, on average ~ 1-2 m wide while at some places going up to 3-4 m on the surface. In various places, the bedrocks are exposed with polished surfaces and clear striation marks indicating the glacier movement. In general, both the boulders and the bedrocks in the Nubra valley display a proper growth of dark-coloured varnish on the surface, indicative of minimal weathering post glaciation.

In the southern Ladakh Ranges, evidence of multiple stages of glaciation has also been identified (Burbank and Fort, 1985; Fort, 1978; Owen et al., 2006). In the stratigraphic order (older to younger), they can be listed as the Indus Valley stage, Leh stage, Kar stage, Bazgo stage, Khaling stage, and recent advances. In the study of Shukla et al. (2020), where they focused only on the Leh/Ganglas valley, they have named the events as Puche Glacier Advance (PGA)-1, 2, and 3, where PGA-1 is the equivalent of the Leh stage. In the present study, the landforms of the PGA-1 advance in the Ganglas valley and the equivalent landforms in the Tharoo valley were studied in detail.

The ~ 6 km long moraine of PGA-1 event is present between the south Pulu and Ganglas villages. The event terminates near the Ganglas village with a latero-frontal moraine. Nearly 1m thick boulders are present on the moraine, and moderate development of varnish was observed on the surfaces. In a few places, fine grained boulders and bedrocks are present, which show a growth of comparatively darker varnish. In the Tharoo valley, the boulders lying on the moraines equivalent of PGA 1 significantly lack varnish development. However, on varnish poor boulder surfaces, the growth of lichens was observed. Bedrocks were rare in both Ganglas and Tharoo valley. Despite a detailed investigation, bedrocks only at three places with appropriate surface conditions (polished with well developed varnish) could be located in the Ganglas valley and were sampled for exposure age dating.

3.6 TCN and Optical Age Dating

In the Himalayan region, glaciation events have been dated primarily using the Optical Stimulated Luminescence (OSL) method and Terrestrial Cosmogenic Nuclide (TCN) method due to the lack of suitable radiocarbon datable material. The dating of glaciation events by TCN is based on the principle that the cosmogenic nuclide concentration on an exposed surface (freshly exposed due to erosion by the glacier) increases with the continuous interaction of rock material (mainly Si and O) with cosmic ray particles (Ivy-Ochs and Kober, 2008). The exposure age dating using cosmogenic nuclides relies upon measuring cosmogenic nuclides concentration in exposed bedrocks and boulders sitting on moraines (Ivy-Ochs and Kober, 2008).

Resetting of the TCN chronometer can be linked with the glaciation events as glacial erosion removes the top TCN rich surface, and a fresh surface is exposed. On the top parts of the exposed surface, cosmogenic production is dominated by spallogenic interaction. Considering a density for granitic rocks (~2.65 $g.cm^{-3}$), the spallogenic production rate reduces to half at each ~40 cm with increasing depth (Balco, 2011). The cosmogenic nuclide production due to spallation becomes almost negligible 2-3 m below the surface. Hence, locally, denudation of 2-3 m of the bedrock ensures the removal of the cosmogenic nuclide-rich layer and exposure of a fresh surface with minimum inheritance (Prud'homme et al., 2020). The presence of inherited cosmogenic nuclides from any prior exposure event leads to apparently older ages (Applegate et al., 2012; Harrison et al., 2010). However, removal of inheritance (the top part of bedrock rich in cosmogenic nuclide) is mainly a function of glacier-bedrock interaction. It depends on various parameters such as the thermal state of the ice base (cold or warm base), the velocity of ice movement by sliding, bedrock topography and lithology, and the amount of transported till (Herman et al., 2015). Temperate glaciers are very effective in erosion as free water is present at the bottom of glacier beds due to the melting of ice (Balco, 2011). TCN ages on surfaces are affected by several geological factors, which include weathering, exhumation, and shielding of the surface by sediment and/or snow, thereby leading to lower ^{10}Be concentrations and hence, younger ages (Ivy-Ochs et al., 2007; Owen et al., 2011). The situation is further complicated, where significant offsets in boulder and bedrock-derived

exposure ages are obtained. Multiple earlier studies have reported older boulder ages compared to polished bedrocks (Prud'homme et al., 2020). Inversely, some of the work have reported otherwise, with higher exposure ages from bedrocks compared to boulders (Bierman et al., 1999; Crest et al., 2017; Jansen et al., 2019).

OSL dating relies upon the measurement of the luminescence signal (induced by surrounding irradiation) intensity emitted by minerals such as quartz or feldspar under light stimulation. In glacial environments, the luminescence method often provides older ages due to inherited luminescence signals within the sampled sediment (Fuchs and Owen, 2008). This inherited signal represents an incomplete resetting of the luminescence signal within the grains before deposition due to limited light exposure and is called partial bleaching. Partial bleaching is common in glacial environments because grains are typically transported over short distances in turbid water or even subglacially (Duller, 2006; Fuchs and Owen, 2008). On the other hand, a few works have reported younger OSL ages possibly associated with the reworking of sediments (Ali et al., 2022, 2013; Ou et al., 2014). Often, the low sensitivity of grains in the glacial environment restricts the use of the luminescence method for dating glacial landforms (Fuchs and Owen, 2008).

In the northwestern Himalayan region chronology of Quaternary glaciation using the TCN method mostly relied on the moraine boulders. A significantly higher spread observed in the ages suggests that the ^{10}Be concentration suffers from the factors discussed above. Hence, prior to constraining the chronology of any particular glaciation event, a detailed investigation of these factors is required. Thus, the chronology of the Tirith I and II stages from the Nubra valley and PGA-1 of Ganglas valley have been investigated with a detailed comparison between the OSL and the TCN ages.

3.7 Chronology of Glaciation in the NW Himalaya

3.7.1 Chronology of Glaciation in the Nubra Valley

Samples representing the Tirith-1 glacial stage have been dated in multiple attempts involving TCN exposure age dating and OSL dating (Dortch et al., 2010; Ganju et al., 2018; Nagar et al., 2013). The ages obtained by the TCN dating of boulders showed a large

spread, with the ages varying between 24 to 64 ka (Dortch et al., 2010). Considering problems associated with both underestimations of ^{10}Be concentration due to erosion (as well as shielding) and overestimation of ^{10}Be concentration incomplete removal of inherited ^{10}Be during the resetting process, the spread in TCN ages expected and is often observed (Dortch et al., 2013, 2010; Orr et al., 2018; Owen et al., 2006). Hence Dortch et al. (2010) removed the younger and older ages considering outliers, and the remaining ages provided a cluster between 45 to 49 ka. However, with further research using the OSL method, Nagar et al. (2013) provided initial hints that the event could be much younger than reported by Dortch et al. (2010). The same was also confirmed based on a much more detailed study employing OSL chronology by Ganju et al. (2018). Thus, these studies gave rise to the question, whether OSL ages were too young or TCN ages were too old.

In the present study, similar observations to Dortch et al. (2010) are also made with large variations in boulder-derived ages (ages varying between ~ 27 - 72 ka). However, different results are obtained from the bedrock, showing ages lying between a narrow range of 23 to 36 ka. The bedrock derived ages are also supported by the OSL ages from the previous studies showing a reasonable overlap (Ganju et al., 2018; Nagar et al., 2013). From these observations, it is reasonable to conclude that the bedrocks are least affected by pre and post-depositional processes that could affect the ^{10}Be inventory (showing less spread). Considering the bedrock derived ages falling on the younger side of boulder derived ages, it also suggests that the boulders are highly affected by pre-depositional inheritance rather than post-depositional shielding or erosion. Therefore, the ages obtained in the present study support the conclusion that the bedrocks are preferentially more suitable samples for deriving the exposure age of glaciation events in Nubra valley.

However, it is also important to note that suitable bedrock samples are always difficult to find, while boulders are more common in such glaciated valleys. Determining the chronology of glaciation from boulders could be critical as they may provide wide spread in obtained ages. Multiple studies (For example, Heyman et al., 2011; Putkonen and Swanson, 2003) have suggested that post-depositional processes affect the boulder-derived exposure ages more compared to pre-depositional inheritance. Thus, they have suggested that the oldest date of moraine boulders best represents the time of glaciation. However, contrary to this, many studies have revealed that inheritance has the predominant effect and

the youngest ages best represent the glaciation time (Benson et al., 2005). In the Tirith-I glacial stage, the boulder ages are older than the bedrock ages. And the younger ages of Dortch et al. (2010) (24.5, 27.6, and 30.9 ka) and from the present study are in overlap with bedrock derived TCN ages. Thus, as in Nubra valley, the boulders primarily suffer due to incomplete removal of inheritance, and the lower age cluster may be considered as the appropriate age for the glaciation event.

Here, it is also important to investigate why the maximum number of boulders in the Nubra valley contains a high amount of inherited ^{10}Be. As the bedrocks in the Nubra valley showed insignificant inheritance, it is also clear that during the advance of the glacier during Tirith-I stage in the Nubra valley, efficient removal of the top ^{10}Be rich layer in the valley rocks had occurred. Hence, the boulders which are derived from subglacial plucking by the glacier would not have retained any inherited ^{10}Be. A few boulders derived through mass wasting could contain inherited ^{10}Be on the previously exposed side. Hence, the removal of exposure from these kinds of boulders could be a function of the distance of transport. And to ensure complete removal of inheritance, ~2-3 m of the surface should be removed. This suggests, considering an ideal inheritance-free situation, that the boulder, with a diameter of 1m, would have a diameter of >5 m during its origin. Another interesting process, which could be responsible for older boulder ages, is the contribution of boulders from small tributaries to the main Nubra valley. The Nubra valley is supplied by many small tributaries such as Layogma, Lagongma, Zingrulma, and Gyongla (Ganju et al., 2018). Lesser glacier thickness in these smaller tributary valleys might have resulted in incomplete removal of inheritance. Thus, in future, it requires that a study be attempted with ^{10}Be exposure age dating from these tributary valleys to check if the bedrocks contain significant inheritance.

Considering both the previously published results from both OSL (Ganju et al., 2018; Nagar et al., 2013) and TCN (Dortch et al., 2010) methods along with ages from the current study (**Figure 3.2**), the ages show multiple clusters at ~28 ka, ~45 ka, and ~65 ka. Considering the issues associated with inheritance (as discussed above), it is clear that the youngest cluster best represents the chronology of the glaciation. The ages in the young cluster vary between 18 to 36 ka, which also shows the maximum relative probability with the maximum number of ages falling in the range. Using the gaussian distribution for the

considered ages, it was estimated that the young Tirith-I advance corresponds to early/mid MIS-2.

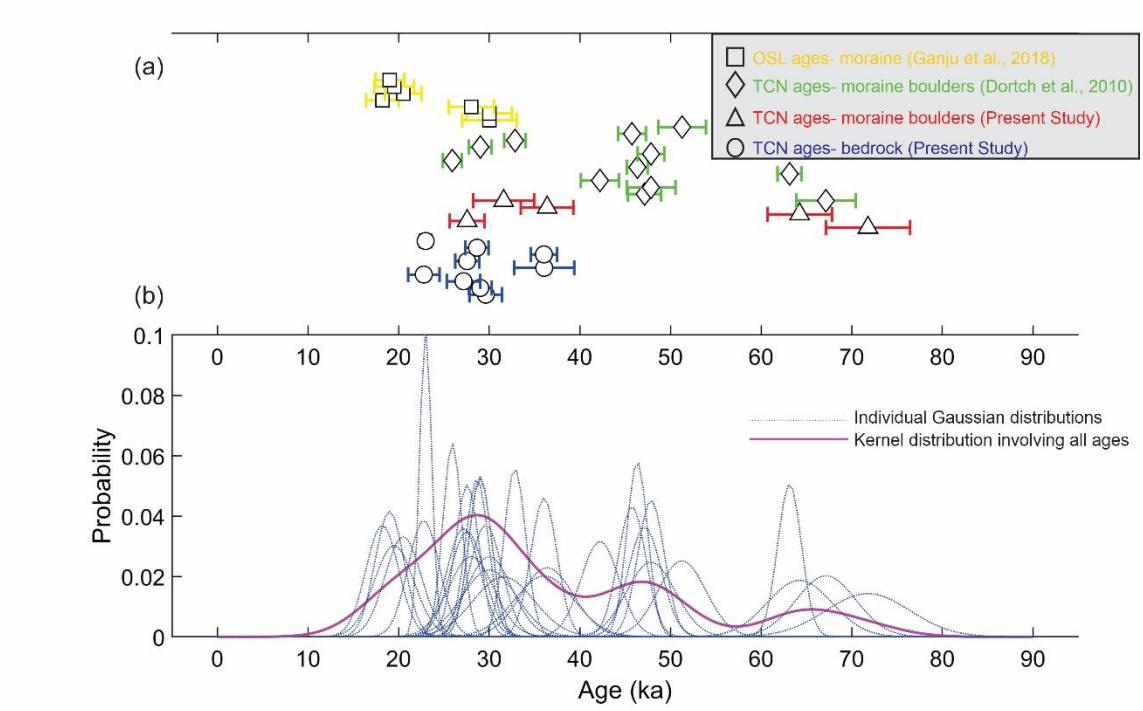

Figure 3.2: *(a) Ages obtained from multiple chronological methods, i.e., OSL* (Ganju et al., 2018; Nagar et al., 2013) *and TCN (Dortch et al., 2010; Present Study) dating for the Tirith-I glacial stage (b) The distribution of each individual ages (dotted blue curve), the kernel distribution curve (pink curve) consisting all ages are shown.*

Though the Tirith-II glacial stage has also been dated by both TCN and OSL dating (Dortch et al., 2010; Ganju et al., 2018), the number of ages obtained is relatively lower compared to Tirith-I glacial stage. The TCN ages from the previous study are based on bedrocks. Though the OSL ages are much younger, it is difficult to constrain the chronology of the glaciation based on a limited number of obtained ages. The maximum number of ages show a cluster between 60 to 90 ka, indicating that the glaciation event occurred during MIS-5/4.

3.7.2 Chronology of Glaciation in the Ganglas Valley

The Puche Glacier Advance (PGA 1) in the Ganglas valley has also been dated using both TCN and OSL methods (Owen et al., 2006; Shukla et al., 2020), providing a

significantly diverse chronology (**Figure 3.3**). The initial attempts using TCN dating of moraine boulders have provided much older ages going as old as 250 ka (Owen et al., 2006). On the contrary, the OSL ages are strongly clustered between 22.7 to 31.5 ka (Shukla et al., 2020), similar to the three ages obtained from bedrocks. In the present study, the ages from moraine boulders also showed a large spread similar to prior studies. The large spread in boulder-derived TCN ages again suggests high inheritance. Hence, considering the older ages as outliers, the chronology of the event is constrained to be early/mid MIS-2.

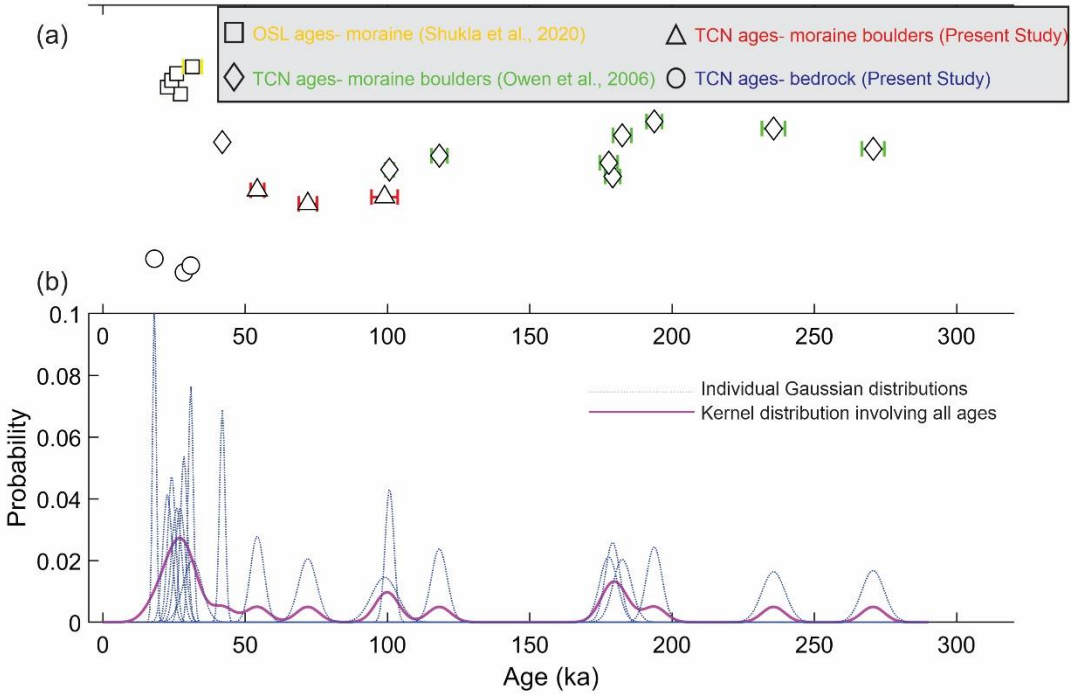

Figure 3.3: *(a) The ages obtained from multiple chronological methods, i.e., OSL* (Shukla et al., 2020) *and TCN dating (Owen et al., 2006; Present Study) for the PGA-1 stage in Ganglas valley (b) The distribution of each individual ages (dotted blue curve), the kernel distribution curve (pink) consisting all ages are shown.*

3.7.3 Chronology of Glaciation in the Tharoo valley

The TCN exposure ages from moraine boulders in the Tharoo valley, as obtained in this study, showed a large spread varying between 60.2 to 217.3 ka. Unfortunately, no suitable bedrock could be sampled in the present study. Hence, considering the ages

obtained from moraine boulders could contain a significant amount of inheritance, more investigation is required prior to assigning any particular age to the glacial event.

3.8 Climatic Controls on the Quaternary Glaciation in the Northwestern (NW) Himalaya

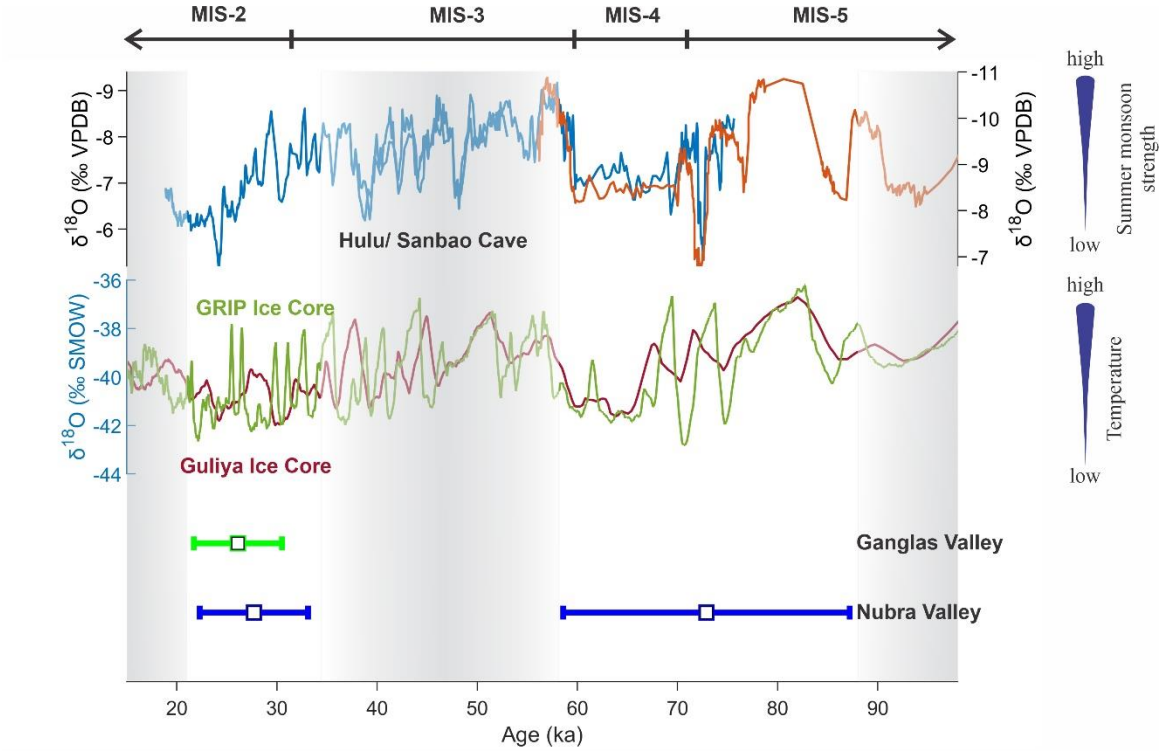

Figure 3.4: *Comparison of Quaternary glaciation events in the northwestern Himalaya with oxygen isotopic variation in the Chinese cave records* (Wang et al., 2008, 2001), *greenland and Guliya ice core* (Grootes et al., 1993; Johnsen et al., 2001, 1997; Thompson et al., 1997).

The oldest glaciation event in the Nubra valley is dated to MIS-5/ MIS 4 (Dortch et al., 2010; Ganju et al., 2018). The glaciation event possibly started during the substage MIS-5b when the temperature was relatively lower (Thompson et al., 1997). During MIS-5b, the strength of the monsoon was moderate (Wang et al., 2008), suggesting it had a minimal role in driving the glaciation. After MIS-5b, there was an increase in temperature during MIS 5a (Thompson et al., 1997). This possibly explains the vertical thinning of glacier ice due to increased melting. The glaciation continued till the end of MIS-4, which was supported by temperature reduction during the time period (Thompson et al., 1997).

Though it is clearly observed that the glaciation was driven by a temperature reduction, the required moisture was possibly contributed by the mid-latitude westerly precipitation (Ali et al., 2013; Benn and Owen, 1998) as the monsoon intensity was relatively lower (Wang et al., 2008, 2001). The same event might correspond to the Pangong-2 stage Pangong Range and the Ladakh-4 stage of the northern Ladakh Range (Dortch et al., 2013). In the Sarchu plain, glaciation has also been dated to 50-79 ka (Saha et al., 2016). In the central Himalaya, multiple studies have observed evidence of pre-MIS-2 glaciations in various valleys such as Saraswati valley (Rana et al., 2019), Pindar valley (Bali et al., 2013), Gori Ganga valley (Ali et al., 2013), Purvi Kamet valley (Bisht et al., 2015). Yet, the ages of pre- MIS-2 glaciation events are limited in central Himalya and are only available for Bhagirathi valley (63 to 85 ka) and Kunti-Banar valley (58 ± 16 ka) (Ali et al., 2022; Sharma and Owen, 1996), suggesting glacial advances during the MIS-4. This observed event of glaciation is concordant with glaciation events observed at multiple regions in the arid western Himalaya-Tibetan orogen (Abramowski et al., 2006; Koppes et al., 2008; Owen et al., 2012; Röhringer et al., 2012). During the MIS-3, increased temperature-induced melting of glaciers would have led to retreat in glaciers. Despite the increase in ISM strength during the MIS-3 (Deplazes et al., 2013; Kumar et al., 2018), an increase in temperate would have resulted in a negative mass balance.

The younger glaciation event (Tirith-I) in Nubra valley (also the PGA-1 stage in Ganglas valley) was dated to be during the Marine Isotopic Stage (MIS-2). The MIS-2 glaciation was driven by temperature reduction (Thompson et al., 1997). During the MIS-2, ISM was comparatively weaker (Kumar et al., 2018; Wang et al., 2001), while a few records have reported an increase in the strength of westerlies (Li et al., 2016). During this time period, evidence of moderate to high moisture supply to the region through westerly precipitation has been observed (Jena et al., 2022b). Thus, it can be summarized during MIS-2 that a reduction in temperature triggered the glacier advance, and the glaciers were sustained by mid-latitude westerlies moisture supply.

Evidence of the MIS-2 glacial advance is also found in Northern Ladakh Ranges (Dortch et al., 2013) and the Zanskar ranges (Sharma et al., 2016; Sharma and Shukla, 2018), indicating contemporary glacial advances in the northwestern Himalaya. The observed MIS-2 glacial advance is also concordant with glaciation in the central Himalayas

(Ali et al., 2013; Bisht et al., 2015) along with various regions in the Himalaya-Tibetan orogen (Abramowski et al., 2006; Owen et al., 2012; Zech et al., 2005). Though the MIS-2 has been observed to be extremely glaciated in global marine records compared to MIS-4 (Lisiecki and Raymo, 2005), the glaciation event during MIS-4 has been found to be more extensive in the Nubra valley

The glacier advances in the northwestern Himalaya occurred during periods of temperature reduction. On the other hand, the valley glaciers showed a significant retreat during the period of increased insolation through, and these periods coincide with the enhanced strength of ISM. This indicates that the glaciation in the northwestern Himalaya was driven by North Atlantic climate oscillations (possibly linked through westerly storm tracks) rather than local climatic phenomena such as ISM.

3.9 Inferences

A detailed investigation of the pre-glaciated valleys in the northwestern Himalaya was performed to reconstruct the chronology of quaternary glaciation. The primary aim of the study was to reconstruct the glaciation history in the northwestern Himalaya and attribute causes for the same. This would require an additional investigation of the possible reasons behind the large offset observed in TCN and OSL ages in the NW Himalaya and find possible solutions for the same. It was observed that the TCN ages derived from boulders show a larger spread compared to ages derived from bedrocks. The bedrock-derived ages nearly overlap with the OSL derived ages. Varying origin of boulders with incomplete removal of inheritance was the primary reason behind observed offsets in previous studies.

The chronology of the glaciation event was reconstructed using previously published OSL and TCN ages along with TCN ages from the present study. The oldest Tirith II glaciation event in the Nubra valley is dated to be MIS 5/4, while the younger Tirith I event was dated to be MIS 2. The PGA 1 glaciation event in Ganglas valley has been dated to MIS 2. The reduction in temperature was found to be the major factor driving the late Quaternary glaciation in the northwestern Himalaya, while the glaciers were

sustained by westerly precipitation. The glaciation events were controlled by the climatic fluctuations in the north Atlantic, while the ISM had much-limited control.

Chapter 4 Past Hydrological Changes in the Northwestern Himalaya during Early to Mid MIS-2

4.1 Introduction

The sediments from proglacial lakes provide near-continuous records of glacier dynamics and climate variability, which can be used to reconstruct the glacier fluctuations at centennial to millennial time scales (Benn and Owen, 1998; Dahl and Nesje, 1996; Karlen and Matthews, 1992; Ohlendorf et al., 1997). The proglacial lakes are intrinsically linked to climate through the surface energy balance and wide geological systems through glacier dynamics, glacial meltwater, and sediment fluxes (Larsen et al., 2011). For example, during periods of warm and humid conditions, streams draining into the lakes transport coarser sediments, whereas the periods of cold and dry climate are represented by the deposition of low-energy fine-textured sediment succession (Ariztegui et al., 1997; Juyal et al., 2009, 2004). Consequently, it can be suggested that relative changes in the lake sedimentation provide information about the glacier meltwater fluctuation in regions dominated by the glacier-fed lakes, and hence the history of past climate (Leemann and Niessen, 1994). Similarly, the geochemical proxies, particularly the detrital proxies, along with the sedimentology, provide a more robust interpretation of hydrological changes associated with minor fluctuations in meltwater discharges (Chen et al., 1999; Engstrom and Wright, 1984).

In the cold and arid NW Ladakh Himalaya well preserved relict proglacial lacustrine sequences are being used to reconstruct the late Quaternary climate variability (Phartiyal et al., 2013; Mujtaba et al., 2018; Lal et al., 2019). However, due to the

chronological inconsistencies, the evolution, and the history of the late Quaternary climate variability still remain debatable. For example, the geomorphic process leading to the proglacial lake at Spituk formation is still contested. For instance, Phartiyal et al. (2005) and Sant et al. (2011a, 2011b) suggested that tectonically induced debris flows obstructing the Indus River resulted in the lake formation. However, Blöthe et al. (2014) and Sangode (2011) were of the opinion that the lake was formed due to the obstruction of the Indus River by the combination of moraines and alluvial fans. Still, the timing and location of the blockage and aggradations of the proglacial lake sedimentation still remain debatable (e.g., Phartiyal et al., 2013). Similarly, the studies on the Spituk Lake deposit (Leh) show a strong divergence in the chronology and hence the interpretation, implying that the sequence still lacks a reliable age estimate (e.g., Phartiyal et al., 2005; 2013; Sangode et al., 2013; Blöthe et al., 2014; Mujtaba et al., 2018; Lal et al., 2019). Finally, the climatic inferences relied largely upon the facies assemblages and textural attributes rather than more robust geochemical and isotopic analyses of the lake sediment.

In view of this, the present study is a renewed attempt to employ the detailed geochemical proxies (major and trace elements) supported by the AMS radiocarbon dating (inorganic and organic carbon) along with optical ages. The specific objectives are (i) to ascertain the pattern of hydrological changes modulated through the glacier fluctuations and (ii) to provide some insight into the causes of chronological discrepancies.

4.2 Study Area

The relict lake deposit is exposed at Spituk near Leh town at an elevation of ~3200 meters in the northern flank of the Indus River abutting the Ladakh Batholith (**Figure 4.1**). The NW-SE trending Ladakh Batholith range extends for ~350 km and consists of granodiorites and biotite-bearing granites dated between 45 to 100 Ma (Ravikant et al., 2009; Upadhyay et al., 2008; Weinberg and Dunlap, 2000). Towards the southern flank of the Indus river are the Zanskar Ranges, which are dominated by fossiliferous limestone, shale, and sandstone and are overlain by ophiolitic mélanges and molasses of cretaceous to tertiary age (Ahmad et al., 1996; Robertson, 2000).

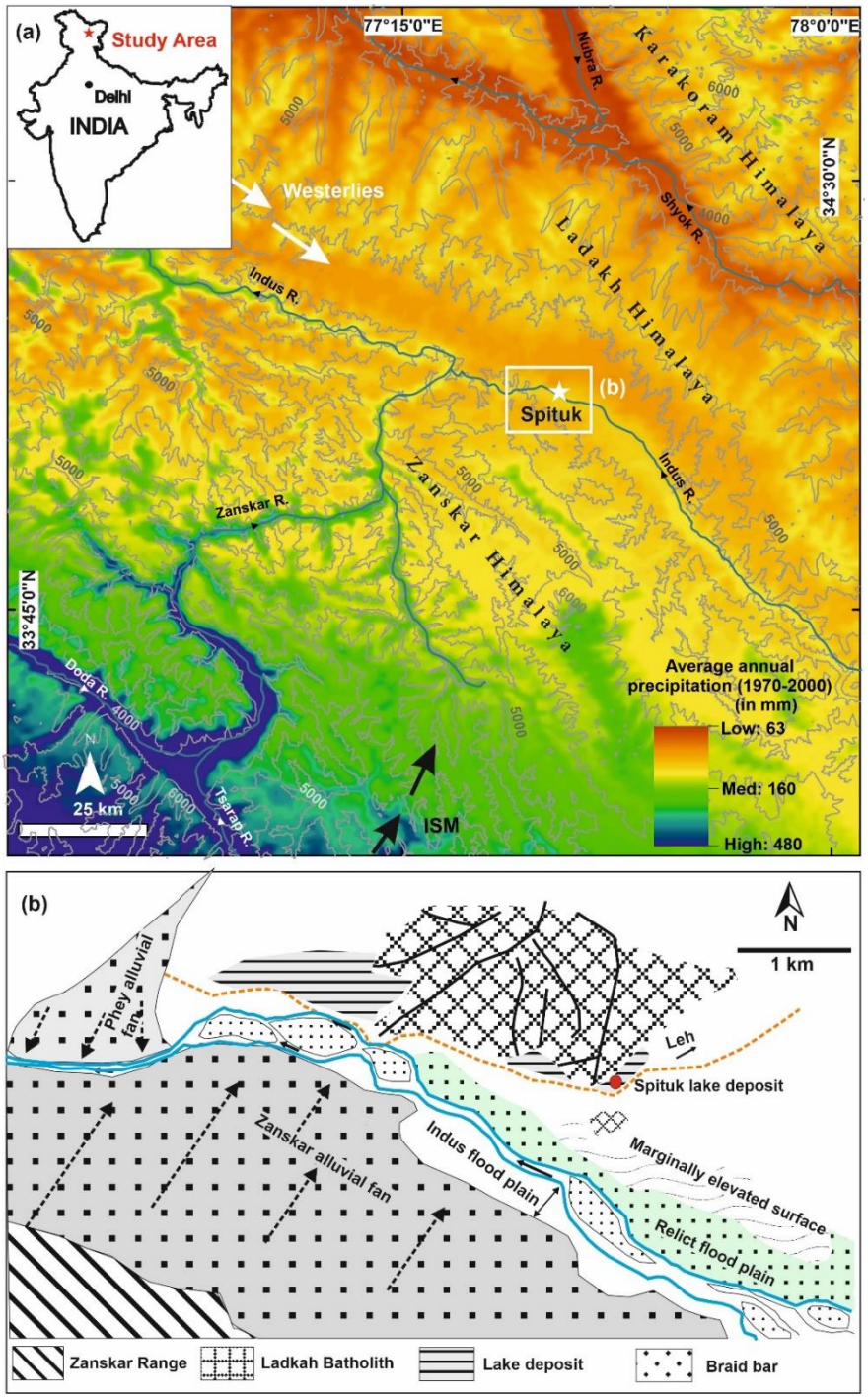

Figure 4.1: *Location map of Spituk paleo lake deposit. (a) The total annual precipitation map of the northwestern Himalaya averaged for 30 years (1970-2000) shows the precipitation gradient across the Higher Himalaya, Zanskar, Ladakh, and Karakoram ranges (Source: www.worldclim.org, Fick and Hijmans, 2017) (b) The geomorphological map of the region showing the exposed Spituk deposit on the southern flank of the Ladakh batholith.*

Due to the orographic effect of the southern higher Himalayan ranges, the Indus Valley lies in the rain shadow zone of the ISM. However, the east-west trending Ladakh Ranges facilitate the eastward migration of the mid-latitude westerlies and provide maximum precipitation during the winter (Bhutiyani et al., 2010). The regional pattern of rainfall variability indicates that from the southern Zanskar Ranges to the northern Karakoram Ranges, there is a steady decline in the mean annual precipitation (decrease in ISM at the expanse of an increase in the mid-latitude westerlies) (**Figure 4.1a**). The mean annual precipitation in the Indus valley is ~100 mm, while the mean annual temperature is around 7 ºC, with winter temperatures going below -28 ºC, whereas the summer temperatures rise up to 35 ºC (Chevuturi et al., 2018).

4.3 Methodology

4.3.1 Geomorphology and Stratigraphy

Around 55 m thick relict lake sequence is exposed along the Leh-Neemu road (34° 07' 51.20" N, 77° 31' 29.98" E), which can be traced from Spituk monastery till the confluence of Fiang Stream with the Indus River (Phartiyal et al., 2005). The lake deposits are nestled between a spur that emanates from the Ladakh Batholith and the hillock on which the Spituk monastery is located. The Indus River flows as a broad braid-meandering channel till the confluence (~5 km down) with a stream that comes from the Phey Valley (**Figure 4.1**). Multiple distributary channels can be seen separated by braid bars implying that stream power is significantly low. The present-day flood plain of the Indus River around Spituk Lake deposit is preferentially located towards the Zanskar alluvial fans (**Figure 4.1**). The geomorphological disposition of the Spituk Lake site suggests that the lake sedimentation probably occurred in a cutoff meander of the Indus River by the obstruction caused by the combination of alluvial fan and debris flow emanating both from the southern Zanskar Ranges and the northern Ladakh Batholith (**Figure 4.1**). The absence of any terminal moraine in the vicinity of the lake deposit indicates that the glaciers were at relatively higher elevations (above 3200 m) during the existence of the lake, for example, around Ganglas village (Shukla et al., 2020). However, the textural attribute (discussed

below) suggests that the lake sedimentation occurred during a period of significantly reduced Indus River discharge (compared to the present).

Stratigraphy of the sediment succession shows variable textural attributes, ranging from well-sorted and poorly laminated sand to massive clay, varve, and rhythmites (**Figure 4.2**). The stratigraphy of the sediment succession is reconstructed using the conventional field-based sedimentological criteria such as grain size and sedimentary structures. Based on this, three major litho units are identified. The lowermost unit-I (45 to 55 m depth) is around 10 m thick and consists of sand-rich horizons with subordinate clay layers. This is overlain by 20 m (25 to 45 m depth; Unit-II) thick clay deposit which is dominated by massive and laminated clay/silty clay. The upper 25 m thick (0 to 25m depth; Unit-III) is dominated by laminated (parallel and cross stratified) sand with occasional clay layers. Samples (for geochemical analysis) were collected after freshly exposing the section at 10 to 20 cm intervals from the middle part of the section (unit-II; depth 25 to 45 m; **Figure 4.2**).

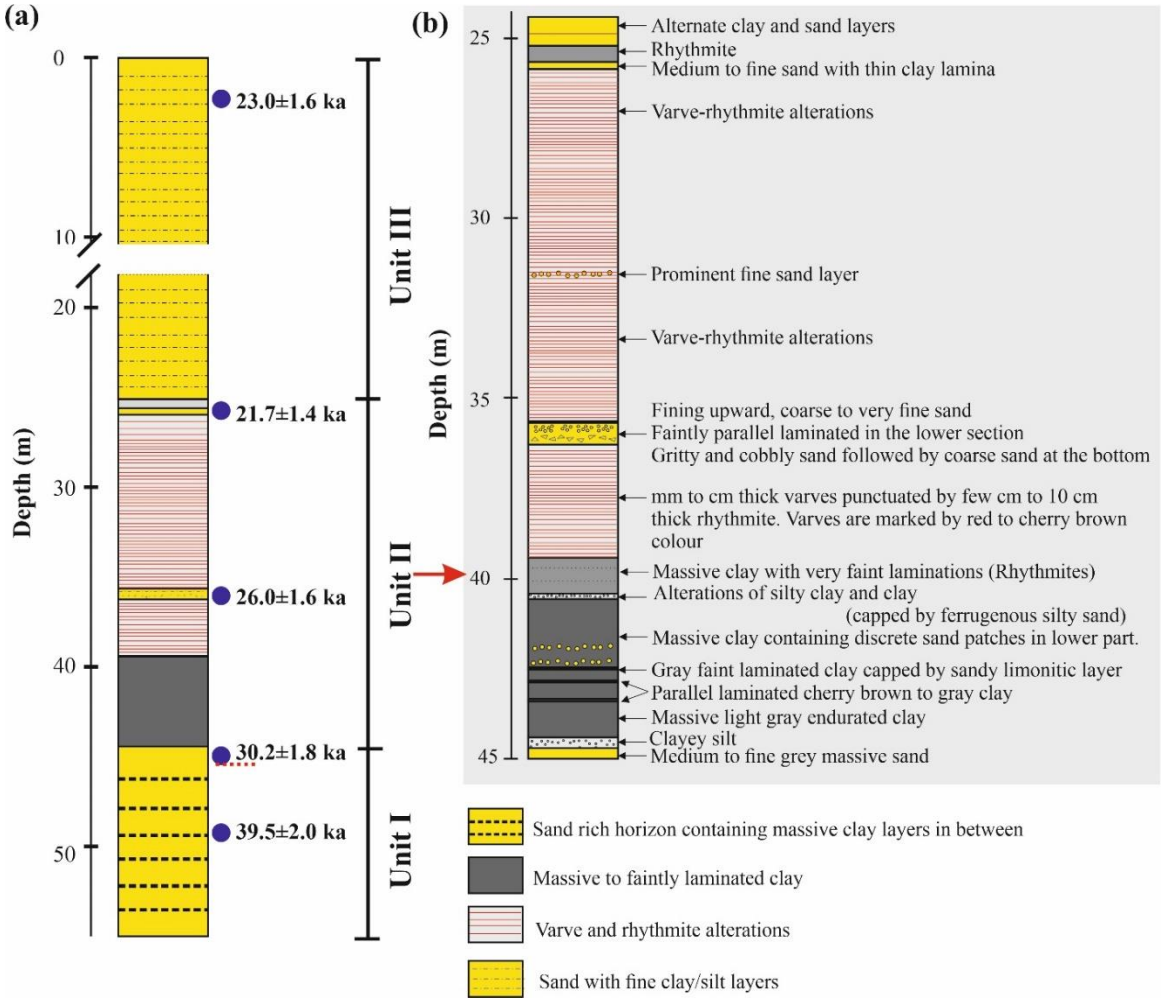

Figure 4.2: *(a) The lithostratigraphy of the Spituk paleo lake deposit shown along with the obtained OSL ages. The middle lacustrine deposit has been subsampled for further geochemical analysis. (b) Detailed stratigraphy of unit-II is shown.*

4.3.2 Chronology and Geochemical Analysis

Radiocarbon of organic as well as inorganic matter, and OSL dating was employed to reconstruct chronology of the studied lake deposit. The lake sediment geochemistry involves the estimation of inorganic carbon (IC), organic carbon (OC) and nitrogen, isotopic analyses of OC, IC, and major and trace element analyses. Methodological details are provided in C**hapter 2**.

4.3.3 Estimation of Dead Carbon Contribution

The inorganic carbon ages were found to be older compared to the luminescence ages (discussed later). This could due to the contribution of dead carbon (DC) from the nearby carbonate terrains (Zanskar Ranges). In view of this, we hypothesize that the inorganic carbon contribution was derived from both atmospheric CO_2 and dead carbon contribution from dissolved bicarbonate transported from the Zanskar Ranges through pulsating alluvial fan aggradation during the existence of the lake (Sant et al., 2011b).

Hence, a simple mixing equation can be considered using the $\Delta^{14}C$ value of atmosphere-derived carbon and $\Delta^{14}C$ of dead carbon as two end members.

$$(1 - f) \times \Delta^{14}C_{(atm.\ fraction)} + f \times \Delta^{14}C_{(dead-carbon)} = \Delta^{14}C_{(inorganic\ carbon)} \quad (4.1)$$

Where 'f' represents the fraction of dead carbon input to the total inorganic fraction.

The ages obtained from the age-depth model using the OSL dating method were treated as calibrated radiocarbon ages, and the corresponding radiocarbon ages were derived from the IntCal 20 calibration curve (Reimer et al., 2020). For these radiocarbon age values, $\Delta^{14}C$ values were calculated by using the formula provided by Stuiver and Polach (1977). These were designated as $\Delta^{14}C_{atm.\ fraction}$ values. The $\Delta^{14}C_{dead\text{-}carbon}$ value was taken to be 0 ‰. Using these values, 'f' was obtained.

4.4 Results

4.4.1 Stratigraphy

The lowermost sand with alternating massive clay horizon in unit-I (45 to 55 m depth) indicates rhythmic variation in the sediment supply. The sand horizon represents increased meltwater/precipitation in the lake catchment, whereas the clay horizons are indicative of reduced meltwater discharge. Considering that the lake appears to have developed as a cutoff meander, we attribute the changes in sediment flux due to temporal changes in the hydrological discharge in the Indus River.

Overlying unit-I is the clay dominant horizon (unit II; 25 to 45 m depth). Unit II can be divided into two prominent subunits, i.e., the massive clay deposit at the bottom and the varve and rhythmites deposits towards the top. Unit-II starts with ~ 5.5 m thick massive light gray coloured indurated clay at the bottom. At places, 5 to 7 cm thick beds of parallel laminated cherry brown to gray clay deposits are present, which were evidently darker compared to the massive clay deposit. In between, a few cm thick parallel laminated fine sandy clay layers are present. Overall, this subunit indicates reduced yet fluctuating meltwater conditions. Above the massive clay section, the 14.5 m thick section consists of alternating varve and rhythmites. The mm to cm thick varves are punctuated by a few cm to 10 cm thick rhythmites. The varves are marked by dark cherry brown-coloured laminas followed by light gray coloured rhythmites. The overlying varve and rhythmites contain limonitic layers. The varve represents a significant reduction in the Indus discharge, implying overall cold condition. Whereas the rhythmites containing reddish-yellow fine-sand to silt rich limonitic layers suggest increased flux of Fe-rich sediment from the catchment (Trauth and Strecker, 1999). Thus, the rhythmic occurrence of limonitic layers in unit-II implies frequent excursions towards short-lived warm intervals during overall cold conditions. Towards the top, an increase in the thickness of rhythmite layers was observed, indicating a shift towards a relatively warmer climate.

The uppermost unit-III, which is dominated by well-graded and laminated sand with intermittent clay layers, suggests deposition under increased discharge (probably represents flooding event). Climatically deposition of unit-III can be attributed to the overall warm phase with a short-term cold excursion (instability). At 46 m depth, a ~100 cm layer of gritty cobbly debris overlain by gritty sand is observed that grades towards fine sand, which has been interpreted as distal alluvial fan facies (Harvey et al., 2005). We observed an increased concentration of carbonate, which further supports the suggestion of southern alluvial fan facies contribution into the lake as also indicated by inorganic $\delta^{13}C$.

4.4.2 Chronology

The five samples dated using OSL method covering all the three units yielded ages of 39.5 ± 2.0 ka (SPOSL 01), 30.2 ± 1.8 ka (SPOSL 02), 26.0 ± 1.6 ka (SPOSL 03), 21.7

± 1.4 ka (SPOSL 04), and 23.0 ± 1.6 ka (SPOSL 05). Details of the radioactivity, equivalent dose, dose rate, and ages obtained are given in **Table 4.1**.

Table 4.1: *Details of radioactivity, dose rate (DR), equivalent dose (Ed), and obtained ages (CAM) of the Spituk paleolake sequence.*

Sample Name (depth)	**No of aliquots**	**U (PPM)**	**Th (PPM)**	**K (%)**	**Water Content (%)**	**Dose Rate (Gy/ ka)**	**Equivalent Dose (Gy)**	**Age (ka)**
SPOSL01 (50 m)	28	1.85 ± 0.08	7.77 ± 0.33	1.42 ± 0.03	10 ± 5	2.4 ± 0.1	94.3 ± 3.1	39.5 ± 2.0
SPOSL02 (44.8 m)	39	2.28 ± 0.09	10.08 ± 0.41	1.55 ± 0.03	10 ± 5	2.7 ± 0.1	80.6 ± 3.6	30.2 ± 1.8
SPOSL03 (36 m)	31	1.61 ± 0.05	7.74 ± 0.22	1.21 ± 0.02	10 ± 5	2.2 ± 0.1	56 .1± 2.8	26.0 ± 1.6
SPOSL04 (26.7 m)	21	1.91 ± 0.07	8.30 ± 0.34	1.56 ± 0.03	10 ± 5	2.7 ± 0.1	57.9 ± 3.1	21.7 ± 1.4
SPOSL05 (1 m)	29	0.91 ± 0.07	4.70 ± 0.31	1.56 ± 0.03	10 ± 5	2.2 ± 0.1	51.2 ± 3.0	23.0 ± 1.6

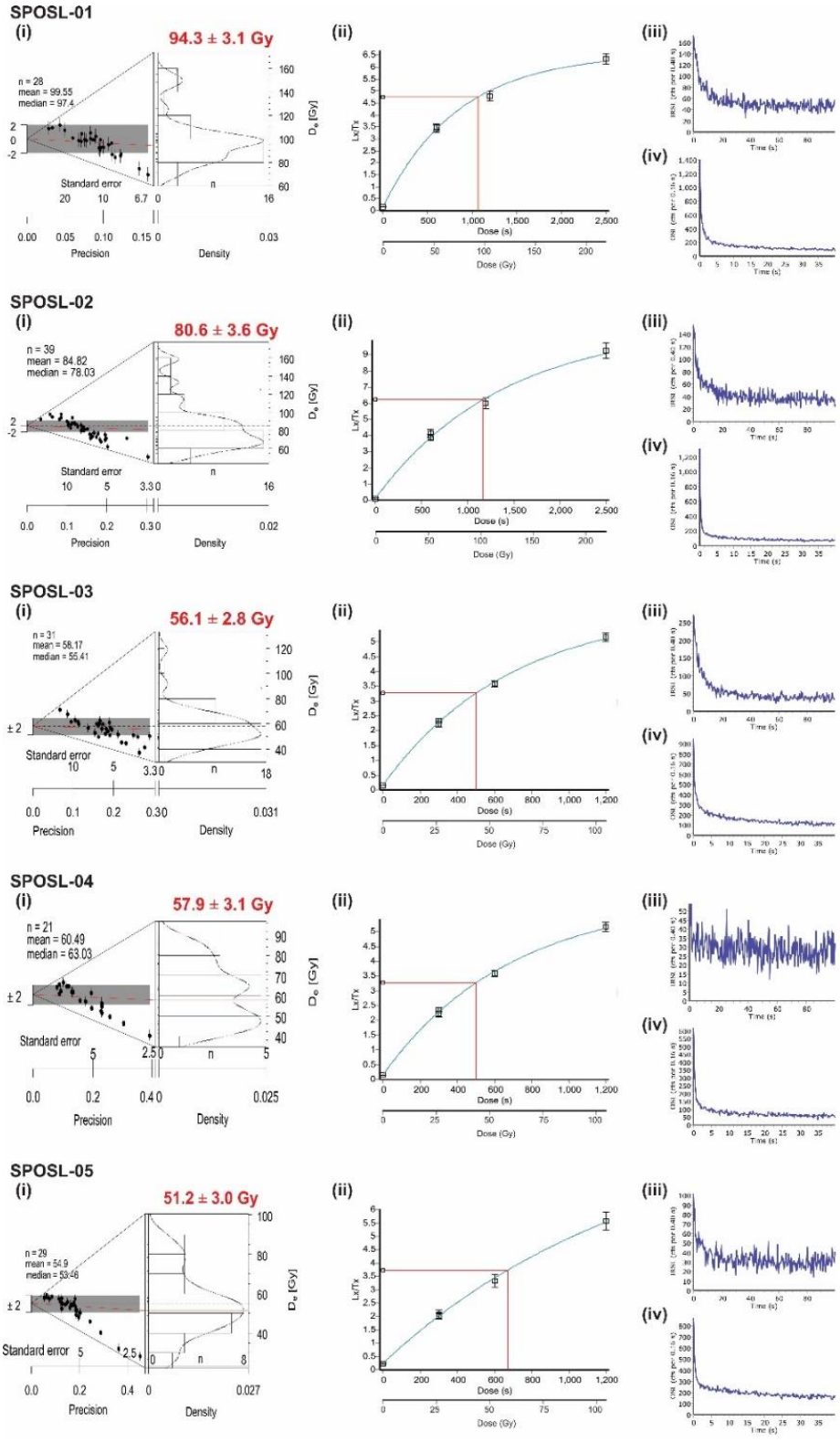

Figure 4.3: *Graphical representation of the luminescence characteristics of each sample. (i) the abanico plots showing the distribution of the equivalent dose (De) values, (ii) the growth curve recorded following the DSAR protocol, (iii) Typical IRSL counts, and (iv) OSL counts. The CAM De used for age calculation is written in red.*

In the middle part of the lacustrine deposit (10 to 30 m; **Figure 4.4**), AMS radiocarbon ages are attempted on both IC (20 samples) and OC (13 samples) (**Figure 4.4**). The stratigraphically inconsistent OC ages vary between 27,155 cal years BP to 17,969 cal years BP. Compared to this, the IC carbon ages are relatively older (51,095 cal years BP to 31,265 cal years BP). But unlike OC ages, the majority of IC ages are stratigraphically consistent but are comparatively older than the OSL ages (**Figure 4.4**). Considering the inconsistencies in the radiocarbon ages, in the subsequent interpretation of the multiproxy data, we used the optical ages. The OSL ages were used to construct the age-depth model assuming a constant sedimentation rate.

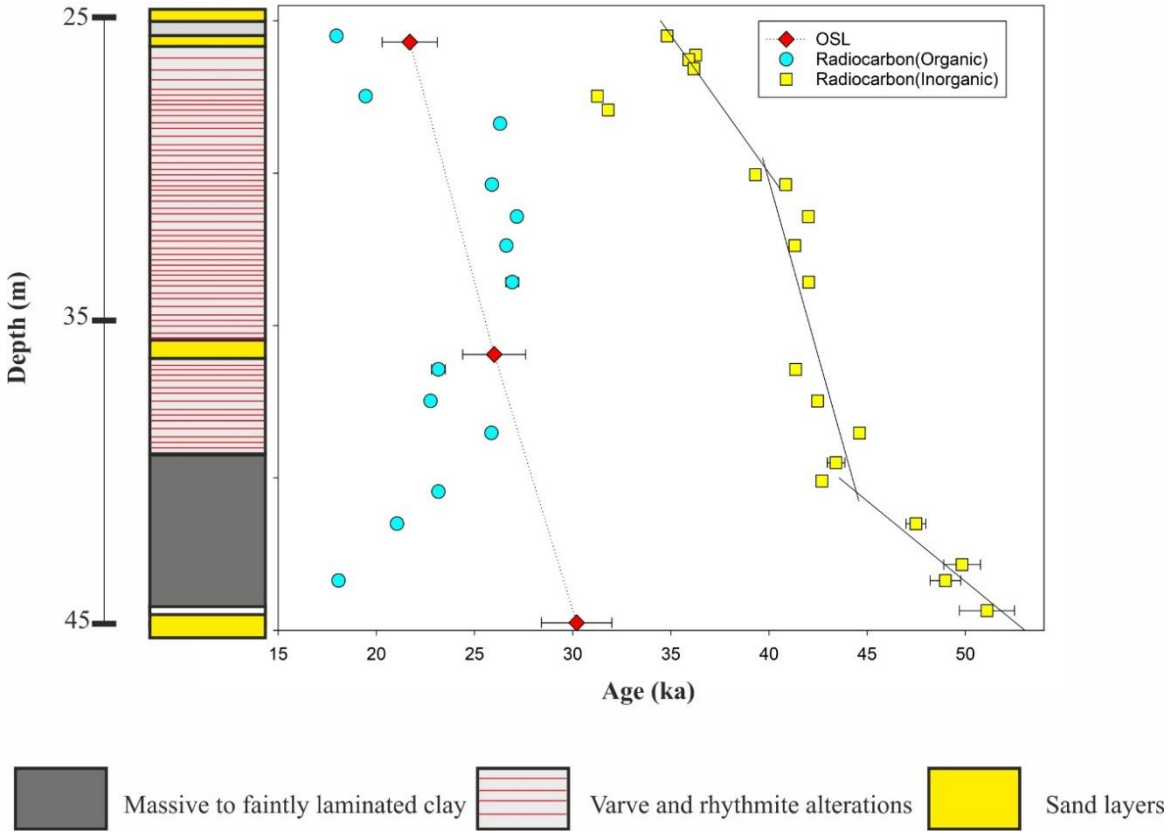

Figure 4.4: *The chronology of the unit-II of Spituk lacustrine deposit. The OSL and Radiocarbon ages (both organic as well as inorganic carbon) are shown. Older ages of inorganic carbon indicate the influence of dead carbon. The organic carbon ages show complex variability and do not follow the stratigraphic trend.*

4.4.3 Temporal Changes in Geochemical Proxies

The catchment response to temporal changes in hydrological discharge (climate variability) is ascertained by the sedimentological and geochemical proxies. The textural attributes in proglacial lakes are the sedimentological manifestation of the variability in meltwater discharge. For example, the coarser sediment fluxes are associated with increased meltwater discharges (warm periods), whereas the periods corresponding to cooler climate (low discharge) are represented by the deposition of finer sediments (Ariztegui et al., 1997; Juyal et al., 2004). Hence, the relative abundance of finer vs. coarser sediments through time can be used as a proxy for the changing glacial cover in the lake catchment. Further, the relative changes in chemical weathering (a surrogate for the prevailing climate) can be ascertained by the Chemical Index of Weathering (CIW), Al_2O_3 %, and Rb/Sr ratio. CIW is a measure of the proportion of Al_2O_3 versus more labile oxides such as CaO, Na_2O (Nesbitt and Young, 1982). It reflects a relative amount of feldspars and clay minerals in the sediments and hence, the chemical weathering in the lake catchment. Similarly, the Rb/Sr ratio variations follow the relative changes in the chemical weathering of the lake catchment (Chen et al., 1999) as weathering of labile minerals such as plagioclase is characterized by significant losses of Ca as well as Sr. Again, the ratio of Ca to detrital derived elements (Ti, Al, Fe) was used to access the past changes in evaporation/ precipitation (E/P). Higher ratios of Ca/$\sum$ (Ti, Fe, Al) reflect dry conditions, and lower ratios reflect wet conditions. This is because, during higher rainfall (lower E/P), the delivery of detrital elements Ti, Fe, and Al to the lake is increased compared to authigenic Ca deposition (Mueller et al., 2009). The temporal variation in detrital proxies has been used to understand the variation in the relative amount of wetness in the region (Bhushan et al., 2018; Juyal et al., 2009; R. A. Shah et al., 2020).

The organic matter in the lake sediments is a combination of both in-situ productivity (autochthonous) and terrestrial organic matter (allochthonous) that is transported to the lake. The C/N ratio can be used to trace the changes in the proportion of both autochthonous versus allochthonous organic matter. For example, aquatic organic matter has a C/N ratio of 4-10, while the allochthonous organic matter has a ratio > 20 (Meyers, 1994). In the Spituk lake sediment, the C/N ratio remained < 10 (**Figure B1**), indicating organic matter is primarily contributed through in-situ productivity (Meyers,

1994). The $\delta^{13}C$ of the lake organic matter could vary in accordance with the relative contribution from C3 and C4 plants. The C3 plants have a typical $\delta^{13}C$ ranging from -35 to -22‰, whereas, for C4 plants, it varies from -10 to -18 ‰ (Cerling et al., 1997). The $\delta^{13}C$ of the organic matter varies narrowly between -22 to -28 ‰, indicating the vegetation fluctuated with the C3 plant community. The minor changes in $\delta^{13}C$ of the organic matter may also reflect changes in lacustrine in-situ productivity (Battarbee et al., 2001). The inorganic carbon % and $\delta^{13}C$ showed significant variation that could reflect changes in the contribution of terrestrial inorganic carbonate (from Zanskar Ranges) (**Figure B1**).

The period between 31 to 27.5 ka (early MIS 2) is marked by the dominance of clay which varies from massive to faintly laminated in character. The genesis of thick clay layers has been debated. Such deposits are common in mountain lakes characterized by a high sedimentation rate and with insignificant seasonal changes in sedimentation (Owen, 1996; Williamson et al., 1998). It is also suggested that a mere absence of ice cover during winter also leads to the deposition of clays (Hart, 1992). The chemical proxies (Al_2O_3 %, CIW, Rb/Sr, and Ca/$\sum$ (Ti, Fe, Al) showed millennial-scale oscillations with a relatively wet period between 30.2 to 29.3 ka, followed by a dry period between 29.3 to 28.1 ka (**Figure 4.5**). Within the massive clay section, the chemical weathering proxies are relatively lower (compared to the varve section), indicating an overall drier climate, which is also supported by a higher Ca/$\sum$ (Ti, Fe, Al) ratio. Overall, from 31 to 27.5 ka, the region experienced an overall cold and dry climatic condition with instability marking the transition between warm MIS 3 to cold MIS 2.

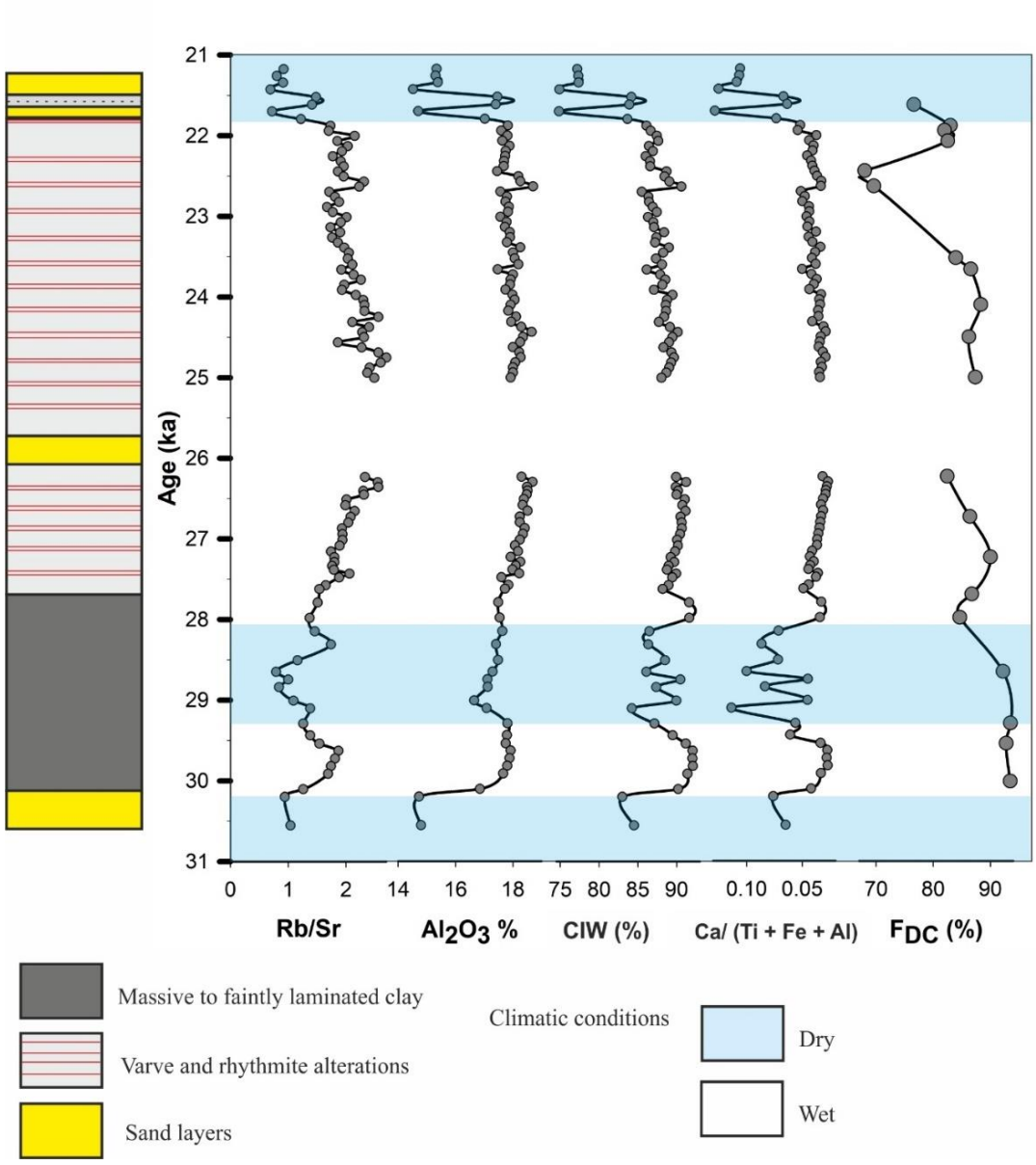

Figure 4.5: *Temporal variation of geochemical proxies in the Spituk relict lake deposit. The higher values of detrital proxies (lower E/P index) indicate warm and humid conditions between 30 ka and <29 ka, an overall cooler condition till around 28 ka. This is succeeded by a steady improvement in the climate until around 26 ka, followed by a steady decline in the climate, which culminated with the prominent decrease in geochemical proxies around 22 ka—a period corresponding to the Last Glacial Maximum* (Mix et al., 2001).

The varve sedimentation during the 27.5–22 ka indicates overall cold conditions with limited sediment supply to the lake system. The varve and rhythmite alterations may

indicate alternate cold and warm climatic conditions with rhythmites deposited under relatively warmer conditions. The geochemical proxies also show centennial-scale fluctuation suggesting frequent instability in the overall cold climate. The period 27.5 ka to 22 ka is associated with higher values of detrital proxies such as CIA, Rb/Sr, indicating a relatively wet climate. This is also supported by lower Ca/∑ (Ti, Fe, Al)) ratio (**Figure 4.5**). This suggests the climatic conditions in Ladakh were not so dry during the mid MIS 2. After 21.5 ka, the rhythmite layer thickness increases towards the top, and the sand layers reappear, indicating the climate shifted towards relatively warmer conditions.

4.5 Discussion

4.5.1 Chronology of the Lake Deposit

Multiple attempts have been made in the earlier studies to build the chronostratigraphy of the Spituk lake succession using radiocarbon and OSL dating methods. For example, Phartiyal et al. (2005) obtained significantly old bulk organic carbon ages, like 50,790 ± 5370, 40,330 ± 1130, 33,440 ± 1160, and 30,980 ± 690 years BP. Thus, based on these ages, they suggested that the Spituk lake sedimentation initiated > 50 ka ago. In a subsequent study employing AMS radiocarbon on organic matter, surprisingly younger Holocene ages (10530 ± 60, 6460 ± 70, 6070 ± 70, and 3250 ± 50 years BP) are obtained by Phartiyal et al. (2013). According to them, the older ages in the initial attempts (Phartiyal et al., 2005) were due to the hard water effect.

Similarly, the optical ages show significant variations with each succeeding attempt (**Figure 4.6**). Sangode et al. (2013) used the quartz extract and dated samples at three depths which yielded ages varying between 72 to 32 ka. Following this, Blöthe et al. (2014) employed the Infrared Stimulated Luminescence (IRSL) of feldspar grains and obtained ages ranging from 177 ka to 72 ka (**Figure 4.6**). Feldspar is hard to bleach compared to quartz but, at the same time, suffers from anomalous fading (Huntley and Lamothe, 2001). However, in the present case, fading does not seem to be the problem because the IRSL ages are significantly higher compared to quartz ages (**Figure 4.6**). Instead, it seems the geological inheritance due to inadequate bleaching may be the reason for age

overestimation (compared to quartz). Following this, Mujtaba et al. (2018) and Lal (2019) dated the quartz extract and obtained ages between 79 to 47 ka. These ages are significantly higher compared to Phartiyal et al. (2013), who dated two samples using quartz extract, and two ages obtained from the topmost sand-rich section are 27 ka and 36 ka. In a recent article, Sharma and Phartiyal (2018) discussed the complexity of various chronological methods. They have also emphasized heterogenous bleaching of quartz grains in glaciated terrains such as the Ladakh region, leading to age overestimation. In order to circumvent the problem of inadequate bleaching and hence the age overestimation, we used the medium to fine grain (90–150 μm), smaller aliquots, and increased the aliquot numbers (>20). The tightly clustered equivalent dose indicates that the samples dated are homogeneously bleached, which is also supported by the fact the narrow scatter allowed us to use the Central Age Model (CAM). Besides inhomogeneous bleaching of quartz, one of the possibilities could be the contribution from feldspar in the quartz signal if the samples are not cleaned adequately. In our case, the feldspar contribution was close to background counts (**Figure 4.3**). A comparison between the results obtained from the present study and previous studies suggests that the paleo dose values are highly overestimated in the previous studies (Lal et al., 2019), while the dose rate estimates are relatively comparable in the studies (Table S3.1). Since we have no access to the feldspar and quartz growth curves of earlier studies (Mujtaba et al., 2018; Sangode et al., 2013), speculatively, the OSL age overestimation (in the case of quartz OSL) could be the inadequate removal of feldspar contamination.

The discrepancy between ages obtained using multiple methods (e.g., luminescence vs. radiocarbon) has been reported in lacustrine deposits in the Indian Himalaya (Beukema et al., 2011; Juyal et al., 2009, 2004). In **Figure 4.4**, a comparison between the OSL and the organic radiocarbon ages shows that both are concordant in the top varve-rhythmite section, while the organic carbon ages are significantly younger in the bottom massive clay section. The organic carbon age overestimation (though smaller) observed in the top varve section could be because of the variable hard water effect. Usually, an overestimation of bulk organic matter radiocarbon ages has been reported from multiple relict lake succession located in the Tethyan limestone catchment in the higher central Himalaya. This includes the relict lacustrine succession of Garbayang in the Kali Ganga valley (Juyal et al., 2004),

the Goting deposit in Dhauli Ganga valley (Juyal et al., 2009), and the Burfu lake deposits in Goriganga valley (Beukema et al. 2011).

However, towards the lower massive clay section (10-15 m), an inversion of ages is observed, where the ^{14}C ages of OC are significantly younger compared to the OSL age. Underestimation of bulk organic matter ^{14}C ages has been previously reported in lacustrine, loess, and riverine deposits (Briant and Bateman, 2009; Lai et al., 2014; Long and Shen, 2015; Pigati et al., 2007; Simms et al., 2009), particularly in arid environments. Secondary contamination in the natural environment and the laboratory and strong reworking of sediments during and after deposition due to rapid accumulation are the common factors that cause radiocarbon age underestimations (Pigati et al., 2007; Song et al., 2015; Zhang et al., 2006). In the present study, the exact mechanism resulting in younger ages could not be deduced. However, the fact remains that the OC ^{14}C ages are stratigraphically inconsistent, whereas the IC ages are broadly stratigraphically consistent but significantly older compared to both OC ^{14}C and OSL ages. In view of this, the AMS radiocarbon ages can not be used to build the chronology of the Spituk lake sequence and the subsequent climatic interpretation of the geochemical proxies.

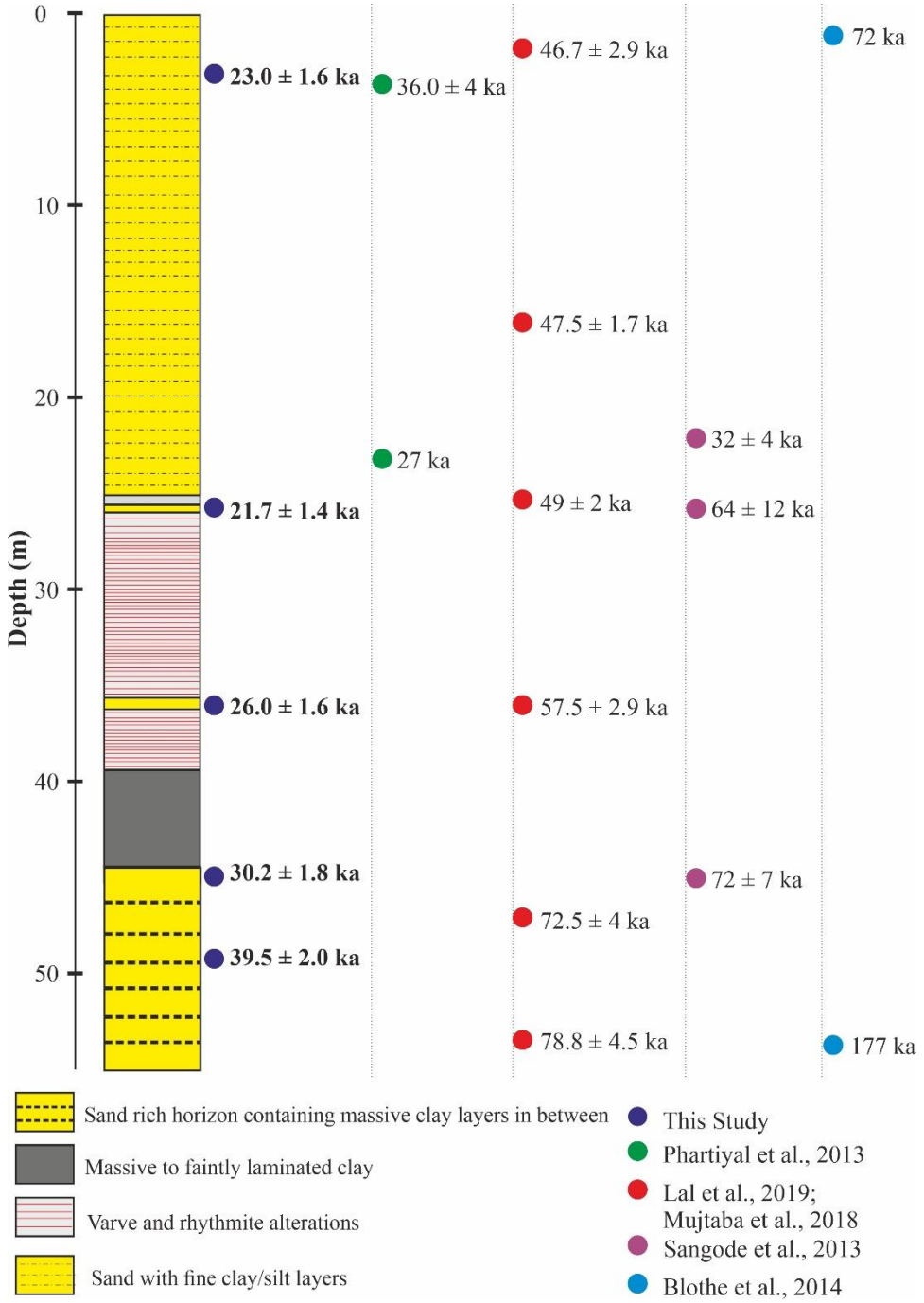

Figure 4.6: *The Spituk paleolake sequence is shown along with the published luminescence ages from previous studies* (Blöthe et al., 2014; Lal et al., 2019; Mujtaba et al., 2018; Phartiyal et al., 2013; Sangode et al., 2013). *(Redrawn after Sharma and Phartiyal, 2018)*

4.5.2 Lake hydrology during MIS-2

In high altitude terrain like Ladakh, relict lake sediments deposited behind the moraine or alluvial fan/debris flow are being used to reconstruct the climate variability particularly associated with the changes in glacier boundary conditions (Lal et al., 2019; Phartiyal et al., 2013; Sant et al., 2011b, 2011a). In view of the fact that the studied lake deposit is located in a probable Indus River meander, it is reasonable to assume that the temporal changes in lake sedimentation would represent the changing hydrological condition. Since the glacier melt is the major contributor to the Indus River discharge (Immerzeel et al., 2010), temporal changes in the sedimentation pattern are likely to represent the past hydrological condition modulated by the glacier fluctuations.

The Spituk Lake lies in the downstream of Puche Glacier (Ganglas Valley). Therefore, it is likely that besides the Indus water contribution, the late Quaternary fluctuations (since MIS-2) as recorded in the moraine stratigraphy of Puche Glacier near Ganglas (Shukla et al., 2020) would be reflected in the lake record. In the Spituk Lake deposit, the deposition of fine clay sediments during 30 to 22 ka (corresponding to the early to mid-MIS-2) indicates sediment deposition under glacial conditions with limited meltwater supply. In the Ganglas Valley, the observed late quaternary fluctuation of valley glaciers also supports the current observations (Shukla et al., 2020). The oldest glaciation event in the Ganglas Valley, named Puche Glacier Advance-1 (PGA-1), is optically dated between 31.5 ± 3.3 ka and 22.7 ± 1.6 ka (Shukla et al., 2020), suggesting a strong coupling between regional glaciation and sedimentation in Spituk Lake. However, in the lake section, the sedimentology of the deposit is not uniform throughout the early and mid-MIS 2, indicating fluctuations in depositional conditions. For example, during the early to mid MIS-2 transition, the lake record shows a distinct change in sedimentology (massive to laminated clay). Again, during the early MIS-2 there have been significant short-term fluctuations in sediment deposition as observed from occasional sand and laminated clay layers within the massive clay deposit. Hence, the present observation clearly states that the growth of the valley glacier was not monotonous since the beginning of the cooler MIS-2 (~30 ka) till the Last Glacial Maximum (LGM). Instead, the glacier expansion was temporarily halted by phases of millennial-scale warming events.

Based on geochemical proxies, the early MIS-2 can be inferred as relatively dry. This observation is at variance with the relatively depleted $\delta^{18}O$ in Hulu Cave stalagmite, indicating enhanced summer precipitation in the region (Wang et al., 2001). The marine core study from the Indian Ocean also suggests strengthened ISM during the early MIS-2 compared to the mid-MIS-2 (Kudrass et al., 2001). (**Figure 4.7**). Despite this, the Indus basin witnessed a drier condition implying that the ISM strength was not significant enough to cross over the orographic barrier of the higher Himalaya during the early MIS-2. Instead, the moisture contribution to the growth of glacier advance was supplied through the enhanced westerlies, as suggested by Shukla et al. (2020).

Progressively from early to mid MIS-2, deposition of varve dated between 27.5 ka and 22 ka indicates the gradual onset of glacial conditions with a significant reduction in meltwater and hence the sediment supply. The inferred cold condition is also supported by the regional glacial advance observed in the southern Ladakh Ranges (Shukla et al., 2020). During this time period, extensive glaciation has been observed in the northwestern Himalaya (Ganju et al., 2018; Sharma et al., 2018, 2016; Shukla et al., 2020) and central Himalaya (Ali et al., 2013; Rana et al., 2019) suggesting contribution from enhanced westerlies. In the present study, a wet climate condition was inferred during the mid MIS 2 (27.5 to 22 ka), indicating enhanced moisture supply. During this period, no significant increase in monsoon strength was observed (Kudrass et al., 2001; Wang et al., 2001), while a few records have reported an increasing strength of mid-latitude westerlies (Li et al., 2016). In view of this, we tend to suggest that the wet climate during mid-MIS 2 can be ascribed to the moisture contribution from enhanced westerlies which possibly was a result of southward migration of the westerlies belt due to the more southerly position of the Intertropical Convergence Zone (ITCZ) (Beghin et al., 2016; Yu et al., 2000).

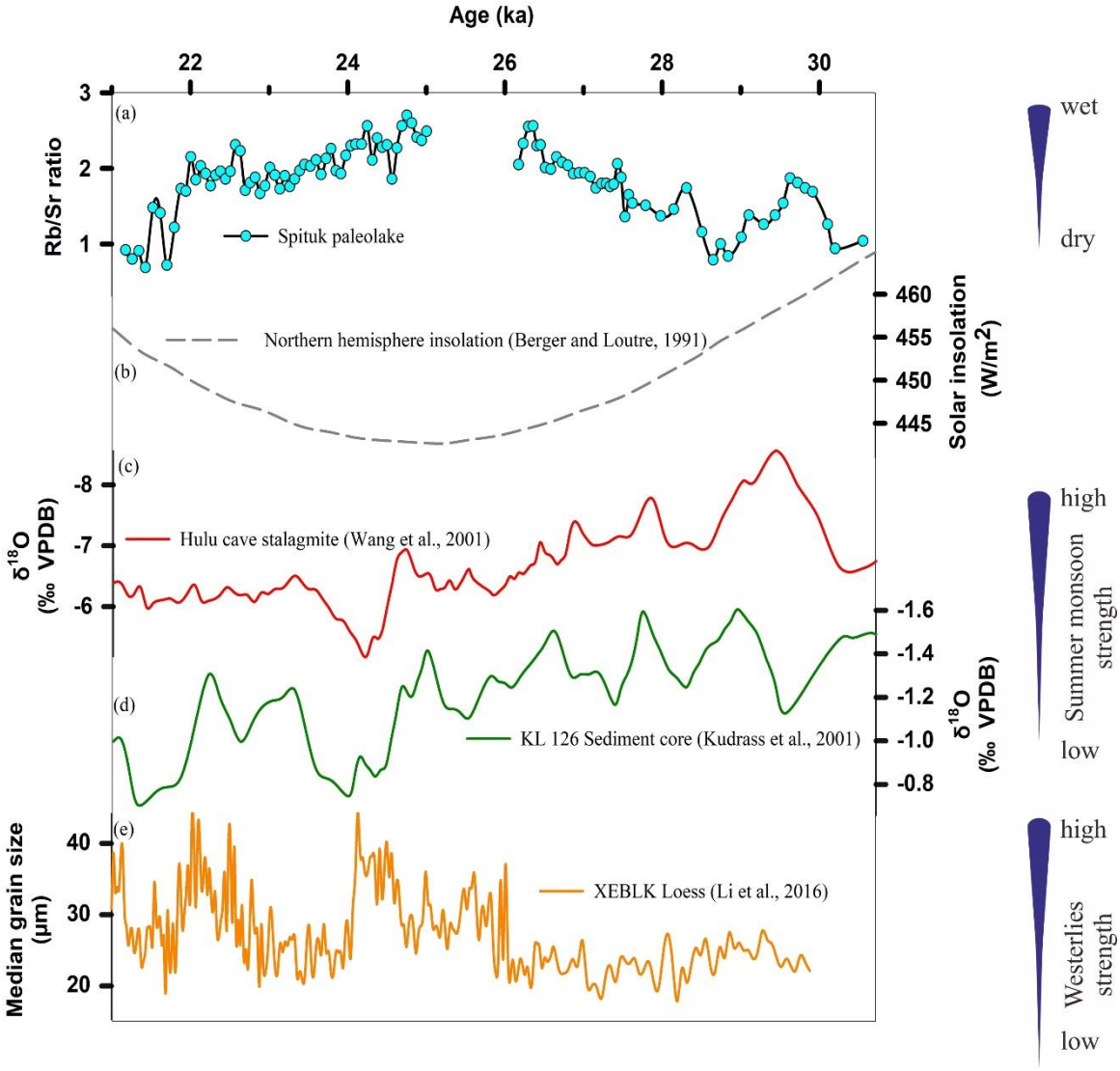

Figure 4.7: *Spituk lake deposit and the regional paleoclimate reconstruction. (a) The Rb/Sr ratio from the Spituk paleolake is compared with (b) Northern hemisphere insolation* (Berger and Loutre, 1991)*, (c)* $\delta^{18}O$ *record of Hulu Cave stalagmite* (Wang et al., 2001)*, (e)* $\delta^{18}O$ *record of foraminifera from a sediment core from the Bay of Bengal* (Kudrass et al., 2001)*, (f) Grain size data from XEBLK loess* (Li et al., 2016).

Towards the mid MIS-2 (22.5 ka), a reduction in dead carbon input indicates the reduction in the chemical weathering due to the expansion of glacier and ice cover in the lake catchment, resulting in a low contribution of dead carbon into the lake. Incidentally, 22.5 ka lies within the postulated range of the continental records of LGM dated between 23-19 ka (Mix et al., 2001). In the central Himalayan region, the LGM has been identified at 22.5 ka in the Goting basin (Juyal et al., 2009) and between 20 ± 3 to 18 ± 3 ka in the

Garbyang basin (Juyal et al., 2004). Within the chronological uncertainties, this accords well with the present observations. Further, supporting observation accrued from the present study comes from the chronometric studies by Shukla et al. (2020). They have found that the Puche glacier had advanced up to the Ganglas village during the same time.

In the lake record, after 22 ka, the sand beds reappear, indicating an enhanced meltwater supply to the lake. In the Ganglas Valley, the glacier was also in a retreating phase during the period (Shukla et al., 2020). Evidence of post-LGM glacier retreat has also been observed in the Nubra Valley from OSL ages of outwash gravel terrace deposits (Ganju et al., 2018). The retreat of valley glaciers during this period can be explained by an increase in insolation and thus enhanced melting (Berger and Loutre, 1991). Evidence for an increase in temperature after LGM has been observed in lacustrine deposits from central Himalaya (Juyal et al., 2009). Overall, it was observed that during MIS-2, the hydrological changes observed in Spituk Lake (and the fluctuations in the extension of valley glaciers) were controlled by the variabilities in the northern latitude ice dynamic. The ISM had rather restricted control in providing moisture to the region and hence driving the glaciations.

4.6 Inferences

The relict lake deposit at Spituk, Leh, allow us to make the following major inferences:

During the MIS-2, the marginally fluctuating climate (shifting from cold and arid to cold and humid) modulated the proglacial lake sedimentation. Chronologically the events were spaced at millennial and multimillennial time scales.

Based on the sedimentology and geochemistry, three phases of dry phases punctuated by two intervals of wet climate can be discerned during the MIS-2. The oldest cooling event occurred between 31 and 30 ka, which led to the advancement in valley glaciers. A short-term increase in humidity can be inferred after 30.2 ka and before 29.3 ka. A reversal towards dry climate occurred between 29.3 ka and 28.1 ka. This was followed by a rhythmic warming and cooling trend (with fluctuations) till before 22 ka.

During 27.5 ka and 22 ka, deposition of varves indicates gradual growth of the valley glaciers.

However, the climate was conducive enough for moderate chemical weathering before 22 ka implying relatively humid climatic conditions compared to the early MIS-2. This we attribute to the enhanced moisture contribution from the mid-latitude westerlies caused due to the southward migration of the ITCZ.

The results thus indicate that the Indus basin responded to the coupled synoptic-scale climate system, which in the present case was the fluctuations in the valley glaciers modulated by the changing strength of the mid-latitude westerlies caused due to the winnowing and waxing of the northern latitude ice dynamic.

Chapter 5 Spatial Distribution of Beryllium Isotopes in the Indian Ocean

5.1 Introduction

One of the primary apprehensions with the application of beryllium isotope systematics in marine archives (such as sediment cores) to understand paleomagnetic and paleoclimatic processes is that it requires a proper understanding of the factors controlling the beryllium isotopic distribution in the present ocean. ^{10}Be, once produced in the atmosphere by the interaction of cosmic-ray particles with oxygen and nitrogen (Dunai, 2010; Lal and Peters, 1967), reaches earth's surface through dry or wet precipitation. Hence, the primary source of ^{10}Be in the marine system is atmospheric deposition, while a minor fraction is contributed from the terrestrial input (Brown et al., 1992b). The ^{10}Be input to the ocean varies spatially as ^{10}Be atmospheric depositional flux changes as a function of multiple parameters such as troposphere-stratosphere exchange, variation in precipitation rate, and variability in aerosol content (Graham et al., 2003; Mann et al., 2011; Willenbring and von Blanckenburg, 2010). At the same time, the stable counterpart of ^{10}Be (^{9}Be) is predominantly of terrestrial origin and has an average value of 2.2 ± 0.5 ppm in the upper continental crust (Rudnick and Gao, 2003). Earlier measurements of ^{9}Be in rivers have indicated that continental runoff significantly contributes to the ^{9}Be budget of the seawater (Measures and Edmond, 1983). Later, studies revealed that ^{9}Be is mostly scavenged within the estuarine and coastal regions itself, and hence its input to the open ocean is minimal (Brown et al., 1992b; Kusakabe et al., 1991). Though hydrothermal fluids have almost 1000 times high ^{9}Be concentration compared to seawater, ^{9}Be released from such sources is rapidly scavenged locally, thus reducing their global significance (Bourlès et al., 1994). Additionally, aeolian dust is known to significantly contribute ^{9}Be to the surface oceans (Brown et al., 1992b).

Several records of the variation of beryllium isotopes in the world ocean through direct measurement in ocean waters (Frank et al., 2009; Ku et al., 1990; Kusakabe et al., 1990, 1987a; Measures et al., 1996; Yang et al., 2003) and in authigenic fraction (seawater derived) from marine archives such as sediment samples (Bourles et al., 1989), and Fe-Mn crusts (Ku et al., 1982; von Blanckenburg et al., 1996) have linked its distribution to various processes. However, there are limited studies to understand spatial (Bourles et al., 1989; Sharma and Somayajulu, 1982; von Blanckenburg et al., 1996) and temporal variation of Be isotopes in the Indian Ocean (Jena et al., 2022a, 2021; Simon et al., 2016b; Valet et al., 2014), rather with no significant contribution from the northern Indian Ocean. With the limited data, it is hard to understand processes controlling beryllium isotopic distribution in the Indian Ocean. Here, we have made a detailed investigation of beryllium isotopic measurements in the surface sediments covering the central and northern Indian Ocean to ascertain the processes controlling the $^{10}Be/^{9}Be$ distribution and its behaviour.

5.2 Sampling Locations

27 samples (within the top 3 cm) of surface sediment from cores collected from the Indian Ocean were analysed for the beryllium isotopic ratios. These samples were collected using gravity corers during multiple oceanographic expeditions (SS-132, 152, 172, and SK-304, 312, 324) and were preserved properly in the laboratory. The details of sampling locations (including latitude, longitude, and water depth) are provided in **Table 5.1**. Sediment samples were crushed thoroughly to ensure homogenization and processed for beryllium extraction and isotopic measurement, as described in **Chapter 2**.

Table 5.1: *Location of sampling stations covering the central and northern Indian Ocean.*

Sl. No.	Station Name	Latitude	Longitude	Water Depth (m)
1	SK-324/08	21.85 ^{0}N	61.50 ^{0}E	3160
2	SK-324/07	21.00 ^{0}N	65.00 ^{0}E	2956
3	SS 2502	21.80 ^{0}N	68.00 ^{0}E	280
*4	SK-312/16	13.00 ^{0}N	65.00 ^{0}E	4350
*5	SK-312/15	10.00 ^{0}N	65.00 ^{0}E	4543

6	SS-132/3268 G5	12.50	^{0}N	74.20	^{0}E	600
7	SS-3121	10.33	^{0}N	75.28	^{0}E	1994
8	SK-304/B18	12.58	^{0}N	93.87	^{0}E	2330
9	SS-172/4037	10.82	^{0}N	94.65	^{0}E	3250
10	SK-304/B16	8.33	^{0}N	95.00	^{0}E	2908
11	SS-172/4038	6.55	^{0}N	94.24	^{0}E	1314
12	SS-172/4028	17.50	^{0}N	86.00	^{0}E	2569
13	SS-152/3843	16.29	^{0}N	82.28	^{0}E	690
14	SS-152/3840	15.42	^{0}N	80.69	^{0}E	193
15	SS-152/3835	12.66	^{0}N	80.62	^{0}E	142
16	SS-152/3830	11.49	^{0}N	80.79	^{0}E	2949
17	SS-152/3844	12.51	^{0}N	84.49	^{0}E	3130
*18	SS-152/3829	8.05	^{0}N	86.03	^{0}E	3669
*19	SS-172/4040	6.03	^{0}N	89.94	^{0}E	2788
*20	SS-172/4041	4.98	^{0}N	85.89	^{0}E	4012
21	SK-304/A 05	5.76	^{0}N	79.41	^{0}E	3408
*22	SS-152/3828	3.89	^{0}N	78.06	^{0}E	3166
*23	SK-312/12	0.01	^{0}N	65.00	^{0}E	3750
*24	SK-312/10	7.98	^{0}S	66.69	^{0}E	4161
*25	SK-312/09	12.00	^{0}S	65.00	^{0}E	3449
*26	SK-312/08	15.98	^{0}S	65.01	^{0}E	3200
*27	SK-304/B 12	5.47	^{0}S	97.37	^{0}E	4206

**Considered as open ocean locations and discussed in the text.*

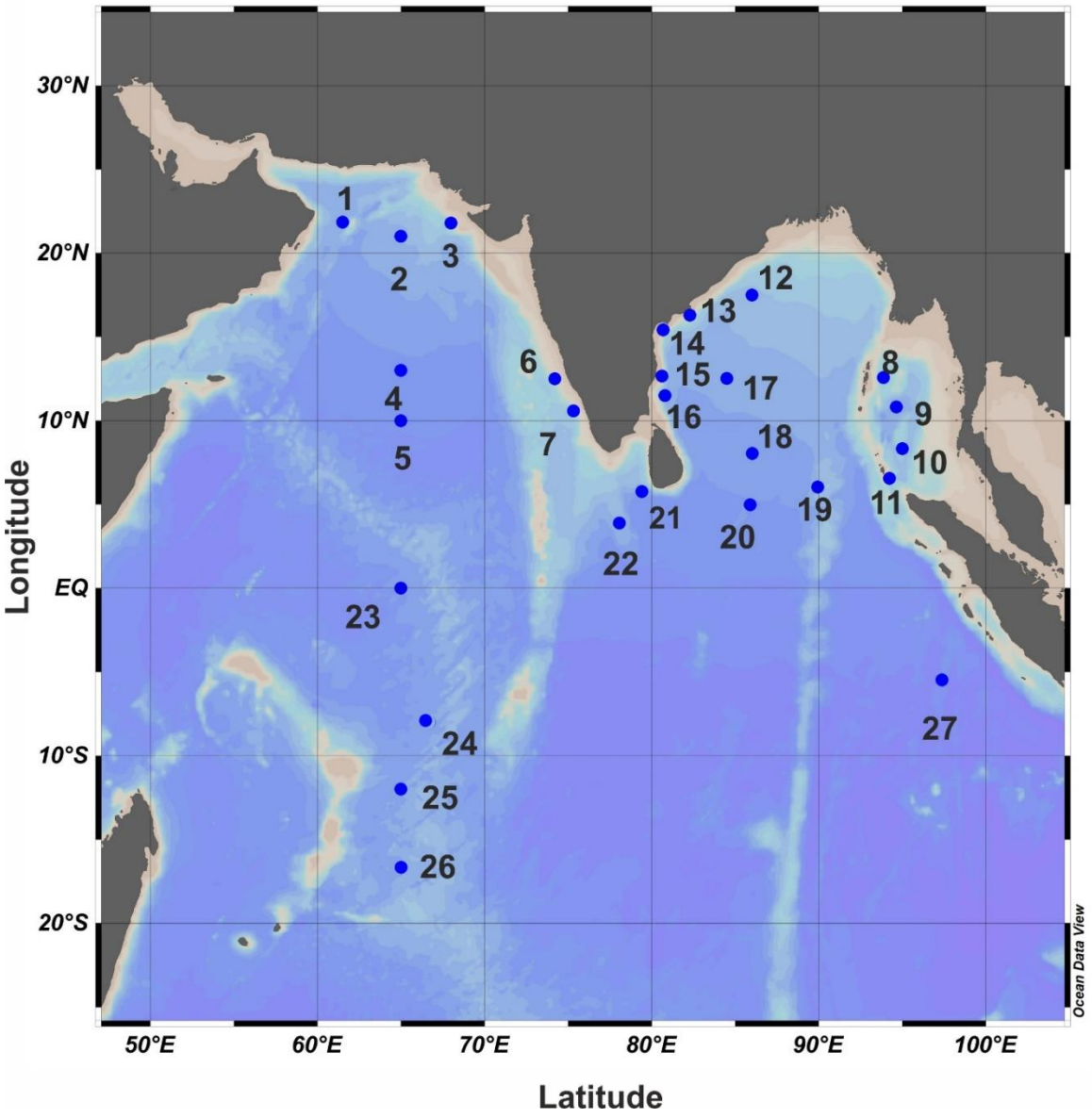

Figure 5.1: *Sampling stations in the central and northern Indian Ocean.*

5.3 Estimation of Residence Time of Be

The residence time of beryllium (τ_{Be}) in the ocean water column was calculated following a procedure similar to von Blanckenburg et al. (1996).

$$\tau_{Be}\ (yr) = \frac{^{10}Be\ inventory\ in\ the\ water\ column\ (atoms.cm^{-2})}{^{10}Be\ input\ (or\ output)\ (atoms.cm^{-2}.yr^{-1})} \quad \text{---------- (5.1)}$$

The ^{10}Be inventory (I) (atoms.cm^{-2}) was calculated using the ^{10}Be/^{9}Be ratio (atoms/atoms), ^{9}Be concentration (atoms.cm^{-3}), and water column depth (cm) using the formula given below.

$$I_{^{10}Be} = \left(\frac{^{10}Be}{^{9}Be}\right)_{water-column} \times [^{9}Be]_{water-column} \times water\ depth \quad \text{---------- (5.2)}$$

The beryllium isotopic ratio measured from the authigenic fraction of the surface sediment samples was considered to be equal to that of the water column at the same location. Since there are no measurements of ^{9}Be from the Indian Ocean water column, the average value of the ^{9}Be from the deep-water column (>1000 m; 24.78 ± 1.85 pmol/kg) estimated from the Atlantic and the Pacific was considered for calculation (Ku et al., 1990; Kusakabe et al., 1987a; Measures et al., 1996). The ^{10}Be atmospheric deposition is considered to be the only source of ^{10}Be to the marine system. This holds true as terrestrial input of ^{10}Be to the marine environment is significantly lower compared to atmospheric deposition (Brown et al., 1992b). The depositional flux of ^{10}Be for each location was calculated based on model estimation by Heikkilä and von Blanckenburg (2015).

5.4 Distribution of Be Isotopes in the Indian Ocean: Role of Terrestrial Input

^{10}Be/^{9}Be ratios obtained from the surface sediments (Present Study, Bourles et al., 1989), and Fe-Mn crusts (von Blanckenburg et al., 1996) from the Indian Ocean show significant spatial variation. A higher value is observed in the central part of the Indian Ocean (0-20^{0}S) (**Figure 5.2**), a region with a much lower contribution of ^{9}Be to the surface sediments. With no direct input from terrestrial sediments (either riverine or dust) contributing to the ^{9}Be inventory in the open ocean (resulting in lower ^{9}Be concentration in sediments), the observed higher ^{10}Be/^{9}Be ratio is due to low ^{9}Be input. In the central Indian Ocean, active hydrothermal vents have been spotted on the central Indian Ridge (Gamo et al., 2001, 1996; Van Dover et al., 2001). Reference is made to the contribution of hydrothermal fluid to the ocean water in the adjacent regions with the measurement of iron in seawater samples (Chinni et al., 2019; Nishioka et al., 2013). However, in the central Indian Ocean region (SK-312/08, 09, and 10), no significant increase in ^{9}Be was observed,

suggesting a minimal contribution of hydrothermal ^{9}Be to the region. Though it demands further investigation, the plausible reason behind minimal hydrothermal ^{9}Be contribution could be the higher scavenging of ^{9}Be within the proximity of hydrothermal vents due to high particle concentrations (Bourlès et al., 1994). Downcore variation of ^{9}Be concentration in sediment core SK-312/09 also showed no drastic increase in ^{9}Be, suggesting no significant hydrothermal ^{9}Be contribution during the past 43 ka (Jena et al., 2022a).

The influence of terrestrial input is distinctly reflected in a lower $^{10}Be/^{9}Be$ ratio in the northern Indian Ocean. The Bay of Bengal (BoB) is one such basin that receives the largest amount of terrestrial sediments resulting in a higher supply of ^{9}Be. The BoB (5-21 ^{0}N and 80-90 ^{0}E) shows relatively higher ^{9}Be and lower $^{10}Be/^{9}Be$ ratios (**Table 5.2; Figure 5.2**). The Bay of Bengal receives contribution from several major rivers, viz. the Ganga, the Brahmaputra, the Mahanadi, the Godavari, the Krishna, etc., with input of ~1.6 x 10^{12} m^3 of freshwater (UNESCO, 1971) and ~ 1.4 x 10^{9} tons of suspended load annually (Galy and France-Lanord, 2001; Milliman and Meade, 1983; Sarin et al., 1989; Singh et al., 2008). The Arabian Sea (adjacent basin in the northern Indian Ocean at similar latitudes as the BoB) receives terrestrial material both from the riverine and dust sources. It receives ~5 x 10^{8} tons of sediment from rivers and ~1 x 10^{8} tons of material from dust deposits annually (Goldberg and Griffin, 1970; Goswami et al., 2012; Kolla et al., 1976; Ramaswamy and Nair, 1994; Sirocko and Sarnthein, 1989). However, the total input through continental flux to the Arabian Sea is much lower when compared to the BoB, which is reflected in the beryllium isotopic ratio obtained.

The low $^{10}Be/^{9}Be$ ratio observed in the southern Indian Ocean (40-60^{0}S) compared to the central Indian Ocean is intriguing as no major terrestrial sources are known to contribute to the ^{9}Be inventory of the region, and the ^{10}Be depositional flux is relatively higher (1.23 x 10^{06} atoms/cm^2/year) (Heikkilä and von Blanckenburg, 2015). Such decreasing trend of the $^{10}Be/^{9}Be$ ratio from the central Indian Ocean towards the southern Indian Ocean possibly suggests the influence of Atlantic water. Earlier studies have indicated the role of thermohaline circulation in controlling the $^{10}Be/^{9}Be$ ratio in the Atlantic Ocean (von Blanckenburg et al., 1996). The ventilation to the deep Indian Ocean has a major contribution from the North Atlantic Deep Water (NADW) (Piotrowski et al.,

2009; Talley, 2013). Significantly lower $^{10}Be/^{9}Be$ ratio (~5 x 10^{-08}) both in the Atlantic waters and authigenic derived proxies (such as Fe-Mn crusts and surface sediments) have been observed (Bourles et al., 1989; Ku et al., 1990; Kusakabe et al., 1987b; von Blanckenburg et al., 1996). However, the short residence time of Be in the Atlantic Ocean suggests that the contribution from the northern Atlantic Ocean Be signal to the Indian Ocean could not be very high (von Blanckenburg et al., 1996). Another possibility could be the influence of hotspots derived beryllium. As the hotspots only contribute to the ^{9}Be inventory, input from hotspots can lead to a lower $^{10}Be/^{9}Be$ ratio (Bourlès et al., 1994). However, at this point, more research is required before drawing a definite conclusion.

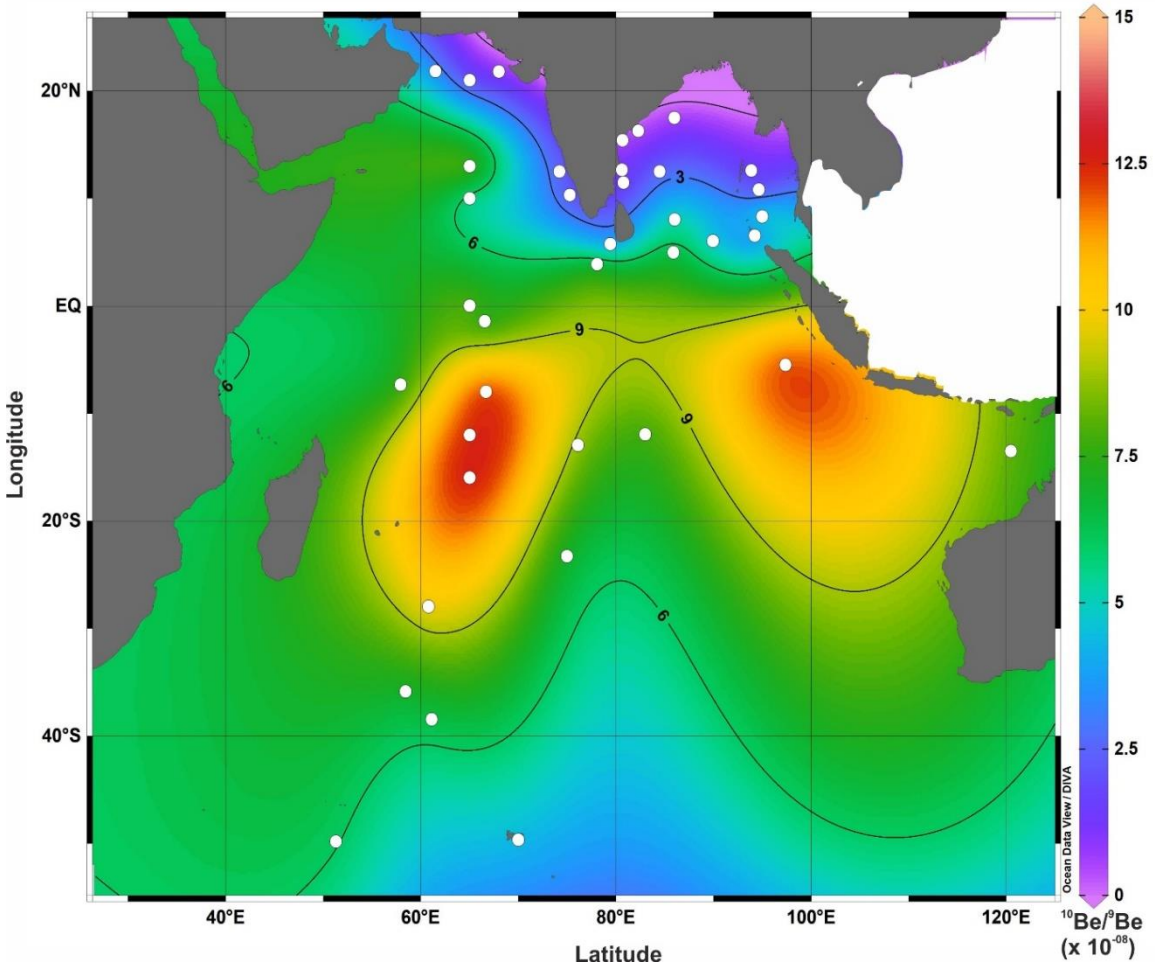

Figure 5.2: *Distribution of $^{10}Be/^{9}Be$ ratio (x 10^{-08}) in the deep-water column of the Indian Ocean. The values are derived from different archives, such as surface sediments (Bourles et al., 1989; present study) and Fe-Mn crusts*(von Blanckenburg et al., 1996). *The sample locations are represented by white circles.*

Table 5.2: *Comparison of ^{9}Be, ^{10}Be concentration, and $^{10}Be/^{9}Be$ between the Indian Ocean basins.*

	BAY OF BENGAL	**ANDAMAN SEA**	**ARABIAN SEA**	**CENTRAL INDIAN OCEAN**
$^{10}Be/^{9}Be$ ($\times 10^{-08}$ atoms/ atoms)	0.37-6.32	1.64-5.42	1.01-7.80	3.31-13.15
^{9}Be concentration ($\times 10^{16}$ atoms/ gram)	0.51-1.94	0.46-1.47	0.55-1.65	0.29-1.54
^{10}Be concentration ($\times 10^{08}$ atoms/ gram)	0.69-6.58	1.01-3.38	0.84-8.43	3.27-7.32

5.5 Beryllium Removal by Scavenging in the Indian Ocean

After its deposition at the sea surface, beryllium sinks to the ocean bottom by scavenging onto the particles. The sediment samples spatially distributed from various regions of the Indian Ocean have been analysed to decipher the behaviour of beryllium isotopes in the ocean. The inverse correlation of $CaCO_3$ with ^{9}Be concentration shows that Be is primarily removed from the water column by scavenging onto the clay/silt particles and not by carbonate particles (**Figure 5.3a**). No distinct correlation could be observed between ^{10}Be and $CaCO_3$ while considering data points from all locations. However, for locations away from the coast (n=11), a negative correlation is observed between $CaCO_3$ and ^{10}Be (**Figure 5.3b**). A strong negative correlation observed between both the beryllium isotopes and $CaCO_3$ content in the open ocean locations indicate the scavenging of beryllium (both ^{10}Be and ^{9}Be) by the non-carbonate fraction. Earlier studies have also reported such a trend of both beryllium isotopes (^{10}Be, ^{9}Be) with $CaCO_3$ in sediment cores (Bourles et al., 1989; Southon et al., 1987), suggesting beryllium is primarily scavenged by non-carbonate fraction, and hence the presence of carbonates results in dilution of the beryllium signal.

With no significant correlation between ^{9}Be and ^{10}Be concentration at all locations, this indicates considerably different sources for both Be isotopes (**Figure 5.3c**). However, they exhibit a positive correlation in open ocean locations, which demonstrates that both isotopes get affected by similar processes in well-mixed conditions of the open ocean water column. This positive correlation observed can be again explained by the scavenging of Be to the sediment column. Generally, after mixing, both the beryllium isotopes exhibit similar properties in the ocean water column(Bourles et al., 1989). Hence, ^{9}Be is considered as an effective tool for normalizing the ^{10}Be signal for secondary input and differential scavenging rates in the open ocean sediments, and, thus, few researchers have employed the $^{10}Be/^{9}Be$ ratio as an alternative to Th normalization (Carcaillet et al., 2004b; Jena et al., 2022a; Simon et al., 2016b).

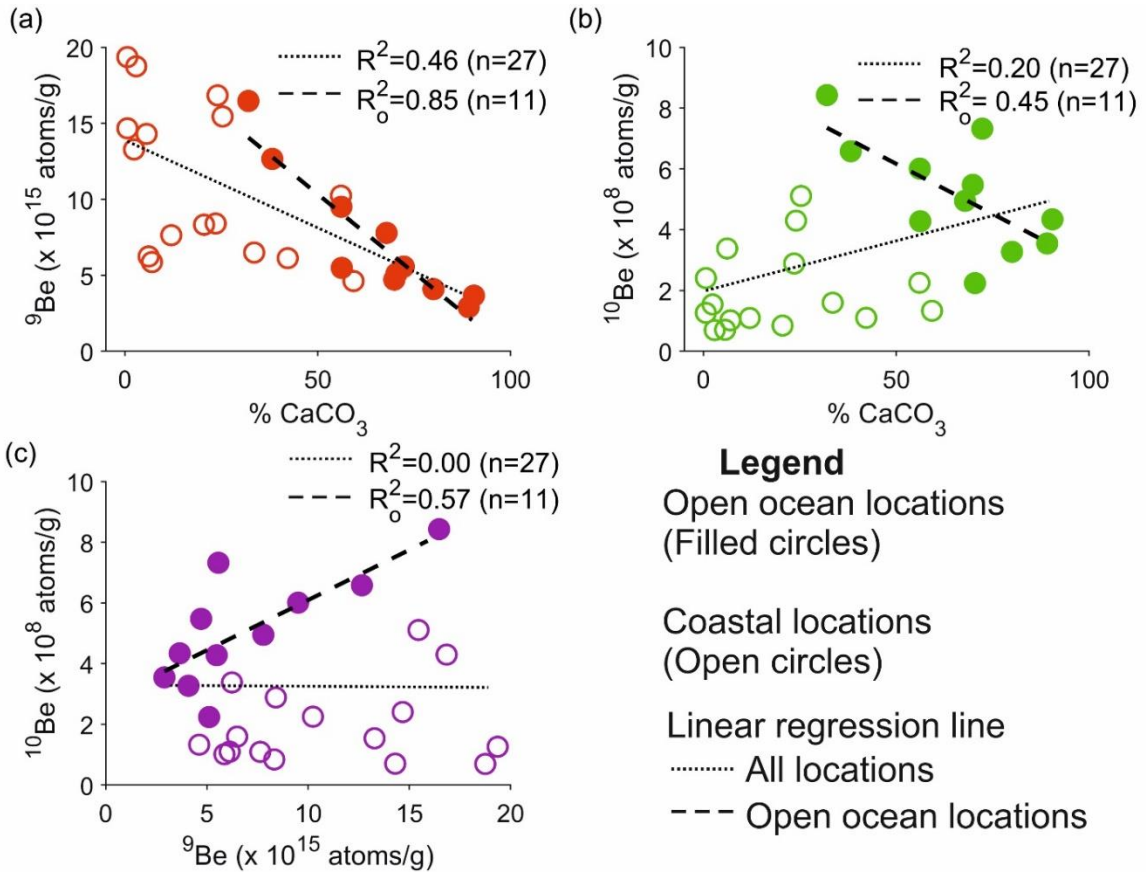

Figure 5.3: *Plot of (a) ^{9}Be concentration vs $\%CaCO_3$ (b) ^{10}Be concentration vs $\%CaCO_3$, and (c) ^{10}Be concentration vs ^{9}Be concentration in surface sediment samples. R is the correlation coefficient considering all the locations (dotted line), and R_O is the correlation coefficient considering only open ocean locations (dashed line).*

5.6 Residence Time of Beryllium in the Indian Ocean

The residence time of Be in the water column is regulated by the source/removal of beryllium isotopes and hence the beryllium isotopic distribution in the ocean water column (von Blanckenburg et al., 1996). Considering an ocean mixing time of ~1000 years, high residence time suggests effective homogenization of elements (i.e., beryllium) in ocean waters. However, the low residence time of Be indicates incomplete mixing of both isotopes (Bourles et al., 1989). There have been several attempts to estimate the average residence time of beryllium in the global ocean water column. Earlier, the average residence time of Be in the global ocean water has been reported to be varying between 500 and 1000 years (Kusakabe et al., 1987a; Merrill et al., 1960; Raisbeck et al., 1980). Drastically different Be residence time for the Pacific (1250 years) and the Atlantic (480 years) Oceans have been reported (Ku et al., 1990). However, with improved depositional flux calculations and Be isotopic measurements from Fe-Mn crusts, the Be residence time for the Atlantic Ocean presently ranges from 210 - 490 years, for the Pacific Ocean between 420 - 740 years, and in the central Indian Ocean from 370 - 540 years (von Blanckenburg et al., 1996).

Here, we report the residence time of beryllium estimated for the northern and central Indian Ocean. Significant variation in residence time observed from basin to basin indicates differential scavenging of beryllium in the water column. The coastal locations have low residence time (<50 years), as the ocean margins are sites for active scavenging for ^{9}Be and ^{10}Be (Ku et al., 1990). Boundary scavenging of beryllium shown in earlier studies indicate near coastal regions accounting for ~50-70 % of scavenging of ^{10}Be deposited in the Pacific Ocean (Anderson et al., 1990; Lao et al., 1992a). Thus, extreme scavenging due to the higher sediment particulate concentration in the water column results in low residence time of beryllium in coastal locations. In the following discussion, which aims to compare residence time from different basins, the locations in the proximity of the coast have not been considered.

The estimates of residence time for Be for the central Indian Ocean based on surface sediments range between 288 and 620 years (**Figure 5.4**). The estimates of residence time for Be for the central Indian Ocean based on surface sediments range between 288 and 620

years (von Blanckenburg et al., 1996). A longer residence time could be the result of a lower concentration of particles, such as terrigenous clay. The central Indian Ocean (SK 312- 08, 09, 10, 12) region is mainly characterized by biogenic carbonates with almost > 70 % carbonate concentration. The longer residence time in the central Indian Ocean further indicates that between carbonates and clay particles, carbonates are less efficient in scavenging beryllium from the water column (Southon et al., 1987).

The northern Indian Ocean shows significantly lower residence time of beryllium when compared to the central Indian Ocean. In particular, the Bay of Bengal and the Andaman Sea have much shorter residence time (< 200 years). The lower residence time results due to the higher concentration of sediment particles responsible for the scavenging of Be. Enhanced suspended load (Galy and France-Lanord, 2001; Milliman and Meade, 1983; Sarin et al., 1989; Singh et al., 2008) from rivers is responsible for active scavenging and thus, the low residence time observed in the Bay of Bengal and the Andaman Sea. Compared to the BoB there is much lower terrestrial input in the Arabian Sea, and thus the residence time varies between 179-443 years. A significant difference in the residence time (274 and 443 years) for the two data points in the central Arabian Sea (SK-312/15 and 16) reflects varying scavenging efficiency due to their $CaCO_3$ content (56 % and 32 %). The Arabian sea is known for its drastic spatial variation in primary productivity leading to varying $CaCO_3$ content in sediments (Naqvi, 1991). To summarize, the observed residence time of beryllium in the Indian Ocean is primarily a function of particle availability in the water column and its subsequent scavenging.

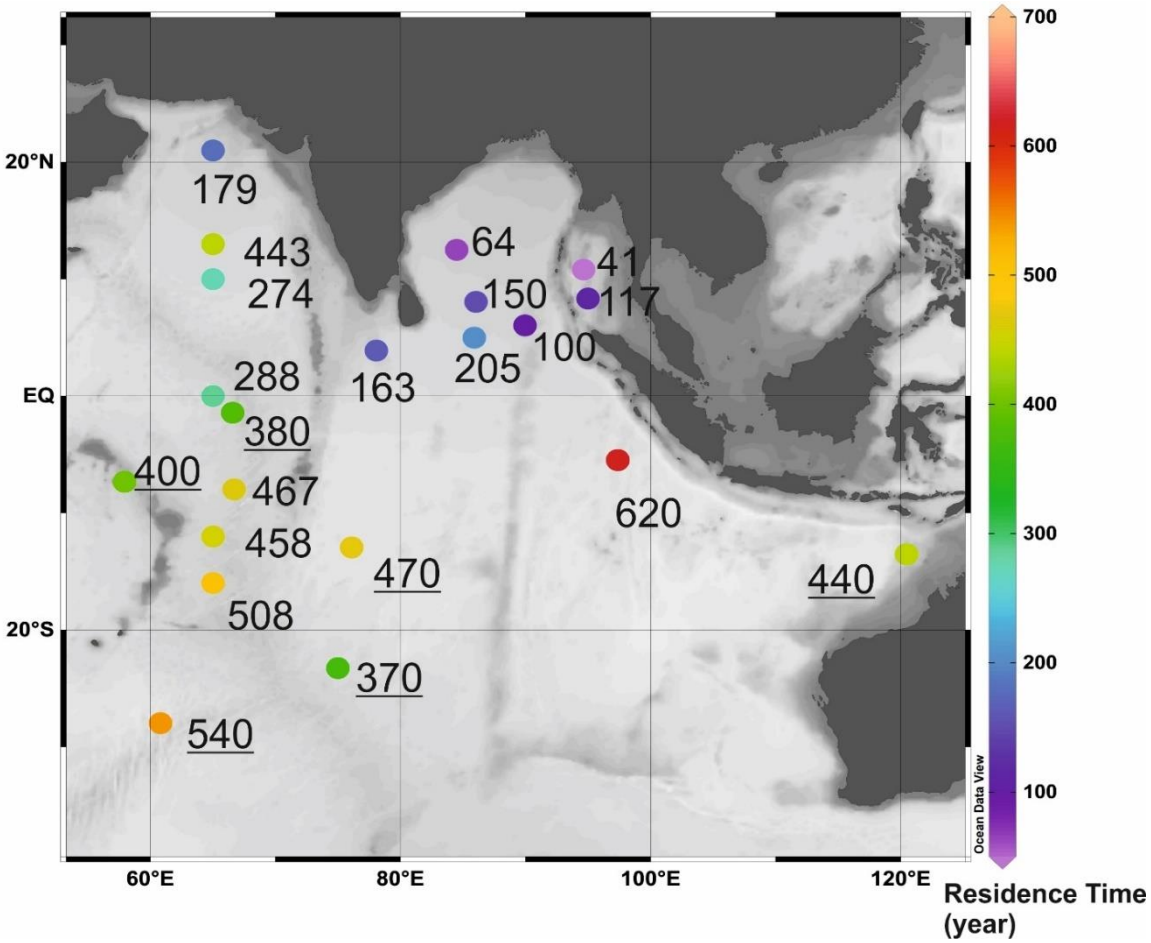

Figure 5.4: *Estimates of residence time (in years) of beryllium in the Indian Ocean water column. The figure also includes Be residence time estimated (shown as underlined texts) from earlier study* (von Blanckenburg et al., 1996).

5.7 Global Distribution of Beryllium Isotopes in Marine Archives

The authigenic fraction extracted from various proxies (surface sediments, Fe-Mn crusts) derives its beryllium isotopic composition from the ambient seawater and can be utilised for comparison between global oceans (Bourles et al., 1989; McHargue et al., 2000; von Blanckenburg et al., 1996). A comparison between $^{10}Be/^{9}Be$ measured in the seawater column and other archives has been provided in **Table 5.3** to assess the reproducibility of the archive measurements with the isotopic ratio of the ambient water column. For the Pacific Ocean, the $^{10}Be/^{9}Be$ ratio, an average value of 10.94×10^{-08} was derived from Fe-

Mn crusts, while the surface sediments give an average value of 9.82 $x10^{-08}$, and for the deep-water column, it is 12.97 $x10^{-08}$. Similarly, for the Atlantic Ocean, nearly similar isotopic ratios were observed from Fe-Mn crusts (4.91 $x10^{-08}$), sediments (5.05 $x10^{-08}$), and deep-water column (6.21 $x10^{-08}$). Though these measurements represent different archives from varied locations, remarkably similar results signify that the authigenic fraction derived from these archives primarily represents the beryllium isotopic signature of seawater. In the absence of beryllium isotopic measurements from the water column of the Indian Ocean, a similar comparison is not possible. Still, the comparable $^{10}Be/^{9}Be$ ratio derived from Fe-Mn crusts (8.07 $x10^{-08}$) and surface sediments (7.05 $x10^{-08}$) in the central Indian Ocean attests the same.

Table 5.3: *Distribution of $^{10}Be/^{9}Be$ in the water column from different ocean regions. The data from direct measurements from both the water column as well as those derived from archives such as surface sediments and Fe-Mn crusts have also been included.*

	$^{10}Be/^{9}Be$ of water column (x 10^{-8})	**References**
Pacific Ocean	**Avg.= 10.96 ± 1.83 (26)**	
	[a]10.94 ± 1.48 (18)	[a] Fe-Mn crusts (von Blanckenburg et al., 1996)
	[b]9.82 ±1.95 (5)	[b] Surface Sediment (Bourles et al., 1989)
	[c]12.97 ± 2.52 (3)	[c] Water column (Kusakabe et al., 1987a)
Atlantic	**Avg. = 5.40 ± 2.30 (24)**	
Ocean	[a]5.08 ± 1.88 (11)	[a]Fe-Mn crusts (von Blanckenburg et al., 1996)
	[b]5.05 ± 3.85 (6)	[b] Surface Sediment (Bourles et al., 1989)
	[c]6.21 ± 0.94 (7)	[c] Water column (Ku et al., 1990; Measures et al., 1996)
	4.11 ± 1.55 (avg. of North Atlantic)	
	7.21 ± 1.95 (avg. of South Atlantic)	
[d]Indian Ocean	**Avg.= 8.43 ± 2.49 (17)**	
	[a]8.07 ± 1.16 (6)	[a]Fe-Mn crusts (von Blanckenburg et al., 1996)
	[b]8.62 ± 3.02 (11)	[b]Surface Sediment (Present Study; Bourles et al., 1989)
Mediterranean	**Avg. = 0.90 ± 0.30 (3)**	
Sea	[b]0.61 (1)	[b] Surface Sediment (Bourles et al., 1989)
	[c]1.11 ± 0.09 (2)	[c] Water column
Arctic Ocean	**Avg. = 6.59 ± 0.97 (5)**	[c] Water column (Frank et al., 2009)
South China Sea	**Avg. = 5.25 ± 2.04 (2)**	[b] Surface Sediment (Bourles et al., 1989)

[a]derived from Fe-Mn crusts; [b]derived from surface sediment; [c]directly measured from the water column (only depths >1000 m has been included);[d]estimations from the central Indian Ocean are shown.

The number of data points is shown in parentheses.

The large geographical variation observed in the beryllium isotopic distribution (**Figure 5.5**) from different oceanic regions signifies the role of ^{10}Be and/or ^{9}Be input to the ocean water. The ^{10}Be input to the ocean water is mainly controlled by atmospheric depositional flux as terrestrial input of ^{10}Be is significantly lower (Brown et al., 1992b). The ^{10}Be input also varies spatially as ^{10}Be flux is a function of troposphere-stratosphere exchange (Graham et al., 2003), variation in precipitation rate (Willenbring and von Blanckenburg, 2010), and variability in aerosol content (Mann et al., 2011). Though the ^{10}Be depositional flux exhibits a latitudinal pattern with maximum deposition in the mid-latitudes, the ^{10}Be/^{9}Be ratio variation does not follow the same latitudinal trend. The low ^{10}Be/^{9}Be ratio observed in the northwest Atlantic Ocean is suspected to be a result of lower ^{10}Be deposition because of lower precipitation in the Saharan region, although there is not enough evidence to support the same (von Blanckenburg et al., 1996). It has also been observed that in regions with low precipitation rates, ^{10}Be depositional flux is dominated by dry deposition (Heikkilä et al., 2013).

The other parameter controlling variation of the ^{10}Be/^{9}Be ratio is the input of ^{9}Be to the ocean water. The ^{9}Be is mostly contributed by riverine flux, dust input, and hydrothermal input. Though terrestrial input of ^{9}Be is believed to be the primary contributor of ^{9}Be in the ocean water (Measures and Edmond, 1983), studies have suggested extensive scavenging of ^{9}Be in the estuarine and coastal regions, and thereby its input to the open ocean is minimal (Brown et al., 1992b; Kusakabe et al., 1991). A significantly lower ^{10}Be/^{9}Be ratio observed in the Mediterranean Sea with higher ^{9}Be concentrations has been attributed to the higher terrestrial influx of ^{9}Be in the form of both riverine and dust input (Bourles et al., 1989; von Blanckenburg et al., 1996). In the present study, though, the role of dust input could not be ascertained, and it was observed that the ^{10}Be/^{9}Be ratio in the Indian Ocean is primarily controlled by the riverine influx. Higher terrestrial input results in a lower ^{10}Be/^{9}Be ratio and higher ^{9}Be concentration in the Bay of Bengal compared to the central Indian Ocean. The contribution of ^{9}Be to ocean water from hydrothermal fluids still remains to be explored. Though hydrothermal fluid has ~1000 times higher ^{9}Be concentration compared to ocean water, ^{9}Be released from hydrothermal fluids is rapidly scavenged locally, thus reducing their global contribution (Bourlès et al., 1994). Similar

observations were also made in this study with minimal ^{9}Be contribution from the hydrothermal fluid. Despite higher terrestrial flux to the Atlantic ocean, it was observed that ^{9}Be concentrations in the Atlantic Ocean water are very much comparable to that from the Pacific Ocean water (Ku et al., 1990; Kusakabe et al., 1990; von Blanckenburg et al., 1996), and the variation in ^{10}Be concentration is primarily the reason behind the observed offset in ^{10}Be/^{9}Be ratio.

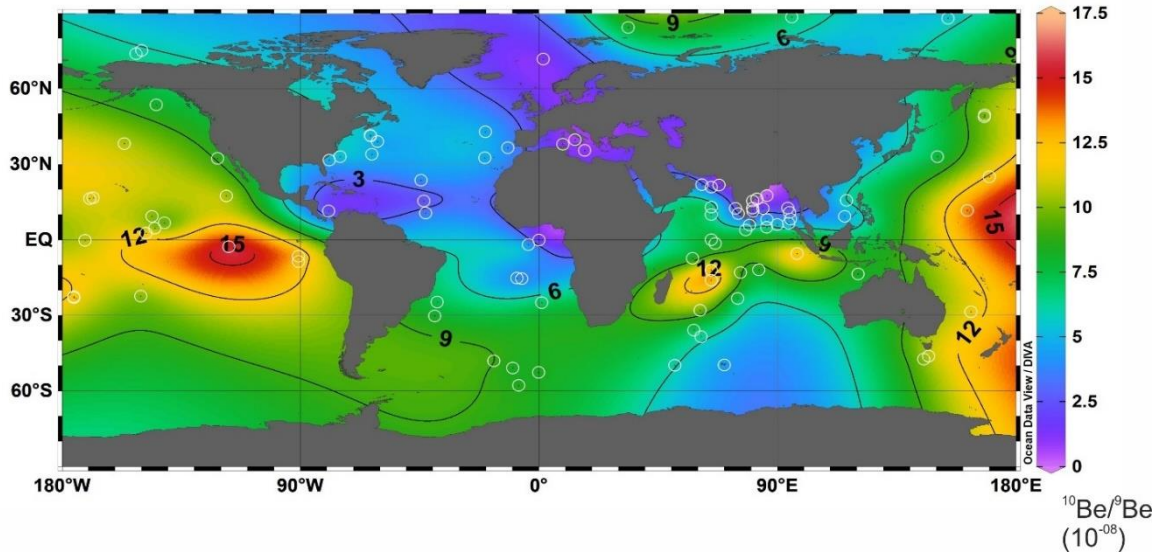

Figure 5.5: *The global deep-water distribution of ^{10}Be/^{9}Be ratio derived from surface sediments (Present Study; Bourles et al., 1989), Fe-Mn crusts* (von Blanckenburg et al., 1996)*, and direct measurements in the ocean water column (>1000 m)* (Frank et al., 2009; Ku et al., 1990; Kusakabe et al., 1990, 1987a, 1982; Measures et al., 1996). *Sample locations are shown in open white circles.*

5.8 Inferences

Being the first such attempt from the region, our study yields important results for constraining the behaviour of beryllium isotopes in the Indian Ocean. Basin wise heterogeneity observed in the ^{10}Be/^{9}Be ratio in the Indian Ocean demonstrates the role of terrestrial sediment input. The Bay of Bengal, with enhanced sediment load input, has a higher ^{9}Be concentration and lower ^{10}Be/^{9}Be ratio. The dominance of clay particles when compared to carbonates assists in the effective scavenging of ^{10}Be and ^{9}Be. Whereas the central Indian Ocean has a higher ^{10}Be/^{9}Be ratio due to no direct terrestrial source.

The residence time of beryllium in the central Indian Ocean is higher compared to the northern Indian Ocean. Large heterogeneity in the residence time of beryllium is due to its scavenging efficiency variation in different regions. Active scavenging of beryllium by sediment particles contributed through various rivers draining into the northern Indian Ocean results in lower residence time of Be. The residence time, as derived based on the $^{10}Be/^{9}Be$ ratio in the surface sediments, ranges between 288-620 years in the central Indian Ocean, 64-205 years in the Bay of Bengal, 41-117 years in the Andaman Sea, and 179-443 years in the Arabian Sea. High residence time in the central Indian Ocean implies that clay particles are more efficient in scavenging beryllium from the water column than carbonates. Regions with a high scavenging rate of Be would be more suitable for deciphering accurate estimates of ^{10}Be depositional flux as required for paleo geomagnetic field intensity reconstruction. The residence time of Be in the Indian Ocean has implications for the paleo reconstruction of geomagnetic field intensity based on ^{10}Be production and its deposition in the ocean.

Chapter 6 Meteoric ^{10}Be as a Tool to Probe Past Geomagnetic Field Intensity Changes

6.1 Introduction

Knowledge of past geomagnetic evolution is important to understand the processes occurring in the earth's interior, as well as building magnetostratigraphy as an important chronology tool (Savranskaia, 2020; Simon et al., 2016b). Paleomagnetic information retrieved from both sediments and lava flows has provided crucial learning about geomagnetic field characteristics (Valet, 2003). Continuous records can be retrieved by analysing magnetic minerals in sediment cores. Yet, various syn-depositional and post-depositional processes tend to modify the magnetic mineral deposition, introducing further complexities in these records (Simon et al., 2020). Hence, cosmogenic nuclide (e.g., ^{10}Be) records in sediment and ice cores provide valuable documentation of past geomagnetic field variations. Despite ^{10}Be/^{9}Be records being an important tool for providing insight into past geomagnetic field intensity changes, such records from the Indian Ocean are scarce. This suggests a need for a ^{10}Be isotopic record from Indian ocean sediment cores for the late Quaternary period. Hence in this study, beryllium isotopic measurement was performed in multiple sediment cores collected in the central Indian Ocean spanning the time period 45 ka to the present. This attempt would provide a high-resolution record of ^{10}Be/^{9}Be from a geographically unexplored location to further improve the understanding of past geomagnetic variations.

6.2 Sediment Core Sampling

During an oceanographic cruise onboard ORV Sagar Kanya (SK-312), sediment cores (SK-312/08, 09, 10) from the central Indian Ocean were collected with the help of a gravity corer (**Figure 6.1**). The sediment section in this core is highly enriched in biogenic carbonate (~90% w/w in SK-312/08 and 09 and ~80% in SK-312/10), and the rest is

predominantly terrigenous clay. No significant changes in sediment characteristics were observed during sub-sampling.

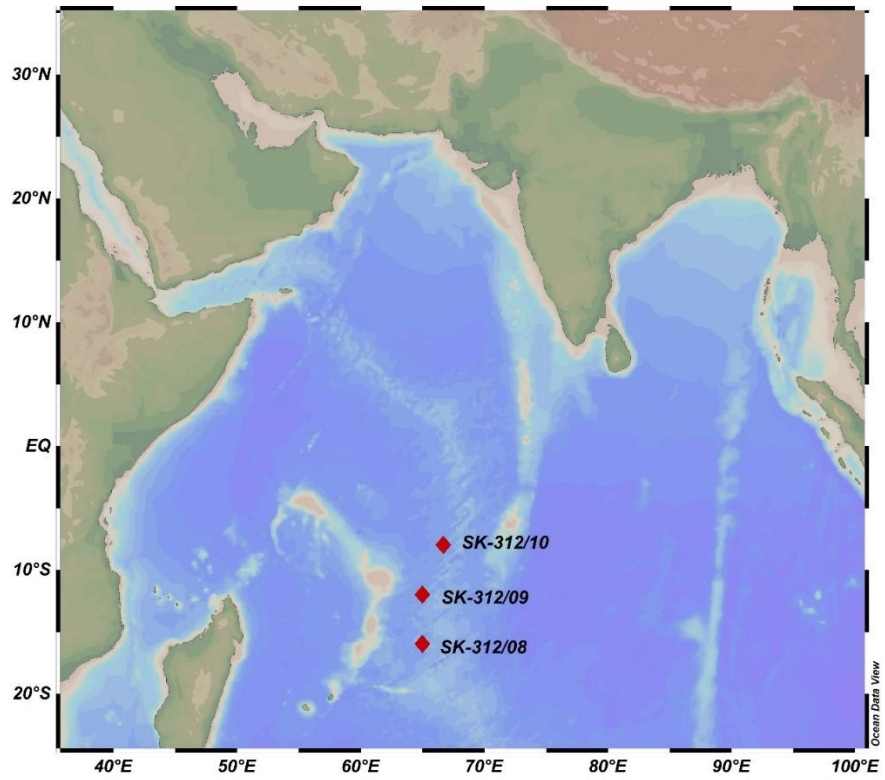

Figure 6.1: *Location of sediment cores SK-312/08, 09, and 10 in the central Indian Ocean.*

6.3 Chronology of the Sediment Cores

For Radiocarbon dating, about 10 mg of selected planktic foraminifera species (G. Ruber) picked from specific depths were graphitized using automated graphitization equipment (AGE3) (Wacker et al., 2013, 2010). The samples were graphitised following the procedure described in **Chapter 2** and measured for cradiocarbon at the Accelerator Mass Spectrometer at PRL Ahmedabad (PRL-AURiS) (Bhushan et al., 2019b). Radiocarbon ages, thus obtained, were calibrated using Calib 8.2 (Heaton et al., 2020) with a reservoir age correction (ΔR) of -64±76 years (Southon et al., 2002). The sediment core SK/312-08 extends up to 43 ka at 60 cm depth, while the core SK-312/09 extends up to 43 ka at 94 cm depth. The sediment core SK-312/10 dates upto 27 ka at 70 cm depth. The age-depth plots built using the bayesian modelling is shown in **Figure 6.2**.

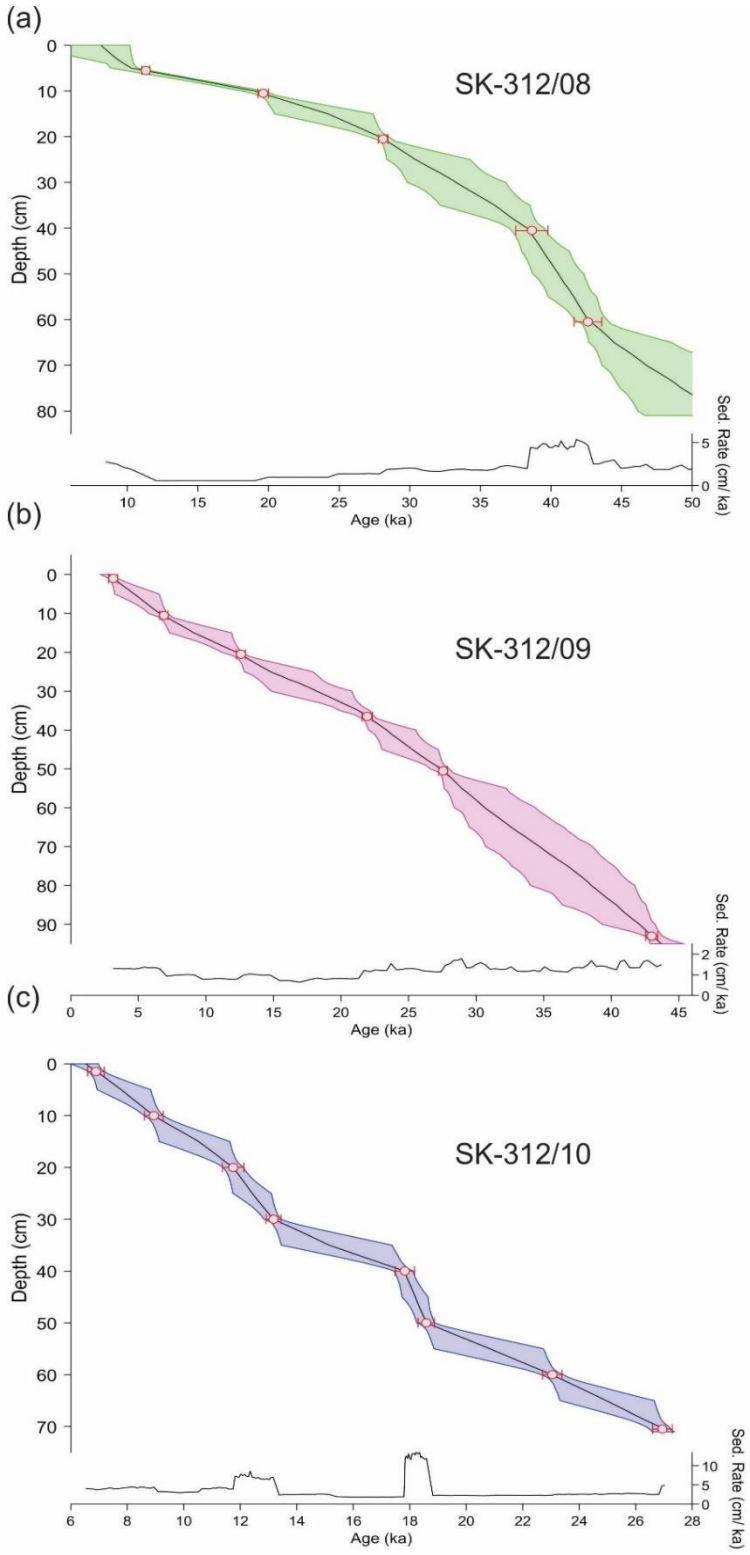

Figure 6.2: *Age-depth plots for the sediment cores SK-312/08, 09, 10*

6.4 Estimation of ^{10}Be Deposition Flux

^{10}Be flux for the location was calculated using two methods. Firstly, it was calculated using ^{10}Be concentration, Dry Bulk Density (DBD), and sedimentation rate (S) by the following formula (Southon et al., 1987) (Method 1).

$$^{10}Be\ flux\ (atom.cm^{-2}.yr^{-1}) = [^{10}Be]\ (atoms.g^{-1}) \times DBD(g.cm^{-3}) \times S\ (cm.yr^{-1}) \quad (6.1)$$

Additionally, the depositional flux has also been estimated from a modified formula from Tanaka et al. (1977), and Tanaka and Inoue (1979). The number of beryllium-10 atoms N(x) as a function of depth x in a sediment column depends on depositional flux (P), sedimentation rate (S), and decay of the radioactive nuclide. Following Tanaka et al. (1977), and Tanaka and Inoue (1979), the depth-dependent sedimentation rate, age, and ^{10}Be concentration can be related as

$$T(x) = -\frac{1}{\lambda} ln\left[1 - \frac{\lambda}{P}\int_0^x N(x)dx\right] \quad (6.2)$$

Hence, for a particular sediment column, ^{10}Be flux can be obtained by rearranging the formula when the time period represented by the sediment column (ΔT) can be obtained from an independent method (Method 2)

$$P = \frac{\lambda N(x)\Delta x}{1-e^{-\lambda(\Delta T)}} \quad (6.3)$$

The decay constant (λ) of ^{10}Be used to calculate the fluxes is 5.00 x 10^{-7} (Chmeleff et al., 2010; Korschinek et al., 2010).

6.5 Impact of Leaching Procedure on ^{10}Be Depositional Flux Estimation

Three samples (representing the Holocene) from the sediment core SK-312/09, were processed with both weak and strong leaching agents. The Holocene ^{10}Be depositional flux estimate based on strong leaching method is calculated to be 9.63 to 13.01 x 10^5

atoms/cm^2/yr, while that from the weak leaching method gives flux values ranging between 6.75 to 8.97 x 10^5 atoms/cm^2/yr. This demonstrated that flux estimations using weak leaching result in 44% underestimation (**Table 6.1**) of flux values due to inefficient leaching by the weak leaching agent (25% acetic acid solution in this study). Simon et al. (2016a) have also noticed ~60% underestimation in flux estimates due to weak leaching in a sediment core from the Portuguese margin. Thus, for flux estimates, sediment samples have to be treated with a strong leaching agent. However, for various applications (i.e., past geomagnetic field intensity reconstruction, sediment core dating) that involve the extraction of the authigenic phases, a weak leaching agent must be preferred. In the following discussions, the flux estimates corrected for leaching yield have been used, while the ^{10}Be/^{9}Be ratio from the weak leaching method has been used to understand past geomagnetic field strength variations.

Table 6.1: *Comparision of the flux estimates from the strong and weak leaching methods. Results show that the flux values computed from weak leaching are 44% underestimated.*

Sl. No.	Sample Name	Sample Depth (cm)	Flux derived from weak leaching (F_w)	Flux derived from strong leaching (F_s)	F_S/F_W
1	SK-312/09 0-2	0-2	8.97 ± 0.88	13.01 ± 1.15	1.45
2	SK-312/09 2-11	2-11	8.92 ± 0.83	12.93 ± 1.21	1.45
3	SK-312/09 11-21	11-21	6.75 ± 0.52	9.63 ± 0.70	1.43
				Average	1.44

6.6 ^{10}Be Depositional Flux Obtained from Sediment Core SK-312/09 and a Global Comparison

The ^{10}Be depositional flux estimates from two methods have been compared. The Holocene ^{10}Be depositional flux estimates vary between 9.63 to 13.01 x 10^{05} atoms/cm^2/year (using strong acid leaching) using method 1, which involves sedimentation rate and DBD (Southon et al., 1987) (**Table 6.2**). Interestingly, the flux values obtained by method 2 (Tanaka and Inoue (1979)) also provided the same results. Minor offsets observed between results from the two methods are insignificant when compared with the associated

errors. However, while using the modified Tanaka and Inoue (1979) method, the ΔT needs to be calculated carefully. Particularly, for the topmost section, where if zero-depth (surface) age is not considered for calculating the ΔT, it may result in an underestimation of ^{10}Be depositional flux. In this study, the extrapolated surface age (2773 cal yr BP) was calculated from an age-depth model built using the Bacon program (Blaauw and Christen, 2011), which is considered for the estimation of the depositional flux of the top section. The high surface age obtained for the core top in this study is due to the mixing of core-top sediments. Additionally, Tanaka and Inoue. (1979) provided a method to calculate depositional flux involving a log N(x) vs. x plot. However, this method is applicable for long sediment cores, where N(x) decreases with depth following radioactive decay of ^{10}Be with time. But, for short cores (as in the present study), age needs to be determined using an independent method. In further discussions, the ^{10}Be depositional flux estimates from method 1 have been used.

***Table 6.2**: Estimates of ^{10}Be depositional flux for the Holocene period (using strong acid leaching) in the sediment core SK-312/09 based on methods of Southon et al., 1987 (Method 1) and Tanaka and Inoue, 1979 (Method 2).*

Sl. No.	Time Period	^{10}Be depositional flux (Error 1σ) (x 10^5 atoms/cm^2/yr) (Method 1)	^{10}Be depositional flux (Error 1σ) (x 10^5 atoms/cm^2/yr) (Method 2)
1	3.5 ka - present	13.01 ± 1.15	13.02 ± 0.82
2	7.1 ka - 3.5 ka	12.93 ± 1.21	12.78 ± 0.88
3	12.8 ka- 7.1 ka	9.63 ± 0.70	9.52 ± 0.60

^{10}Be depositional flux at the study location (11.999ºS, 64.9997ºE) based on the output of global model has been calculated to be 1.33 x 10^6 atoms/cm^2/yr (Heikkilä et al., 2013; Heikkilä and von Blanckenburg, 2015). Whereas the ^{10}Be depositional flux derived from the sediment core ranges from 9.63 x 10^5 to 13.01 x 10^5 atoms/cm^2/yr during the Holocene time period. The modelled ^{10}Be depositional flux for this region is found to be ~2 to 28% higher compared to the sediment-derived flux. There could be multiple factors responsible for the offset between the modelled flux and sediment core-derived flux. A

number of local processes can modify the ^{10}Be inventory in the water column and its further scavenging to the sediment column. The central Indian Ocean basin is ventilated by the Upper Circumpolar Deep Water (UCDW), which has a major contribution from the North Atlantic Deep Water (NADW) (Piotrowski et al., 2009; Talley, 2013). Therefore, there exists a possibility of transport of the beryllium isotopic signal from the Atlantic Ocean to this region. The ^{10}Be concentration in the deep Atlantic waters varies between ~800 to 1050 atoms/g, which is nearly half the concentration estimated for the Pacific Ocean (~1800-2000 atoms/g) (Ku et al., 1990; Kusakabe et al., 1987a; Measures et al., 1996). On the other hand, a significantly lower $^{10}Be/^{9}Be$ ratio (~5 x 10^{-08}) in Atlantic waters and authigenic derived proxies (such as Fe-Mn crusts and surface sediments) have been observed (Bourles et al., 1989; Ku et al., 1990; Kusakabe et al., 1987a; von Blanckenburg et al., 1996). Thus, the contribution from the Atlantic water should result in a lower $^{10}Be/^{9}Be$ ratio in the water column and the authigenic fraction of sediments derived from it. However, the $^{10}Be/^{9}Be$ ratio (~1.2 x 10^{-07}) obtained from the sediment core in the present study is the highest among those obtained from the Indian Ocean and does not support the possibility of beryllium isotopic contribution from the Atlantic Ocean. Another important factor controlling the ^{10}Be deposition into the ocean sediment column is boundary scavenging. Evidence of boundary scavenging of ^{10}Be has been shown by previous workers in the Pacific and the Atlantic Ocean (Anderson et al., 1994, 1990; Lao et al., 1992a). In the Indian Ocean, no previous work has estimated the extent of boundary scavenging of ^{10}Be. Anderson et al. (1990) and Lao et al. (1992a) have found that near coastal regions account for ~50-70 % of scavenging of ^{10}Be deposited to the Pacific Ocean despite constituting 10% of the total ocean surface area. As the present study location lies in the open Indian Ocean, a part of the underestimation in ^{10}Be depositional flux can be explained by minimal scavenging of ^{10}Be due to limited availability of scavenging particles such as clay particles. The reduced ^{10}Be flux for the depth 12-21 cm is associated with a decrease in the sedimentation rate (1.8 cm/ka). This indicates the sediment deposition rate can strongly influence the ^{10}Be depositional flux due to a change in the amount of available scavenging particles. Considering the top two samples, which provide flux estimates of 13.01 and 12.93 x 10^{05} atoms/cm^2/year, the obtained fluxes are very much similar to the modelled atmospheric depositional flux value with a marginal offset of ~2-3%. This indicates that at the studied site, the lateral input of Be isotopes and boundary scavenging in the Indian

Ocean have a minimal effect on ^{10}Be depositional flux, while the rate of sediment deposition has greater control.

The ^{10}Be depositional flux depends on its production in the atmosphere and the processes affecting its transport to the earth's surface. The production of ^{10}Be is maximum in the higher latitudes, and more than 60% of the production takes place in the stratosphere. However, due to a long residence time of nearly one year (Raisbeck et al., 1981), it is efficiently mixed in the stratosphere (Heikkilä et al., 2013). The variation of ^{10}Be flux is a function of troposphere-stratosphere exchange (Graham et al., 2003), variation in precipitation rate (Willenbring and von Blanckenburg, 2010), and variability in aerosol content (Mann et al., 2011). Hence, the maximum deposition of ^{10}Be occurs at the mid-latitudes (**Figure 6.3**; Heikkilä et al., 2008b), where the air exchange between the troposphere and the stratosphere happens (Appenzeller et al., 1996). Heikkilä et al. (2013) have also observed that the ^{10}Be depositional flux is highly correlated with the precipitation rate. However, in desert areas, the dry deposition dominates. Though the ^{10}Be production mostly varies at the low latitudes during geomagnetic excursions and reversals, variation in depositional flux by ~two times has been observed at all latitudes due to well mixing within the stratosphere (Heikkilä et al., 2013).

The ^{10}Be depositional flux has been estimated from various sediment cores in the Pacific and the Atlantic Oceans mainly to understand the past variation of depositional flux resulting from the geomagnetic field changes (Christl et al., 2010, 2007; Frank et al., 1997; Simon et al., 2016b; Valet et al., 2014). Lao et al. (1992), and Frank et al. (1997) have provided the spatially distributed ^{10}Be depositional flux variation in the Pacific and Atlantic Oceans for a similar period as in the present study (the Holocene). However, when compared to the modelled ^{10}Be depositional flux, nearly 50% of the locations show significant overestimation in flux values. The estimated depositional fluxes are almost 2 to 10 times higher than the modelled fluxes. Though there is always a possibility of an offset in depositional flux due to local factors, the reason behind such significant over-estimation in ^{10}Be depositional flux remains uncertain. Hence, in the following discussion, these locations have not been considered. Results from a few more sediments core-derived ^{10}Be fluxes have been included in the discussion (Christl et al., 2010, 2007; Simon et al., 2016a). In the Indian Ocean, the flux estimates covering the Holocene time period are not available,

though significant work has been conducted to understand the flux variation during the last geomagnetic reversal (Simon et al., 2018b; Valet et al., 2014). The flux estimates outside the peak region have been included in the discussion, assuming it to be similar to the Holocene flux.

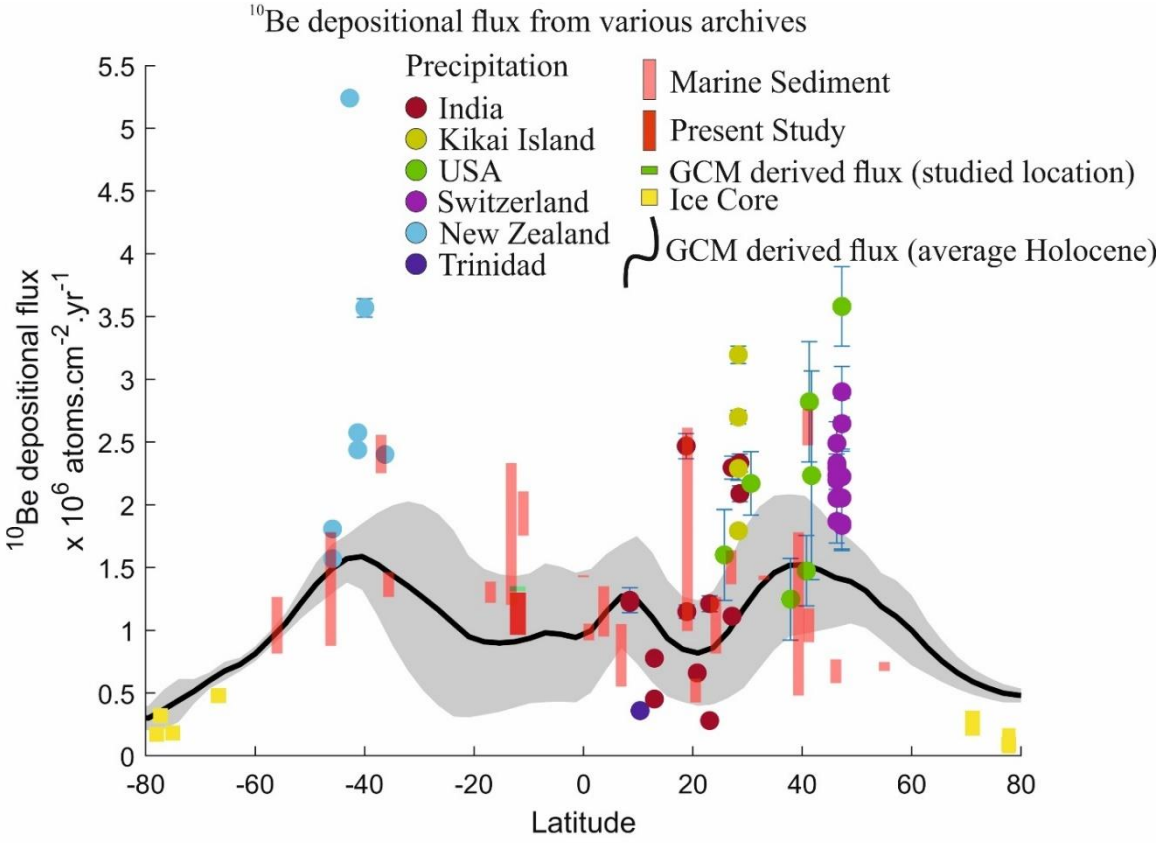

Figure 6.3: *Comparison between the modeled ^{10}Be depositional flux and the flux estimated from direct precipitation measurements (circles; Brown et al., 1992a; Graham et al., 2003; Heikkilä et al., 2008a; Maejima et al., 2005; Monaghan et al., 1986; Somayajulu et al., 1984), ice cores (yellow squares; Baroni et al., 2011; Heikkilä et al., 2008c; Horiuchi et al., 2008; Muscheler et al., 2005; Pedro et al., 2006) and from sediment cores (transparent red bars; Christl et al., 2010, 2007; Frank et al., 1997; Lao et al., 1992; Simon et al., 2016b, 2016a; Valet et al., 2014). The black curve shows the mean of ^{10}Be depositional flux derived from general atmospheric circulation modelling (GCM), representing the average for Holocene* (Heikkilä and von Blanckenburg, 2015), *and the gray area represents the standard deviation of its longitudinal variation. The result from the present study is shown as a thick red bar, and the model-derived flux for the study location is shown as a light green rectangle.*

In **Figure 6.3**, the ^{10}Be depositional flux values estimated from the marine sediment cores have been compared to those calculated from the model (Heikkilä et al., 2013;

Heikkilä and von Blanckenburg, 2015). During Holocene, ^{10}Be depositional fluxes from a few locations show major variation (two to four times). In contrast, the geomagnetic field strength shows minor variations during the Holocene period as estimated using various proxies (Frank et al., 1997; Steinhilber et al., 2012). One possible explanation for this ^{10}Be depositional flux variation could be change in factors affecting the removal of beryllium from water to the sediment column, such as varying sediment composition. As a result of varying sediment contribution, scavenging of ^{10}Be to the sediment column may also vary (Southon et al., 1987). Simon et al. (2016a) have demonstrated that the ^{10}Be flux in a sediment core from the central Baffin Bay varies significantly with changing sedimentology. The available data shows that the depositional fluxes estimated from marine sediment cores are in good agreement with those calculated from the models (**Figure 6.3**). Though both over-estimation and under-estimation have been observed in the ^{10}Be depositional fluxes obtained from marine sediments compared to the model-derived fluxes, and no decipherable latitudinal trend could be seen in obtained flux values. There are estimates of ^{10}Be flux from direct measurements from precipitation samples from India (Somayajulu et al., 1984), the U.S.A (Monaghan et al., 1986), New Zealand (Graham et al., 2003), Kikai Island, Japan (Maejima et al., 2005), and Switzerland (Heikkilä et al., 2008). Two data points from New Zealand show substantially higher depositional flux values (5.2 & 3.6 x 10^6 atoms/cm^2/yr), which could have been affected by the seasonal cycles, considering the observation period is nearly 100-150 days (Graham et al., 2003). Yet, by comparing the rest of the data with the modelled flux, it is observed that the precipitation-derived data mostly shows an overestimation in estimated ^{10}Be depositional fluxes (except for 0-30^{0}N where both over and underestimations are observed). Even the global average flux derived from precipitation measurements (~2 x 10^{06} atoms/cm^2/yr) is almost twice the value derived from the models. The precipitation-derived ^{10}Be flux may show deviated values, as these numbers are affected by short-term processes (modulation due to changes in solar activity, and changes in aerosol content) and may not represent the average Holocene flux derived from models (Deng et al., 2020a). However, Deng et al. (2020a) observed similar offsets, even after normalizing the precipitation derived ^{10}Be flux values with a common solar modulation and comparing it with the industrial run of Heikkilä and Smith (2013) model. On the other hand, ^{10}Be flux values derived from soil archives are largely underestimated (Deng et al., 2020a; Graly et al., 2011), probably

because of partial retention of ^{10}Be, and surface erosion (Deng et al., 2021, 2020a). While estimating ^{10}Be depositional flux from soil profiles or terraces, sampling at proper(deeper) depths must be performed to evaluate the inherited ^{10}Be (Deng et al., 2021). We have also plotted available ice core derived ^{10}Be depositional fluxes both from Greenland (Heikkilä et al., 2008b; Muscheler et al., 2005; Zheng et al., 2020) and Antarctica (Baroni et al., 2011; Horiuchi et al., 2008; Pedro et al., 2006) covering a timespan of one year (Pedro et al., 2006) to the Holocene (Muscheler et al., 2005). The ^{10}Be flux records from Antarctica (varying between 0.2-0.64 x 10^{06} atoms/cm^2/yr) show a good correlation with the model-derived fluxes with minor underestimation in the values. However, records of ^{10}Be depositional fluxes derived from Greenland were under-estimated compared to the modelled fluxes. As these records span short time scales (except (Muscheler et al., 2005)), they may be affected by seasonal cycles. In addition to production in the atmosphere, the ^{10}Be records in ice cores are affected by changes in atmospheric mixing, transport pathways, and variation in snowfall rate (Finkel and Nishiizumi, 1997; Muscheler et al., 2005; Yiou et al., 1997). The regional flux estimates obtained from various model runs may give an offset value due to various factors such as lower resolution (2.8° x 2.8° in ECHAM5-HAM), use of production functions that are still being updated, changes in aerosol concentration in the past, and due to various local effects on depositional fluxes which are not considered in the models (Deng et al., 2021, 2020a; Heikkilä et al., 2013).

There have been significant efforts to estimate atmospheric ^{10}Be depositional fluxes through model calculations. Despite multiple attempts, it has been difficult to validate the models as a large offset is observed when compared to the depositional flux values obtained from various proxies. Particularly for Earth science applications, where millennial-scale average flux estimates are required, soil profiles can be regarded as one of the best suited terrestrial archives, as precipitation measurements are affected by short-term changes. However, as discussed above, the soil-derived proxies provide the lower limit of local ^{10}Be depositional fluxes. In a recent work, Deng et al. (2021) attempted to correct the associated underestimation in river terrace derived flux values and provided an average depositional flux estimate for the Taiwan Orogen based on measurements from multiple terraces. Though in this study, from an open ocean sediment core, the modelled and sediment-derived flux estimates were found to be close, the effects of local processes cannot be neglected. During paleomagnetic reconstructions, the climate-induced changes can affect

the ^{10}Be record, which can be removed by normalizing with ^{9}Be or $^{230}Th_{ex}$. Similarly, in a recent work based on ^{10}Be measurements in ice cores, Zheng et al. (2020) proposed a normalization method

6.7 Temporal Be Isotopic Record from the Sediment Cores

6.7.1 High Resolution Be Isotopic Record from the Sediment Core SK-312/10

Changes in the production of ^{10}Be in the atmosphere recorded in marine sediment cores have been utilised to reconstruct past geomagnetic field intensity changes. In the present study (SK-312/10), a significant difference was observed between the ^{10}Be concentration and the $^{10}Be/^{9}Be$ ratio. The ^{10}Be concentration shows the maximum value at ~18-20 ka, while the maximum $^{10}Be/^{9}Be$ ratio is observed during 22-26 ka (**Figure 6.4**). It clearly suggests, in the present study ^{10}Be concentration record actually indicates changes in beryllium scavenging rather than changes in ^{10}Be production. Hence, it further emphasizes on proper normalisation of the ^{10}Be record. As discussed by Savranskaia et al. (2021), there could still be minor environmental signatures in $^{10}Be/^{9}Be$ records which shows variation due to local processes. Minor fluctuations in the $^{10}Be/^{9}Be$ record observed during the Holocene could be associated with such factors.

The relation between earth's magnetic field intensity and cosmogenic radionuclide production is very well understood. During events of low geomagnetic field intensity, high production of cosmogenic nuclides is expected due to lower cutoff rigidity (Lal and Peters, 1967). An inverse relationship between the $^{10}Be/^{9}Be$ and geomagnetic field strength ratio has also been well documented by various studies (Carcaillet et al., 2004b; Knudsen et al., 2008; Ménabréaz et al., 2014; Valet et al., 2014). During 26 to 21 ka, the $^{10}Be/^{9}Be$ shows a higher value (~25 %) compared with the $^{10}Be/^{9}Be$ ratio during 21 to 6 ka. The higher $^{10}Be/^{9}Be$ ratio can be attributed to low geomagnetic field strength that could have led to increased cosmogenic nuclide production. In the marine ^{10}Be stack of Frank et al. (1997),

a higher ^{10}Be deposition rate also has been observed during the same time. In the sediment core MD05-2930, a similar increase in the ^{10}Be/^{9}Be ratio is observed during 21-26 ka. Thus, the increase in the ^{10}Be/^{9}Be ratio during 26 to 21 ka is attributed to the ^{10}Be production increase due to lower geomagnetic field strength observed in dipole moment reconstructions (Laj et al., 2004; Laj and Kissel, 2015; Simon et al., 2020).

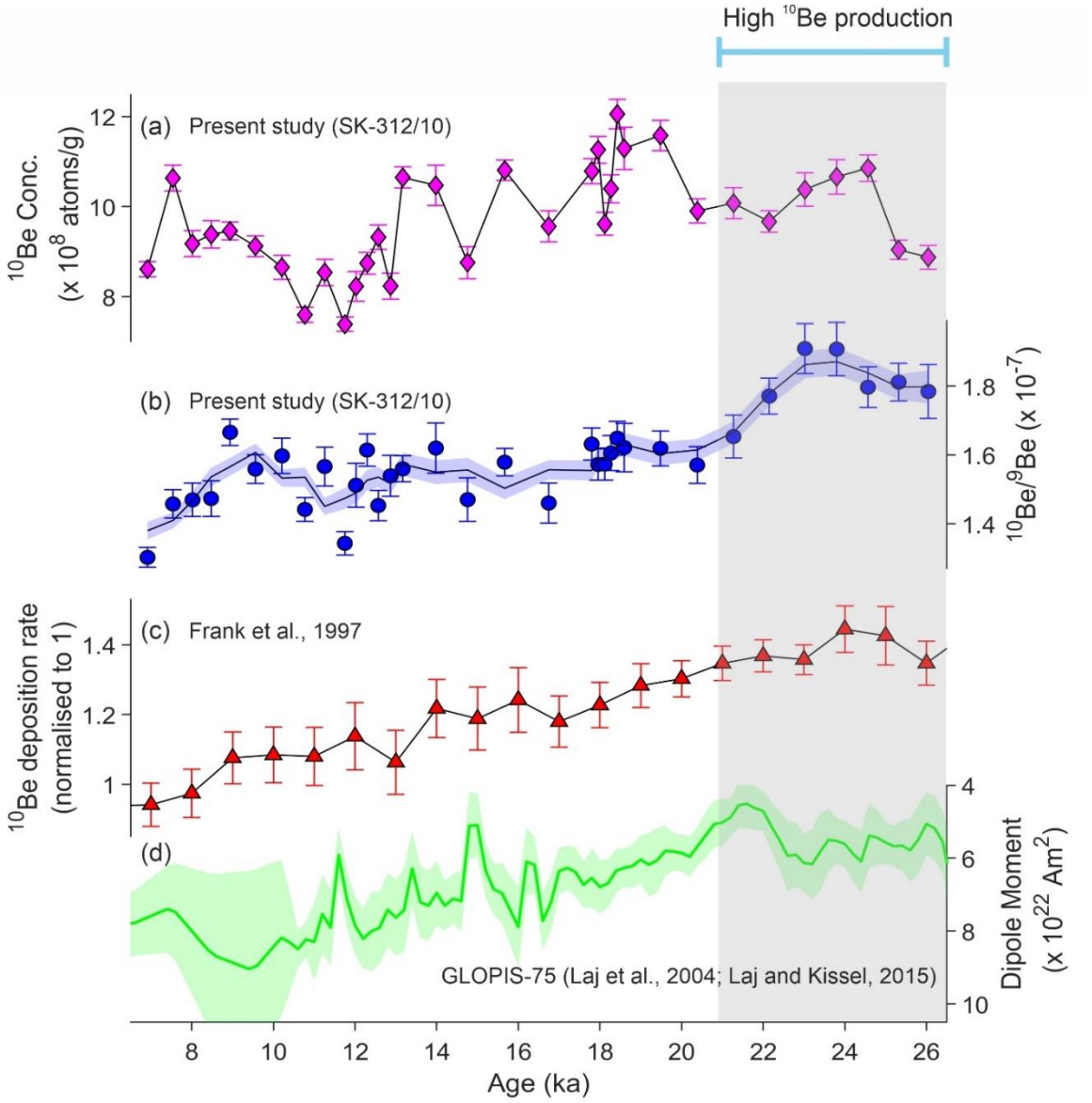

Figure 6.4: *Comparison of Be isotopic record from the present study with global records. The ^{10}Be concentration (a) and ^{10}Be/^{9}Be ratio (b) estimated from the present study is compared with (c) normalized ^{10}Be deposition rate* (Frank et al., 1997), *(d) Dipole Moment variation records GLOPIS-75* (Laj et al., 2004; Laj and Kissel, 2015),.

6.7.2 ^{10}Be Production Changes during the Laschamp Event

Records from both the sediment cores SK-312/08 and 09 extend up to ~44 ka and thus can provide an understanding of ^{10}Be production changes during the Laschamp event (~41 ka). **Figure 6.5** shows the present estimates of ^{10}Be depositional flux and ^{10}Be/^{9}Be ratio from the sediment core SK/312-09, compared with the available global ^{10}Be flux records. The ^{10}Be/^{9}Be ratio is nearly constant from 27.7 ka to the present, suggesting minor changes in geomagnetic field strength. However, a significant decrease in the ^{10}Be depositional flux was observed during 27.7 to 7.1 ka, which is associated with a reduction in average sedimentation rate for the time period (1.8 cm/kyr) and may not represent a change in geomagnetic field intensity. It further suggests that ^{10}Be flux at a particular location can vary as a function of changing sediment deposition rate (which can further be a function of climate change), and ^{10}Be concentrations from the sediment samples need to be normalized with ^{9}Be. During 43.4-27.7 ka, an increase in ^{10}Be flux (16.1 x 10^{5} atoms/cm^{2}/yr) and ^{10}Be/^{9}Be (1.49 x 10^{-07}) ratio has been observed. This can be attributed to the lower geomagnetic field intensity during the time period (Channell et al., 2009; Simon et al., 2020). During the same time period, an overall increase is observed in the average normalized ^{10}Be depositional flux (obtained from various sediment cores from the Pacific and the Atlantic Ocean) (Frank et al., 1997) and ^{10}Be/^{9}Be ratio from various sediment cores (Simon et al., 2020, 2016b).

Nine highly resolved data points in the core SK-312/09 show an elevated ^{10}Be/^{9}Be ratio and ^{10}Be flux between 40-43 ka (**Figure 6.5**). This has been attributed to the Laschamp geomagnetic excursion. The peak ^{10}Be/^{9}Be ratio (1.93 x 10^{-07}) was observed at 41.2 ka. In the sediment core SK-312/08, an increase in the ^{10}Be/^{9}Be ratio is observed at 50-70 cm, with a peak at 53-54 cm (**Figure 6.6**) corresponding to 41.4 ka from a Bayesian age-depth model using Bacon (Blaauw and Christen, 2011). The Laschamp event is one of the well-studied excursion events and has been dated to be ~41 ka (Guillou et al., 2004; Ménabréaz et al., 2011; Nilsson et al., 2011; Singer et al., 2009). During the Laschamp event, the geomagnetic dipole moment was reduced up to 1.6 x 10^{22} Am^{2} (Simon et al., 2020). In the sediment core SK-312/09, an increase in the ^{10}Be/^{9}Be ratio of ~ 60% , and in the sediment core ~40 % increase was observed during the Laschamp event compared to the present-day value, which is also consistent with the previous records (Simon et al.,

2020). The similar ^{10}Be overproduction observed from various records indicates that ^{10}Be is rapidly homogenized in the atmosphere (Heikkilä et al., 2013). During the Laschamp event, an increase in ^{10}Be production up to twice the present-day value has been computed from models (Heikkilä et al., 2013). Simon et al. (2020) have also reported a short-term dip in the ^{10}Be/^{9}Be ratio during the overall increase in the ^{10}Be/^{9}Be ratio associated with the Laschamp event. However, in the present study, a continuous increase in the ^{10}Be/^{9}Be ratio was observed up to 41.2 ka without any short-term dip.

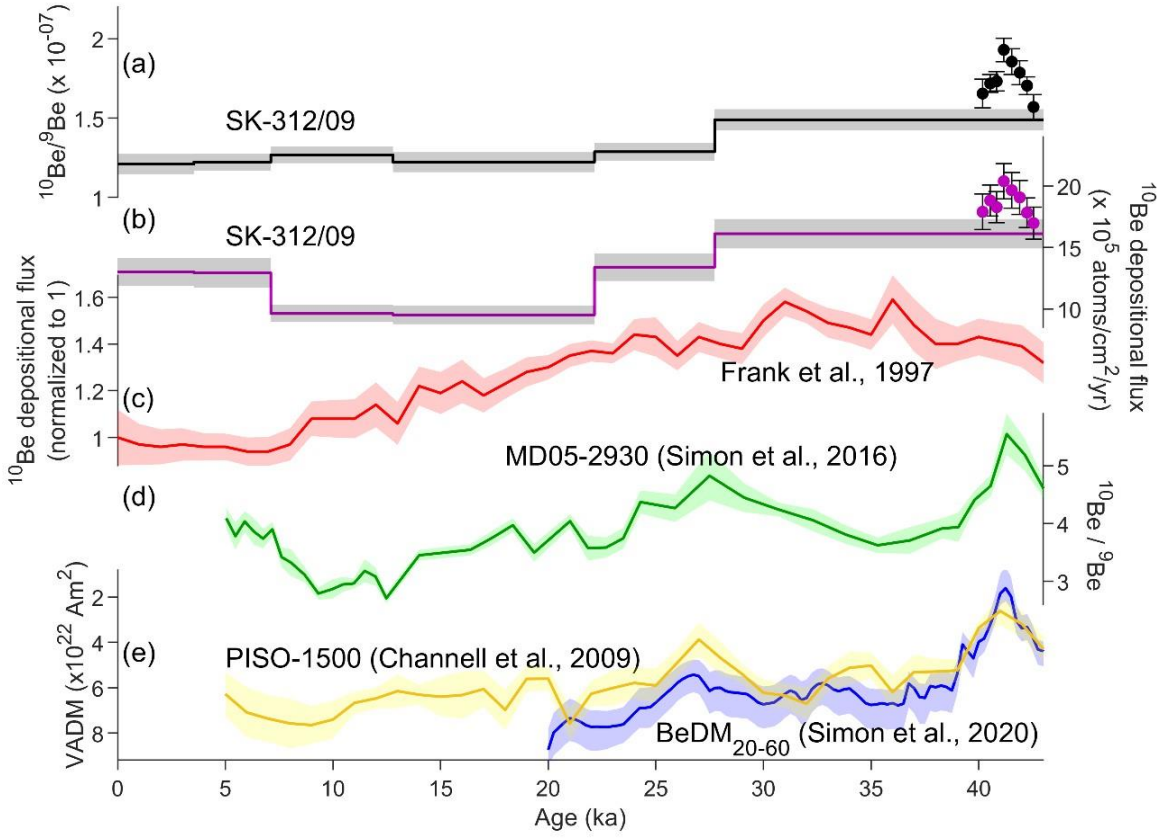

Figure 6.5: *The temporal variation in (a)^{10}Be/^{9}Be ratio in core SK-312/09 and (b)^{10}Be depositional flux in core SK-312/09 (obtained using method 1; corrected for leaching yield), (c) highly resolved global average ^{10}Be depositional flux (normalized to 1) by* (Frank et al., 1997), *(d) ^{10}Be depositional flux variation obtained from MD05-2930* (Simon et al., 2016b), *and (e) virtual axial dipole moment (VADM) record* (Channell et al., 2009; Simon et al., 2020).

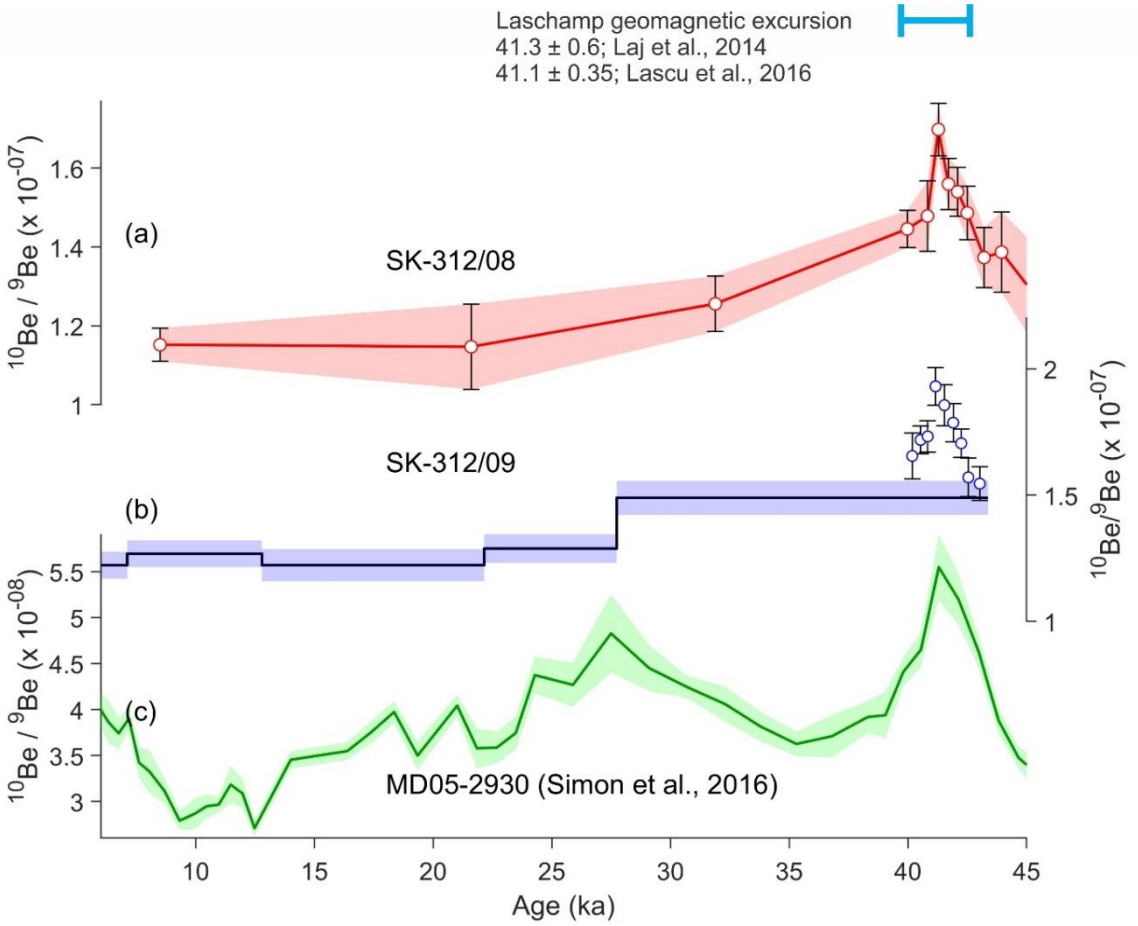

Figure 6.6: *Variation of $^{10}Be/^{9}Be$ ratio in the last 45 kyr in the sediment core SK-312/08 compared with $^{10}Be/^{9}Be$ record from sediment core SK/312-09, MD05-2930* (Simon et al., 2016b).

6.8 Inferences

A record of ^{10}Be depositional flux and ^{10}Be/^{9}Be ratio from three sediment cores from the central Indian Ocean was constructed. Salient outcomes from the present study are outlined below.

- The ^{10}Be depositional flux estimates from the weak leaching method result in ~44% underestimation compared to the strong acid leaching in the sediment core SK-312/09. This is because of the inefficient leaching of ^{10}Be by a weak acid. The extent of the underestimation may vary with the sedimentology of a marine core.

- The Holocene ^{10}Be depositional flux varies between 9.63 to 13.01 x 10^{05} atoms/cm^2/year in the central Indian Ocean region. The modelled and sediment core-derived depositional fluxes were found to be very similar. A minor offset obtained can be explained by local processes affecting ^{10}Be deposition into the sediment column, such as boundary scavenging of ^{10}Be in the Indian Ocean, rate of sediment deposition and/or offsets associated with the model calculations.
- A high-resolution record of Be isotopic ratio was built using the sediment core SK-312/10. The record shows a higher $^{10}Be/^{9}Be$ ratio during 26 to 21 ka suggesting an increase in ^{10}Be production.
- The peak in the $^{10}Be/^{9}Be$ ratio was found to be at 41.2 ka in sediment core SK-312/09 and at 41.4 ka at SK-312/08 can be associated with the Laschamp event, which shows ~40 to 60% increase in ^{10}Be production.

Chapter 7 Meteoric ^{10}Be as a Chronometer for Marine Sediment Cores

7.1 Introduction

Various chronological methodologies play a significant role in the reconstruction of quaternary paleoclimatic and paleomagnetic events using marine sediment cores. The widely used techniques used in dating marine sediment cores are radioisotope dating, including natural (^{234}Th, ^{210}Pb, ^{230}Th, ^{226} Ra, etc.), artificial (^{137}Cs, ^{239,240}Pu, etc.), and cosmogenic (^{14}C, ^{10}Be, ^{26}Al, etc.) nuclides (Li et al., 2021). Along with radionuclides, stratigraphic (utilising δ^{18}O of foraminifera as well as magnetostratigraphy), luminescence and electron spin resonance (ESR) dating have also been utilized for the same purpose (Li et al., 2021). In the Indian Ocean, most of the quaternary studies are limited to the last 50 ka, and ^{14}C (longer sediment cores) and ^{210}Pb (short and coastal sediment cores) methods are the most widely used (i.e., Bhushan et al., 2019a, 2001; Chandana et al., 2017; Nambiar et al., 2020; Shah et al., 2020). Only a few limited studies have utilised the stratigraphic and natural radionuclides to date older sediment cores (Beaufort, 1996; Bolton et al., 2013; Gupta et al., 2006; Pattan et al., 2005), suggesting a need for testing various such methods in terms of applicability and limitations. ^{10}Be, with a half-life of $1.387\pm 0.012 \times 10^6$ years (Chmeleff et al., 2010; Korschinek et al., 2010), has proven to be a diagnostic chronological tool for dating events up to ~10-12 Ma, though its applications are limited globally as well as from the Indian Ocean.

As part of this study, a ~6 m long sediment core from the central Indian Ocean was investigated for beryllium isotopic variations. The sediment core was dated using both the ^{10}Be decay method and the ^{10}Be depositional flux method. A detailed investigation was performed regarding the applicability and limitations of both methods.

7.2 Sampling Location

A sediment core (SK-312/08) from a water depth of ~3200 m in the central Indian Ocean (15.982ºS, 65.007ºE) was collected using a gravity corer (**Figure 7.1**) during oceanographic cruise ORV Sagar Kanya SK-312. The length of the sediment core was 5.78 m, which was subsampled at an interval of 1 cm using a non-metallic knife to avoid contamination.

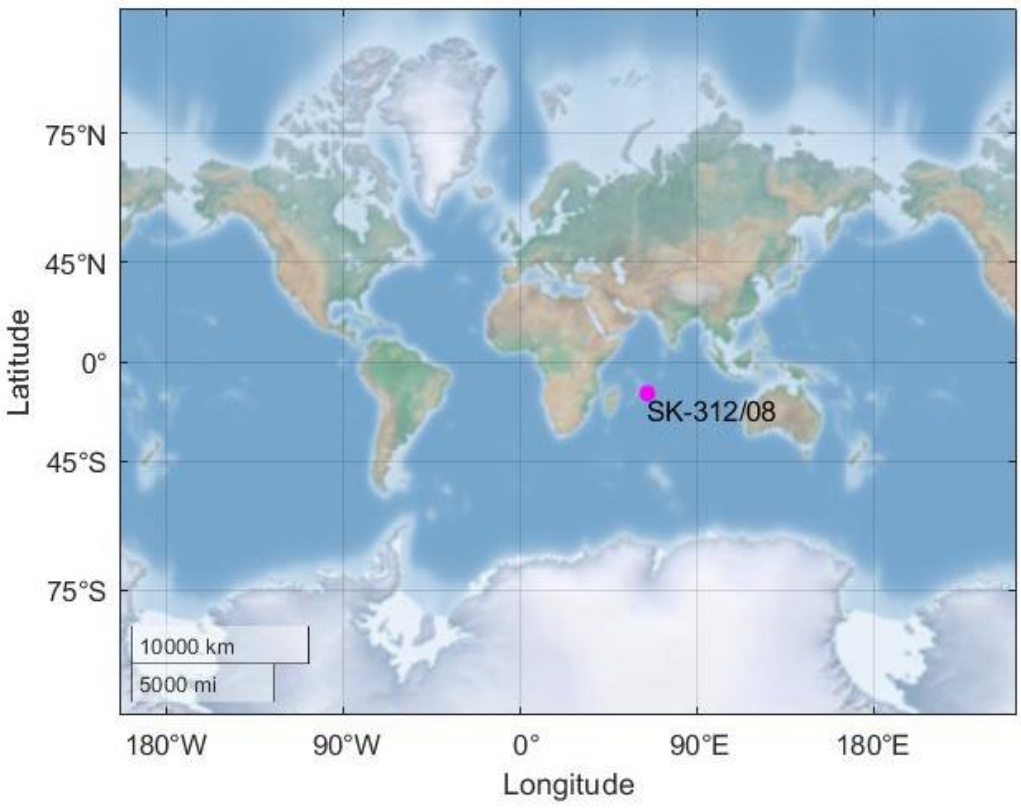

Figure 7.1: *Location of the sediment core SK-312/08.*

7.3 Dating of Marine Sediment Cores Utilising Decay and Depositional Flux of ^{10}Be

In the past, two methods involving meteoric ^{10}Be have been employed for dating the sediment core based on meteoric ^{10}Be. The first method provided by Tanaka et al. (1977) and Tanaka and Inoue (1979) (^{10}Be depositional flux method) requires ^{10}Be inventory in the sediment column. This can be achieved by the measurement of ^{10}Be concentration (N(x)) in various sections covering the whole sediment core. This method also involves an independent estimation of depositional flux (P) for the core location. The formula for age estimation using the ^{10}Be depositional flux method can be stated as

$$T(x) = -\frac{1}{\lambda} ln \left[1 - \frac{\lambda}{P} \int_0^x N(x)dx\right] \quad (7.1)$$

The second method (^{10}Be decay method) involves the measurement of the ^{10}Be/^{9}Be ratio at various depths ((^{10}Be/^{9}Be)$_x$) in a sediment core, including the surface, and is based on the decay of ^{10}Be. The ^{10}Be/^{9}Be ratio for the surface sediments ((^{10}Be/^{9}Be)$_0$) is assumed to be the present-day activity, and the formula for the ^{10}Be decay method can be stated as

$$T(x) = -\frac{1}{\lambda} ln \left[\frac{\left(\frac{^{10}Be}{^{9}Be}\right)_x}{\left(\frac{^{10}Be}{^{9}Be}\right)_0}\right] \quad (7.2)$$

7.4 Be Isotopic Variation in the Sediment Core SK-312/08

Figure 7.2 shows the downcore variation of both beryllium isotopes and the ^{10}Be/^{9}Be ratio. A general decreasing trend is observed for the ^{10}Be/^{9}Be ratio except for two major excursions at ~53 cm and ~300 cm, which can probably be explained by the increase in ^{10}Be production associated with a decrease in the geomagnetic field intensity. Such departure in the ^{10}Be/^{9}Be ratio from the expected decreasing trend inhibits the reconstruction of the decay curve as required for chronology. However, by excluding such data points which experienced sudden excursion in the ^{10}Be/^{9}Be ratio due to variation in

the geomagnetic field intensity, a general decreasing trend in the $^{10}Be/^{9}Be$ ratio is observed throughout the sediment core. This continuous decrease is associated with the decay of ^{10}Be, which can be effectively used to date marine sediment cores.

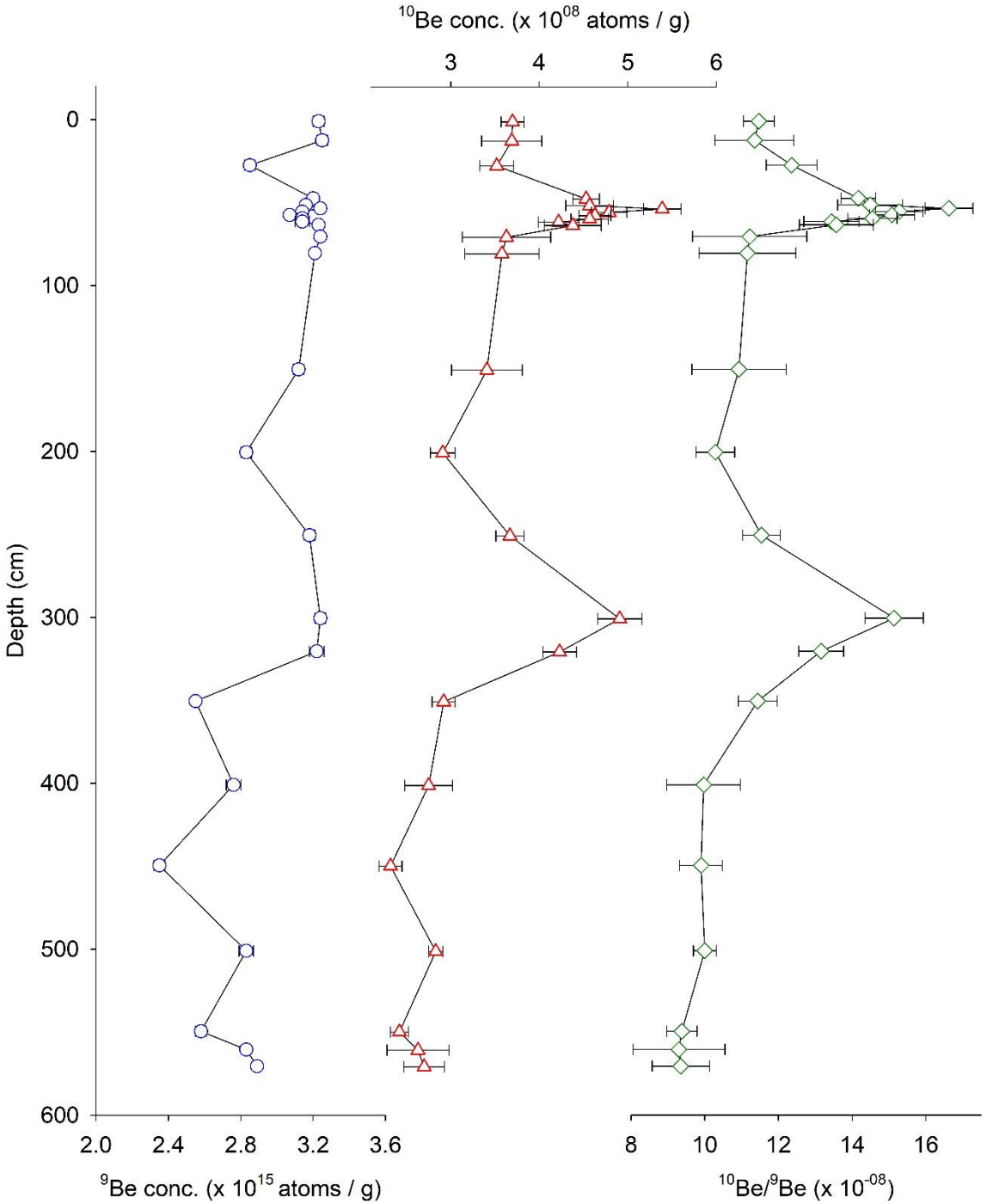

Figure 7.2: *Downcore variation of beryllium isotopes and $^{10}Be/^{9}Be$ ratio in the core SK-312/08.*

7.5 ^{10}Be Based Chronology of Marine Sediment Core

There have been several attempts to utilise meteoric ^{10}Be for building chronology of sediment cores (Bourles et al., 1989; Frank et al., 2008; Tanaka et al., 1977; Tanaka and Inoue, 1979). Tanaka et al. (1977) and Tanaka and Inoue (1979) have developed a formula to calculate the age of sediment core using ^{10}Be concentration measured from the sediment column and ^{10}Be depositional flux (assumed to be constant throughout). The ^{10}Be depositional flux, as required for age calculation, can be estimated from the plot of depth vs. log ^{10}Be concentration, where ^{10}Be concentration decreases with depth as a function of radioactive decay of ^{10}Be with time (Tanaka and Inoue, 1979). The ^{10}Be depositional flux for a specific geographical location can also be estimated based on model calculations (Heikkilä et al., 2013; Heikkilä and von Blanckenburg, 2015). This method has shown a considerably good correlation with obtained ages from the magnetic method (Tanaka and Inoue, 1979). However, there are multiple intricacies associated with this method that need to be addressed before it can be used widely for building chronology. This method requires an independent estimate of depositional flux for the location. The model-based ^{10}Be depositional fluxes provide the atmospheric deposition of ^{10}Be, which could be significantly different from the ^{10}Be deposition in the marine sediment column. At locations near the coastal regions, the ^{10}Be depositional flux in sediment column is higher compared to the atmospheric deposition due to active scavenging, while for open ocean locations, it is the opposite (Anderson et al., 1994, 1990; Lao et al., 1992a). Hence, using the atmospheric ^{10}Be depositional flux estimated from models to calculate deposition ages may not provide accurate results. ^{10}Be concentration (without normalisation with ^{9}Be) could also vary due to the extraction procedure followed (such as weak vs. strong leaching) (Jena et al., 2022a), which too requires a proper normalisation. Additionally, this method requires a ^{10}Be inventory of the sediment column, for which measurement from sediment intervals covering the whole sediment core is required rather than at particular depths.

In another method that involves the decay of ^{10}Be, ^{10}Be concentration is normalised with ^{9}Be, considering the similar behaviour of both isotopes in the ocean water column (Bourles et al., 1989). Thus, normalizing with authigenic ^{9}Be corrects for secondary contributions and differential scavenging (Bourles et al., 1989; Brown et al., 1992b). This

method has also been employed in several studies to date marine cores going back a few million years and has provided satisfactory results (Bourles et al., 1989; Frank et al., 2008). However, there are multiple factors that constrain its use to date marine sediment cores younger than 1 Ma. Since the change associated with the decay of ^{10}Be concentration (hence the ^{10}Be/^{9}Be ratio) is too small for shorter time scales, it leads to high uncertainties in age estimation below 1 Ma. For example, for a sediment core going back in time to 500 ka, the decrease in the ^{10}Be/^{9}Be ratio due to the decay of ^{10}Be is ~22%. At the same time, the errors associated with the ^{10}Be measurement could be ~ 2 to 5%. Additionally, there could be significant changes associated with magnetic field intensity variations, as it results in more than 50 % change in the ^{10}Be/^{9}Be ratio during events of reversal or excursions (Simon et al., 2020, 2016b).

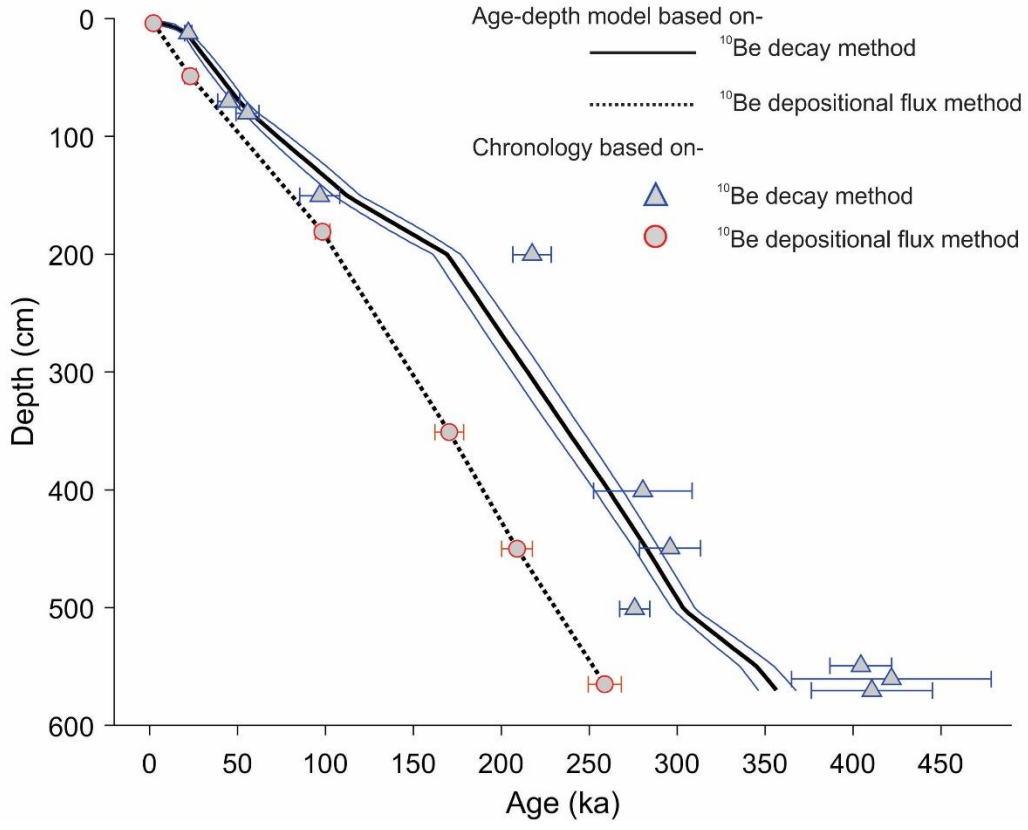

Figure 7.3: *The ages based on the meteoric ^{10}Be dating method. The depositional flux method* (Tanaka et al., 1977; Tanaka and Inoue, 1979) *shows younger ages compared to the ^{10}Be decay methods* (Bourles et al., 1989)

In the present study, the chronology of the sediment core was established using both methods discussed above. Using the method of Tanaka et al. (1977) and Tanaka and Inoue (1979) (^{10}Be depositional flux method), ^{10}Be concentrations throughout the sediment column are required. For the same, the whole sediment column was divided into six sections, and ^{10}Be concentrations were measured in the sections covering the whole sediment core. Based on the ^{10}Be depositional flux method, the core SK-312/08 is dated to be 259 ka at 565 cm with an average sedimentation rate of 2 cm/ka (**Figure 7.3; Table 7.1**).

Table 7.1: *Ages obtained for sediment core SK-312/08 using the ^{10}Be depositional flux method.*

Sample Depth (cm) (SK-312/08)	**Age (ka) , Error 1σ**
4	2.3 ± 0.2
49	22.7 ± 3.2
181	96.1 ± 4.1
351	166.8 ± 8.1
450	206.8 ± 8.6
565	254.9 ± 9.3

The ^{10}Be/^{9}Be ratios were estimated in the sediment core SK-312/08 based on both ^{10}Be and ^{9}Be measurements in the authigenic fraction. For building chronology of the sediment core, the sample points corresponding to those depths having a higher ^{10}Be/^{9}Be ratio compared to the surface value were excluded, which were possibly associated with geomagnetic field intensity changes. Two such events with higher ^{10}Be/^{9}Be ratio were noticed at ~53 cm and ~300 cm, respectively. After excluding the anomalous data points, the decay equation was applied to the remaining data points to obtain the chronology of various depths. The surface ^{10}Be/^{9}Be ratio (11.47 x 10^{-08}) was considered to be the present-day activity ((^{10}Be/^{9}Be)$_0$). Finally, based on a ^{10}Be half-life of 1.387 ± 0.012 Ma, the ages were calculated. Despite the exclusion of the data points with major increases in the ^{10}Be/^{9}Be ratio, there is a possibility of small changes in the ^{10}Be/^{9}Be ratio in the remaining data points caused by paleosecular variation in the geomagnetic field. This can be noticed in the obtained ages, as the ages derived from the decay equation do not strictly follow a

linear relation with depth. However, this issue can be partially resolved with a large number of data points and the use of the bayesian age-depth model based on Bayesian modelling (Blaauw and Christen, 2011). Finally, based on the age-depth plot built using the Bacon programme, the sediment core dates to be ~350 ka at 570 cm (**Figure 7.3; Table 7.2**) with an average sedimentation rate of 1.6 cm/ ka.

Table 7.2: *^{10}Be ages obtained using the ^{10}Be decay method.*

Sample Depth (cm) (SK-312/08)	**Age (ka)[a], Error 1σ**	**Age (ka)[b], Error 1σ**	**Sedimentation rate (cm/ ka)**
12-13	22.0 ± 2.1	20.3 ± 2.1	
70-71	44.9 ± 6.2	51.1 ± 3.9	1.9
80-81	55.7 ± 6.5	57.7 ± 4.2	1.5
150-151	96.8 ± 11.3	112.5 ± 7.7	1.3
200-201	217.5 ± 10.9	169.2 ± 7.8	0.9
400-402	280.5 ± 28.0	261.3 ± 7.9	2.2
449-450	296.0 ± 17.3	282.5 ± 7.1	2.3
500-502	275.9 ± 8.5	303.9 ± 6.6	2.4
549-550	404.5 ± 17.6	344.8 ± 9.8	1.2
560-561	421.9 ± 56.7	351.2 ± 10.3	1.7
570-571	410.7 ± 34.4	356.4 ± 10.7	1.9

[a] *calculated using the decay equation.*
[b] *estimated from the bayesian age-depth model using the ^{10}Be decay ages*

Almost similar sedimentation rates have been obtained with both the dating methods utilising meteoric ^{10}Be. The sedimentation rate estimated based on the ^{10}Be decay method is 1.6 cm/ka, and from the ^{10}Be depositional flux method is 2 cm/ka. This is also comparable to the radiocarbon method (1.8 cm/ka) for the core SK/312-08. However, a significant offset can be observed between the ages obtained from the meteoric ^{10}Be-depositional flux method and the ^{10}Be-decay method (**Figure 7.3**). The ages obtained from the meteoric ^{10}Be-depositional flux method are significantly younger compared to the meteoric ^{10}Be-decay method. The most probable explanation could be the offset associated with incomplete extraction of ^{10}Be due to weak leaching. And this could have resulted in an underestimated ^{10}Be inventory in the sediment column. On the other hand, the choice

of depositional flux for chronology estimation could have led to an offset in obtained ages. As the study location is present in the open ocean location, the ^{10}Be depositional flux in the sediment column is expected to be lower due to reduced scavenging by sediment particles (Anderson et al., 1994, 1990; Jena et al., 2022a; Lao et al., 1992a).

The ages obtained using all three methods (^{10}Be decay, ^{10}Be depositional flux, and radiocarbon) are compared for the top 50 ka (**Figure 7.4**). It is worth noting that dating sediment cores < 50 ka using the decay of the ^{10}Be method is almost not feasible, as changes associated with the decay of ^{10}Be are insignificant. On the contrary, there could be a drastic change in the ^{10}Be/^{9}Be ratio due to past magnetic field changes (Jena et al., 2022a; Simon et al., 2020, 2016b). Hence in **Figure 7.3**, the ^{10}Be decay method plot basically indicates the age-depth plot obtained from Bacon. Interestingly, it is observed that both the radiocarbon and meteoric ^{10}Be dating method show a good correlation. Both the ^{10}Be decay method and ^{10}Be depositional flux method provide similar results in terms of sedimentation rate, which is very much comparable with the radiocarbon method (1.8 cm/ ka). As the sediment core lies in the open Indian Ocean, such lower sedimentation rates are expected. Such lower sedimentation rates have also been reported from sediment cores in nearby regions (Gupta et al., 2006; Jena et al., 2022a). Despite various limitations, the ^{10}Be dating method has provided promising results in dating marine sediment cores.

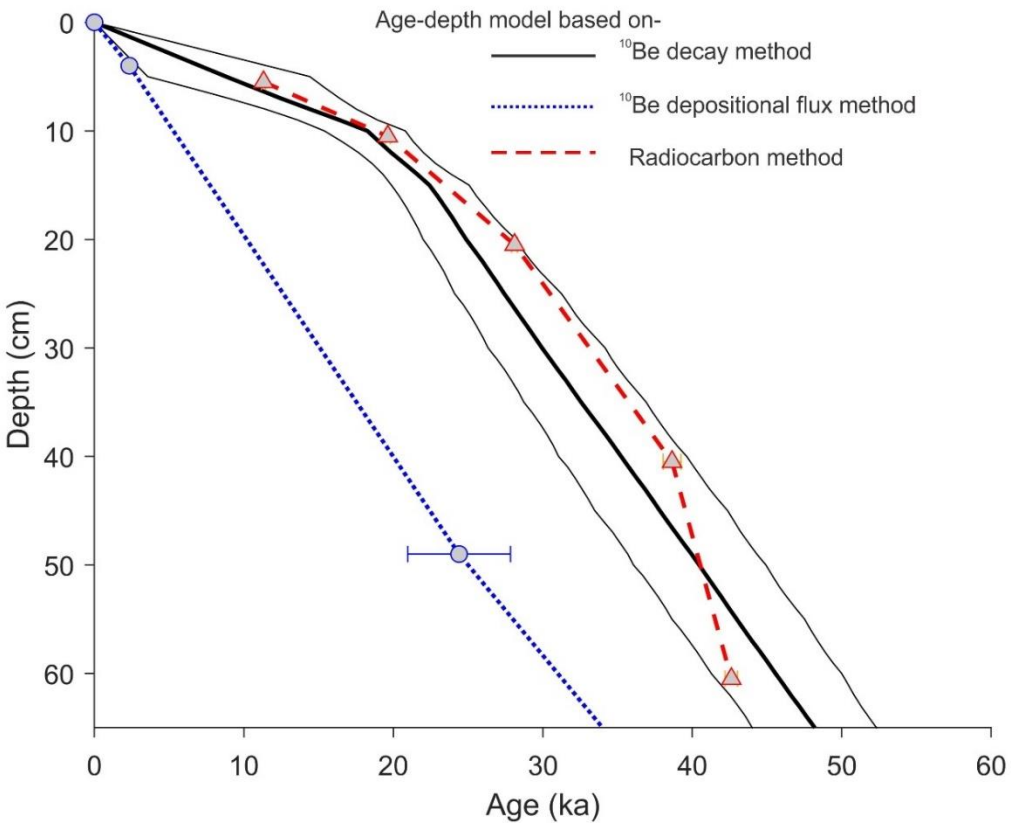

Figure 7.4: *Comparison between ages obtained from meteoric ^{10}Be dating method and radiocarbon method.*

7.6 Inferences

The ^{10}Be/^{9}Be ratio measurement in an open ocean sediment core has been interpreted in terms of changes in the production of ^{10}Be due to magnetic field intensity changes and decay of ^{10}Be. Based on the decay of ^{10}Be decay, the sediment core was dated to be ~350 ka at 570 cm with an average sedimentation rate of 1.6 cm/ka, consistent with the other records from the region. Relatively lower ages obtained using the ^{10}Be depositional flux method could be due to underestimated ^{10}Be inventory due to weak leaching and offset due to the choice of ^{10}Be depositional flux.

Chapter 8 Summary and Future Scope

8.1 Summary

This study is an attempt to understand past climatic and past magnetic changes using both in-situ and meteoric cosmogenic nuclides (^{10}Be). In-situ ^{10}Be was used to reconstruct the chronology of Quaternary glaciation in the northwestern Himalaya to identify drivers of glacial advance and retreat. A paleolake sequence was studied to decipher continuous hydrological changes in northwestern Himalya during the MIS-2. To understand processes controlling Be isotopic distribution in the Indian Ocean, Be isotopes were measured in surface sediments. Based on this investigation, sediment cores from the central Indian Ocean (away from the terrestrial ^{9}Be source) were chosen for temporal Be isotopic reconstruction. Downcore Be isotopic measurements have been carried out to decipher the past geomagnetic field intensity variation for the last 44 ka. The Be isotopic variations during the last 44 ka have been reconstructed to decipher the past geomagnetic field intensity variation. The Laschamp event, known for significant geomagnetic field intensity variation, was identified at 41 ka. The cosmogenic ^{10}Be, with a half-life of 1.36 Ma has the potential to be utilised as a chronometer to date samples upto 10 Ma. This was tested and explored with meteoric ^{10}Be dating from a sediment core. Overall, based on in-situ and meteoric ^{10}Be analysis of terrestrial and marine deposits, this study contributed to the following salient findings:

- Two major events of glaciation were studied in the Nubra Valley when the Siachen Glacier advanced up to the Nubra-Shyok confluence. Cosmogenic nuclide exposure age dating was employed to build the chronology of the glaciation events. The older Tirith-II glacial stage was dated to be MIS-5/ 4. The younger Tirith-I glacial stage was dated to be early/mid MIS-2. The PGA-1 stage in the Ganglas Valley was found to be contemporary with the Tirith-I glacial stage. The glaciation events in the northwestern Himalaya were

primarily driven by temperature reduction, while moisture required for sustaining the glaciers was sourced by the mid-latitude westerlies.

- The relict lake deposit at Spituk, Leh studied to reconstruct late quaternary hydrological changes in the northwestern Himalaya demonstrated that the marginally fluctuating climate (shifting from cold and arid to cold and humid) modulated the proglacial lake sedimentation during the MIS-2. Chronologically the events could be identified at millennial and multimillennial time scales. Three phases of dry phases punctuated by two intervals of wet climate can be discerned during the MIS-2. The oldest cooling event, which led to the advancement in valley glaciers, was identified at ~30 ka. A short-term increase in humidity can be inferred after 30.2 ka and before 29.3 ka, with a reversal towards dry climate between 29.3 ka and 28.1 ka. This was followed by a rhythmic warming and cooling trend (with fluctuations) till before 22 ka. Deposition of varves indicates gradual growth of the valley glaciers during 27.5 ka and 22 ka.

- The authigenic fraction of beryllium isotopes spatially distributed in sediments from the Indian Ocean was studied to constrain the behaviour of beryllium isotopes in the Indian Ocean. Basin-wise heterogeneity was observed in the $^{10}Be/^{9}Be$ ratio in the Indian Ocean, which demonstrated the role of terrestrial sediment input. The Bay of Bengal, with enhanced sediment load input, has a higher ^{9}Be concentration and lower $^{10}Be/^{9}Be$ ratio. The dominance of clay particles, when compared to carbonates, is responsible for the effective scavenging of ^{10}Be and ^{9}Be. In contrast, the central Indian Ocean has a higher $^{10}Be/^{9}Be$ ratio primarily due to no direct terrestrial source.

- One of the salient outcomes of this study was providing estimates of the residence time of beryllium for the central and northern Indian Ocean water column. The residence time of beryllium in the central Indian Ocean is found to be higher compared to the northern Indian Ocean. Large heterogeneity in the residence time of beryllium is due to its varying scavenging efficiency in different regions. In the proximity of coastal regions, active scavenging of beryllium by sediment particles contributed through various rivers draining

into the northern Indian Ocean results in lower residence time of Be. Based on the $^{10}Be/^{9}Be$ ratio in the surface sediments, the residence time as derived ranges between 288-620 years for the central Indian Ocean, 64-205 years for the Bay of Bengal, 41-117 years for the Andaman Sea, and 179-443 years for the Arabian Sea. High residence time in the central Indian Ocean signifies clay particles being more efficient in scavenging beryllium from the water column than carbonates.

- The depositional flux of ^{10}Be and $^{10}Be/^{9}Be$ ratio were estimated up to 44 ka based on combined results from measurements made in three marine sediment cores from the central Indian Ocean (SK-312/08, 09, 10). High-resolution data from the sediment core SK-312/10 shows a higher $^{10}Be/^{9}Be$ ratio during 21 to 26 ka associated with an increase in ^{10}Be production.
- The Laschamp event, known for enhanced ^{10}Be production was identified by a sharp peak in the $^{10}Be/^{9}Be$ ratio observed at 41.2 ka in the sediment core SK-312/09 and at 41.4 ka in SK-312/08. This event experienced ~ 40-60% higher $^{10}Be/^{9}Be$ ratio compared to the present ^{10}Be production.
- To explore the potential of ^{10}Be as tool for chronometer, a sediment core from the central Indian Ocean (SK-312/08) was dated using meteoric ^{10}Be based on the decay of ^{10}Be. The sediment core could be dated to be ~350 ka at 570 cm with an average sedimentation rate of 1.6 cm/ka, consistent with the other records from the region. The dates obtained based on ^{10}Be decay are relatively lower compared to the ^{10}Be depositional flux method. This could be due to the offset associated with the appropriate estimate of ^{10}Be depositional flux and inefficient leaching.

8.2 Future Scope of the Study

The work investigated the potential of cosmogenic nuclide application in Quaternary events. The results show that the cosmogenic ^{10}Be can be efficiently used to reconstruct the paleoclimatic and paleomagnetic events during the Quaternary. This study

provides further impetus to utilise Be isotopes for further understanding of the Quaternary events and their impact on human evolution.

In this study, both glacial and lacustrine records were used to understand the past fluctuations in glacial cover in the northwestern Himalaya. The study has enormous scope to extend the ^{10}Be application in the central Himalaya to attest whether glaciation events in the central Himalaya are concurrent with the northwestern Himalaya. These two regions being significantly different in terms of annual precipitation and moisture source, a variation in timing and extent of Quaternary glaciation is expected. Earlier studies based on OSL dating demonstrate that both regions show contemporary glacial advances during MIS-2. However, the region lacks chronology of pre-MIS-2 landforms due to the absence of suitable OSL datable material. Thus, applications of TCN dating in this region would further help in attesting to the synchronous or asynchronous response of glaciers to Quaternary climate change.

This study explored the spatial distribution of Be isotopes using surface sediments, which is the first such extensive study from the northern Indian Ocean. Yet to date, there are no measurements of beryllium isotopes available in the water column of the Indian Ocean. The Be isotopic profiles from the water column in the Pacific and the Atlantic Ocean show a significant difference, suggesting strong control of local processes. Hence, measurements in the Indian Ocean water column would help constrain the processes that control Be isotopic distribution. Additionally, the measurement of Be isotopes and direct estimation of ^{10}Be inventory for the water column can further constrain Be residence time in the Indian Ocean.

This study has made a maiden attempt to reconstruct Be isotopic record from the Indian Ocean for the last 44 ka. This can be further extended in time to understand changes in ^{10}Be production and hence, fluctuations in geomagnetic field intensity using long sediment cores. The last geomagnetic reversal (~780 ka) experienced a major increase in ^{10}Be production, and another short excursion event was reported at ~190 ka in global records. Thus, the long-term records from the Indian Ocean can be further extended in time to understand geomagnetic field intensity changes during these events.

Appendix A (Exposure Age Data from NW Himalaya)

In general, the $^{10}Be/^{9}Be$ ratio of the samples varied between 2.33 to 62.99 x 10^{-13}. The $^{10}Be/^{9}Be$ ratio of the blanks varied between 0.42 to 1.89 x 10^{-14} and is nearly 10 to 100 times lower compared to the $^{10}Be/^{9}Be$ ratio of the samples. To check the repeatability of the chemical procedure and AMS measurement, one sample (TAR 4) was repeated by varying quartz weight, and amount of carrier added. The analysis showed good reproducibility, with ^{10}Be concentration varying within the associated errors (**Table 1**).

Table A1: *The sample TAR 4 was processed in four different ways with varying amounts of quartz and carrier to check the reproducibility of the procedure.*

Sl. No.	**Weight of quartz (grams)**	**Carrier added (micrograms)**	**$^{10}Be/^{9}Be$ ratio (x 10^{-13}) (obtained from AMS)**	**^{10}Be conc. (x 10^{06} atoms/ gram of quartz)**
1	2.64	290.48 ± 2.29	21.17 ± 1.15	15.59 ± 0.85
2	3.38	482.06 ± 3.81	16.72 ± 0.89	15.95 ± 0.86
3	13.72	495.42 ± 3.91	62.99 ± 2.95	15.22 ± 0.72
4	8.27	501.41 ± 3.96	38.23 ± 1.45	15.51 ± 0.60

Table A2: *Results of ^{10}Be exposure ages and surface conditions of samples collected in the Nubra, Tharoo, and Ganglas Valleys from this study. Exposure ages have been calculated using multiple scaling models i.e. Lal Stone time-independent (St) (Lal, 1991; Stone, 2000), Lal-Stone time dependant (Lm) (Lal, 1991; Nishiizumi et al., 1989; Stone, 2000), Lifton-Sato-Dunai (LSDn) (Lifton et al., 2014). However, the ages are reported using the latest scaling model i.e., Lifton-Sato-Dunai (LSDn) (Lifton et al., 2014).*

SL. No.	Sample name	Lat. (^{0}N)	Long. (^{0}N)	Weight of Quartz (g)	^{10}Be conc. (x 10^6 atoms/ g quartz)	Exposure Age (ka, LSDn)
1	TIR 1A	34.575	77.627	14.53	2.11 ± 0.13	59.8 ± 5.2
2	TIR 1B	34.575	77.627	11.46	2.62 ± 0.13	72.9 ± 5.7
3	TIR 1C	34.575	77.627	9.81	1.82 ± 0.12	49.3 ± 4.4
4	TIR 1D	34.575	77.627	13.48	3.82 ± 0.31	104.8 ± 10.7
5	TIR 2A	34.572	77.626	11.37	1.05 ± 0.06	29.6 ± 2.5
6	TIR 2B	34.572	77.626	18.76	0.99 ± 0.04	29.0 ± 2.1
7	TIR 3A	34.572	77.626	17.62	0.96 ± 0.06	27.2 ± 2.5
8	TIR 4	34.572	77.626	18.54	2.50 ± 0.16	71.8 ± 6.3
9	TIR 4B	34.572	77.626	8.81	0.98 ± 0.07	27.6 ± 2.5
10	TIR 5	34.572	77.626	18.26	2.24 ± 0.12	64.3 ± 5.2
11	TIR 6	34.572	77.626	19.71	1.27 ± 0.10	36.4 ± 3.6
12	PAN 1A	34.726	77.569	13.14	0.78 ± 0.06	22.8 ± 2.2
13	PAN 2B	34.725	77.569	13.98	1.08 ± 0.11	31.6 ± 3.9
14	PAN 3	34.726	77.569	23.97	1.26 ± 0.11	36.1 ± 3.8
15	PAN 4	34.722	77.569	11.83	0.87 ± 0.04	27.6 ± 2.1
16	T1	34.568	77.620	20.21	1.14 ± 0.05	36.0 ± 2.6
17	T2	34.568	77.619	22.77	0.90 ± 0.04	28.7 ± 2.1
18	T3	34.568	77.619	10.33	0.71 ± 0.02	23.0 ± 1.5
19	TBR 1	34.535	77.664	15.24	2.36 ± 0.10	72.5 ± 5.4
20	TBR 2	34.534	77.665	21.13	2.40 ± 0.11	75.4 ± 5.8
21	TBR 3	34.534	77.665	18.22	3.38 ± 0.13	104.4 ± 7.5

22	R2 1A	34.546	77.640	22.75	1.51 ± 0.10	44.7 ± 4.0
23	R2 1C	34.546	77.640	22.56	1.50 ± 0.13	43.8 ± 4.7
24	R2 2	34.546	77.640	21.95	1.98 ± 0.09	61.7 ± 4.7
25	R2 3	34.548	77.641	14.66	2.00 ± 0.09	62.3 ± 4.8
26	R1 1	34.549	77.653	18.58	2.44 ± 0.10	72.0 ± 5.3
27	R1 2	34.541	77.654	17.70	3.00 ± 0.10	86.8 ± 6.0
28	R1 3	34.541	77.654	14.77	2.66 ± 0.11	76.7 ± 5.7
29	R1 4	34.549	77.654	15.80	2.15 ± 0.09	62.1 ± 4.5
30	GGL 1	34.229	77.627	20.15	1.54 ± 0.07	28.5 ± 2.1
31	GGL 2	34.229	77.627	24.80	1.79 ± 0.05	30.9 ± 2.0
32	GGL 3	34.219	77.614	16.66	4.32 ± 0.19	72.0 ± 5.4
33	GGL 4	34.203	77.643	11.37	5.06 ± 0.23	99.0 ± 7.5
34	GGL 5	34.194	77.604	9.46	0.82 ± 0.03	18.1 ± 1.2
35	GGL 6	34.189	77.598	20.25	2.50 ± 0.11	54.3 ± 4.0
36	TAR-1A	34.210	77.434	11.27	10.34 ± 0.57	217.3 ± 18.6
37	TAR-1B	34.210	77.434	14.31	7.36 ± 0.33	153.4 ± 11.9
38	TAR-2A	34.212	77.434	16.87	2.76 ± 0.18	60.2 ± 5.3
39	TAR-2B	34.212	77.434	15.98	8.69 ± 0.34	181.0 ± 13.4
40	TAR-3	34.210	77.434	10.10	8.04 ± 0.41	169.0 ± 13.8
41	TAR-4	34.205	77.420			327.4 ± 27.0

The ages are calculated by taking a density of 2.65 g.cm^{-3} and assuming a zero erosion rate.

Appendix B (Data from the Spituk Paleolake Sequence)

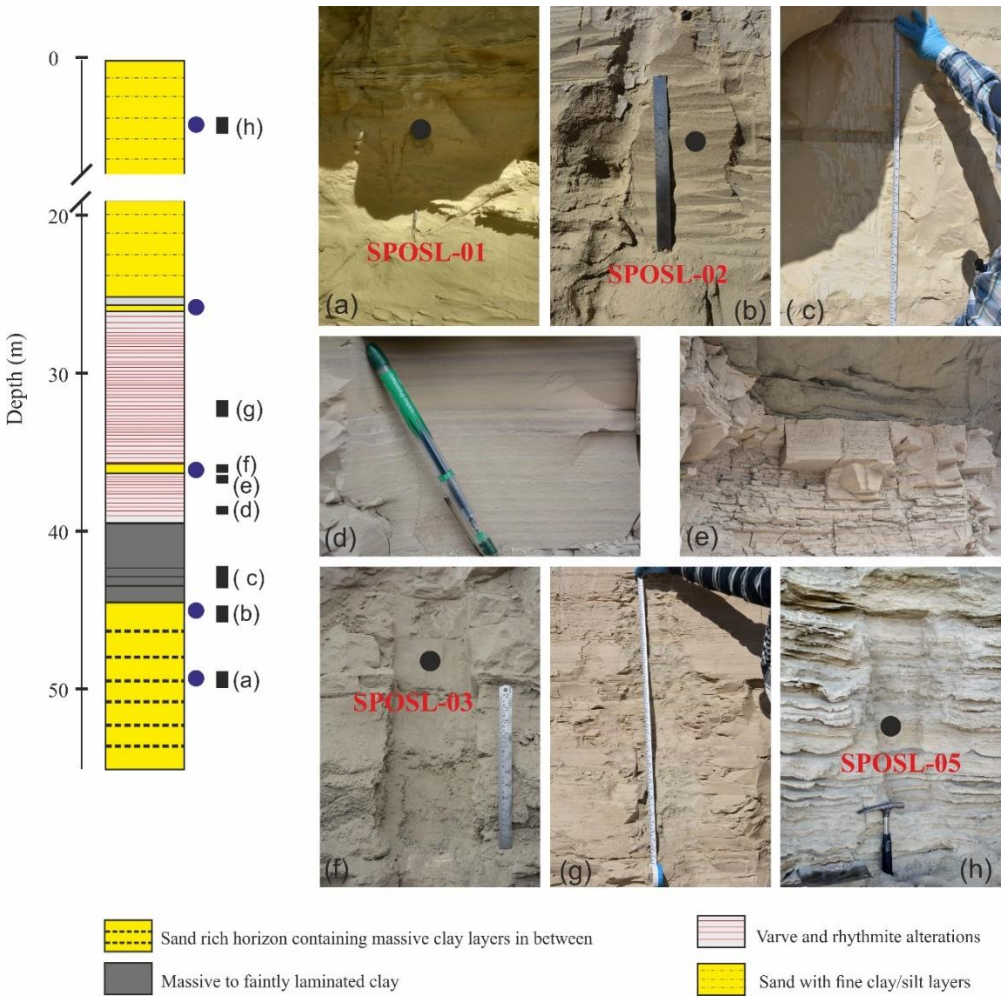

Figure B1: *Field photographs of the Spituk paleolake deposit are shown against their position (black rectangles) in the lithostratigraphy. Samples collected for luminescence dating are shown as filled circles, and the respective sample names are shown in red.*

Table B1: *Results of radiocarbon dating of bulk organic matter.*

Sample Code	Depth (m)	Lab ID	Radiocarbon age (± 1σ yrs BP)	Calibrated Age Range (cal yrs BP)	Median Age (cal yrs BP)
SPL H 1940-1960	25.50	AURIS-01750	14654 ± 83	17860-18131	17969
SPL H 1745-1760	27.47	AURIS-01115	16132 ± 130	19249-19591	19457
SPL H 1655-1670	28.37	AURIS-01114	22096 ± 142	26046-26431	26297
SPL G 1455-1470	30.37	AURIS-01770	21595 ± 97	25818-25950	25884
SPL G 1350-1365	31.42	AURIS-01112	22808 ± 139	27055-27278	27155
SPL F 1255-1270	32.37	AURIS-01747	22247 ± 85	26361-26854	26621
SPL F 1135-1150	33.57	AURIS-01109	22583 ± 136	26510-27167	26922
SPL D 850-862	36.44	AURIS-01108	19195 ± 160	22950-23652	23158
SPL D 745-760	37.47	AURIS-01744	18861 ± 117	22628-22934	22759
SPL A 640-655	38.52	AURIS-01769	21552 ± 94	25794-25927	25860
SPL B 450-460	40.45	AURIS-01102	19216 ± 133	22975-23300	23163
SPL B 340-360	41.50	AURIS-01101	17426 ± 126	20869-21231	21053
SPL A 160-167	43.36	AURIS-01741	14745 ± 64	17996-18187	18075

Table B2*: Results of radiocarbon dating of inorganic carbon.*

Sample Code	Depth (m)	Lab ID	Radiocarbon age (± 1σ yrs BP)	Calibrated Age Range (cal yrs BP)	Median Age (Cal yrs BP)
SPL H 1940-1960	25.50	AURIS-01727	30408	34570 – 35065	34810
SPL H 1880-1895	26.13	AURIS-03193	31929	36131 – 36387	36265
SPL H 1865-1880	26.28	AURIS-03192	31565	35700 – 36157	35911
SPL H 1835-1850	26.58	AURIS-03191	31806	36053 – 36303	36170
SPL H 1745-1760	27.48	AURIS-01725	27281	31143 – 31334	31256
SPL H 1700-1715	27.93	AURIS-03190	27893	31668 – 31917	31797
SPL G 1485-1505	30.05	AURIS-03189	34096	39164 – 39450	39305

SPL G 1455-1470	30.38	AURIS-01723	35689	40674 – 41030	40846
SPL G 1350-1365	31.43	AURIS-01722	37280	41894 – 42123	42000
SPL F 1255-1270	32.38	AURIS-01721	36285	41069 – 41529	41311
SPL F 1135-1150	33.58	AURIS-01720	37367	41880 – 42194	42018
SPL D 850-862	36.44	AURIS-01719	36343	41147 – 41519	41350
SPL D 745-760	37.48	AURIS-01718	38575	42348 - 42576	42468
SPL D 640-655	38.53	AURIS-01717	41797	44403 – 44789	44602
SPL C 540-560	39.50	AURIS-01716	40209	42960 – 43849	43410
SPL C 480-500	40.10	AURIS-03209	39159	42581 – 42794	42690
SPL B 340-360	41.50	AURIS-01714	45195	46948 – 47968	47480
SPL A 213-218	42.85	AURIS-01712	47290	48717 – 50585	49832
SPL A 160-167	43.37	AURIS-01711	46560	48198 – 49760	48977
SPL A 60-70	44.35	AURIS-01710	48152	49530 – 52336	51095

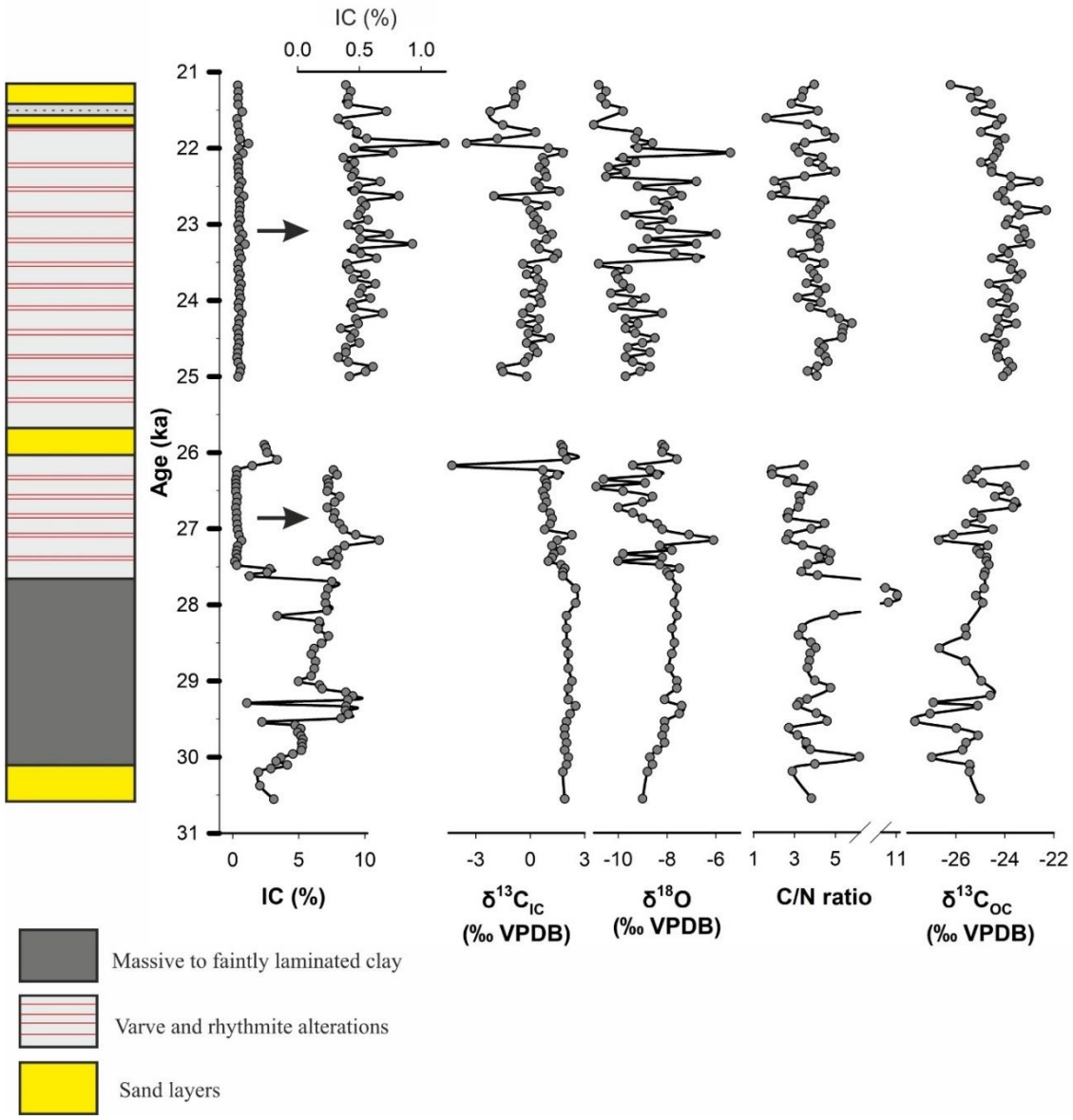

Figure B3: *Temporal variation of inorganic carbon %, $\delta^{13}C$ and $\delta^{18}O$ of carbonate fraction, organic carbon / total nitrogen ratio, and $\delta^{13}C$ of organic matter in the Spituk paleolake deposit.*

Appendix C (Radiocarbon Dates of Sediment Cores SK-312/08, 09, 10)

Table C1: *Radiocarbon age and calibrated age range obtained for the core SK-312/10.*

Sl. No	Radiocarbon Age (yr BP), Error 1σ	Calibrated Age Range (1σ, cal yr BP)	Median Age (cal yr BP)
1	6541 ± 83	6737 - 7041	6893
2	8462 ± 73	8770 - 9110	8943
3	10554 ± 57	11572 - 11934	11749
4	11793 ± 79	13059 - 13312	13181
5	15328 ± 71	17660 - 18020	17828
6	16032 ± 69	18424 - 18747	18585
7	19864 ± 82	22892 - 23201	23049
8	23459 ± 97	26805 - 27128	26944

Table C2.*: AMS Radiocarbon age and calibrated age range for the core SK-312/09.*

Sl. No	Sample Depth (cm) (SK-312/09)	Lab ID	Radiocarbon Age (yr BP), Error 1σ	Calibrated Age Range (1σ yr BP)
1	0-2	AURIS-01165	3382±106	2972-3322
2	10-11	AURIS-01164	6545±105	6730-7066
3	20-21	AURIS-01163	11183±107	12466-12734
4	36-37	AURIS-01162	18812±109	21770-22140
5	50-51	AURIS-01161	24195±147	27388-27723
6	92-94	AURIS-01160	40703±239	42781-43164

Table C3: *Radiocarbon age and calibrated age range obtained for the core SK-312/08.*

Sl. No	**Sample Depth (cm) (SK-312/08)**	**Lab ID**	**Radiocarbon Age (yr BP), Error 1σ**	**Calibrated Age Range (1σ yr BP)**
1	5-6	AURIS-00243	10257 ± 40	11172-11448
2	10-11	AURIS-00242	16939 ± 86	19452-19810
3	20-21	AURIS-00241	24743 ± 69	27913-28283
4	40-41	AURIS-00240	34488 ± 473	38108-39289
5	60-61	AURIS-00239	39880 ± 745	42153-42992

Appendix D (Be Isotopic Data from the Sediment Core SK-312/09)

Table D1: *$^{10}Be/^{9}Be$, ^{10}Be concentration, DBD, and sedimentation rate for the core SK-312/09.*

[a]The values are corrected for decay.

[b] The density was calculated based on the formula provided by (Clemens et al., 1987) for samples free from ice-rafted debris.

$$DBD = 6.530 \times 10^{-5} \times (\%CaCO_3)^2 + 1.112 \times 10^{-5} \times (\%CaCO_3) + 0.410$$

Sl. No.	Sediment Depth (cm)	Age (ka)	Carrier Added (µg)	LAB ID	$^{10}Be/^{9}Be$ (10^{-11}) (From AMS)	^{10}Be atoms /gram of sediment ± 1σ (10^{8}) [a]	Dry Bulk Density (g/cm^3)[b]	Sedimentation Rate (cm/ka)
1	SK-312/09 0-2	3.5-present	290.28 ± 2.29	AURIS-02901	1.64 ± 0.08	3.77 ± 0.19	0.91 ± 0.05	2.6 ± 0.20
2	SK-312/09 2-11	7.1-3.5	290.57 ± 2.29	AURIS-03021	1.58 ± 0.07	3.82 ± 0.16	0.92 ± 0.05	2.5 ± 0.16
3	SK-312/09 11-21	12.8-7.1	290.28 ± 2.29	AURIS-03022	1.59 ± 0.06	4.06 ± 0.15	0.93 ± 0.05	1.8 ± 0.07
4	SK-312/09 21-37	22.2-12.8	292.44 ± 2.31	AURIS-03023	1.51 ± 0.07	3.94 ± 0.19	0.95 ± 0.05	1.8 ± 0.04
5	SK-312/09 37-51	27.7-22.2	296.37 ± 2.34	AURIS-03024	1.44 ± 0.06	3.88 ± 0.16	0.95 ± 0.05	2.5 ± 0.11
6	SK-312/09 51-94	43.4-27.7	294.80 ± 2.33	AURIS-03025	1.54 ± 0.06	4.20 ± 0.17	0.95 ± 0.05	2.8 ± 0.05
	High-resolution samples							
7	SK-312/09 84-85	40.2	294.80 ± 2.33	AURIS-03814	1.57 ± 0.08	4.65 ± 0.25	0.95 ± 0.05	2.8 ± 0.05
8	SK-312/09 85-86	40.5	295.68 ± 2.33	AURIS-03815	1.64 ± 0.04	4.89 ± 0.15	0.95 ± 0.05	2.8 ± 0.05
9	SK-312/09 86-87	40.8	298.63 ± 2.36	AURIS-03809	1.56 ± 0.04	4.75 ± 0.17	0.95 ± 0.05	2.8 ± 0.05
10	SK-312/09 87-88	41.2	298.63 ± 2.36	AURIS-03046	1.91 ± 0.06	5.29 ± 0.20	0.95 ± 0.05	2.8 ± 0.05
11	SK-312/09 88-89	41.5	297.15 ± 2.35	AURIS-03808	1.75 ± 0.07	5.10 ± 0.22	0.95 ± 0.05	2.8 ± 0.05
12	SK-312/09 89-90	41.9	297.06 ± 2.35	AURIS-03817	1.67 ± 0.06	4.95 ± 0.21	0.95 ± 0.05	2.8 ± 0.05
13	SK-312/09 90-91	42.2	297.45 ± 2.35	AURIS-03816	1.68 ± 0.04	4.63 ± 0.15	0.95 ± 0.05	2.8 ± 0.05
14	SK-312/09 91-92	42.5	297.64 ± 2.35	AURIS-03818	1.52 ± 0.06	4.41 ± 0.21	0.95 ± 0.05	2.8 ± 0.05
15	SK-312/09 92-94	43.0	299.12 ± 2.36	AURIS-03810	1.34 ± 0.05	4.20 ± 0.18	0.95 ± 0.05	2.8 ± 0.05
	Samples leached with HCl							
16	SK-312/09 0-2		295.64 ± 2.33	AURIS-03868	2.10 ± 0.06	5.47 ± 0.16	0.91 ± 0.05	2.6 ± 0.20
17	SK-312/09 2-11		291.03 ± 2.30	AURIS-03869	2.20 ± 0.08	5.53 ± 0.22	0.92 ± 0.05	2.5 ± 0.16
18	SK-312/09 11-21		297.06 ± 2.35	AURIS-03870	2.18 ± 0.06	5.79 ± 0.16	0.93 ± 0.05	1.8 ± 0.07

Appendix E (Be Isotopic Data from the Sediment Core SK-312/08)

Table E1: *Beryllium isotopic ratio measured in the core SK-312/08 with AMS. (The values are not corrected for decay)*

Sl. No	Sample Depth (cm) (SK-312/08)	Lab ID	^{10}Be concentration (x 10^8 atoms/g), Error 1σ	^{9}Be concentration (x 10^{15} atoms/ g), Error 1σ	^{10}Be/^{9}Be ± 1σ (10^{-8}), Error 1σ
1	0-2	AURIS-03761	3.70 ± 0.13	3.23 ± 0.03	11.47 ± 0.42
2	12-13	AURIS-02973	3.69 ± 0.34	3.25 ± 0.03	11.35 ± 1.07
3	27-28	AURIS-03762	3.52 ± 0.19	2.85 ± 0.03	12.36 ± 0.69
4	47-48	AURIS-03772	4.53 ± 0.15	3.20 ± 0.01	14.17 ± 0.47
5	51-52	AURIS-03773	4.57 ± 0.27	3.16 ± 0.02	14.49 ± 0.88
6	53-54	AURIS-02976	5.39 ± 0.21	3.24 ± 0.02	16.63 ± 0.65
7	55-56	AURIS-02977	4.79 ± 0.20	3.14 ± 0.02	15.28 ± 0.64
8	57-58	AURIS-03767	4.63 ± 0.18	3.07 ± 0.02	15.08 ± 0.61
9	59-60	AURIS-03766	4.57 ± 0.21	3.14 ± 0.03	14.55 ± 0.67
10	61-62	AURIS-03763	4.22 ± 0.23	3.14 ± 0.04	13.44 ± 0.75
11	63-64	AURIS-03765	4.38 ± 0.32	3.23 ± 0.02	13.57 ± 1.00
12	70-71	AURIS-02978	3.63 ± 0.50	3.24 ± 0.02	11.22 ± 1.55
13	80-81	AURIS-02979	3.58 ± 0.42	3.21 ± 0.01	11.16 ± 1.31
14	150-151	AURIS-02984	3.41 ± 0.40	3.12 ± 0.03	10.93 ± 1.28
15	200-201	AURIS-03769	2.91 ± 0.14	2.83 ± 0.03	10.29 ± 0.52
16	250-251	AURIS-03771	3.67 ± 0.16	3.18 ± 0.03	11.54 ± 0.51
17	300-301	AURIS-02980	4.91 ± 0.25	3.24 ± 0.03	15.14 ± 0.79
18	320-321	AURIS-03768	4.23 ± 0.19	3.22 ± 0.04	13.16 ± 0.61
19	350-351	AURIS-03775	2.92 ± 0.13	2.55 ± 0.02	11.44 ± 0.53
20	400-402	AURIS-02986	2.75 ± 0.27	2.76 ± 0.04	9.97 ± 1.00
21	449-450	AURIS-02988	2.32 ± 0.13	2.35 ± 0.03	9.90 ± 0.58
22	500-502	AURIS-02989	2.83 ± 0.08	2.83 ± 0.04	10.00 ± 0.31
23	549-550	AURIS-03770	2.42 ± 0.10	2.58 ± 0.03	9.38 ± 0.41
24	560-561	AURIS-02982	2.63 ± 0.35	2.83 ± 0.02	9.30 ± 1.25
25	570-571	AURIS-02971	2.70 ± 0.23	2.89 ± 0.02	9.35 ± 0.78

Bibliography

Abramowski, U., Bergau, A., Seebach, D., Zech, R., Glaser, B., Sosin, P., Kubik, P.W., Zech, W., 2006. Pleistocene glaciations of Central Asia: results from ^{10}Be surface exposure ages of erratic boulders from the Pamir (Tajikistan), and the Alay-Turkestan range (Kyrgyzstan). Quat. Sci. Rev. 25, 1080–1096. https://doi.org/10.1016/J.QUASCIREV.2005.10.003

Ahmad, T., Islam, R., Khanna, P.P., Thakur, V.C., 1996. Geochemistry, petrogenesis and tectonic significance of the basic volcanic units of the zildat ophiolitic mélange, indus suture zone, eastern ladakh (india). Geodin. Acta 9, 222–233. https://doi.org/10.1080/09853111.1996.11105287

Ahmad, T., Tanaka, T., Sachan, H.K., Asahara, Y., Islam, R., Khanna, P.P., 2008. Geochemical and isotopic constraints on the age and origin of the Nidar Ophiolitic Complex, Ladakh, India: Implications for the Neo-Tethyan subduction along the Indus suture zone. Tectonophysics 451, 206–224. https://doi.org/10.1016/j.tecto.2007.11.049

Aitken, M.J., 1998. Introduction to optical dating: the dating of Quaternary sediments by the use of photon-stimulated luminescence. Clarendon Press.

Ali, S.N., Biswas, R.H., Shukla, A.D., Juyal, N., 2013. Chronology and climatic implications of Late Quaternary glaciations in the Goriganga valley, central Himalaya, India. Quat. Sci. Rev. 73, 59–76. https://doi.org/10.1016/j.quascirev.2013.05.016

Ali, S.N., Singh, P., Arora, P., Bisht, P., Morthekai, P., 2022. Luminescence dating of late pleistocene glacial and glacio-fluvial sediments in the Central Himalaya, India. Quat. Sci. Rev. 284, 107464. https://doi.org/10.1016/J.QUASCIREV.2022.107464

Anderson, R.F., Fleisher, M.Q., Biscaye, P.E., Kumar, N., Dittrich, B., Kubik, P., Suter, M., 1994. Anomalous boundary scavenging in the Middle Atlantic Bight: evidence from ^{230}Th, ^{231}Pa, ^{10}Be and ^{210}Pb. Deep Sea Res. Part II Top. Stud. Oceanogr. 41, 537–561. https://doi.org/10.1016/0967-0645(94)90034-5

Anderson, R.F., Lao, Y., Broecker, W.S., Trumbore, S.E., Hofmann, H.J., Wolfli, W., 1990. Boundary scavenging in the Pacific Ocean: a comparison of ^{10}Be and ^{231}Pa. Earth Planet. Sci. Lett. 96, 287–304. https://doi.org/10.1016/0012-821X(90)90008-L

Appenzeller, C., Holton, J.R., Rosenlof, K.H., 1996. Seasonal variation of mass transport across the tropopause. J. Geophys. Res. Atmos. 101, 15071–15078. https://doi.org/10.1029/96JD00821

Applegate, P.J., Urban, N.M., Keller, K., Lowell, T. V., Laabs, B.J.C., Kelly, M.A., Alley, R.B., 2012. Improved moraine age interpretations through explicit matching of geomorphic process models to cosmogenic nuclide measurements from single landforms. Quat. Res. 77, 293–304. https://doi.org/10.1016/J.YQRES.2011.12.002

Ariztegui, D., Bianchi, M.M., Masaferro, J., Lafargue, E., Niessen, F., 1997. Interhemispheric synchrony of Late-glacial climatic instability as recorded in proglacial Lake Mascardi, Argentina. J. Quat. Sci. 12, 333–338. https://doi.org/10.1002/(sici)1099-1417(199707/08)12:4<333::aid-jqs312>3.0.co;2-0

Bailey, R.M., Arnold, L.J., 2006. Statistical modelling of single grain quartz De distributions and an assessment of procedures for estimating burial dose. Quat. Sci. Rev. 25, 2475–2502. https://doi.org/10.1016/j.quascirev.2005.09.012

Balco, G., 2011. Contributions and unrealized potential contributions of cosmogenic-nuclide exposure dating to glacier chronology, 1990-2010. Quat. Sci. Rev. 30, 3–27. https://doi.org/10.1016/J.QUASCIREV.2010.11.003

Balco, G., Briner, J., Finkel, R.C., Rayburn, J.A., Ridge, J.C., Schaefer, J.M., 2009. Regional beryllium-10 production rate calibration for late-glacial northeastern North

America. Quat. Geochronol. 4, 93–107. https://doi.org/10.1016/J.QUAGEO.2008.09.001

Balco, G., Stone, J.O., Lifton, N.A., Dunai, T.J., 2008. A complete and easily accessible means of calculating surface exposure ages or erosion rates from ^{10}Be and ^{26}Al measurements. Quat. Geochronol. 3, 174–195. https://doi.org/10.1016/j.quageo.2007.12.001

Bali, R., Nawaz Ali, S., Agarwal, K.K., Rastogi, S.K., Krishna, K., Srivastava, P., 2013. Chronology of late Quaternary glaciation in the Pindar valley, Alaknanda basin, Central Himalaya (India). J. Asian Earth Sci. 66, 224–233. https://doi.org/10.1016/j.jseaes.2013.01.011

Barnett, T.P., Adam, J.C., Lettenmaier, D.P., 2005. Potential impacts of a warming climate on water availability in snow-dominated regions. Nat. 2005 4387066 438, 303–309. https://doi.org/10.1038/nature04141

Baroni, M., Bard, E., Petit, J.R., Magand, O., Bourlès, D., 2011. Volcanic and solar activity, and atmospheric circulation influences on cosmogenic ^{10}Be fallout at Vostok and Concordia (Antarctica) over the last 60 years. Geochim. Cosmochim. Acta 75, 7132–7145. https://doi.org/10.1016/j.gca.2011.09.002

Battarbee, R.W., Cameron, N.G., Golding, P., Brooks, S.J., Switsur, R., Harkness, D., Appleby, P., Oldfield, F., Thompson, R., Monteith, D.T., McGovern, A., 2001. Evidence for Holocene climate variability from the sediments of a Scottish remote mountain lake. J. Quat. Sci. 16, 339–346. https://doi.org/10.1002/JQS.597

Beaufort, L., 1996. Dynamics of the monsoon in the equatorial Indian Ocean over the last 260,000 years. Quat. Int. 31, 13–18. https://doi.org/10.1016/1040-6182(95)00017-D

Beghin, P., Charbit, S., Kageyama, M., Combourieu-Nebout, N., Hatté, C., Dumas, C., Peterschmitt, J.Y., 2016. What drives LGM precipitation over the western Mediterranean? A study focused on the Iberian Peninsula and northern Morocco.

Clim. Dyn. 46, 2611–2631. https://doi.org/10.1007/s00382-015-2720-0

Benn, D.I., Owen, L.A., 2002. Himalayan glacial sedimentary environments: A framework for reconstructing and dating the former extent of glaciers in high mountains. Quat. Int. 97–98, 3–25. https://doi.org/10.1016/S1040-6182(02)00048-4

Benn, D.I., Owen, L.A., 1998. The role of the Indian summer monsoon and the mid-latitude westerlies in Himalayan glaciation: review and speculative discussion. J. Geol. Soc. London. 155, 353–363. https://doi.org/10.1144/gsjgs.155.2.0353

Benson, L., Madole, R., Landis, G., Gosse, J., 2005. New data for Late Pleistocene Pinedale alpine glaciation from southwestern Colorado. Quat. Sci. Rev. 24, 49–65. https://doi.org/10.1016/J.QUASCIREV.2004.07.018

Berger, A., Loutre, M.F., 1991. Insolation values for the climate of the last 10 million years. Quat. Sci. Rev. 10, 297–317. https://doi.org/10.1016/0277-3791(91)90033-Q

Beukema, S.P., Krishnamurthy, R. V., Juyal, N., Basavaiah, N., Singhvi, A.K., 2011. Monsoon variability and chemical weathering during the late Pleistocene in the Goriganga basin, higher central Himalaya, India. Quat. Res. 75, 597–604. https://doi.org/10.1016/j.yqres.2010.12.016

Bhattacharyya, A., 1989. Vegetation and climate during the last 30,000 years in Ladakh. Palaeogeogr. Palaeoclimatol. Palaeoecol. 73, 25–38. https://doi.org/10.1016/0031-0182(89)90042-4

Bhushan, R., Dutta, K., Somayajulu, B.L.K., 2001. Concentrations and burial fluxes of organic and inorganic carbon on the eastern margins of the Arabian Sea. Mar. Geol. 178, 95–113. https://doi.org/10.1016/S0025-3227(01)00179-7

Bhushan, R., Sati, S.P., Rana, N., Shukla, A.D., Mazumdar, A.S., Juyal, N., 2018. High-resolution millennial and centennial scale Holocene monsoon variability in the Higher Central Himalayas. Palaeogeogr. Palaeoclimatol. Palaeoecol. 489, 95–104.

https://doi.org/10.1016/j.palaeo.2017.09.032

Bhushan, R., Yadava, M.G., Shah, M.S., Banerji, U.S., Raj, H., Shah, C., Dabhi, A.J., 2019a. First results from the PRL Accelerator Mass Spectrometer. Curr. Sci. 116, 361–363.

Bhushan, R., Yadava, M.G., Shah, M.S., Raj, H., 2019b. Performance of a new 1MV AMS facility (AURiS) at PRL, Ahmedabad, India. Nucl. Instruments Methods Phys. Res. Sect. B Beam Interact. with Mater. Atoms 439, 76–79. https://doi.org/10.1016/j.nimb.2018.12.003

Bhutiyani, M.R., Kale, V.S., Pawar, N.J., 2010. Climate change and the precipitation variations in the northwestern Himalaya: 1866-2006. Int. J. Climatol. 30, 535–548. https://doi.org/10.1002/joc.1920

Bierman, P.R., Marsella, K.A., Patterson, C., Davis, P.T., Caffee, M., 1999. Mid-Pleistocene cosmogenic minimum-age limits for pre-Wisconsinan glacial surfaces in southwestern Minnesota and southern Baffin Island: a multiple nuclide approach. Geomorphology 27, 25–39. https://doi.org/10.1016/S0169-555X(98)00088-9

Bisht, P., Ali, S.N., Shukla, A.D., Negi, S., Sundriyal, Y.P., Yadava, M.G., Juyal, N., 2015. Chronology of late Quaternary glaciation and landform evolution in the upper Dhauliganga valley, (Trans Himalaya), Uttarakhand, India. Quat. Sci. Rev. 129, 147–162. https://doi.org/10.1016/j.quascirev.2015.10.017

Bisht, P., Nawaz Ali, S., Rana, N., Singh, S., Poonam, Sundriyal, Y.P., Bagri, D.S., Juyal, N., 2017. Pattern of Holocene glaciation in the monsoon-dominated Kosa Valley, central Himalaya, Uttarakhand, India. Geomorphology 284, 130–141. https://doi.org/10.1016/J.GEOMORPH.2016.11.023

Blaauw, M., Christen, J.A., 2011. Flexible paleoclimate age-depth models using an autoregressive gamma process. Bayesian Anal. 6, 457–474. https://doi.org/10.1214/11-BA618

Blackwell, B.A.B., Skinner, A.R., Blickstein, J.I.B., Montoya, A.C., Florentin, J.A., Baboumian, S.M., Ahmed, I.J., Deely, A.E., 2016. ESR in the 21st century: From buried valleys and deserts to the deep ocean and tectonic uplift. Earth-Science Rev. 158, 125–159. https://doi.org/10.1016/J.EARSCIREV.2016.01.001

Blöthe, J.H., Munack, H., Korup, O., Fülling, A., Garzanti, E., Resentini, A., Kubik, P.W., 2014. Late Quaternary valley infill and dissection in the Indus River, western Tibetan Plateau margin. Quat. Sci. Rev. 94, 102–119. https://doi.org/10.1016/J.QUASCIREV.2014.04.011

Boaretto, E., Bryant, C., Carmi, I., Cook, G., Gulliksen, S., Harkness, D., Heinemeier, J., McClure, J., McGee, E., Naysmith, P., Possnert, G., Scott, M., Van Der Plicht, H., Van Strydonck, M., 2002. Summary findings of the fourth international radiocarbon intercomparison (FIRI)(1998–2001). J. Quat. Sci. 17, 633–637. https://doi.org/10.1002/JQS.702

Bolch, T., Kulkarni, A., Kääb, A., Huggel, C., Paul, F., Cogley, J.G., Frey, H., Kargel, J.S., Fujita, K., Scheel, M., Bajracharya, S., Stoffel, M., 2012. The state and fate of himalayan glaciers. Science. 336, 310–314. https://doi.org/10.1126/science.1215828

Bolton, C.T., Chang, L., Clemens, S.C., Kodama, K., Ikehara, M., Medina-Elizalde, M., Paterson, G.A., Roberts, A.P., Rohling, E.J., Yamamoto, Y., Zhao, X., 2013. A 500,000 year record of Indian summer monsoon dynamics recorded by eastern equatorial Indian Ocean upper water-column structure. Quat. Sci. Rev. 77, 167–180. https://doi.org/10.1016/J.QUASCIREV.2013.07.031

Bourles, D., Raisbeck, G.M., Yiou, F., 1989. ^{10}Be and ^{9}Be in marine sediments and their potential for dating. Geochim. Cosmochim. Acta 53, 443–452. https://doi.org/10.1016/0016-7037(89)90395-5

Bourlès, D.L., Brown, E.T., German, C.R., Measures, C.I., Edmond, J.M., Raisbeck, G.M., Yiou, F., 1994. Examination of hydrothermal influences on oceanic beryllium using

fluids, plume particles and sediments from the TAG hydrothermal field. Earth Planet. Sci. Lett. 122, 143–157. https://doi.org/10.1016/0012-821X(94)90056-6

Briant, R.M., Bateman, M.D., 2009. Luminescence dating indicates radiocarbon age underestimation in late Pleistocene fluvial deposits from eastern England. J. Quat. Sci. 24, 916–927. https://doi.org/10.1002/jqs.1258

Broecker, W.S., Thurber, D.L., Goddard, J., Ku, T.L., Matthews, R.K., Mesolella, K.J., 1968. Milankovitch Hypothesis Supported by Precise Dating of Coral Reefs and Deep-Sea Sediments. Science. 159, 297–300. https://doi.org/10.1126/SCIENCE.159.3812.297

Brown, E.T., Bendick, R., Bourlès, D.L., Gaur, V., Molnar, P., Raisbeck, G.M., Yiou, F., 2002. Slip rates of the Karakorum fault, Ladakh, India, determined using cosmic ray exposure dating of debris flows and moraines. J. Geophys. Res. Solid Earth 107, ESE 7-1-ESE 7-13. https://doi.org/10.1029/2000JB000100

Brown, E.T., Edmond, J.M., Raisbeck, G.M., Bourlès, D.L., Yiou, F., Measures, C.I., 1992a. Beryllium isotope geochemistry in tropical river basins. Geochim. Cosmochim. Acta 56, 1607–1624. https://doi.org/10.1016/0016-7037(92)90228-B

Brown, E.T., Measures, C.I., Edmond, J.M., Bourlès, D.L., Raisbeck, G.M., Yiou, F., 1992b. Continental inputs of beryllium to the oceans. Earth Planet. Sci. Lett. 114, 101–111. https://doi.org/10.1016/0012-821X(92)90154-N

Brown, T.A., Nelson, D.E., Southon, J.R., Vogel, J.S., 1985. The extraction of ^{10}Be from lake sediments leaching versus total dissolution. Chem. Geol. Isot. Geosci. Sect. 52, 375–378. https://doi.org/10.1016/0168-9622(85)90047-8

Burbank, D.W., Fort, M.B., 1985. Bedrock Control on Glacial Limits: Examples from the Ladakh and Zanskar Ranges, North-Western Himalaya, India. J. Glaciol. 31, 143–149. https://doi.org/10.3189/s0022143000006389

Carcaillet, J.T., Bourlès, D.L., Thouveny, N., 2004a. Geomagnetic dipole moment and 10Be production rate intercalibration from authigenic $^{10}Be/^{9}Be$ for the last 1.3 Ma. Geochemistry, Geophys. Geosystems 5. https://doi.org/10.1029/2003GC000641

Carcaillet, J.T., Bourlès, D.L., Thouveny, N., Arnold, M., 2004b. A high resolution authigenic $^{10}Be/^{9}Be$ record of geomagnetic moment variations over the last 300 ka from sedimentary cores of the Portuguese margin. Earth Planet. Sci. Lett. 219, 397–412. https://doi.org/10.1016/S0012-821X(03)00702-7

Carcaillet, J.T., Thouveny, N., Bourlès, D.L., 2003. Geomagnetic moment instability between 0.6 and 1.3 Ma from cosmonuclide evidence. Geophys. Res. Lett. 30, 1792. https://doi.org/10.1029/2003GL017550

Carrivick, J.L., Tweed, F.S., 2013. Proglacial Lakes: Character, behaviour and geological importance. Quat. Sci. Rev. 78, 34–52. https://doi.org/10.1016/j.quascirev.2013.07.028

Cerling, T.E., Harris, J.M., MacFadden, B.J., Leakey, M.G., Quade, J., Eisenmann, V., Ehieringer, J.R., 1997. Global vegetation change through the Miocene/Pliocene boundary. Nature. https://doi.org/10.1038/38229

Chandana, K.R., Bhushan, R., Jull, A.J.T., 2017. Evidence of Poor Bottom Water Ventilation during LGM in the Equatorial Indian Ocean. Front. Earth Sci. 0, 84. https://doi.org/10.3389/FEART.2017.00084

Channell, J.E.T., Xuan, C., Hodell, D.A., 2009. Stacking paleointensity and oxygen isotope data for the last 1.5 Myr (PISO-1500). Earth Planet. Sci. Lett. 283, 14–23. https://doi.org/10.1016/J.EPSL.2009.03.012

Chen, J., An, Z., Head, J., 1999. Variation of Rb/Sr Ratios in the Loess-Paleosol Sequences of Central China during the Last 130,000 Years and Their Implications for Monsoon Paleoclimatology. Quat. Res. 51, 215–219. https://doi.org/10.1006/QRES.1999.2038

Chevuturi, A., Dimri, A.P., Thayyen, R.J., 2018. Climate change over Leh (Ladakh), India. Theor Appl Clim. 131, 531–545. https://doi.org/10.1007/s00704-016-1989-1

Chinni, V., Singh, S.K., Bhushan, R., Rengarajan, R., Sarma, V.V.S.S., 2019. Spatial variability in dissolved iron concentrations in the marginal and open waters of the Indian Ocean. Mar. Chem. 208, 11–28. https://doi.org/10.1016/j.marchem.2018.11.007

Chmeleff, J., von Blanckenburg, F., Kossert, K., Jakob, D., 2010. Determination of the 10Be half-life by multicollector ICP-MS and liquid scintillation counting. Nucl. Instruments Methods Phys. Res. Sect. B Beam Interact. with Mater. Atoms 268, 192–199. https://doi.org/10.1016/j.nimb.2009.09.012

Christl, M., Lippold, J., Steinhilber, F., Bernsdorff, F., Mangini, A., 2010. Reconstruction of global ^{10}Be production over the past 250ka from highly accumulating Atlantic drift sediments. Quat. Sci. Rev. 29, 2663–2672. https://doi.org/10.1016/j.quascirev.2010.06.017

Christl, M., Mangini, A., Kubik, P.W., 2007. Highly resolved Beryllium-10 record from ODP Site 1089-A global signal? Earth Planet. Sci. Lett. 257, 245–258. https://doi.org/10.1016/j.epsl.2007.02.035

Clemens, S.C., Prell, W.L., Howard, W.R., 1987. Retrospective dry bulk density estimates from southeast Indian Ocean sediments - Comparison of water loss and chloride-ion methods. Mar. Geol. 76, 57–69. https://doi.org/10.1016/0025-3227(87)90017-X

Coplen, T.B., Brand, W.A., Gehre, M., Gröning, M., Meijer, H.A.J., Toman, B., Verkouteren, R.M., 2006. New guidelines for delta13C measurements. Anal. Chem. 78, 2439–2441. https://doi.org/10.1021/AC052027C

Costa, J.E., Schuster, R.L., 1988. The formation and failure of natural dams. Geol. Soc. Am. Bull. 100, 1054–1068.

Crest, Y., Delmas, M., Braucher, R., Gunnell, Y., Calvet, M., 2017. Cirques have growth spurts during deglacial and interglacial periods: Evidence from ^{10}Be and ^{26}Al nuclide inventories in the central and eastern Pyrenees. Geomorphology 278, 60–77. https://doi.org/10.1016/J.GEOMORPH.2016.10.035

Cruz, R.V., Harasawa, H., Lal, M., Wu, S., Anokhin, Y., Punsalmaa, B., Honda, Y., Jafari, M., Li, C., Ninh, N.H., 2007. Asia. climate change 2007: impacts, adaptation and vulnerability. Contribution of Working Group II to the Fourth Assessment Report of the Intergovernmental Panel on Climate Change.

Dahl, S.O., Nesje, A., 1996. A new approach to calculating Holocene winter precipitation by combining glacier equilibrium-line altitudes and pine-tree limits: A case study from Hardangerjøkulen, central southern Norway. Holocene 6, 381–398. https://doi.org/10.1177/095968369600600401

Dannhaus, N., Wittmann, H., Krám, P., Christl, M., von Blanckenburg, F., 2018. Catchment-wide weathering and erosion rates of mafic, ultramafic, and granitic rock from cosmogenic meteoric ^{10}Be/^{9}Be ratios. Geochim. Cosmochim. Acta 222, 618–641. https://doi.org/10.1016/j.gca.2017.11.005

Demske, D., Tarasov, P.E., Wünnemann, B., Riedel, F., 2009. Late glacial and Holocene vegetation, Indian monsoon and westerly circulation in the Trans-Himalaya recorded in the lacustrine pollen sequence from Tso Kar, Ladakh, NW India. Palaeogeogr. Palaeoclimatol. Palaeoecol. 279, 172–185. https://doi.org/10.1016/j.palaeo.2009.05.008

Deng, K., Wittmann, H., Hsieh, M.-L., Yang, S., von Blanckenburg, F., 2021. Deposition and retention of meteoric ^{10}Be in Holocene Taiwan river terraces. Quat. Sci. Rev. 265, 107048. https://doi.org/10.1016/J.QUASCIREV.2021.107048

Deng, K., Wittmann, H., von Blanckenburg, F., 2020a. The depositional flux of meteoric cosmogenic 10Be from modeling and observation. Earth Planet. Sci. Lett. 550,

116530. https://doi.org/10.1016/j.epsl.2020.116530

Deng, K., Yang, S., von Blanckenburg, F., Wittmann, H., 2020b. Denudation Rate Changes Along a Fast-Eroding Mountainous River With Slate Headwaters in Taiwan From ^{10}Be (Meteoric)/^{9}Be Ratios. J. Geophys. Res. Earth Surf. 125. https://doi.org/10.1029/2019JF005251

Deplazes, G., Lückge, A., Peterson, L.C., Timmermann, A., Hamann, Y., Hughen, K.A., Röhl, U., Laj, C., Cane, M.A., Sigman, D.M., Haug, G.H., 2013. Links between tropical rainfall and North Atlantic climate during the last glacial period. Nat. Geosci. 6, 213–217. https://doi.org/10.1038/ngeo1712

Dimri, A.P., Chevuturi, A., 2016. Western disturbances - An Indian meteorological perspective, Western Disturbances - An Indian Meteorological Perspective. https://doi.org/10.1007/978-3-319-26737-1

Dimri, A.P., Chevuturi, A., 2014. Model sensitivity analysis study for western disturbances over the Himalayas. Meteorol. Atmos. Phys. 123, 155–180. https://doi.org/10.1007/S00703-013-0302-4/FIGURES/16

Dimri, A.P., Niyogi, D., Barros, A.P., Ridley, J., Mohanty, U.C., Yasunari, T., Sikka, D.R., 2015. Western Disturbances: A review. Rev. Geophys. https://doi.org/10.1002/2014RG000460

Dortch, J.M., Owen, L.A., Caffee, M.W., 2013. Timing and climatic drivers for glaciation across semi-arid western Himalayan-Tibetan orogen. Quat. Sci. Rev. 78, 188–208. https://doi.org/10.1016/j.quascirev.2013.07.025

Dortch, J.M., Owen, L.A., Caffee, M.W., 2010. Quaternary glaciation in the Nubra and Shyok valley confluence, northernmost Ladakh, India. Quat. Res. 74, 132–144. https://doi.org/10.1016/j.yqres.2010.04.013

Duller, G.A.T., 2006. Single grain optical dating of glacigenic deposits. Quat. Geochronol.

1, 296–304. https://doi.org/10.1016/J.QUAGEO.2006.05.018

Dunai, T.J., 2010. Cosmogenic Nuclides. Cambridge University Press, Cambridge. https://doi.org/10.1017/CBO9780511804519

Durcan, J.A., King, G.E., Duller, G.A.T., 2015. DRAC: Dose Rate and Age Calculator for trapped charge dating. Quat. Geochronol. 28, 54–61. https://doi.org/10.1016/j.quageo.2015.03.012

Emiliani, C., 2015. Pleistocene Temperatures. https://doi.org/10.1086/626295 63, 538–578. https://doi.org/10.1086/626295

Engstrom, D.R., Wright, H.E.E., 1984. Chemical stratigraphy of lake sediments as a record of environmental change. Lake sediments Environ. Hist. 11–67.

Eugster, P., Scherler, D., Thiede, R.C., Codilean, A.T., Strecker, M.R., 2016. Rapid Last Glacial Maximum deglaciation in the Indian Himalaya coeval with midlatitude glaciers: New insights from 10Be-dating of ice-polished bedrock surfaces in the Chandra Valley, NW Himalaya. Geophys. Res. Lett. 43, 1589–1597. https://doi.org/10.1002/2015GL066077

Fick, S.E., Hijmans, R.J., 2017. WorldClim 2: new 1-km spatial resolution climate surfaces for global land areas. Int. J. Climatol. 37, 4302–4315. https://doi.org/10.1002/JOC.5086

Finkel, R.C., Nishiizumi, K., 1997. Beryllium 10 concentrations in the Greenland Ice Sheet Project 2 ice core from 3-40 ka. J. Geophys. Res. Ocean. 102, 26699–26706. https://doi.org/10.1029/97JC01282

Fort, M., 1978. Observations sur la géomorphologie du Ladakh (Geomorphology of the Ladakh). Bull. Assoc. Geogr. Fr. 55, 159–175. https://doi.org/10.3406/BAGF.1978.5027

Frank, M., Gersonde, R., Rutger Van Der Loeff, M., Bohrmann, G., Nürnberg, C.C., Kubik,

P.W., Suter, M., Mangini, A., 2000. Similar glacial and interglacial export bioproductivity in the Atlantic sector of the Southern Ocean: Multiproxy evidence and implications for glacial atmospheric CO2. Paleoceanography 15, 642–658. https://doi.org/10.1029/2000PA000497

Frank, M., Porcelli, D., Andersson, P., Baskaran, M., Björk, G., Kubik, P.W., Hattendorf, B., Guenther, D., 2009. The dissolved Beryllium isotope composition of the Arctic Ocean. Geochim. Cosmochim. Acta 73, 6114–6133. https://doi.org/10.1016/j.gca.2009.07.010

Frank, M., Schwarz, B., Baumann, S., Kubik, P.W., Suter, M., Mangini, A., 1997. A 200 kyr record of cosmogenic radionuclide production rate and geomagnetic field intensity from 10Be in globally stacked deep-sea sediments. Earth Planet. Sci. Lett. 149, 121–129. https://doi.org/10.1016/s0012-821x(97)00070-8

Frank, Martin, Backman, Jan, Jakobsson, Martin, Moran, Kate, O'regan, Matthew, King, John, Haley, Brian A, Kubik, Peter W, Garbe-Schönberg, Dieter, Frank, M, Backman, J, Jakobsson, M, Moran, K, O'regan, M, King, J, Haley, B A, Kubik, P W, Garbe-Schönberg, D, 2008. Beryllium isotopes in central Arctic Ocean sediments over the past 12.3 million years: Stratigraphic and paleoclimatic implications. https://doi.org/10.1029/2007PA001478

Franklin, A.D., Prescott, J.R., Scholefield, R.B., 1995. The mechanism of thermoluminescence in an Australian sedimentary quartz. J. Lumin. 63, 317–326. https://doi.org/10.1016/0022-2313(94)00068-N

Fuchs, M., Owen, L.A., 2008. Luminescence dating of glacial and associated sediments: review, recommendations and future directions. Boreas. https://doi.org/10.1111/j.1502-3885.2008.00052.x

Galy, A., France-Lanord, C., 2001. Higher erosion rates in the Himalaya: Geochemical constraints on riverine fluxes. Geology 29, 23–26. https://doi.org/10.1130/0091-

7613(2001)029<0023:HERITH>2.0.CO;2

Gamo, T., Chiba, H., Yamanaka, T., Okudaira, T., Hashimoto, J., Tsuchida, S., Ishibashi, J. ichiro, Kataoka, S., Tsunogai, U., Okamura, K., Sano, Y., Shinjo, R., 2001. Chemical characteristics of newly discovered black smoker fluids and associated hydrothermal plumes at the Rodriguez Triple Junction, Central Indian Ridge. Earth Planet. Sci. Lett. 193, 371–379. https://doi.org/10.1016/S0012-821X(01)00511-8

Gamo, T., Nakayama, E., Shitashima, K., Isshiki, K., Obata, H., Okamura, K., Kanayama, S., Oomori, T., Koizumi, T., Matsumoto, S., Hasumoto, H., 1996. Hydrothermal plumes at the Rodriguez triple junction, Indian ridge. Earth Planet. Sci. Lett. 142, 261–270. https://doi.org/10.1016/0012-821x(96)00087-8

Ganju, A., Nagar, Y.C., Sharma, L.N., Sharma, S., Juyal, N., 2018. Luminescence chronology and climatic implication of the late quaternary glaciation in the Nubra valley, Karakoram Himalaya, India. Palaeogeogr. Palaeoclimatol. Palaeoecol. 502, 52–62. https://doi.org/10.1016/J.PALAEO.2018.04.022

Goldberg, E.D., Griffin, J.J., 1970. The sediments of the northern Indian Ocean. Deep. Res. Oceanogr. Abstr. 17, 513–537. https://doi.org/10.1016/0011-7471(70)90065-3

Gosse, J.C., Phillips, F.M., 2001. Terrestrial in situ cosmogenic nuclides: Theory and application. Quat. Sci. Rev. 20, 1475–1560. https://doi.org/10.1016/S0277-3791(00)00171-2

Goswami, V., Singh, S.K., Bhushan, R., 2012. Dissolved redox sensitive elements, Re, U and Mo in intense denitrification zone of the Arabian Sea. Chem. Geol. 291, 256–268. https://doi.org/10.1016/j.chemgeo.2011.10.021

Graham, I., Ditchburn, R., Barry, B., 2003. Atmospheric deposition of ^{7}Be and ^{10}Be in New Zealand rain (1996-98). Geochim. Cosmochim. Acta 67, 361–373. https://doi.org/10.1016/S0016-7037(02)01092-X

Graly, J.A., Reusser, L.J., Bierman, P.R., 2011. Short and long-term delivery rates of meteoric ^{10}Be to terrestrial soils. Earth Planet. Sci. Lett. 302, 329–336. https://doi.org/10.1016/j.epsl.2010.12.020

Grootes, P.M., Stuiver, M., 1997. Oxygen 18/16 variability in Greenland snow and ice with 10-3- to 105-year time resolution. J. Geophys. Res. Ocean. 102, 26455–26470. https://doi.org/10.1029/97JC00880

Grootes, P.M., Stuiver, M., White, J.W.C., Johnsen, S., Jouzel, J., 1993. Comparison of oxygen isotope records from the GISP2 and GRIP Greenlandice cores. Nature 366, 552–554.

Guillou, H., Singer, B.S., Laj, C., Kissel, C., Scaillet, S., Jicha, B.R., 2004. On the age of the Laschamp geomagnetic excursion. Earth Planet. Sci. Lett. 227, 331–343. https://doi.org/10.1016/j.epsl.2004.09.018

Gupta, A.K., Sarkar, S., Mukherjee, B., 2006. Paleoceanographic changes during the past 1.9 Myr at DSDP Site 238, Central Indian Ocean Basin: Benthic foraminiferal proxies. Mar. Micropaleontol. 60, 157–166. https://doi.org/10.1016/j.marmicro.2006.04.001

Harrison, S., Glasser, N., Anderson, E., Ivy-Ochs, S., Kubik, P.W., 2010. Late Pleistocene mountain glacier response to North Atlantic climate change in southwest Ireland. Quat. Sci. Rev. 29, 3948–3955. https://doi.org/10.1016/J.QUASCIREV.2010.09.015

Hart, J.K., 1992. Sedimentary environments associated with Glacial Lake Trimingham, Norfolk, UK. Boreas 21, 119–136. https://doi.org/10.1111/j.1502-3885.1992.tb00020.x

Harvey, A.M., Mather; A. E., Stokes; M., 2005. Alluvial Fans, Gemorphology, Sedimentology, Dynamics: Geomorphology, Sedimentology, Dynamics (Geological Society Special Publication). Geol. Soc. London, Spec. Publ. No 251 256.

Heaton, T.J., Köhler, P., Butzin, M., Bard, E., Reimer, R.W., Austin, W.E.N., Bronk

Ramsey, C., Grootes, P.M., Hughen, K.A., Kromer, B., Reimer, P.J., Adkins, J., Burke, A., Cook, M.S., Olsen, J., Skinner, L.C., 2020. Marine20 - The Marine Radiocarbon Age Calibration Curve (0-55,000 cal BP). Radiocarbon 62, 779–820. https://doi.org/10.1017/RDC.2020.68

Heikkilä, U., Beer, · J, Abreu, J.A., Steinhilber, · F, 2013. On the Atmospheric Transport and Deposition of the Cosmogenic Radionuclides (^{10}Be): A Review. Sp. Sci Rev 176, 321–332. https://doi.org/10.1007/s11214-011-9838-0

Heikkilä, U., Beer, J., Alfimov, V., 2008a. Beryllium-10 and beryllium-7 in precipitation in Dübendorf (440 m) and at Jungfraujoch (3580 m), Switzerland (1998-2005). J. Geophys. Res. Atmos. 113, D11104. https://doi.org/10.1029/2007JD009160

Heikkilä, U., Beer, J., Feichter, J., 2008b. Modeling cosmogenic radionuclides 10Be and 7Be during the maunder minimum using the ECHAM5-HAM general circulation Model. Atmos. Chem. Phys. 8, 2797–2809. https://doi.org/10.5194/acp-8-2797-2008

Heikkilä, U., Beer, J., Jouzel, J., Feichter, J., Kubik, P., 2008c. ^{10}Be measured in a GRIP snow pit and modeled using the ECHAM5-HAM general circulation model. Geophys. Res. Lett. 35, L05817. https://doi.org/10.1029/2007GL033067

Heikkilä, U., Smith, A.M., 2013. Production rate and climate influences on the variability of 10 Be deposition simulated by ECHAM5-HAM: Globally, in Greenland, and in Antarctica. J. Geophys. Res. Atmos. 118, 2506–2520. https://doi.org/10.1002/jgrd.50217

Heikkilä, U., von Blanckenburg, F., 2015. The global distribution of Holocene meteoric 10Be fluxes from atmospheric models. Distribution maps for terrestrial Earth surface applications. GFZ Data Serv. 10.

Henken-Mellies, W.U., Beer, J., Heller, F., Hsü, K.J., Shen, C., Bonani, G., Hofmann, H.J., Suter, M., Wölfli, W., 1990. 10Be and 9Be in South Atlantic DSDP Site 519: Relation to geomagnetic reversals and to sediment composition. Earth Planet. Sci. Lett. 98,

267–276. https://doi.org/10.1016/0012-821X(90)90029-W

Herman, F., Beyssac, O., Brughelli, M., Lane, S.N., Leprince, S., Adatte, T., Lin, J.Y.Y., Avouac, J.P., Cox, S.C., 2015. Erosion by an Alpine glacier. Science. 350, 193–195. https://doi.org/10.1126/SCIENCE.AAB2386

Heslop, D., 2007. Are hydrodynamic shape effects important when modelling the formation of depositional remanent magnetization? Geophys. J. Int. 171, 1029–1035. https://doi.org/10.1111/J.1365-246X.2007.03588.X/3/171-3-1029-FIG004.JPEG

Heyman, J., Stroeven, A.P., Harbor, J.M., Caffee, M.W., 2011. Too young or too old: Evaluating cosmogenic exposure dating based on an analysis of compiled boulder exposure ages. Earth Planet. Sci. Lett. 302, 71–80. https://doi.org/10.1016/J.EPSL.2010.11.040

Horiuchi, K., Uchida, T., Sakamoto, Y., Ohta, A., Matsuzaki, H., Shibata, Y., Motoyama, H., 2008. Ice core record of ^{10}Be over the past millennium from Dome Fuji, Antarctica: A new proxy record of past solar activity and a powerful tool for stratigraphic dating. Quat. Geochronol. 3, 253–261. https://doi.org/10.1016/j.quageo.2008.01.003

Hughes, P.D., Gibbard, P.L., 2015. A stratigraphical basis for the Last Glacial Maximum (LGM). Quat. Int. 383, 174–185. https://doi.org/10.1016/j.quaint.2014.06.006

Huntley, D.J., Godfrey-Smith, D.I., Thewalt, M.L.W., 1985. Optical dating of sediments. Nat. 1985 3135998 313, 105–107. https://doi.org/10.1038/313105a0

Huntley, D.J., Lamothe, M., 2001. Ubiquity of anomalous fading in K-feldspars and the measurement and correction for it in optical dating. Can. J. Earth Sci. 38, 1093–1106.

Immerzeel, W.W., Van Beek, L.P.H., Bierkens, M.F.P., 2010. Climate change will affect the asian water towers. Science. 328, 1382–1385. https://doi.org/10.1126/science.1183188

Ivy-Ochs, S., Kerschner, H., Schlüchter, C., 2007. Cosmogenic nuclides and the dating of Lateglacial and Early Holocene glacier variations: The Alpine perspective. Quat. Int. 164–165, 53–63. https://doi.org/10.1016/J.QUAINT.2006.12.008

Ivy-Ochs, S., Kober, F., 2008. Surface exposure dating with cosmogenic nuclides. E&G Quat. Sci. J. 57, 179–209. https://doi.org/10.3285/EG.57.1-2.7

Jackson, A., Jonkers, A.R.T., Walker, M.R., 2000. Four centuries of geomagnetic secular variation from historical records. Philos. Trans. R. Soc. London. Ser. A Math. Phys. Eng. Sci. 358, 957–990. https://doi.org/10.1098/RSTA.2000.0569

Jansen, J.D., Knudsen, M.F., Andersen, J.L., Heyman, J., Egholm, D.L., 2019. Erosion rates in Fennoscandia during the past million years. Quat. Sci. Rev. 207, 37–48. https://doi.org/10.1016/J.QUASCIREV.2019.01.010

Jena, P.S., Bhushan, R., Ajay, S., Bharti, N., Sudheer, A.K., 2022a. ^{10}Be depositional flux variation in the central Indian Ocean during the last 43 ka. Sci. Total Environ. 802, 149808. https://doi.org/10.1016/j.scitotenv.2021.149808

Jena, P.S., Bhushan, R., Raj, H., Dabhi, A.J., Sharma, S., Shukla, A.D., Juyal, N., 2022b. Relict proglacial lake of Spituk (Leh), northwest (NW) Himalaya: A repository of hydrological changes during Marine Isotopic Stage (MIS)-2. Palaeogeogr. Palaeoclimatol. Palaeoecol. 111164. https://doi.org/10.1016/j.palaeo.2022.111164

Jena, P.S., Bhushan, R., Shivam, A., Nambiar, R., Bharti, N., 2021. Production rate variation and changes in sedimentation rate of marine core dated with meteoric ^{10}Be and ^{14}C. J. Environ. Radioact. 237, 106678. https://doi.org/10.1016/j.jenvrad.2021.106678

Johnsen, S.J., Clausen, H.B., Dansgaard, W., Gundestrup, N.S., Hammer, C.U., Andersen, U., Andersen, K.K., Hvidberg, C.S., Dahl-Jensen, D., Steffensen, J.P., Shoji, H., Sveinbjörnsdóttir, Á.E., White, J., Jouzel, J., Fisher, D., 1997. The δ^{18}O record along the Greenland Ice Core Project deep ice core and the problem of possible Eemian

climatic instability. J. Geophys. Res. Ocean. 102, 26397–26410. https://doi.org/10.1029/97JC00167

Johnsen, S.J., Dahl-Jensen, D., Gundestrup, N., Steffensen, J.P., Clausen, H.B., Miller, H., Masson-Delmotte, V., Sveinbjörnsdottir, A.E., White, J., 2001. Oxygen isotope and palaeotemperature records from six Greenland ice-core stations: Camp Century, Dye-3, GRIP, GISP2, Renland and NorthGRIP. J. Quat. Sci. 16, 299–307. https://doi.org/10.1002/jqs.622

Juyal, N., 2014. Ladakh: The High-Altitude Indian Cold Desert, in: World Geomorphological Landscapes. Springer, pp. 115–124. https://doi.org/10.1007/978-94-017-8029-2_10

Juyal, N., Pant, R.K., Basavaiah, N., Bhushan, R., Jain, M., Saini, N.K., Yadava, M.G., Singhvi, A.K., 2009. Reconstruction of Last Glacial to early Holocene monsoon variability from relict lake sediments of the Higher Central Himalaya, Uttrakhand, India. J. Asian Earth Sci. 34, 437–449. https://doi.org/10.1016/j.jseaes.2008.07.007

Juyal, N., Pant, R.K., Basavaiah, N., Yadava, M.G., Saini, N.K., Singhvi, A.K., 2004. Climate and seismicity in the higher Central Himalaya during 20–10 ka: evidence from the Garbayang basin, Uttaranchal, India. Palaeogeogr. Palaeoclimatol. Palaeoecol. 213, 315–330. https://doi.org/10.1016/j.palaeo.2004.07.017

Kääb, A., Treichler, D., Nuth, C., Berthier, E., 2015. Brief Communication: Contending estimates of 2003-2008 glacier mass balance over the Pamir-Karakoram-Himalaya. https://doi.org/10.5194/tc-9-557-2015

Karlen, W., Matthews, J.A., 1992. Reconstructing Holocene glacier variations from glacial lake sediments: studies from Nordvestlandet and Jostedalsbreen- Jotunheimen, southern Norway. Geogr. Ann. Ser. A 74 A, 327–348. https://doi.org/10.1080/04353676.1992.11880374

Kelly, M.A., Lowell, T. V., Applegate, P.J., Phillips, F.M., Schaefer, J.M., Smith, C.A.,

Kim, H., Leonard, K.C., Hudson, A.M., 2015. A locally calibrated, late glacial ^{10}Be production rate from a low-latitude, high-altitude site in the Peruvian Andes. Quat. Geochronol. 26, 70–85. https://doi.org/10.1016/J.QUAGEO.2013.10.007

Klein, M.G., Mous, D.J.W., Gottdang, A., 2006. A compact 1 MV multi-element AMS system. Nucl. Instruments Methods Phys. Res. Sect. B Beam Interact. with Mater. Atoms 249, 764–767. https://doi.org/10.1016/J.NIMB.2006.03.135

Knudsen, M.F., Henderson, G.M., Frank, M., Mac Niocaill, C., Kubik, P.W., 2008. In-phase anomalies in Beryllium-10 production and palaeomagnetic field behaviour during the Iceland Basin geomagnetic excursion. Earth Planet. Sci. Lett. 265, 588–599. https://doi.org/10.1016/j.epsl.2007.10.051

Kohl, C.P., Nishiizumi, K., 1992. Chemical isolation of quartz for measurement of in-situ -produced cosmogenic nuclides. Geochim. Cosmochim. Acta. https://doi.org/10.1016/0016-7037(92)90401-4

Kolla, V., Henderson, L., Biscaye, P.E., 1976. Clay mineralogy and sedimentation in the western Indian ocean. Deep. Res. Oceanogr. Abstr. 23, 949–961. https://doi.org/10.1016/0011-7471(76)90825-1

Koppes, M., Gillespie, A.R., Burke, R.M., Thompson, S.C., Stone, J., 2008. Late Quaternary glaciation in the Kyrgyz Tien Shan. Quat. Sci. Rev. 27, 846–866. https://doi.org/10.1016/J.QUASCIREV.2008.01.009

Korschinek, G., Bergmaier, A., Faestermann, T., Gerstmann, U.C., Knie, K., Rugel, G., Wallner, A., Dillmann, I., Dollinger, G., von Gostomski, C.L., Kossert, K., Maiti, M., Poutivtsev, M., Remmert, A., 2010. A new value for the half-life of 10Be by Heavy-Ion Elastic Recoil Detection and liquid scintillation counting. Nucl. Instruments Methods Phys. Res. Sect. B Beam Interact. with Mater. Atoms 268, 187–191. https://doi.org/10.1016/j.nimb.2009.09.020

Kotlia, B., Hinz-Schallreuter, I., Singh Kotlia, B., Hinz-schallreuter, I., Schallreuter, R.,

Schwarz, J., 1998. Evolution of Lamayuru palaeolake in the Trans Himalaya: Palaeoecological implications. Artic. E&G Quat. Sci. J. 48, 177–191. https://doi.org/10.3285/eg.48.1.16

Kramer, M., Kotlia, • B S, Wünnemann, • B, Kotlia, B.S., Wünnemann, B., 2014. A late quaternary ostracod record from the Tso Kar basin (North India) with a note on the distribution of recent species. J Paleolimnol 51, 549–565. https://doi.org/10.1007/s10933-014-9773-7

Kreutzer, S., Burow, C., Dietze, M., Fuchs, M.C., Schmidt, C., Fischer, M., Friedrich, J., Mercier, N., Smedley, R.K., Christophe, C., others, 2021. Package 'Luminescence.'

Ku, T.L., Kusakabe, M., Measures, C.I., Southon, J.R., Cusimano, G., Vogel, J.S., Nelson, D.E., Nakaya, S., 1990. Beryllium isotope distribution in the western North Atlantic: a comparison to the Pacific. Deep Sea Res. Part A, Oceanogr. Res. Pap. 37, 795–808. https://doi.org/10.1016/0198-0149(90)90007-I

Ku, T.L., Kusakabe, M., Nelson, D.E., Southern, J.R., Korteling, R.G., Vogel, J., Nowikow, I., 1982. Constancy of oceanic deposition of ^{10}Be as recorded in manganese crusts. Nature 299, 240–242. https://doi.org/10.1038/299240a0

Kudrass, H.R., Hofmann, A., Doose, H., Emeis, K., Erlenkeuser, H., 2001. Modulation and amplification of climatic changes in the Northern Hemisphere by the Indian summer monsoon during the past 80 k.y. Geology 29, 63–66. https://doi.org/10.1130/0091-7613(2001)029<0063:MAAOCC>2.0.CO;2

Kumar, A., Negi, H.S., Kumar, K., 2020. Long-term mass balance modelling (1986–2018) and climate sensitivity of Siachen Glacier, East Karakoram. Environ. Monit. Assess. 192, 1–16. https://doi.org/10.1007/S10661-020-08323-0/FIGURES/7

Kumar, N., Anderson, R.F., Mortlock, R.A., Froelich, P.N., Kubik, P., Dittrich-Hannen, B., Suter, M., 1995. Increased biological productivity and export production in the glacial southern Ocean. Nature 378, 675–680. https://doi.org/10.1038/378675a0

Kumar, P.K., Band, S.T., Ramesh, R., Awasthi, N., 2018. Monsoon variability and upper ocean stratification during the last ~ 66 ka over the Andaman Sea : Inferences from the δ ^{18}O records of planktonic foraminifera Monsoon variability and upper ocean strati fi cation during the last ~ 66 ka over the Andaman Se. Quat. Int. 0–1. https://doi.org/10.1016/j.quaint.2018.03.025

Kumar, V., Shukla, T., Mishra, A., Kumar, A., Mehta, M., 2020. Chronology and climate sensitivity of the post-LGM glaciation in the Dunagiri valley, Dhauliganga basin, Central Himalaya, India. Boreas 49, 594–614. https://doi.org/10.1111/bor.12440

Kusakabe, M., Ku, T.-L., Southon, J.R., Measures, C.I., 1990. Beryllium isotopes in the ocean. Geochem. J. 24, 263–272. https://doi.org/10.2343/geochemj.24.263

Kusakabe, M., Ku, T.L., Southon, J.R., Shao Liu, Vogel, J.S., Nelson, D.E., Nakaya, S., Cusimano, G.L., 1991. Be isotopes in rivers/estuaries and their oceanic budgets. Earth Planet. Sci. Lett. 102, 265–276. https://doi.org/10.1016/0012-821X(91)90022-A

Kusakabe, M., Ku, T.L., Southon, J.R., Vogel, J.S., Nelson, D.E., Measures, C.I., Nozaki, Y., 1987a. Distribution of ^{10}Be and ^{9}Be in the Pacific Ocean. Earth Planet. Sci. Lett. 82, 231–240. https://doi.org/10.1016/0012-821X(87)90198-1

Kusakabe, M., Ku, T.L., Southon, J.R., Vogel, J.S., Nelson, D.E., Measures, C.I., Nozaki, Y., 1987b. The distribution of ^{10}Be and ^{9}Be in ocean water. Nucl. Inst. Methods Phys. Res. B 29, 306–310. https://doi.org/10.1016/0168-583X(87)90255-2

Kusakabe, M., Ku, T.L., Vogel, J., Southon, J.R., Nelson, D.E., Richards, G., 1982. ^{10}Be profiles in seawater. Nature 299, 712–714. https://doi.org/10.1038/299712a0

Lai, Z.P., Mischke, S., Madsen, D., 2014. Paleoenvironmental implications of new OSL dates on the formation of the “Shell Bar” in the Qaidam Basin, northeastern Qinghai-Tibetan Plateau. J. Paleolimnol. https://doi.org/10.1007/s10933-013-9710-1

Laj, C., Kissel, C., 2015. An impending geomagnetic transition? Hints from the past. Front.

Earth Sci. 3, 61. https://doi.org/10.3389/feart.2015.00061

Laj, C., Kissel, C., Beer, J., 2004. High resolution global paleointensity stack since 75 kyr (GLOPIS-75) calibrated to absolute values, in: Geophysical Monograph Series. Blackwell Publishing Ltd, pp. 255–265. https://doi.org/10.1029/145GM19

Lal, D., 1991. Cosmic ray labeling of erosion surfaces: in situ nuclide production rates and erosion models. Earth Planet. Sci. Lett. 104, 424–439. https://doi.org/10.1016/0012-821X(91)90220-C

Lal, D., Peters, B., 1967. Cosmic Ray Produced Radioactivity on the Earth. Springer, Berlin, Heidelberg. https://doi.org/10.1007/978-3-642-46079-1_7

Lal, R., Saini, H.S., Pant, N.C., Mujtaba, S.A.I., 2019. Tectonics induced switching of provenance during the Late Quaternary aggradation of the Indus River Valley, Ladakh, India. Geosci. Front. 10, 285–297. https://doi.org/10.1016/j.gsf.2017.12.016

Lao, Y., Anderson, R.F., Broecker, W.S., Trumbore, S.E., Hofmann, H.J., Wolfli, W., 1992a. Transport and burial rates of ^{10}Be and ^{231}Pa in the Pacific Ocean during the Holocene period. Earth Planet. Sci. Lett. 113, 173–189. https://doi.org/10.1016/0012-821X(92)90218-K

Lao, Y., Anderson, R.F., Broecker, W.S., Trumbore, S.E., Hofmann, H.J., Wolfli, W., 1992b. Increased production of cosmogenic ^{10}Be during the last glacial maximum. Nature 357, 576–578. https://doi.org/10.1038/357576a0

Larsen, D.J., Miller, G.H., Geirsdóttir, Á., Thordarson, T., 2011. A 3000-year varved record of glacier activity and climate change from the proglacial lake Hvítárvatn, Iceland. Quat. Sci. Rev. 30, 2715–2731. https://doi.org/10.1016/j.quascirev.2011.05.026

Leemann, A., Niessen, F., 1994. Holocene glacial activity and climatic variations in the Swiss Alps: reconstructing a continuous record from proglacial lake sediments. The

Holocene 4, 259–268. https://doi.org/10.1177/095968369400400305

Li, W., Li, X., Mei, X., Zhang, F., Xu, J., Liu, C., Wei, C., Liu, Q., 2021. A review of current and emerging approaches for Quaternary marine sediment dating. Sci. Total Environ. 780, 146522. https://doi.org/10.1016/j.scitotenv.2021.146522

Li, Y., Song, Y., Lai, Z., Han, L., An, Z., 2016. Rapid and cyclic dust accumulation during MIS 2 in Central Asia inferred from loess OSL dating and grain-size analysis. Sci. Rep. 6, 1–6. https://doi.org/10.1038/srep32365

Lifton, N., Sato, T., Dunai, T.J., 2014. Scaling in situ cosmogenic nuclide production rates using analytical approximations to atmospheric cosmic-ray fluxes. Earth Planet. Sci. Lett. 386, 149–160. https://doi.org/10.1016/j.epsl.2013.10.052

Lifton, N., Smart, D.F., Shea, M.A., 2008. Scaling time-integrated in situ cosmogenic nuclide production rates using a continuous geomagnetic model. Earth Planet. Sci. Lett. 268, 190–201. https://doi.org/10.1016/J.EPSL.2008.01.021

Lisiecki, L.E., Raymo, M.E., 2005. A Pliocene-Pleistocene stack of 57 globally distributed benthic $\delta^{18}O$ records. Paleoceanography 20, n/a-n/a. https://doi.org/10.1029/2004PA001071

Long, H., Shen, J., 2015. Underestimated 14C-based chronology of late Pleistocene high lake-level events over the Tibetan Plateau and adjacent areas: Evidence from the Qaidam Basin and Tengger Desert. Sci. China Earth Sci. 58, 183–194. https://doi.org/10.1007/s11430-014-4993-2

Maejima, Y., Matsuzaki, H., Higashi, T., 2005. Application of cosmogenic 10Be to dating soils on the raised coral reef terraces of Kikai Island, southwest Japan. Geoderma 126, 389–399. https://doi.org/10.1016/j.geoderma.2004.10.004

Mann, M., Beer, J., Steinhilber, F., Abreu, J.A., Christl, M., Kubik, P.W., 2011. Variations in the depositional fluxes of cosmogenic beryllium on short time scales. Atmos.

Environ. 45, 2836–2841. https://doi.org/10.1016/j.atmosenv.2011.03.005

Martin, L.C.P., Blard, P.H., Balco, G., Lavé, J., Delunel, R., Lifton, N., Laurent, V., 2017. The CREp program and the ICE-D production rate calibration database: A fully parameterizable and updated online tool to compute cosmic-ray exposure ages. Quat. Geochronol. 38, 25–49. https://doi.org/10.1016/J.QUAGEO.2016.11.006

Masarik, J., Beer, J., 1999. Simulation of particle fluxes and cosmogenic nuclide production in the Earth's atmosphere. J. Geophys. Res. Atmos. 104, 12099–12111. https://doi.org/10.1029/1998JD200091

Masarik, J., Reedy, R.C., 1995. Terrestrial cosmogenic-nuclide production systematics calculated from numerical simulations. Earth Planet. Sci. Lett. 136, 381–395. https://doi.org/10.1016/0012-821X(95)00169-D

McHargue, L.R., Damon, P.E., 1991. The global beryllium 10 cycle. Rev. Geophys. 29, 141–158. https://doi.org/10.1029/91RG00072

McHargue, L.R., Donahue, D., Damon, P.E., Sonett, C.P., Biddulph, D., Burr, G., 2000. Geomagnetic modulation of the late Pleistocene cosmic-ray flux as determined by ^{10}Be from Blake Outer Ridge marine sediments. Nucl. Instruments Methods Phys. Res. Sect. B Beam Interact. with Mater. Atoms 172, 555–561. https://doi.org/10.1016/S0168-583X(00)00092-6

McHargue, L.R., Jull, A.J.T., Cohen, A., 2011. Measurement of 10Be from Lake Malawi (Africa) drill core sediments and implications for geochronology. Palaeogeogr. Palaeoclimatol. Palaeoecol. 303, 110–119. https://doi.org/10.1016/j.palaeo.2010.02.012

Measures, C.I., Edmond, J.M., 1983. The geochemical cycle of ^{9}Be: a reconnaissance. Earth Planet. Sci. Lett. 66, 101–110. https://doi.org/10.1016/0012-821X(83)90129-2

Measures, C.I., Ku, T.L., Luo, S., Southon, J.R., Xu, X., Kusakabe, M., 1996. The

distribution of ^{10}Be and ^{9}Be in the South Atlantic. Deep Sea Res. Part I Oceanogr. Res. Pap. 43, 987–1009. https://doi.org/10.1016/0967-0637(96)00049-0

Ménabréaz, L., Thouveny, N., Bourlès, D.L., Deschamps, P., Hamelin, B., Demory, F., 2011. The Laschamp geomagnetic dipole low expressed as a cosmogenic ^{10}Be atmospheric overproduction at ~41ka. Earth Planet. Sci. Lett. 312, 305–317. https://doi.org/10.1016/j.epsl.2011.10.037

Ménabréaz, L., Thouveny, N., Bourlès, D.L., Vidal, L., 2014. The geomagnetic dipole moment variation between 250 and 800 ka BP reconstructed from the authigenic ^{10}Be/^{9}Be signature in West Equatorial Pacific sediments. Earth Planet. Sci. Lett. 385, 190–205. https://doi.org/10.1016/j.epsl.2013.10.037

Merrill, J.R., Lyden, E.F.X., Honda, M., Arnold, J.R., 1960. The sedimentary geochemistry of the beryllium isotopes. Geochim. Cosmochim. Acta 18, 108–129. https://doi.org/10.1016/0016-7037(60)90022-3

Meyers, P.A., 1994. Preservation of elemental and isotopic source identification of sedimentary organic matter. Chem. Geol. 114, 289–302. https://doi.org/10.1016/0009-2541(94)90059-0

Milliman, J.D., Meade, R.H., 1983. World-wide delivery of sediment to the oceans. J. Geol. 91, 1–21. https://doi.org/10.1086/628741

Mishra, P.K., Anoop, A., Schettler, G., Prasad, S., Jehangir, A., Menzel, P., Naumann, R., Yousuf, A.R., Basavaiah, N., Deenadayalan, K., Wiesner, M.G., Gaye, B., 2015. Reconstructed late Quaternary hydrological changes from Lake Tso Moriri, NW Himalaya. Quat. Int. 371, 76–86. https://doi.org/10.1016/j.quaint.2014.11.040

Mix, A.C., Bard, E., Schneider, R., 2001. Environmental processes of the ice age: Land, oceans, glaciers (EPILOG). Quat. Sci. Rev. 20, 627–657. https://doi.org/10.1016/S0277-3791(00)00145-1

Monaghan, M.C., Krishnaswami, S., Turekian, K.K., 1986. The global-average production rate of 10Be. Earth Planet. Sci. Lett. 76, 279–287. https://doi.org/10.1016/0012-821X(86)90079-8

Mueller, A.D., Islebe, G.A., Hillesheim, M.B., Grzesik, D.A., Anselmetti, F.S., Ariztegui, D., Brenner, M., Curtis, J.H., Hodell, D.A., Venz, K.A., 2009. Climate drying and associated forest decline in the lowlands of northern Guatemala during the late Holocene. Quat. Res. 71, 133–141. https://doi.org/10.1016/J.YQRES.2008.10.002

Mujtaba, S.A.I., Lal, R., Saini, H.S., Kumar, P., Pant, N.C., 2018. Formation and breaching of two palaeolakes around Leh, Indus valley, during the late Quaternary. Geol. Soc. Spec. Publ. 462, 23–34. https://doi.org/10.1144/SP462.3

Muscheler, R., Beer, J., Kubik, P.W., Synal, H.A., 2005. Geomagnetic field intensity during the last 60,000 years based on ^{10}Be and ^{36}Cl from the Summit ice cores and 14C. Quat. Sci. Rev. 24, 1849–1860. https://doi.org/10.1016/j.quascirev.2005.01.012

Nag, D., Phartiyal, B., Singh, D. Sen, 2016. Sedimentary characteristics of palaeolake deposits along the indus river valley, Ladakh, Trans-Himalaya: Implications for the depositional environment. Sedimentology 63, 1765–1785. https://doi.org/10.1111/sed.12289

Nagar, Y.C., Ganju, A., Satyawali, P.K., Juyal, N., 2013. Preliminary optical chronology suggests significant advance in nubra valley glaciers during the last glacial maximum. Curr. Sci. https://doi.org/10.2307/24092683

Nambiar, R., Bhushan, R., Raj, H., 2020. Geochemical data of sediment core from the central Arabian Sea. figshare. Dataset. https://doi.org/10.6084/m9.figshare.12958487.v1

Naqvi, W.A., 1991. Geographical extent of denitrification in the Arabian Sea in relation to some physical processes. Oceanol. Acta 14, 281–290.

Němec, M., Wacker, L., Gäggeler, H., 2010. Optimization of the graphitization process AT AGE-1. Radiocarbon 52, 1380–1393. https://doi.org/10.1017/S0033822200046464

Nesbitt, H.W., Young, G.M., 1982. Early Proterozoic climates and plate motions inferred from major element chemistry of Intites. Nature 299.

Nilsson, A., Muscheler, R., Snowball, I., Aldahan, A., Possnert, G., Augustinus, P., Atkin, D., Stephens, T., 2011. Multi-proxy identification of the Laschamp geomagnetic field excursion in Lake Pupuke, New Zealand. Earth Planet. Sci. Lett. 311, 155–164. https://doi.org/10.1016/j.epsl.2011.08.050

Nishiizumi, K., 2022. Preparation of new 10Be and 26Al AMS standard reference materials. Nucl. Instruments Methods Phys. Res. Sect. B Beam Interact. with Mater. Atoms 530, 43–47. https://doi.org/10.1016/J.NIMB.2022.09.014

Nishiizumi, K., Imamura, M., Caffee, M.W., Southon, J.R., Finkel, R.C., McAninch, J., 2007. Absolute calibration of ^{10}Be AMS standards. Nucl. Instruments Methods Phys. Res. Sect. B Beam Interact. with Mater. Atoms 258, 403–413. https://doi.org/10.1016/j.nimb.2007.01.297

Nishiizumi, K., Winterer, E.L., Kohl, C.P., Klein, J., Middleton, R., Lal, D., Arnold, J.R., 1989. Cosmic ray production rates of ^{10}Be and ^{26}Al in quartz from glacially polished rocks. J. Geophys. Res. 94, 17907. https://doi.org/10.1029/JB094iB12p17907

Nishioka, J., Obata, H., Tsumune, D., 2013. Evidence of an extensive spread of hydrothermal dissolved iron in the Indian Ocean. Earth Planet. Sci. Lett. 361, 26–33. https://doi.org/10.1016/j.epsl.2012.11.040

Ohlendorf, C., Niessen, F., Weissert, H., 1997. Glacial Varve Thickness and 127 Years of Instrumental Climate Data: A Comparison, in: Climatic Change at High Elevation Sites. Springer Netherlands, pp. 159–179. https://doi.org/10.1007/978-94-015-8905-5_9

Orr, E.N., Owen, L.A., Saha, S., Caffee, M.W., Murari, M.K., 2018. Quaternary glaciation of the Lato Massif, Zanskar Range of the NW Himalaya. Quat. Sci. Rev. 183, 140–156. https://doi.org/10.1016/j.quascirev.2018.01.005

Ou, X.J., Lai, Z.P., Zhou, S.Z., Zeng, L.H., 2014. Timing of glacier fluctuations and trigger mechanisms in eastern Qinghai–Tibetan Plateau during the late Quaternary. Quat. Res. 81, 464–475. https://doi.org/10.1016/J.YQRES.2013.09.007

Owen, L.A., 1996. Quaternary lacustrine deposits in a high-energy semi-arid mountain environment, Karakoram Mountains, northern Pakistan. J. Quat. Sci. 11, 461–483. https://doi.org/10.1002/(sici)1099-1417(199611/12)11:6<461::aid-jqs282>3.0.co;2-g

Owen, L.A., Caffee, M.W., Bovard, K.R., Finkel, R.C., Sharma, M.C., 2006. Terrestrial cosmogenic nuclide surface exposure dating of the oldest glacial successions in the Himalayan orogen: Ladakh Range, northern India. Geol. Soc. Am. Bull. 118, 383–392. https://doi.org/10.1130/B25750.1

Owen, L.A., Chen, J., Hedrick, K.A., Caffee, M.W., Robinson, A.C., Schoenbohm, L.M., Yuan, Z., Li, W., Imrecke, D.B., Liu, J., 2012. Quaternary glaciation of the Tashkurgan Valley, Southeast Pamir. Quat. Sci. Rev. 47, 56–72. https://doi.org/10.1016/J.QUASCIREV.2012.04.027

Owen, L.A., Dortch, J.M., 2014. Nature and timing of Quaternary glaciation in the Himalayan–Tibetan orogen. Quat. Sci. Rev. 88, 14–54. https://doi.org/10.1016/J.QUASCIREV.2013.11.016

Owen, L.A., Finkel, R.C., Caffee, M.W., Gualtieri, L., 2002. Timing of multiple late Quaternary glaciations in the Hunza Valley, Karakoram Mountains, northern Pakistan: Defined by cosmogenic radionuclide dating of moraines. Geol. Soc. Am. Bull. 114, 593–604. https://doi.org/10.1130/0016-7606(2002)114<0593:TOMLQG>2.0.CO;2

Owen, L.A., Frankel, K.L., Knott, J.R., Reynhout, S., Finkel, R.C., Dolan, J.F., Lee, J.,

2011. Beryllium-10 terrestrial cosmogenic nuclide surface exposure dating of Quaternary landforms in Death Valley. Geomorphology 125, 541–557. https://doi.org/10.1016/j.geomorph.2010.10.024

Pattan, J.N., Masuzawa, T., Borole, D. V., Parthiban, G., Jauhari, P., Yamamoto, M., 2005. Biological productivity, terrigenous influence and noncrustal elements supply to the Central Indian Ocean Basin: Paleoceanography during the past ~ 1 Ma. J. Earth Syst. Sci. 114, 63–74. https://doi.org/10.1007/BF02702009

Pedro, J., van Ommen, T., Curran, M., Morgan, V., Smith, A., McMorrow, A., 2006. Evidence for climate modulation of the ^{10}Be solar activity proxy. J. Geophys. Res. Atmos. 111. https://doi.org/10.1029/2005JD006764

Phartiyal, B., Sharma, A., Kothyari, &, Ch, G., 2013. Damming of River Indus during Late Quaternary in Ladakh Region of Trans-Himalaya, NW India: Implications to Lake formation-climate and tectonics. Chin Sci Bull (Chin Ver) 58, 142–155. https://doi.org/10.1360/tb-2013-suppl008

Phartiyal, B., Sharma, A., Upadhyay, R., Ram-Awatar, Sinha, A.K., 2005. Quaternary geology, tectonics and distribution of palaeo- and present fluvio/glacio lacustrine deposits in Ladakh, NW Indian Himalaya—a study based on field observations. Geomorphology 65, 241–256. https://doi.org/10.1016/J.GEOMORPH.2004.09.004

Phartiyal, B., Singh, R., Joshi, P., Nag, D., 2020. Late-Holocene climatic record from a glacial lake in Ladakh range, Trans-Himalaya, India. Holocene 30, 1029–1042. https://doi.org/10.1177/0959683620908660

Phillips, F.M., Stone, W.D., Fabryka-Martin, J.T., 2001. An improved approach to calculating low-energy cosmic-ray neutron fluxes near the landratmosphere interface. Chem. Geol. 175, 689–701.

Pigati, J.S., Quade, J., Wilson, J., Jull, A.J.T., Lifton, N.A., 2007. Development of low-background vacuum extraction and graphitization systems for ^{14}C dating of old (40-

60 ka) samples. Quat. Int. 166, 4–14. https://doi.org/10.1016/j.quaint.2006.12.006

Piotrowski, A.M., Banakar, V.K., Scrivner, A.E., Elderfield, H., Galy, A., Dennis, A., 2009. Indian Ocean circulation and productivity during the last glacial cycle. Earth Planet. Sci. Lett. 285, 179–189. https://doi.org/10.1016/j.epsl.2009.06.007

Portenga, E.W., Bierman, P.R., Trodick, C.D., Greene, S.E., DeJong, B.D., Rood, D.H., Pavich, M.J., 2019. Erosion rates and sediment flux within the Potomac River basin quantified over millennial timescales using beryllium isotopes. Bull. Geol. Soc. Am. 131, 1295–1311. https://doi.org/10.1130/B31840.1

Prud'homme, C., Vassallo, R., Crouzet, C., Carcaillet, J., Mugnier, J.-L., Cortés-Aranda, J., 2020. Paired ^{10}Be sampling of polished bedrock and erratic boulders to improve dating of glacial landforms: an example from the Western Alps. Earth Surf. Process. Landforms 45, 1168–1180. https://doi.org/10.1002/ESP.4790

Putkonen, J., Swanson, T., 2003. Accuracy of cosmogenic ages for moraines. Quat. Res. 59, 255–261. https://doi.org/10.1016/S0033-5894(03)00006-1

Rahaman, W., Wittmann, H., von Blanckenburg, F., 2017. Denudation rates and the degree of chemical weathering in the Ganga River basin from ratios of meteoric cosmogenic ^{10}Be to stable ^{9}Be. Earth Planet. Sci. Lett. 469, 156–169. https://doi.org/10.1016/j.epsl.2017.04.001

Raina, V.K., Sangewar, C., 2007. Siachen glacier of Karakoram Mountains, Ladakh-its secular retreat. J. Geol. Soc. India (Online Arch. from Vol 1 to Vol 78) 70, 11–16.

Raisbeck, G.M., Yiou, F., Fruneau, M., Loiseaux, J.M., Lieuvin, M., Ravel, J.C., 1981. Cosmogenic ^{10}Be/^{7}Be as a probe of atmospheric transport processes. Geophys. Res. Lett. 8, 1015–1018. https://doi.org/10.1029/GL008I009P01015

Raisbeck, G.M., Yiou, F., Fruneau, M., Loiseaux, J.M., Lieuvin, M., Ravel, J.C., Reyss, J.M., Guichard, F., 1980. 10Be concentration and residence time in the deep ocean.

Earth Planet. Sci. Lett. 51, 275–278. https://doi.org/10.1016/0012-821X(80)90210-1

Raj, H., 2020. High resolution paleoclimatic study using corals. Indian Institute of Technology Gandhinagar.

Ramaswamy, V., Nair, R.R., 1994. Fluxes of material in the Arabian Sea and Bay of Bengal - Sediment trap studies. Proc. Indian Acad. Sci. - Earth Planet. Sci. 103, 189–210. https://doi.org/10.1007/BF02839536

Rana, N., Sharma, S., Ali, S.N., Singh, S., Shukla, A.D., 2019. Investigating the sensitivity of glaciers to climate variability since the MIS-2 in the upper Ganga catchment (Saraswati valley), Central Himalaya. Geomorphology 346, 106854. https://doi.org/10.1016/j.geomorph.2019.106854

Ravikant, V., Wu, F.Y., Ji, W.Q., 2009. Zircon U-Pb and Hf isotopic constraints on petrogenesis of the Cretaceous-Tertiary granites in eastern Karakoram and Ladakh, India. Lithos 110, 153–166. https://doi.org/10.1016/j.lithos.2008.12.013

Reimer, P.J., Austin, W.E.N., Bard, E., Bayliss, A., Blackwell, P.G., Bronk Ramsey, C., Butzin, M., Cheng, H., Edwards, R.L., Friedrich, M., Grootes, P.M., Guilderson, T.P., Hajdas, I., Heaton, T.J., Hogg, A.G., Hughen, K.A., Kromer, B., Manning, S.W., Muscheler, R., Palmer, J.G., Pearson, C., van der Plicht, J., Reimer, R.W., Richards, D.A., Scott, E.M., Southon, J.R., Turney, C.S.M., Wacker, L., Adolphi, F., Büntgen, U., Capano, M., Fahrni, S.M., Fogtmann-Schulz, A., Friedrich, R., Köhler, P., Kudsk, S., Miyake, F., Olsen, J., Reinig, F., Sakamoto, M., Sookdeo, A., Talamo, S., 2020. The IntCal20 Northern Hemisphere Radiocarbon Age Calibration Curve (0–55 cal kBP). Radiocarbon 62, 725–757. https://doi.org/10.1017/rdc.2020.41

Rhodes, E.J., 1988. Methodological considerations in the optical dating of quartz. Quat. Sci. Rev. 7, 395–400. https://doi.org/10.1016/0277-3791(88)90035-2

Roberts, A.P., Tauxe, L., Heslop, D., 2013. Magnetic paleointensity stratigraphy and high-resolution Quaternary geochronology: Successes and future challenges. Quat. Sci.

Rev. 61, 1–16. https://doi.org/10.1016/j.quascirev.2012.10.036

Roberts, A.P., Turner, G.M., 2013. Geomagnetic Excursions and Secular Variations, 2nd ed, Encyclopedia of Quaternary Science: Second Edition. Elsevier B.V. https://doi.org/10.1016/B978-0-444-53643-3.00053-4

Roberts, A.P., Winklhofer, M., 2004. Why are geomagnetic excursions not always recorded in sediments? Constraints from post-depositional remanent magnetization lock-in modelling. Earth Planet. Sci. Lett. 227, 345–359. https://doi.org/10.1016/J.EPSL.2004.07.040

Robertson, A.H.F., 2000. Formation of melanges in the Indus Suture Zone, Ladakh Himalaya by successive subduction-related, collisional and post-collisional processes during Late Mesozoic-Late Tertiary time. Geol. Soc. Spec. Publ. 170, 333–374. https://doi.org/10.1144/GSL.SP.2000.170.01.19

Röhringer, I., Zech, R., Abramowski, U., Sosin, P., Aldahan, A., Kubik, P.W., Zöller, L., Zech, W., 2012. The late Pleistocene glaciation in the Bogchigir Valleys (Pamir, Tajikistan) based on ^{10}Be surface exposure dating. Quat. Res. 78, 590–597. https://doi.org/10.1016/J.YQRES.2012.09.002

Rozanski, K., Stichler, W., Gonfiantini, R., Scott, E.M., Beukens, R.P., Kromer, B., Plicht, J. Van Der, 1992. The IAEA 14C Intercomparison Exercise 1990. Radiocarbon 34, 506–519. https://doi.org/10.1017/S0033822200063761

Rudnick, R.L., Gao, S., 2003. Composition of the Continental Crust, Treatise on Geochemistry. Elsevier Inc. https://doi.org/10.1016/B0-08-043751-6/03016-4

Saha, S., Sharma, M.C., Murari, M.K., Owen, L.A., Caffee, M.W., 2016. Geomorphology, sedimentology and minimum exposure ages of streamlined subglacial landforms in the NW Himalaya, India. Boreas 45, 284–303. https://doi.org/10.1111/bor.12153

Sangode, S.J., Phadtare, N.R., Meshram, D.C., Rawat, S., Suresh, N., 2011. A record of

lake outburst in the Indus valley of Ladakh Himalaya, India. Curr. Sci. 100, 1712–1718.

Sangode, S.J., Rawat, S., Meshram, D.C., Phadtare, N.R., Suresh, N., 2013. Integrated mineral magnetic and lithologic studies to delineate dynamic modes of depositional conditions in the Leh valley basin, Ladakh Himalaya, India. J. Geol. Soc. India 82, 107–120. https://doi.org/10.1007/s12594-013-0129-0

Sant, D.A., Wadhawan, S.K., Ganjoo, R.K., Basavaiah, N., Sukumaran, P., Bhattacharya, S., 2011a. Linkage of paraglacial processes from last glacial to recent inferred from Spituk sequence, Leh valley, Ladakh Himalaya. J. Geol. Soc. India 78, 147–156. https://doi.org/10.1007/s12594-011-0074-8

Sant, D.A., Wadhawan, S.K., Ganjoo, R.K., Basavaiah, N., Sukumaran, P., Bhattacharya, S., 2011b. Morphostratigraphy and palaeoclimate appraisal of the Leh valley, Ladakh Himalayas, India. J. Geol. Soc. India 77, 499–510. https://doi.org/10.1007/s12594-011-0057-9

Sarin, M.M., Krishnaswami, S., Dilli, K., Somayajulu, B.L.K., Moore, W.S., 1989. Major ion chemistry of the Ganga-Brahmaputra river system: Weathering processes and fluxes to the Bay of Bengal. Geochim. Cosmochim. Acta 53, 997–1009. https://doi.org/10.1016/0016-7037(89)90205-6

Sarnthein, M., Pflaumann, U., Weinelt, M., 2003. Past extent of sea ice in the northern North Atlantic inferred from foraminiferal paleotemperature estimates. Paleoceanography 18. https://doi.org/10.1029/2002PA000771

Sati, S.P., Ali, S.N., Rana, N., Bhattacharya, F., Bhushan, R., Shukla, A.D., Sundriyal, Y., Juyal, N., 2014. Timing and extent of Holocene glaciations in the monsoon dominated Dunagiri valley (Bangni glacier), Central Himalaya, India. J. Asian Earth Sci. 91, 125–136. https://doi.org/10.1016/j.jseaes.2014.05.008

Savranskaia, T., 2020. Records of paleomagnetic field intensity in sediments: Crossover

approach between relative paleointensity and cosmogenic 10Be. Université de Paris (2019-....).

Savranskaia, T., Egli, R., Valet, J.P., Bassinot, F., Meynadier, L., Bourlès, D.L., Simon, Q., Thouveny, N., 2021. Disentangling magnetic and environmental signatures of sedimentary $^{10}Be/^{9}Be$ records. Quat. Sci. Rev. 257, 106809. https://doi.org/10.1016/j.quascirev.2021.106809

Schaefer, J.M., Oberholzer, P., Zhao, Z., Ivy-Ochs, S., Wieler, R., Baur, H., Kubik, P.W., Schlüchter, C., 2008. Cosmogenic beryllium-10 and neon-21 dating of late Pleistocene glaciations in Nyalam, monsoonal Himalayas. Quat. Sci. Rev. 27, 295–311. https://doi.org/10.1016/J.QUASCIREV.2007.10.014

Scott, E.M., Cook, G.T., Naysmith, P., 2010. The Fifth International Radiocarbon Intercomparison (VIRI): An Assessment of Laboratory Performance in Stage 3. Radiocarbon 52, 859–865. https://doi.org/10.1017/S003382220004594X

Shah, C., Banerji, U.S., Chandana, K.R., Bhushan, R., 2020. ^{210}Pb dating of recent sediments from the continental shelf of western India: factors influencing sedimentation rates. Environ. Monit. Assess. 192, 1–17. https://doi.org/10.1007/S10661-020-08415-X/TABLES/3

Shah, R.A., Achyuthan, H., Lone, A.M., Kumar, S., Kumar, P., Sharma, R., Amir, M., Singh, A.K., Dash, C., 2020. Holocene palaeoenvironmental records from the high-altitude Wular Lake, Western Himalayas. The Holocene 30, 733–743. https://doi.org/10.1177/0959683619895592

Sharma, A., Phartiyal, B., 2018. Late Quaternary Palaeoclimate and Contemporary Moisture Source to Extreme NW India: A Review on Present Understanding and Future Perspectives. Front. Earth Sci. https://doi.org/10.3389/feart.2018.00150

Sharma, M.C., Owen, L.A., 1996. Quaternary glacial history of NW Garhwal, Central himalayas. Quat. Sci. Rev. 15, 335–365. https://doi.org/10.1016/0277-

3791(95)00061-5

Sharma, P., Somayajulu, B.L.K., 1982. ^{10}Be dating of large manganese nodules from world oceans. Earth Planet. Sci. Lett. 59, 235–244. https://doi.org/10.1016/0012-821X(82)90128-5

Sharma, S., Chand, P., Bisht, P., Shukla, A.D., Bartarya, S.K., Sundriyal, Y.P., Juyal, N., 2016. Factors responsible for driving the glaciation in the Sarchu Plain, eastern Zanskar Himalaya, during the late Quaternary. J. Quat. Sci. 31, 495–511. https://doi.org/10.1002/jqs.2874

Sharma, S., Hussain, A., Mishra, A.K., Lone, A., Solanki, T., Khan, M.K., 2018. Geomorphic investigation of the late-quaternary landforms in the southern Zanskar Valley, NW Himalaya. J. Earth Syst. Sci. 127, 1–20. https://doi.org/10.1007/s12040-017-0911-2

Sharma, S., Shukla, A.D., 2018. Factors governing the pattern of glacier advances since the Last Glacial Maxima in the transitional climate zone of the Southern Zanskar Ranges, NW Himalaya. Quat. Sci. Rev. 201, 223–240. https://doi.org/10.1016/J.QUASCIREV.2018.10.006

Shukla, A.D., 2011. Geochemical and isotopic studies of some sedimentary sequences of the Vindhyan Super group, India. [Unpubl. Ph. D. thesis Submitt. to MS Univ. Baroda].

Shukla, A.D., Bhandari, N., Shukla, P.N., 2002. Chemical signatures of the Permian-Triassic transitional environment in Spiti Valley, India. Spec. Pap. Soc. Am. 445–454.

Shukla, A.D., Sharma, S., Rana, N., Bisht, P., Juyal, N., 2020. Optical chronology and climatic implication of glacial advances from the southern Ladakh Range, NW Himalaya, India. Palaeogeogr. Palaeoclimatol. Palaeoecol. 539. https://doi.org/10.1016/j.palaeo.2019.109505

Simms, A.R., DeWitt, R., Rodriguez, A.B., Lambeck, K., Anderson, J.B., 2009. Revisiting marine isotope stage 3 and 5a (MIS3-5a) sea levels within the northwestern Gulf of Mexico. Glob. Planet. Change 66, 100–111. https://doi.org/10.1016/j.gloplacha.2008.03.014

Simon, Q., Bourlès, D.L., Thouveny, N., Horng, C.S., Valet, J.P., Bassinot, F., Choy, S., 2018a. Cosmogenic signature of geomagnetic reversals and excursions from the Réunion event to the Matuyama–Brunhes transition (0.7–2.14 Ma interval). Earth Planet. Sci. Lett. 482, 510–524. https://doi.org/10.1016/j.epsl.2017.11.021

Simon, Q., Thouveny, N., Bourlès, D.L., Bassinot, F., Savranskaia, T., Valet, J.P., 2018b. Increased production of cosmogenic ^{10}Be recorded in oceanic sediment sequences: Information on the age, duration, and amplitude of the geomagnetic dipole moment minimum over the Matuyama–Brunhes transition. Earth Planet. Sci. Lett. 489, 191–202. https://doi.org/10.1016/j.epsl.2018.02.036

Simon, Q., Thouveny, N., Bourlès, D.L., Nuttin, L., Hillaire-Marcel, C., St-Onge, G., 2016a. Authigenic ^{10}Be/^{9}Be ratios and ^{10}Be-fluxes (^{230}Th$_{xs}$-normalized) in central Baffin Bay sediments during the last glacial cycle: Paleoenvironmental implications. Quat. Sci. Rev. 140, 142–162. https://doi.org/10.1016/j.quascirev.2016.03.027

Simon, Q., Thouveny, N., Bourlès, D.L., Valet, J.P., Bassinot, F., 2020. Cosmogenic ^{10}Be production records reveal dynamics of geomagnetic dipole moment (GDM) over the Laschamp excursion (20–60 ka). Earth Planet. Sci. Lett. 550. https://doi.org/10.1016/j.epsl.2020.116547

Simon, Q., Thouveny, N., Bourlès, D.L., Valet, J.P., Bassinot, F., Ménabréaz, L., Guillou, V., Choy, S., Beaufort, L., 2016b. Authigenic ^{10}Be/^{9}Be ratio signatures of the cosmogenic nuclide production linked to geomagnetic dipole moment variation since the Brunhes/Matuyama boundary. J. Geophys. Res. Solid Earth 121, 7716–7741. https://doi.org/10.1002/2016JB013335

Singer, B.S., Guillou, H., Jicha, B.R., Laj, C., Kissel, C., Beard, B.L., Johnson, C.M., 2009. $^{40}Ar/^{39}Ar$, K-Ar and ^{230}Th-^{238}U dating of the Laschamp excursion: A radioisotopic tie-point for ice core and climate chronologies. Earth Planet. Sci. Lett. 286, 80–88. https://doi.org/10.1016/j.epsl.2009.06.030

Singh, M.S., 1963. Upper air circulation associated with a Western Disturbance. Indian J. Meteorol. Geophys 14, 156–172.

Singh, S.K., Rai, S.K., Krishnaswami, S., 2008. Sr and Nd isotopes in river sediments from the Ganga Basin: Sediment provenance and spatial variability in physical erosion. J. Geophys. Res. 113, F03006. https://doi.org/10.1029/2007JF000909

Sirocko, F., Sarnthein, M., 1989. Wind-Borne Deposits in the Northwestern Indian Ocean: Record of Holocene Sediments Versus Modern Satellite Data, Paleoclimatology and Paleometeorology: Modern and Past Patterns of Global Atmospheric Transport. Springer Netherlands, Dordrecht. https://doi.org/10.1007/978-94-009-0995-3_17

Solomina, O., Haeberli, W., Kull, C., Wiles, G., 2008. Historical and Holocene glacier–climate variations: General concepts and overview. Glob. Planet. Change 60, 1–9. https://doi.org/10.1016/j.gloplacha.2007.02.001

Somayajulu, B.L.K., Sharma, P., Beer, J., Bonani, G., Hofmann, H.J., Morenzoni, E., Nessi, M., Suter, M., Wölfli, W., 1984. ^{10}Be annual fallout in rains in India. Nucl. Inst. Methods Phys. Res. B 5, 398–403. https://doi.org/10.1016/0168-583X(84)90549-4

Song, Y.G., Lai, Z.P., Li, Y., Chen, T., Wang, Y.X., 2015. Comparison between luminescence and radiocarbon dating of late Quaternary loess from the Ili Basin in Central Asia. Quat. Geochronol. 30, 405–410. https://doi.org/10.1016/j.quageo.2015.01.012

Southon, J., Kashgarian, M., Fontugne, M., Metivier, B., Yim, W.W.S., 2002. Marine reservoir corrections for the Indian Ocean and Southeast Asia. Radiocarbon 44, 167–180. https://doi.org/10.1017/S0033822200064778

Southon, J.R., Ku, T.L., Nelson, D.E., Reyss, J.L., Duplessy, J.C., Vogel, J.S., 1987. 10Be in a deep-sea core: implications regarding ^{10}Be production changes over the past 420 ka. Earth Planet. Sci. Lett. 85, 356–364. https://doi.org/10.1016/0012-821X(87)90133-6

Steinhilber, F., Abreu, J.A., Beer, J., Brunner, I., Christl, M., Fischer, H., Heikkilä, U., Kubik, P.W., Mann, M., McCracken, K.G., Miller, H., Miyahara, H., Oerter, H., Wilhelms, F., 2012. 9,400 Years of cosmic radiation and solar activity from ice cores and tree rings. Proc. Natl. Acad. Sci. U. S. A. 109, 5967–5971. https://doi.org/10.1073/pnas.1118965109

Stokes, S., 1992. Optical dating of young (modern) sediments using quartz: Results from a selection of depositional environments. Quat. Sci. Rev. 11, 153–159. https://doi.org/10.1016/0277-3791(92)90057-F

Stone, J.O., 2000. Air pressure and cosmogenic isotope production. J. Geophys. Res. Solid Earth 105, 23753–23759. https://doi.org/10.1029/2000JB900181

Stuiver, M., Polach, H.A., 1977. Discussion reporting of ^{14}C data. Radiocarbon 19, 355–363.

Talley, L.D., 2013. Closure of the global overturning circulation through the Indian, Pacific, and southern oceans. Oceanography 26, 80–97. https://doi.org/10.5670/oceanog.2013.07

Tanaka, S., Inoue, T., 1979. ^{10}Be dating of North Pacific sediment cores up to 2.5 million years B.P. Earth Planet. Sci. Lett. 45, 181–187. https://doi.org/10.1016/0012-821X(79)90119-5

Tanaka, S., Inoue, T., Imamura, M., 1977. The ^{10}Be method of dating marine sediments - Comparison with the paleomagnetic method. Earth Planet. Sci. Lett. 37, 55–60. https://doi.org/10.1016/0012-821X(77)90145-5

Taylor, P.J., Mitchell, W.A., 2000. The Quaternary glacial history of the Zanskar Range, north-west Indian Himalaya, in: Quaternary International. Pergamon, pp. 81–99. https://doi.org/10.1016/S1040-6182(99)00038-5

Tessier, A., Campbell, P.G.C., Bisson, M., 1979. Sequential Extraction Procedure for the Speciation of Particulate Trace Metals, ANALYTICAL CHEMISTRY. UTC.

Thayyen, R.J., Dimri, A.P., 2014. Factors controlling Slope Environmental Lapse Rate (SELR) of temperature in the monsoon and cold-arid glacio-hydrological regimes of the Himalaya. Cryosph. Discuss. 8, 5645–5686. https://doi.org/10.5194/TCD-8-5645-2014

Thellier, E., 1959. On the intensity of the Earth's magnetic field in the historical and geological past 15, 285–376.

Thompson, L.G., Yao, T., Davis, M.E., Henderson, K.A., Mosley-Thompson, E., Lin, P.N., Beer, J., Synal, H.A., Cole-Dai, J., Bolzan, J.F., 1997. Tropical climate instability: The last glacial cycle from a Qinghai- Tibetan ice core. Science. 276, 1821–1825. https://doi.org/10.1126/science.276.5320.1821

Tomczak, M., Godfrey, J.S., 2003. Regional oceanography: an introduction. Daya books.

Trauth, M.H., Strecker, M.R., 1999. Formation of landslide-dammed lakes during a wet period between 40,000 and 25,000 yr B.P. in northwestern Argentina. Palaeogeogr. Palaeoclimatol. Palaeoecol. 153, 277–287. https://doi.org/10.1016/S0031-0182(99)00078-4

UNESCO, 1971. Discharge of selected rivers of the world, vol. III (. ed. Unesco.

Upadhyay, R., Frisch, W., Siebel, W., 2008. Tectonic implications of new U-Pb zircon ages of the Ladakh batholith, Indus suture zone, northwest Himalaya, India. Terra Nov. 20, 309–317. https://doi.org/10.1111/j.1365-3121.2008.00822.x

Valet, J.P., 2003. Time variations in geomagnetic intensity. Rev. Geophys. 41.

https://doi.org/10.1029/2001RG000104

Valet, J.P., Bassinot, F., Bouilloux, A., Bourlès, D., Nomade, S., Guillou, V., Lopes, F., Thouveny, N., Dewilde, F., 2014. Geomagnetic, cosmogenic and climatic changes across the last geomagnetic reversal from Equatorial Indian Ocean sediments. Earth Planet. Sci. Lett. 397, 67–79. https://doi.org/10.1016/j.epsl.2014.03.053

Van Dover, C.L., Humphris, S.E., Fornari, D., Cavanaugh, C.M., Collier, R., Goffredi, S.K., Hashimoto, J., Littey, M.D., Reysenbach, A.L., Shank, T.M., Von Damm, K.L., Banta, A., Gallant, R.M., Götz, D., Green, D., Hall, J., Harmer, T.L., Hurtado, L.A., Johnson, P., McKiness, Z.P., Meredith, C., Olson, E., Pan, I.L., Turnipseed, M., Won, Y., Young, C.R., Vrijenhoek, R.C., 2001. Biogeography and ecological setting of Indian Ocean hydrothermal vents. Science. 294, 818–823. https://doi.org/10.1126/science.1064574

Vance, D., Bickle, M., Ivy-Ochs, S., Kubik, P.W., 2003. Erosion and exhumation in the Himalaya from cosmogenic isotope inventories of river sediments. Earth Planet. Sci. Lett. 206, 273–288. https://doi.org/10.1016/S0012-821X(02)01102-0

von Blanckenburg, F., Bouchez, J., Wittmann, H., 2012. Earth surface erosion and weathering from the ^{10}Be (meteoric)/ ^{9}Be ratio. Earth Planet. Sci. Lett. 351–352, 295–305. https://doi.org/10.1016/j.epsl.2012.07.022

von Blanckenburg, F., O'Nions, R.K., Belshaw, N.S., Gibb, A., Hein, J.R., 1996. Global distribution of beryllium isotopes in deep ocean water as derived from Fe-Mn crusts. Earth Planet. Sci. Lett. 141, 213–226. https://doi.org/10.1016/0012-821X(96)00059-3

Wacker, L., Fülöp, R.H., Hajdas, I., Molnár, M., Rethemeyer, J., 2013. A novel approach to process carbonate samples for radiocarbon measurements with helium carrier gas. Nucl. Instruments Methods Phys. Res. Sect. B Beam Interact. with Mater. Atoms 294, 214–217. https://doi.org/10.1016/j.nimb.2012.08.030

Wacker, L., Němec, M., Bourquin, J., 2010. A revolutionary graphitisation system: Fully automated, compact and simple. Nucl. Instruments Methods Phys. Res. Sect. B Beam Interact. with Mater. Atoms 268, 931–934. https://doi.org/10.1016/j.nimb.2009.10.067

Walker, M., 2005. Quaternary dating methods. John Wiley and Sons.

Wang, Y., Cheng, H., Edwards, R.L., Kong, X., Shao, X., Chen, S., Wu, J., Jiang, X., Wang, X., An, Z., 2008. Millennial- and orbital-scale changes in the East Asian monsoon over the past 224,000 years. Nature 451, 1090–1093. https://doi.org/10.1038/nature06692

Wang, Y.J., Cheng, H., Edwards, R.L., An, Z.S., Wu, J.Y., Shen, C.C., Dorale, J.A., 2001. A high-resolution absolute-dated late pleistocene monsoon record from Hulu Cave, China. Science. 294, 2345–2348. https://doi.org/10.1126/science.1064618

Weinberg, R.F., Dunlap, W.J., 2000. Growth and deformation of the Ladakh Batholith, Northwest Himalayas: Implications for timing of continental collision and origin of calc-alkaline batholiths. J. Geol. 108, 303–320. https://doi.org/10.1086/314405

Willenbring, J.K., von Blanckenburg, F., 2010. Meteoric cosmogenic Beryllium-10 adsorbed to river sediment and soil: Applications for Earth-surface dynamics. Earth-Science Rev. 98, 105–122. https://doi.org/10.1016/j.earscirev.2009.10.008

Williamson, D., Jelinowska, A., Kissel, C., Tucholka, P., Gibert, E., Gasse, F., Massault, M., Taieb, M., Van Campo, E., Wieckowski, K., 1998. Mineral-magnetic proxies of erosion/oxidation cycles in tropical maar-lake sediments (Lake Tritrivakely, Madagascar): paleoenvironmental implications. Earth Planet. Sci. Lett. 155, 205–219. https://doi.org/10.1016/S0012-821X(97)00217-3

Wittmann, H., Von Blanckenburg, F., Bouchez, J., Dannhaus, N., Naumann, R., Christl, M., Gaillardet, J., 2012. The dependence of meteoric ^{10}Be concentrations on particle size in Amazon River bed sediment and the extraction of reactive ^{10}Be/ ^{9}Be ratios.

Chem. Geol. 318–319, 126–138. https://doi.org/10.1016/j.chemgeo.2012.04.031

Wittmann, H., Von Blanckenburg, F., Dannhaus, N., Bouchez, J., Gaillardet, J., Guyot, J.L., Maurice, L., Roig, H., Filizola, N., Christl, M., 2015. A test of the cosmogenic ^{10}Be(meteoric)/^{9}Be proxy for simultaneously determining basin-wide erosion rates, denudation rates, and the degree of weathering in the Amazon basin. J. Geophys. Res. F Earth Surf. 120, 2498–2526. https://doi.org/10.1002/2015JF003581

Wünnemann, B., Demske, D., Tarasov, P., Kotlia, B.S., Reinhardt, C., Bloemendal, J., Diekmann, B., Hartmann, K., Krois, J., Riedel, F., Arya, N., 2010. Hydrological evolution during the last 15 kyr in the Tso Kar lake basin (Ladakh, India), derived from geomorphological, sedimentological and palynological records. Quat. Sci. Rev. 29, 1138–1155. https://doi.org/10.1016/j.quascirev.2010.02.017

Yadava, M.G., Ramesh, R., 1999. Speleothems—useful proxies for past monsoon rainfall.

Yang, Y.L., Kusakabe, M., Southon, J.R., 2003. 10Be profiles in the East China Sea and the Okinawa Trough. Deep. Res. Part II Top. Stud. Oceanogr. 50, 339–351. https://doi.org/10.1016/S0967-0645(02)00458-7

Yiou, F., Raisbeck, G.M., Baumgartner, S., Beer, J., Hammer, C., Johnsen, S., Jouzel, J., Kubik, P.W., Lestringuez, J., Stiévenard, M., Suter, M., Yiou, P., 1997. Beryllium 10 in the Greenland Ice Core Project ice core at Summit, Greenland. J. Geophys. Res. Ocean. 102, 26783–26794. https://doi.org/10.1029/97JC01265

Yu, G., Xue, B., Wang, S.M., Liu, J., 2000. Lake-level records of China during the Last Glacial Maximum and its climatic implications. Chin. Sci. Bull 45, 25.

Zech, R., Abramowski, U., Glaser, B., Sosin, P., Kubik, P.W., Zech, W., 2005. Late Quaternary glacial and climate history of the Pamir Mountains derived from cosmogenic 10Be exposure ages. Quat. Res. 64, 212–220. https://doi.org/10.1016/J.YQRES.2005.06.002

Zhang, H.C., Ming, Q.Z., Lei, G.L., Zhang, W.X., Fan, H.F., Chang, F.Q., Wünnemann, B., Hartmann, K., 2006. Dilemma of dating on lacustrine deposits in an hyperarid inland basin of NW China. Radiocarbon 48, 219–226. https://doi.org/10.1017/S0033822200066418

Zheng, M., Adolphi, F., Sjolte, J., Aldahan, A., Possnert, G., Wu, M., Chen, P., Muscheler, R., 2020. Solar and climate signals revealed by seasonal ^{10}Be data from the NEEM ice core project for the neutron monitor period. Earth Planet. Sci. Lett. 541, 116273. https://doi.org/10.1016/J.EPSL.2020.116273

Zhou, Y., Li, Z., Li, J., 2017. Slight glacier mass loss in the Karakoram region during the 1970s to 2000 revealed by KH-9 images and SRTM DEM. J. Glaciol. 63, 331–342. https://doi.org/10.1017/JOG.2016.142

List of Publications

Associated with the thesis work:

1. **Jena, P.S.,** Bhushan, R., Ajay, S., Bharti, N., Sudheer, A.K., 2022. ^{10}Be depositional flux variation in the central Indian Ocean during the last 43 ka. *Science of the Total Environment.* 802, 149808. https://doi.org/10.1016/j.scitotenv.2021.149808
2. **Jena, P.S**., Bhushan, R., Shivam, A., Nambiar, R., Bharti, N., 2021. Production rate variation and changes in sedimentation rate of marine core dated with meteoric ^{10}Be and ^{14}C. *Journal of Environmental Radioactivity*. 237, 106678. https://doi.org/10.1016/j.jenvrad.2021.106678
3. **Jena, P.S.**, Bhushan, R., Raj, H., Dabhi, A.J., Sharma, S., Shukla, A.D., Juyal, N., 2022. Relict proglacial lake of Spituk (Leh), northwest (NW) Himalaya: A repository of hydrological changes during Marine Isotopic Stage (MIS)-2. *Palaeogeography, Palaeoclimatology, Palaeoecology.* 111164. https://doi.org/10.1016/j.palaeo.2022.111164

Other publications

4. Ali, S.N., Agrawal, S., Sharma, A., Phartiyal, B., Morthekai, P., Govil, P., Bhushan, R., Farooqui, S., **Jena, P.S.,** Shivam, A., 2020. Holocene hydroclimatic variability in the Zanskar Valley, Northwestern Himalaya, India. *Quaternary Research*. 1–17. https://doi.org/10.1017/qua.2020.22
5. Barik, S.S., Singh, R.K., **Jena, P.S.,** Tripathy, S., Sharma, K., Prusty, P., 2019. Spatio-temporal variations in ecosystem and CO_2 sequestration in coastal lagoon: A foraminiferal perspective. *Marine Micropaleontology*. 147, 43–56. https://doi.org/10.1016/j.marmicro.2019.02.003

6. Bharti, N., Bhushan, R., Skinner, L., Muruganantham, M., **Jena, P.S.,** Dabhi, A., Shivam, A., 2022. Evidence of poorly ventilated deep Central Indian Ocean during the last glaciation. *Earth and Planetary Science Letters*. 582, 117438. https://doi.org/10.1016/J.EPSL.2022.117438
7. Phartiyal, B., Ali, S.N., Sharma, A., Agrawal, S., Nag, D., Tiwari, P., Kumar, M., Morthekai, P., Govil, P., Thakur, B., Bhushan, R., **Jena, P.S.**, Shivam, A., 2022. Palaeoclimatic variability during last eight millennia from a morainal lake in Zanskar, northwest Himalaya. *Journal of Palaeosciences* 71, 75–88.
8. Patel, N., Trivedi, P., Agnihotri, R., Rai, N., Sathe, V., Khonde, N., Bhushan, R., **Jena, P.S.**, Shivam, A., Kumar, A., 2022. New chronology for megalithic burials in vidarbha (central india): insights into contemporary hydro-climate and food habits. *Radiocarbon* 00, 1–17. https://doi.org/10.1017/RDC.2022.47
9. Raj, H., Bhushan, R., Banerji, U.S., **Jena, P.S.,** Dabhi, A.J., 2022. Seasonal variation of surface seawater radiocarbon in the Andaman Sea as recorded in coral. *Journal of Environmental Radioactivity.* 255, 107021. https://doi.org/10.1016/J.JENVRAD.2022.107021
10. Samal, P., Singarasubramanian, S. R., Srivastava, **Jena, P.S.,** Shivam, A., Bhushan, R. Coastal vegetation dynamics in response to climatic and relative sea level changes in Mahanadi River delta, NE coast of India. *Palynology.* (accepted)